2018

Investigation of Geothermal Heat Extraction Using Supercritical Carbon Dioxide (sCO2) and Its Utilization in sCO2-based Power Cycles and Organic Rankine Cycles - A Thermodynamic & Economic Perspective

Xingchao Wang
Lehigh University

Investigation of Geothermal Heat Extraction Using Supercritical Carbon Dioxide (sCO_2) and Its Utilization in sCO_2-based Power Cycles and Organic Rankine Cycles - A Thermodynamic & Economic Perspective

by

Xingchao Wang

Presented to the Graduate and Research Committee
of Lehigh University
in Candidacy for the Degree of
Doctor of Philosophy

in

Mechanical Engineering

Lehigh University
May, 2018

DISSERTATION SIGNATURE SHEET

Approved and recommended for acceptance as a dissertation in partial fulfillment of the requirements for the degree of Doctor of Philosophy.

Student Name: Xingchao Wang

Dissertation Title: Investigation of Geothermal Heat Extraction Using Supercritical Carbon Dioxide (sCO_2) and Its Utilization in sCO_2-based Power Cycles and Organic Rankine Cycles - A Thermodynamic & Economic Perspective

_____
Date

_____
Dr. Alparslan Oztekin, Dissertation Advisor

_____
Accepted Date

Committee Members:

_____
Dr. Alparslan Oztekin, Committee Chairman

_____
Dr. Edward K. Levy, Committee Member

_____
Dr. Carlos E. Romero, Committee Member

_____
Dr. Arindam Banerjee, Committee Member

_____
Dr. Justin W. Jaworski, Committee Member

Acknowledgements

Firstly, I would like to highly thank my advisor, Dr. Edward K. Levy, the emeritus professor and the former Director of the Energy Research Center (ERC) at Lehigh University, for his continuous support and patience during my doctoral study. Dr. Levy has been an exceptional advisor, both for my study and life. He is always full of passion about the research work, even if he is retired. I was astonished that he was diagnosed with cancer just before the accomplishment of this dissertation. Sadly, he would not be able to be my committee member anymore due to his fight with cancer. Although, he is not able to review my final dissertation at this time, I wish I could present the work to him as it contains his efforts and concerns.

My special thanks to Dr. Carlos E. Romero, the Director of the Energy Research Center at Lehigh University. His professionalism dealing with research will greatly benefit my career. He is both a friend and a mentor to me, and this great relationship helps gain a fast understanding of the energy industry and academic areas in the United States. Without his help, my doctoral study at the ERC would not have gone so smoothly.

I would also like to thank my committee chair, Dr. Alparslan Oztekin, and the other committee members, Dr. Arindam Banerjee and Dr. Justin W. Jaworski, who are the professors of the Department of Mechanical Engineering at Lehigh University, for their valuable suggestions and rigorous attitude in research to make this piece of work better and more consummate.

I would like to thank Mr. Zheng Yao, a research scientist, Mrs. Colleen Munion, the administrative manager at Lehigh's ERC, and Mrs. Ursla Levy, the former administrative

manager at Lehigh's ERC, for their help during my doctoral study. Thanks to my lab mate, Mr. Chunjian Pan, for his efforts to help me to set up the very time intensive simulation work. Thanks to my lab mate, Mr. Joshua Charles, for his help during my graduate study. We had a lot of meaningful and enjoyable conversations which made life not so boring. Thanks to Professor Zongliang Qiao, from Southeast University in China and also a visiting scholar at the ERC, with whom I had a lot of helpful discussions during the final accomplishment of this dissertation. I would also like to thank Dr. Lehua Pan from the Lawrence Berkeley National Laboratory of University of California, Berkeley, for the helpful suggestions on the geothermal heat extraction simulation.

This study was funded by the Mexican National Council of Science and Technology (CONACYT in Spanish), under the Sectorial Fund for Energy Sustainability, CONACYT-Secretary of Energy (No. S0019-2012-04). I thank the administrators of the Mexican Center for Innovation in Energy-Geothermal (CEMIE-Geo in Spanish) for their support and administration of the program. Additionally, I would like to thank the Lawrence Berkeley National Laboratory of University of California, Berkeley, for providing the research version of the T2Well/ECO2N v.2 code for high temperature simulations.

Lastly, I am grateful for my family. Without them, I could not have finished this dissertation. Thank you for continuously supporting me in my research. Thank my wife, Menglu Gao, and my son, Lucas Wang, for being in my life and bringing me happiness and courage. I am also grateful to both our parents, especially my mother, Mrs. Xueqin Li. Thank you for all you have done for me.

Table of Contents

List of Tables

List of Figures

Nomenclature

Roman symbols

L_0	Geothermal reservoir length [m]
H_0	Distance from surface of the ground to bottom of the reservoir [m]
H_1	Distance from the ground surface to cap rock [m]
H_2	Distance from cap rock to the bottom of reservoir [m]
z	Vertical distance below the ground surface, well depth [m]
R	The radial distance from the injection well to production well [m]
m_{VG}	Van Genuchten parameter
Q	Heat duty [MW_{th}]
T	Temperature [℃]
p	Pressure [MPa]
h	Specific enthalpy [kJ/kg]
s	Specific entropy [$kJ/kg \cdot K$]
e	Specific exergy [kJ/kg]
$\dot{m}$	Mass flow rate [kg/s]
W	Power output [MW_e]
w	Specific power output [$kW_e/(kg/s)$]
ΔT	Temperature difference [℃]
g	Gravitational acceleration [m/s^2]
v	Velocity [m/s]

Z	Compressibility factor
r	Interest rate
n	Period of loan in months
b_{CO_2}	CO_2 sequestration credits [$/t]
E_{tot}	Total power generation [kWh]
F_p	Pressure factor
C_p	Purchase cost
C_{BM}	Purchase cost
F_{BM}	Bare module cost factor
F_{add}	Additional cost factor
F_{contcy}	Contingency cost factor

Subscripts

inj	Injection	*cond*	Condenser
prod	Production	*cr*	Critical point
reinj	Re-injection	*tn*	Turning point
geo	Geothermal	*sv*	Saturated vapor
well	Geothermal well	*th*	Thermal
net	Net value	*ex*	Exergy
i	Location point	*scrit*	Supercritical
evp	Evaporator	*pinch*	Pinch point
pump	Pump	*s*	Isentropic process
t	Turbine	*a*	Actual process
comp	Compressor	*cal*	Calculated value

real	Real value	*err*	Error [%]
opt	Optimal	*cyc*	Cycle
0	Reference state	*sys*	System
min	Minimum	*tot*	Total
max	Maximum	*WF*	Working fluid
in	Inlet	*SH*	Superheating
out	Outlet		

Greek letters

υ	Specific Volume [m^3/kg]
ρ	Density [kg/m^3]
ξ	The slope of saturated vapor curve
η	Efficiency [%]
ε	Working fluid type classification factor
σ	Molecular complexity

Acronyms

RHS	Right Hand Side	ORC	Organic Rankine cycle
LHS	Left Hand Side	HX	Heat exchanger
GWP	Global warming potential	*CV*	Control volume
ODP	Ozone depletion potential	*PF*	Payment factor
NFPA	National Fire Protection Association		
IHX	Intermediate heat exchanger		
sCO_2	Supercritical carbon dioxide		
LCOE	Levelized Cost of Electricity		
O&M	Operations and maintenance		

Abstract

CO_2 capture and sequestration in deep saline aquifers is widely considered to be a leading option for controlling greenhouse gas emissions. One such possibility involves injection of supercritical carbon dioxide (sCO_2) into a high-permeability geothermal reservoir. In addition to the benefit of sequestering the CO_2 in reservoirs, the CO_2 can be used to mine geothermal heat for utilization above ground. This study adopts TOUGH2-T2Well/ECO2N multi-phase flow solver which has the capability to model fully coupled geothermal wellbores and reservoir to obtain desirable sCO_2 production flow rates, temperatures and pressures for power generations.

As geothermal energy is widely recognized as a low grade heat source, power cycles with capabilities to convert low grade energy into electricity, such as Organic Rankine Cycle (ORC), have been considered. Additionally, sCO_2-based power cycles have also been investigated comprehensively, since the similar temperature profiles between produced sCO_2 from geothermal reservoirs and working fluid sCO_2 potentially offer the advantages of avoiding pinch points to achieve better cycle performance. Moreover, the unique physical properties near critical point of CO_2 are significant contributors for the considerably low compression work leading to higher net power output. Regarding thermodynamic optimization analyses, the maximum net power output is selected as the objective of optimizing cycle performance both for sCO_2-based power cycles and ORCs.

Possible cycle improvement methods have been taken into consideration and different configurations of sCO_2-based power cycles have been analyzed thermodynamically. The

direct turbine expansion, sCO_2 Brayton cycle with pre-compression and inter-cooling, and transcritical sCO_2 cycle have been chosen to perform cost estimation and optimization analyses. On the other hand, working fluid selection criteria have been proposed for ORCs to find out the most suitable working fluids using hot produced sCO_2 from geothermal reservoirs. Considering cycle performance, working fluid physical property, operating pressure level and design complexity, a subcritical ORC with R245fa as working fluid is selected as the most competent ORC. Accordingly, to compare with the conventional geothermal power generation system, the cost estimation and optimization analyses have been accomplished by finding the minimum levelized cost of electricity (LCOE) for a nominal power plant capacity of 30 MW_e. The plant capital cost, well cost, and operations and maintenance (O&M) cost are taken into account. The optimal results indicate that the LCOEs of selected four promising power generation technologies range from \$0.276/kWh to \$0.316/kWh in which more than half the portion is contributed by the O&M costs of cooling loads of rejecting heat for power cycles and geothermal loop CO_2 re-injections.

Analyses have been performed to investigate the effects of reducing the cooling O&M cost and counting CO_2 credit of sequestration on the LCOEs. It has been found if the cooling O&M cost is reduced to one quarter of the original value, the LCOEs can decrease 43 – 48% without counting the CO_2 credit. On the other hand, if the counted CO_2 credit is over \$2/t for all new proposed power generation options where the largest breakeven point occurs, then they are all competitive compared to conventional geothermal power plants. Furthermore, improvements for reducing LCOEs of power generation options have been discussed and suggested, such as performing more detailed geothermal heat mining simulations, and adopting different cooling techniques to reduce O&M costs.

Chapter 1 Introduction and Background

Geothermal power generation is using the thermal energy from the hot subsurface of the Earth to generate electric power. Typically, hot brine is used as heat extraction working fluid to bring heat underground and the portion of the thermal energy is converted into electricity through power generation systems. Then, cold brine is re-injected through injection wells back into a geothermal reservoir. However, such conventional hydrothermal geothermal power generation system is limited in size and location, which are big uncertainties of geothermal fluid significantly affecting the design parameters of the power plant downstream [1]. These disadvantages impede the development of using geothermal energy and access the high geothermal energy potential for electric power generation as a renewable energy source with relatively low cost. Moreover, most of geothermal energy is contained in rocks which have low fracture permeability and lack of fluid circulation [2]. Therefore, emerging technologies are needed to access and extract the abundant of geothermal energy.

1.1 Enhanced Geothermal System (EGS) and CO_2-Plume Geothermal (CPG) system

Enhanced Geothermal Systems (EGS), sometimes called engineered geothermal systems, were firstly developed at the Los Alamos National Laboratory (LANL) in the U.S. which offers the chance to expand the use of geothermal resources for power generation [3]. The concept of EGS, often referred to as “Hot Dry Rock” (HDR), is to extract thermal energy by creating artificial geothermal reservoirs where water can be added to be heated by contact with the hot rocks and then flows back to the surface. These EGS systems typically

use water to extract geothermal energy by creating a subsurface fracture system. Furthermore, for an EGS, a maintaining fluid circulation is set up through the fracture network and wellbores which connect the surface and underground. There are several EGS sites tested around the world which provide operation experiences and keep improving this technology [4-11]. It was predicted by MIT that using EGS and other unconventional geothermal resources can provide 100,000 MW_e of base-load electric power generation capacity by 2050 [9].

Using CO_2 as a heat extraction working fluid in geothermal heat extraction has been gaining importance since 2000s. Coupling carbon capture system with geothermal heat mining is a novel and attractive technology [12, 13]. Supercritical CO_2 (sCO_2) was first proposed as a more efficient heat extraction fluid than water for heat mining in EGS in 2000 by Brown et al. [14]. Brown et al. indicated that using sCO_2 as the heat mining working fluid in EGS will have potential advantages like lower pumping power near its critical point, high mobility and good ability being used above the critical point of water since silica will dissolve in water significantly above the critical point of water. Pruess then stated that CO_2 would achieve more favorable heat extraction than brine and CO_2 may avoid unfavorable rock-fluid interactions which occurs in water-based systems [15]. In addition to the benefits of using CO_2 to mine geothermal heat, a portion of injected CO_2 will be simultaneously sequestrated permanently. Moreover, sCO_2 was also considered to generate electricity before it was re-injected underground. Studies, projects and attempts were implemented to demonstrate the feasibilities and superiorities of using CO_2 as heat extraction fluid in place of water for geothermal heat extraction as well as utilizing the extracted thermal energy to generate electric power. Gurgenic et al. proposed a power

generation system using sCO_2 as a working fluid which was from EGS and predicted achieving potential high power conversion efficiency [16]. A CO_2 thermosiphon design power plant was also discussed to directly use CO_2 produced from EGS. The simulation results showed that a CO_2-based system had a comparable net power output to a conventional geothermal plant with simpler system design [17, 18]. However, an EGS is a man-made or engineered geothermal reservoir created by hydro-fracturing which potentially can cause seismicity since the critical fracture stresses of geologic formations are intentionally exceeded. In addition, significantly large flow resistance is expected due to this permeability-enhancing technology by the critical fracture stresses of geologic formations, which potentially requires excessive compression work.

Recently, studies on high-permeability hydrothermal geothermal reservoirs were conducted by Randolph, Adams and Saar et al.. A concept of CO_2-Plume Geothermal (CPG) system involving CO_2 injection and production was proposed, which sCO_2 has been proven to work more efficiently for power generation than water/brine geothermal systems due to its high mobility and larger density change with temperature, resulting in a buoyance-driven loop to reduce or eliminate recompression of CO_2 to re-inject it back to the geothermal reservoir. They stated that CPG system is utilizing existing, high-permeability and high-porosity geologic reservoirs with a low permeable caprock. Moreover, such natural geothermal reservoirs have considerably larger size than EGS reservoirs. Consequently, CPG systems are expected to have much larger CO_2 sequestration potential than EGS. [12, 19-22]. All these investigations and studies indicated that CO_2 can achieve better thermodynamic and economic performance compared to geothermal hot water in power generation applications. An additional benefit

is that the injected CO_2 will be trapped into the geothermal reservoir permanently which is another benefit of this novel application. Differ from CO_2-EGS, CPG is using CO_2 to extract heat from naturally permeable, or sedimentary basins [12]. As CO_2 is injected into a geothermal reservoir, the brine initially occupying the reservoir is displaced by CO_2. A CO_2-plume then is formed and hot CO_2 is produced by a production wellbore [19].

Regarding this novel heat extraction process, simulation studies of CO_2-based geothermal heat extraction were conducted by many researches using TOUGH2, which is a multi-phase flow solver. TOUGH2 developed at the Lawrence Berkeley National Laboratory (LBNL) in the early 1980s has the capability to model multi-phase and multi-components in porous media like geothermal reservoirs [23]. On the basis of TOUGH2, ECO2N, a fluid property module, was developed considering the thermodynamics and thermo-physical properties of H_2O-NaCl-CO_2 mixtures in a single phase as well as two-phase mixtures. An upgraded version of ECO2N (ECO2N v2.0) was released in 2017 which has the capability to model the H_2O-NaCl-CO_2 mixtures system up to 300 ℃ [24, 25]. Furthermore, in order to be able to simulate the non-isothermal, multiphase and multi-component flows in the integrated wellbore-reservoir system, the extension of TOUGH2 called T2Well was also developed by LBNL in 2014 [26, 27]. With the techniques introduced above, geothermal heat mining simulations have been performed comprehensively in this study. To make the study more specific and realistic, an assessment of the feasibility of using sCO_2 for heat mining for twenty-one geothermal sites in Mexico was reported by the research group of the Energy Research Center (ERC) at Lehigh University [28]. Consequently, the inputs of the geothermal heat mining simulation are based on the Mexican geological conditions.

1.2 Supercritical CO_2-based Power Cycles

CO_2 as a non-corrosive and non-toxic substance has been gaining attention to be used as a working fluid of power cycles. Moreover, since no pinch point occurs between hot produced sCO_2 from geothermal reservoirs and CO_2 as a cycle working fluid, better heat transfer performance potentially can be achieved which can lead to a higher cycle thermodynamic efficiency. In addition, the liquid-like large density and gas-like low dynamic viscosity near the critical point of CO_2 offer advantages of low compression work and compactness of turbine machinery. Another advantage of sCO_2 Brayton cycle is that it has simpler cycle design than the steam Rankine cycle. This technology may also indirectly contribute to reducing CO_2 emissions by sequestrating CO_2 as well as emitting no CO_2 during the power generation process.

SCO_2 Brayton cycle was first proposed by Feher in 1960s and was identified as a promising power cycle due to its high thermal efficiency [29]. Then, Angelino found the recompression sCO_2 cycles exhibits better efficiencies than reheat steam Rankine cycles at turbine inlet temperature higher than 650 ℃ [30]. Recently, sCO_2 Brayton cycles have gained a great interest in its nuclear reactors application due to its compactness, safety, simple design, efficient performance and economy [31-37]. In addition, many researchers were also considering using it in other applications, such as concentrated solar power (CSP), coal-fired power plant, and waste heat recovery [38-45]. However, these applications were only focusing on using the heat sources with temperature higher than 450 ℃.

Various configurations of sCO_2-based power cycle designs were proposed by applying cycle improvement methods including recuperating, pre-compression, inter-cooling, reheating, etc. in order to achieve better cycle performance [46, 47]. Turchi et al. summarized the major considerations to improve the efficiency of a sCO_2 power cycle: (1) Increase turbine inlet temperature; (2) Split compression duty to a main compressor and a recompression compressor; (3) Use compressor intercooling; (4) Split turbine into two with reheating; (5) Adopt dual shaft designs to separate the compressor from the power turbine to make each run at an optimized rotational speed; (6) Add bottom cycle (such as ORC) or cascade sCO_2 cycle; (7) Combine above options [47]. The more detailed configuration design has been performed in this work specifically for utilizing sCO_2 produced from geothermal reservoirs. Direct turbine expansion is another more straightforward way to utilize sCO_2 produced from geothermal reservoirs to generate electricity, while the hot sCO_2 directly expands through a turbine to generate electric power. Adams et al. generally talked about the CO_2 direct power generation system with the CPG system but no cost estimation and optimization were taken into account [20]. Transcritical sCO_2 cycle, as partial cycle is operating below the critical point is classified as sCO_2-based power cycle, which was discussed thermodynamically by many researchers for different applications, such as geothermal energy, solar thermal energy and waste heat [48-56]. Wang and Song et al. both introduced the transcritical sCO_2 cycle employing liquefied natural gas as the heat sink of transcritical sCO_2 cycle which potentially needs large cooling loads [48, 51]. The Water temperature of 60 – 90 ℃ was selected as a low grade heat by Li et al. to investigate a supercritical of transcritical sCO_2 cycle with ejector and a thermal efficiency ranging from 6 – 8% was predicted [56]. A combined sCO_2-based

and ORC power system was proposed by a research group working with Lehigh's ERC, to utilize the produced CO_2 from geothermal reservoirs with only generic production conditions as the inputs of power systems [57]. A prototype sCO_2 Brayton cycle test facility was set up by Sandia National Laboratory (SNL) in 2010 to obtain experimental data on CO_2 compression near the critical point of CO_2. These early tests were measuring leakage flow rates, windage loses, balance thrust loads and compressor performance characteristics. The next step for SNL is building a recompression sCO_2 Brayton cycle with capacity of 250 kW_e [58].

Cost studies of sCO_2-based systems are also limited. Atrens et al. came up with and summarized a series of correlations to well-estimated component costs of CO_2-EGS [59]. Kouta et al. tried to the recompression sCO_2 cycle, regeneration sCO_2 cycle, solar field and storage costs but only used rough estimations from literature [60]. An assessment of sCO_2 plant for the nuclear reactor was performed by MIT in 2004, which the prediction was based on the helium based system working at a temperature higher than 550 ℃ [61]. In sum, no specific cost analysis for sCO_2-based power cycle for low-temperature heat sources and even less for hot sCO_2 as a heat source.

Despite advantages and thermodynamic performance of sCO_2-based power cycles over conventional power cycles have been demonstrated extensively, however, no full scale and commercialized sCO_2-based power plant exists. In addition, the theoretical cost estimations for sCO_2-bsed power cycles are also very limited. Furthermore, no comprehensive analyses combining with geothermal heat mining systems are available.

1.3 ORCs and Working Fluid Selection

In addition to sCO_2-based power cycles, employing ORCs to generate electricity has been widely studied for different low- and medium-grade heat sources, such as waste heat, solar thermal energy, and geothermal energy etc.. The performance of ORCs significantly depends on the working fluid used. Hence, the working fluid selection is very critical for different heat sources to achieve the optimal performance. However, it is still challenging to establish universal ORC working fluid selection criteria since the selection process consists of a combination of thermal performance, cost and environmental impacts with different heat sources conditions. Research on working fluid selection was carried out for biomass power generation, waste heat, geothermal hot water, and solar thermal energy, etc. [62-75]. Different selection criteria were presented and specific working fluids were selected for certain heat sources and ORC layouts. A more comprehensive working fluid selection method with screening 35 selected working fluids was developed by Chen et al. and the different layouts of ORCs were also discussed. A chart named $T-\xi$ was proposed by the authors to categorize working fluids by their critical temperature and fluid type (dry, wet or isentropic) [76]. Working fluid selection and evaluation studies were performed by Zhang et al. using thermal efficiency, exergy efficiency, recovery efficiency, heat exchanger area per unit power output and levelized energy cost to evaluate the performance of 10 different working fluids with a heat source of geothermal water with a temperature of 90 ℃. It was found that R123 in subcritical provided the largest cycle efficiencies and R125 had the largest recovery efficiency without considering the environmental and safety impacts [77]. Maraver et al. attempted to provide optimization

guidelines for a wide range of operating conditions, i.e. different heat sources [78]. However, the temperature profiles in this study were selected from the approximate combination of typical heat sources, which may not work for sCO_2.

Pinch point is another very critical parameter for the evaporator design and cycle performance of the ORC system. Liu et al. investigated the effects of the different geothermal water temperatures and the pinch points on the net power output and system investment of a subcritical ORC system with R245fa as the working fluid [79]. A parameter named *PREDICTOR* was defined by Yu et al. to predict the pinch point and then determined the optimal working fluid and operating conditions [67]. A method to seek the location of heat transfer pinch point in the evaporator was introduced by Guo et al. [80].

Since ORC power generation technology is still under development, it is difficult to accurately estimate the cost of a general ORC plant. The ORC plant cost is significantly related to the characteristics of heat source, working fluid, and configuration of ORC. Astolfi et al. conducted a techno-economic optimization analysis for ORCs as a binary system to convert geothermal energy into electricity. It was found that the ORC plant costs significantly depend on working fluid type and only four working fluids were investigated [81, 82]. Another cost study of the ORC system was performed to compare the wet cooling tower or air-cooled condenser was more cost-effective. It was concluded that the investment of the wet cooling tower was much lower than the air-cooled condenser, but the water used for spray cooling should be available and in a reasonable price range [83]. Barse et al. conducted a simple cost analysis to find out the relationship between LCOE and critical temperature of working fluid. The LCOE is around $0.045/kWh was calculated

by NREL's simple LCOE calculator, which can only be used as an indicator to select working fluid but not the realistic cost data [84]. A more detailed cost estimation employing widely-used empirical equations was performed by Yang et al.. Yang et al. selected working fluids recommended from previous reviewed work to perform cost analysis. However, only capital cost was estimated and no actual system LCOE was reported [85]. A LCOE of $0.344/kWh was reported for an ORC powered by line-focusing concentrating solar collectors (parabolic trough or linear Fresnel reflector) with R113 as working fluid [66].

Although the existing ORC studies include working fluid selection, economic analysis, and cycle thermodynamic analysis, no comprehensive analyses using produced sCO_2 from geothermal reservoirs are available. Furthermore, since CO_2 has significantly different physical properties than geothermal water, solar thermal heat transfer fluid as well as fossil-fired plant flue gas which have been widely investigated, it is necessary to perform a comprehensive thermodynamic analysis for converting the heat from the novel geothermal heat mining system.

1.4 Dissertation Scope

Although numbers of research focusing on utilizing the geothermal heat extracted by CO_2 were conducted, no research is found to consider both power generation systems in the surface and geothermal heat mining system in the subsurface together for the cost estimation study as well as the optimization analyses. Figure 1–1 illustrates this concept of the integrated system for power generation and CO_2 is simultaneously sequestrated in the geothermal reservoir. In this study, to comprehensively investigate accessing and utilizing

geothermal energy extracted by sCO_2, the geothermal heat mining techniques, integrated with the power cycle systems to convert the geothermal energy have been examined thermodynamically and economically. The optimization algorithms have been used to obtain the most cost-effective and feasible design. Meanwhile, the minimum LCOE has been calculated.

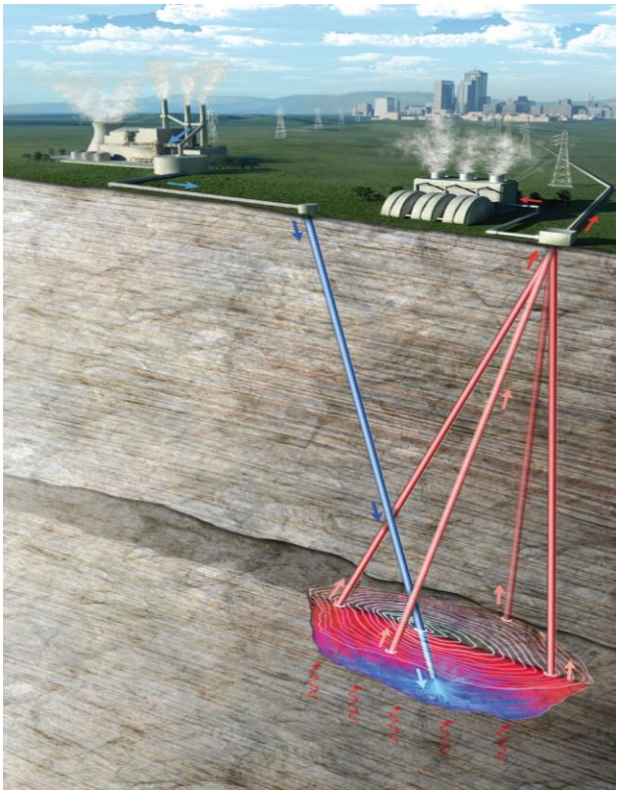

Figure 1–1 Illustration of sCO_2 injection into a geothermal reservoir for heat mining and above-the-ground geothermal energy utilization.

Injecting sCO_2 into a high-permeability geothermal reservoir has been selected as the technique to mine the geothermal heat particularly with the practical geological conditions in Mexico with the assessment of a geothermal heat mining feasibility study for Mexico [28]. Additionally, a research version of TOUGH2-T2Well/ECO2N simulator is employed for the parametric study and optimization analyses. The baseline conditions, which are also

the inputs for power cycle analyses, have been obtained with having the grid convergence study done.

As discussed above, it has been widely considered using different power cycles to convert geothermal energy produced by hydrothermal system, water-EGS or CO_2-EGS. However, studies focusing on utilizing the geothermal heat extracted by CO_2 from a porous media geothermal reservoir are very limited. As CO_2 has been suggested as a better heat extraction fluid than water in geothermal heat mining, the physical properties and characteristics of CO_2 working in the temperature and pressure ranges of geothermal heat sources have been investigated to have better theoretical fundamentals for cycle design and to demonstrate the advantages of sCO_2-based power cycle. In addition, cycle performance improvement methods, including recuperating, pre-compressing, inter-cooling and reheating, have also been investigated. Furthermore, the heat exchanger selection and design for sCO_2-based power cycles are necessary to be performed for cost estimation and optimization.

The selection of organic fluid is a key factor for ORC performance. The detailed analyses have been conducted in this study to select proper organic working fluids for different configurations of ORC with hot produced CO_2 as the heat source. Moreover, cost estimation and optimization analyses have been performed combining both geothermal heat mining simulations and thermodynamic performance of ORC. The comprehensive comparisons have also been conducted.

Chapter 2 Modeling of Geothermal Heat Mining Using CO_2

In this study, geothermal heat mining simulation using CO_2 has been carried out with the TOUGH2, which is a numerical simulator for non-isothermal, multi-phase and multi-component flows. This simulator developed by the Lawrence Berkeley National Laboratory (LBNL) named TOUGH2 is a well-validated commercial software and generally for geothermal reservoir engineering, nuclear waste disposal, environmental assessment and remediation and unsaturated and saturated zone hydrology [86]. However, difficulties for solving the different governing equations together for flow and transport in an integrated system with both wellbores and a porous media geothermal reservoir are: 1). efficiently solving the different governing equations in a uniform framework, 2). the large contrast in temporal and spatial scale between the wellbore and the reservoir which leads to a set of hard solving partial differential equations, 3). interactions between the wellbore and reservoir introducing complexities. In this study, a research version of the T2Well/ECO2N software was provided by the LBNL which is based on the standard TOUGH2 code. This new upgraded and expanded simulator is capable of modeling an integrated system with wellbores connected to a geothermal reservoir [27].

In the T2Well/ECO2N software, the integrated system includes two subdomains where the wellbore is using 1-D two-phase momentum equation and the reservoir is using the 3-D multiphase Darcy's Law. The mass and energy balance equations solved in T2Well/ECO2N are listed in Appendix A1. The essential differences between the governing equations for the wellbore and reservoir are the definitions of energy-flow terms

and the phase velocities. The wellbore energy-balance equations include both kinetic energy and gravitational potential energy. However, in the energy-balance for the reservoir, they are all neglected since the flow velocities are typically very small. Meanwhile, the phase velocities are calculated by the 3-D multiphase Darcy's Law. On the other hand, in the wellbore, the phase velocities are governed by the two-phase momentum equations which also can be found in Appendix A1. The governing equations for the wellbore are simplified to 1-D to obtain mixture velocity with the Drift-Flux-Model (DFM) [87]. The DFM provides an efficient way to obtain two-phase flow velocity. Pan et al. described the theory followed by TOUGH2 to work out the integrated system [27]. Basically, the empirical equation including the gas velocity u_G, the volumetric flux of the mixture j, as well as the drift velocity of gas u_d can be written as:

$$u_G = C_0 j + u_d \tag{2.1}$$

where C_0 is the profile parameter to evaluate local gas saturation and velocity profiles over the pipe cross-section. The volumetric flux of the mixture j can be calculated by:

$$j \equiv S_G u_G + (1 - S_G) u_L \tag{2.2}$$

where S_G is the gas phase saturation, and u_L is the liquid velocity:

$$u_L = \frac{1 - S_G C_0}{1 - S_G} j - \frac{S_G}{1 - S_G} u_d \tag{2.3}$$

With the DFM Equations (2.1) to (2.3), a single equation can be simplified from the momentum equations of two-phase flow in a wellbore:

$$\frac{\partial}{\partial t}\left(\rho_m u_m\right)+\frac{1}{A}\frac{\partial}{\partial z}\left[A\left(\rho_m u_m^2+\gamma\right)\right]=-\frac{\partial P}{\partial z}-\frac{\Gamma f \rho_m |u_m| u_m}{2A}-\rho_m g\cos\theta \tag{2.4}$$

where $\gamma=\left(S_G/1-S_G\right)\left(\left(\rho_G\rho_L\rho_m\right)/\rho_m^{*2}\right)\left[\left(C_0-1\right)u_m+u_d\right]^2$ is caused by slip between the two phases. A is the cross section area of the well bore. Γ is the perimeter of the cross-section. f is the apparent friction which is the function of wall roughness and flow regime. The terms ρ_m, u_m, ρ_m^* and u_d are the mixture velocity, the profile-adjusted average density of the mixture and the drift velocity, respectively. These terms can be expressed as:

$$\rho_m=S_G\rho_G+(1-S_G)\rho_L \tag{2.5}$$

$$u_m=\frac{S_G\rho_G u_G+(1-S_G)\rho_L u_L}{\rho_m} \tag{2.6}$$

$$\rho_m^*=S_G C_0\rho_G+(1-S_G C_0)\rho_L \tag{2.7}$$

In Equation (2.4), the first term on left hand side represents the temporal change and the second term on left hand side states the spatial acceleration. The three terms on the right hand side of Equation (2.4) from left to right express the pressure gradient, the friction of the wellbore wall and the gravity force, respectively. At this point, the momentum equations are simplified to solve Equations (2.4) to obtain the mixture velocity. In addition, the drift velocity u_d is calculated by:

$$u_d=\frac{(1-S_G)u_c K(S_G,K_u)m(\theta)f(G,X)}{S_G\sqrt{\rho_G/\rho_L}-1-S_G} \tag{2.8}$$

The Equation (2.8) was modified by Pan. et al. from Shi. et al. to introduce a cosine-type function K to make a smooth transition of u_d between the bubbling rising and the film flooding. Furthermore, the adjustment function $f(G,X)$ is defined to be equal to zero as the state point in the mist flow region and u_d becomes zero. If the system moves away from the mist region, $f(G,X)$ it increases to 1, in which G is the flow rate across the section in kg/m^2·s and X is the gas mass fraction [87, 88].

In TOUGH2, terms of mass and energy equations listed in Appendix A1 are discretized with the conventional integral finite-difference in space for both wellbore and reservoir. In addition, time discretization is also used with a backward, first order, fully implicit finite-different method. Then, the discretized equations are expressed as the forms of the residual as functions of primary variables. The Newton-Raphson iteration is carried out in which all elements in the Jacobian matric are evaluated by numerical differentiation. The detailed implementation of solving momentum equations were stressed by Pan et al. which will not be covered here [27, 86].

A base case result presented in this chapter is used as the baseline inputs for the following power generation analyses. Furthermore, parametric studies considering different well distances, CO_2 injection rates, CO_2 injection temperatures, reservoir permeabilities, and production well bottom pressures have been carried out.

2.1 Initial Conditions and Well Pattern for Modeling

The modeling has been conducted with the most promising and generic geothermal site conditions in Mexico. The assumed geothermal reservoir is 500 m thick porous media with

fixed physical properties listed in Table 2–1. The reservoir is initially filled with water with the temperature of 225 ℃. The initial pressure in the reservoir from the top to bottom ranges from 20 – 25 MPa due to the elevation change. It is also assumed the reservoir has a single porosity with a value of 0.1, specific heat of cap rock equals to 920 J/(kg·K) and the thermal conductivity is 2.51 W/(m·K).

Table 2–1 Input parameters and initial values for the geothermal CO_2 heat mining model

Parameter	Unit	Value
Reservoir Characteristics		
Reservoir Porosity	-	0.1
Rock Specific Heat	J/(kg·K)	920
Rock Thermal Conductivity	W/(m·K)	2.51
Parameters for Relative Permeability		
Residual Gas Saturation	-	0.01
m_{VG}	-	0.65
Residual Liquid Saturation	-	0.05
Saturated Liquid Saturation	-	1.00
Parameters for Capillary Pressure		
Residual Liquid Saturation	-	0.03
m_{VG}	-	0.4118
Alpha	Pa^{-1}	6.08×10^{-5}
Maximum Capillary Pressure	Pa	6.40×10^{7}
Saturated Liquid Saturation	-	1.00
Reservoir and Injection Well Initial Conditions		
Reservoir Initial Fluid	-	water
Reservoir Initial Temperature	℃	225
Reservoir Initial Pressure	MPa	20-25

CO_2 from fossil fired power plant or industrial processes is considered to be injected into deep saline aquifers through injection wells and then produced through four production wells. One pair of injection and production wells are modeled as part of a symmetric five-well arrangement shown in Figure 2–1. The one quarter of modeling domain has been meshed, which includes one fourth of an injection well and a full production well. Meanwhile, one fourth of total injection flow rate was used but full production rate was obtained. For the molding domain shown in Figure 2–1, there are no heat and mass flow through all sides. In addition, no heat and mass flow boundaries of the reservoir top and bottom are considered in this modeling. The reservoir bottom is specified with constant temperature of 225 ℃ throughout all analyses. However, the model includes the heat flow between the wellbore and the caprock (see Figure 2–2). To eliminate the effect of reservoir boundaries (zero heat and mass flux), reservoir length and width ($2L_0$) of 4000 m are assumed.

As illustrated in Figure 2–1, the injected CO_2 flows radially outward from the injection well locating in the center, with part of it being captured by the four production wells. In addition, a portion of injected CO_2 is bypassing the production wells and forming a CO_2 plume in the region beyond the production wells where the CO_2 is permanently sequestrated.

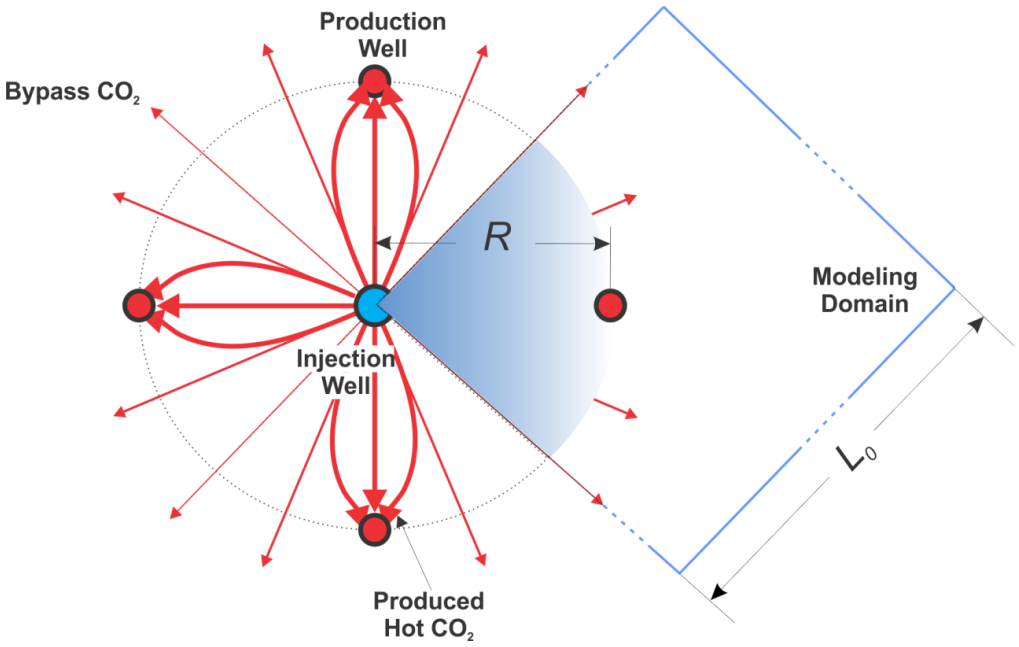

Figure 2–1 Plan view of geothermal well pattern and CO_2 stream lines in geothermal reservoir

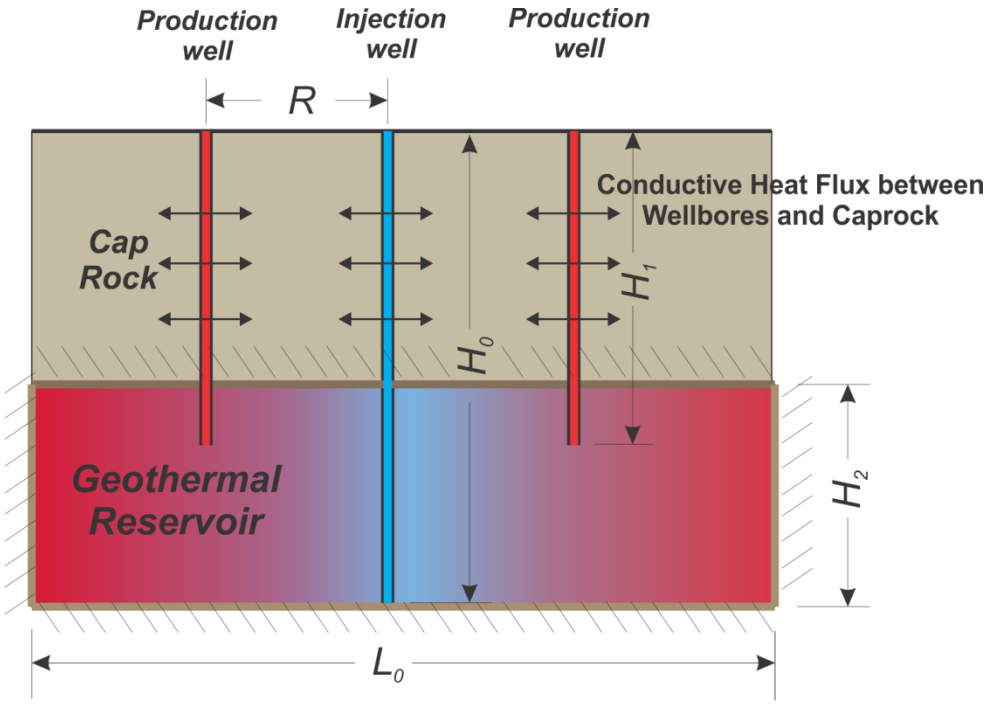

Figure 2–2 Schematic to illustrate heat flux boundary conditions and geometry parameters

Simulation has been performed with the geometries including well depths, reservoir depth, and well diameters presented in Figure 2–2 and Table 2–2. The injection well depth is 2500 m from the surface all the way to the bottom of the reservoir. For the part of the injection well in the reservoir, the injected CO_2 is evenly distributed. As the CO_2 plume moves towards the production wells, it is driven by the buoyance force to move upwards in the meantime of moving outwards. Therefore, the bottom of the production well is closer to the top of the reservoir than the bottom of the injection well which reduces drilling cost as well as tends to produce hot sCO_2 with high fraction potentially. Along the wellbores, a linear temperature distribution of 30 to 225 ℃ is assumed.

Table 2–2 Reservoir and wellbore geometry for geothermal heat mining model using CO_2

Parameters	Units	Values
Injection Well Depth (H_0)	m	2500
Production Well Depth (H_1)	m	2150
Reservoir Depth (H_2)	m	500
Reservoir Length and Width ($2L_0$)	m	4000
Injection Well Diameter	m	0.64
Production Well Diameter	m	0.32

2.2 Grid Convergence Study

It is necessary to conduct a grid convergence examination to determine if the grid used in this simulation is sufficiently refined. Since the wellbore simulation is 2-D which has been well validated, only reservoir mesh size in between the injection and production wells has

been varied. The base case described in this section is referred to as the regular mesh size. The nodes number for the regular mesh case is $40\times40\times6$ in a $X\times Y\times Z$ Cartesian coordinate system. Similarly for the fine mesh case and coarse mesh case, the nodes numbers are $50\times50\times8$ and $35\times35\times5$ respectively (see Figure 2–3). The finer mesh sizes are set near the wellbores and coarser mesh sizes are selected far away from the wellbores. The simulation results of CO_2 production flow rates, CO_2 precaution temperature, injection well head pressure, and production well head pressure are presented in Figure 2–4 and Figure 2–5. Although some minor instabilities occur at the early time of the simulation, the results are highly consistent which means the simulations are grid independent.

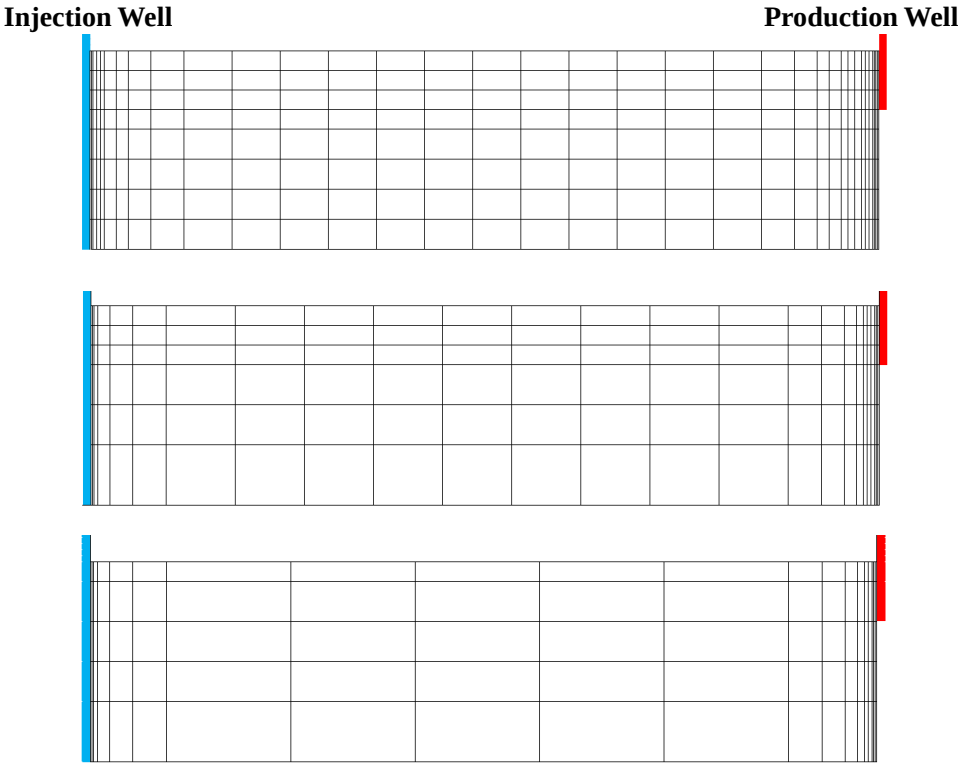

Figure 2–3 Illustration of different mesh sizes (from top to bottom: fine, regular, and coarse).

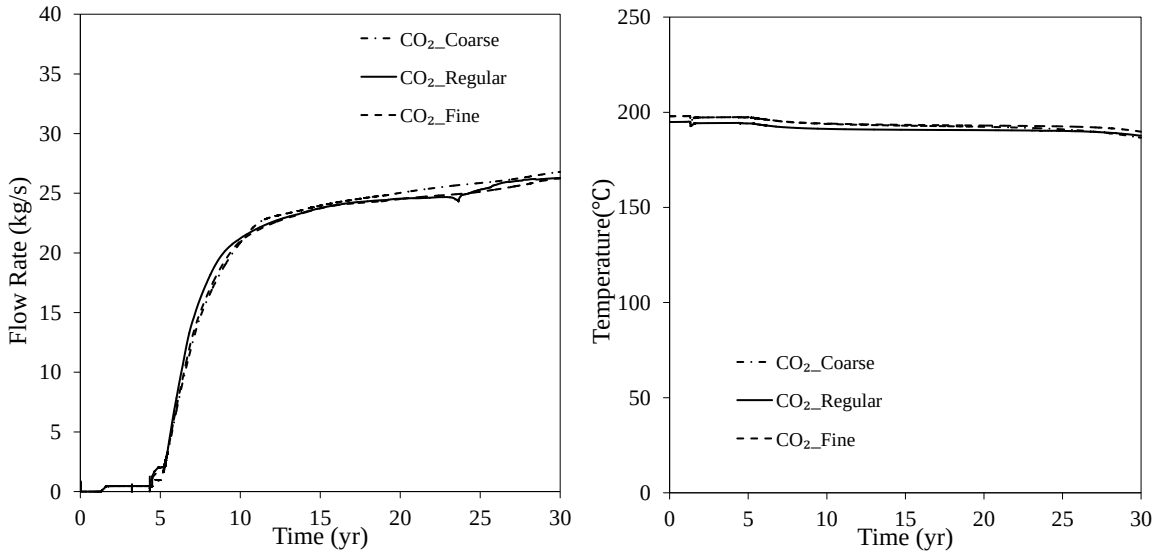

Figure 2–4 CO_2 flow rate and CO_2 production temperature of different mesh sizes over 30 years.

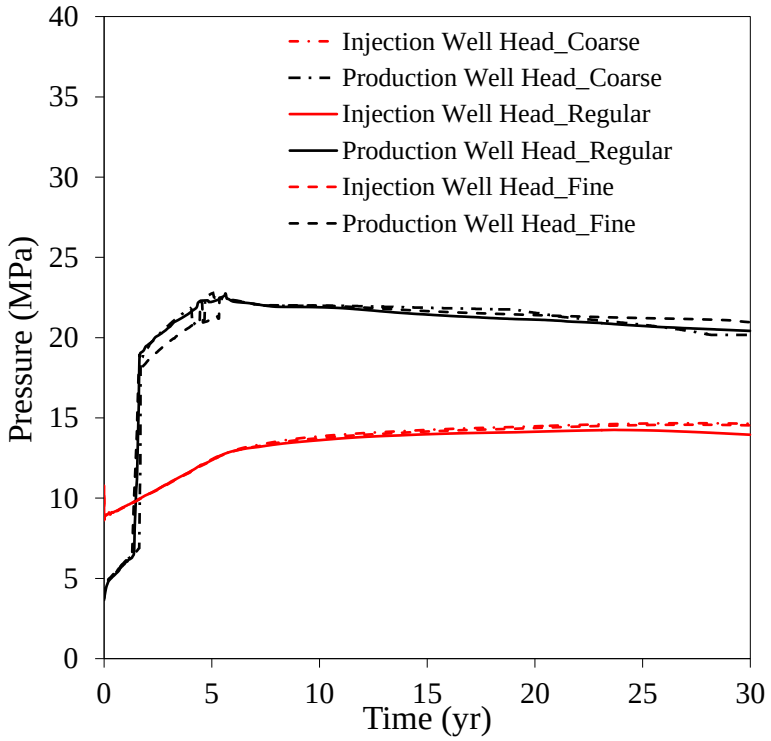

Figure 2–5 Well head pressures of different mesh sizes over 30 years.

2.3 Simulation Results of Geothermal Heat Mining Using CO_2

As mentioned previously, five parameters including well distance, CO_2 injection rate, CO_2 injection temperature, reservoir permeability and production well bottom pressure have been carefully examined for their effects on produced CO_2 temperature, fraction and pressure which are very critical to power generation systems. Nevertheless, a base case with fixed inputs is necessary for the evaluation of thermodynamic performance for the power generation system candidates discussed in this study.

2.3.1 Base Case Conditions and Results of Geothermal Heat Mining Modeling

Table 2–3 presents the base case values of the parameters with significant influence on the geothermal heat mining simulation. A 120 kg/s injection mass flow rate of CO_2, which is the total amount of CO_2 generated by a 600 MW_e coal-fired power plant, is fixed for the base case. At the same time, the CO_2 injection temperature of 30 ℃ has been selected at the injection well head. According to the results published by the author of this dissertation, the production temperature starts to drop in a well distance of 425 m with keeping other conditions the same as shown in Table 2–3 [89]. Hence, the well distance of 500 m is selected as the smallest feasible well distance for a given CO_2 injection rate of 120 kg/s.

Table 2–3 Base Case Conditions of Geothermal Heat Mining Modeling

Parameters	Units	Values
Well Distance	m	500
CO_2 Injection Rate	kg/s	120
CO_2 Injection Temperature	℃	30
Reservoir Permeability	mD	30
Production Well Bottom Pressure	MPa	27

Figure 2–6 indicates the injection and production of CO_2 last a period of 30 years. To get the expected fraction of CO_2 production stream, the production well is set to be closed at early time to monitor the production well bottom pressure. Meanwhile, the CO_2 plume is formed and the reservoir pressure increases since the brine initially retained is pushed outwards. Figure 2–9 illustrates the CO_2 plume forms and gradually propagates at years 5, 10, 20 and 30. In the base case, when a production well bottom pressure reaches 27 MPa, the production well opens and the production is controlled by the reservoir head pressure thereafter. After 10 years, the production well flow rate reaches a relatively steady state. Separation equipment is necessary to separate sCO_2 and water due to the mixture being produced (Figure 2–6).

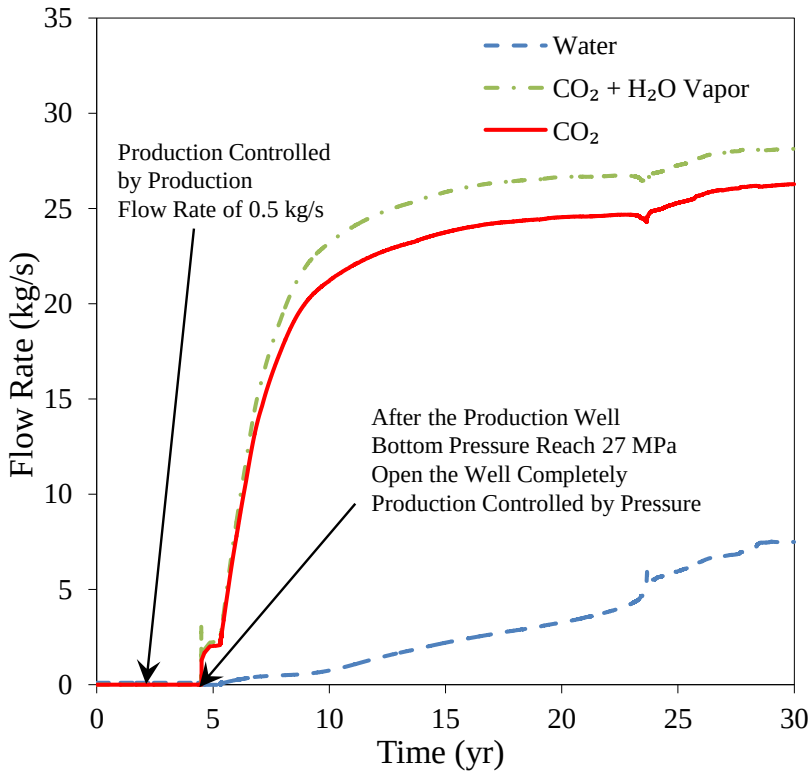

Figure 2–6 Predicted production streams over 30 years for the base case.

Figure 2–7 a) plots the temperatures of the CO_2 at the injection well bottom and at the top of the reservoir. After the initiation of the injection process, the injection well decrease from 225 to 50 ℃ over a period of 8 hours. After this transient process, the temperature profile of wellbores and reservoir stay constant throughout 30 years. It can be noticed in Figure 2–7 b) that a slight decrease of production temperature occurs after 30 years. However, such degradation is not large enough to have an impact on the downstream power generation.

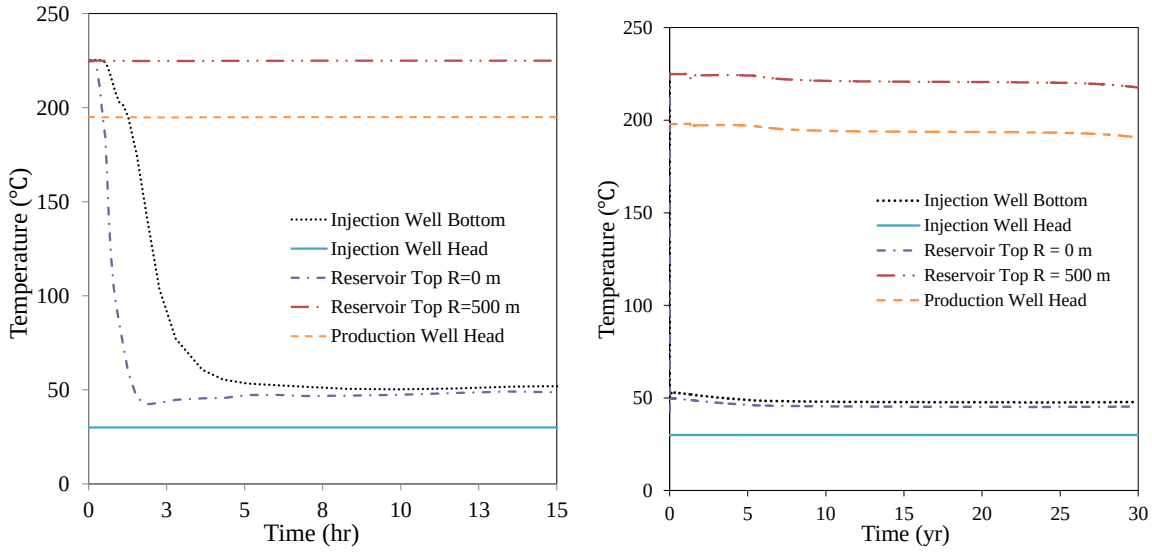

Figure 2–7 a). Predicted temperatures in wellbores and reservoir at the early time for the base case (LHS); b). Predicted temperatures in wellbores and reservoir over 30 years for the base case (RHS).

Figure 2–8 shows the production well head pressure which is more than 5 MPa larger than the injection pressure during the steady production which eliminates the need for a CO_2 compressor for reinjection. This pressure difference is generated by the density difference between the CO_2 between the injection and production wells. In addition, the pressure drops of hot sCO_2 passing through the CO_2-H_2O separator and the evaporator are ignored due to this large pressure difference between the injection well and the production wells

which can be recognized as a thermosiphon effect in CO_2-Plume Geothermal (CPG) [21]. The contours of pressure in Figure 2–11 show the highest pressure occurs at the production well bottom and the lowest pressure is located at the production well. The pressure contours are also consistent with the pressure values shown in Figure 2–8. After the production starts, the pressure of the production well head quickly achieves a steady value, which is 22.5 MPa for the base case. Meanwhile, pressures at other locations in the wellbores and reservoir stop increasing. With the diffusion of CO_2, the pressure level in the reservoir decreases slightly in the later period of 30 years and especially after 20 years (Figure 2–11).

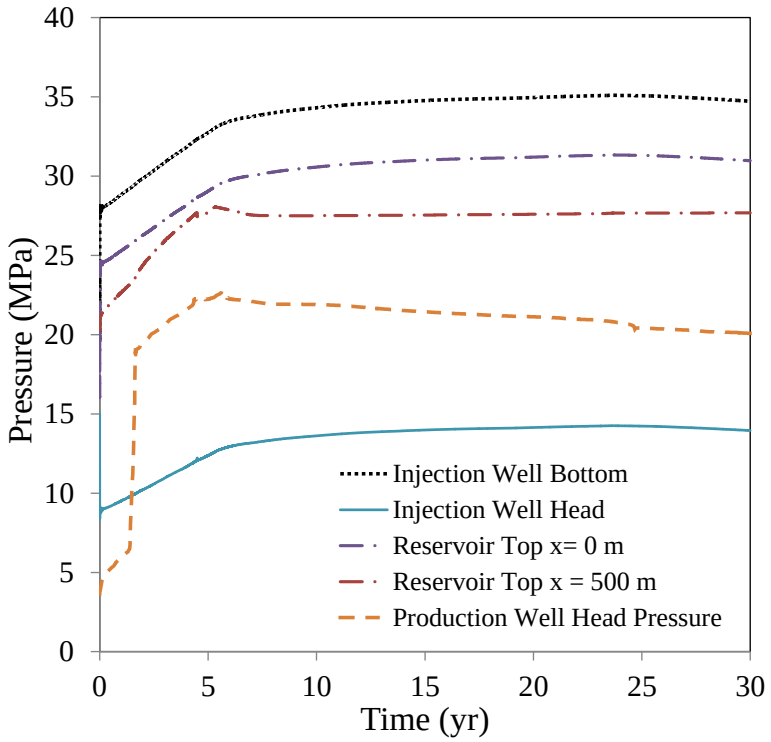

Figure 2–8 Predicted pressure in wellbores and reservoir over 30 years for the base case.

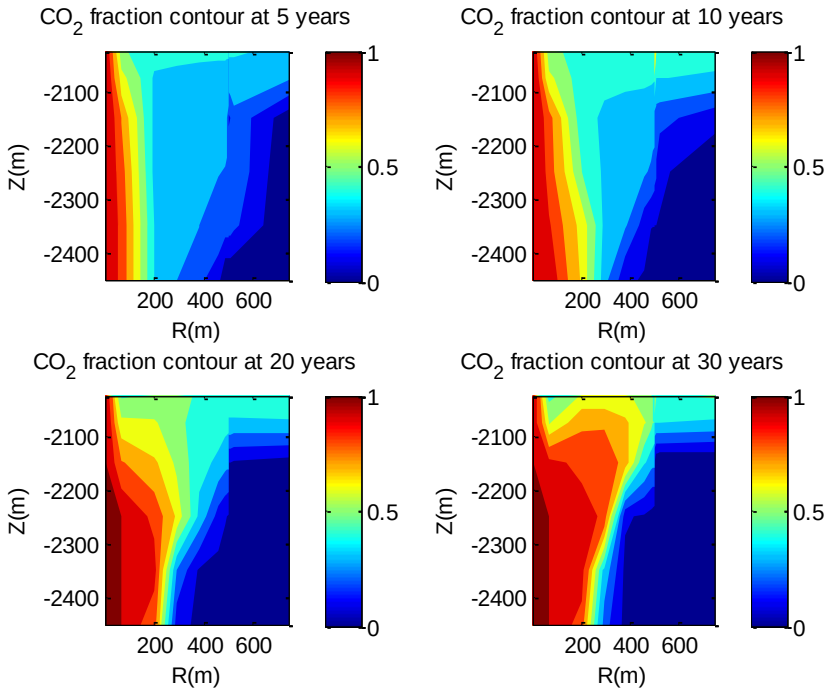

Figure 2–9 Predicted CO_2 saturation contour in the geothermal reservoir at 5, 10, 20, 30 years for the base case.

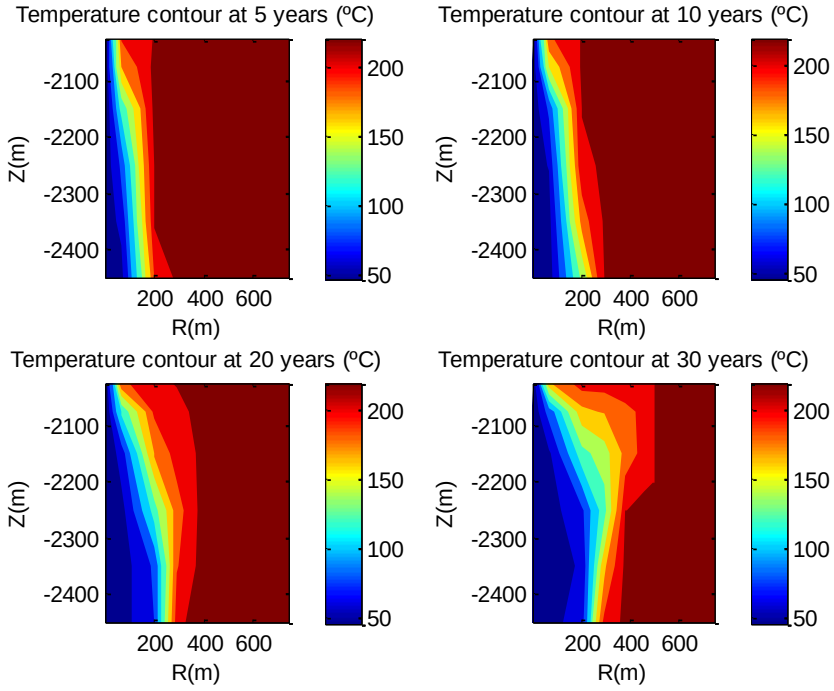

Figure 2–10 Predicted temperature (in ℃) contour in the geothermal reservoir at 5, 10, 20, 30 years for the base case.

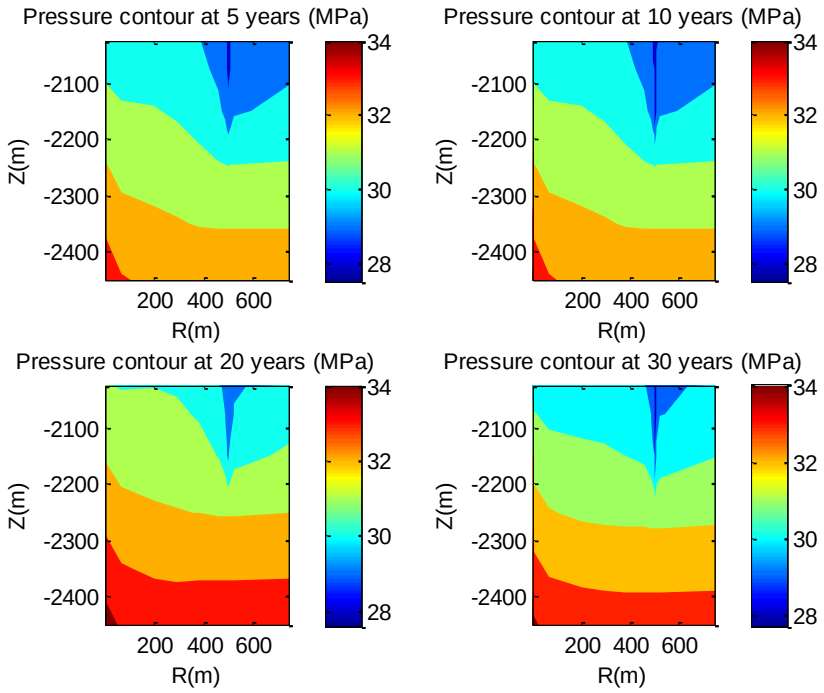

Figure 2–11 Predicted pressure (in MPa) contour in the geothermal reservoir at 5, 10, 20, 30 years for the base case.

The geothermal heat mining base case simulation results are presented in this section. It is found that the production flow rate can be treated as a constant after 10 years. In addition, the CO_2 production pressure and temperature reaches a steady state as well. In summary, a CO_2 production rate of 22.5 kg/s for each production well, which is equivalent to 90 kg/s for the whole well set, is taken into account. Similarly, the average produced CO_2 pressure and temperature are 22.5 MPa and 195 ℃, which can be obtained from the results above.

For 20 year of plant life, such an amount of geothermal energy extracted, temperature and pressure of produced CO_2 are adequate and steady enough for multiple types of power generation applications.

2.3.2 Parametric Study for Geothermal Heat Mining Modeling

A parametric study of five input variables has been performed (see Table 2–3) for the geothermal heat mining modeling. For each variable, the simulation results are presented in terms of produced CO_2 and H_2O flow rates, injection and production well head pressures, produced CO_2 temperature, and well head pressure difference. The purpose of this parametric study is to find out parameters with significant and dominated impacts for the further global optimization integrated with power generation systems.

2.3.2.1 Injection and Production Well Distance

To demonstrate the sensitivity to varying the well distance for the simulation, the well distances range from 300 m all the way to 1000 m with a resolution of 100 m are screened.

At the well distance of 300 m, the approximate total CO_2 production rate of 110 kg/s with only about 6 kg/s water production (see Figure 2–12). It also benefits much from CO_2 thermosiphon effect with less influence of pressure drop occurring in the reservoir, which can be inferred from Figure 2–13 that the smaller injection well head pressure and the larger production well head pressure are obtained with 300 m well distance. However, the downside of premature production temperature drop is crucial to make the long term power generation unfeasible (see the left hand side (LHS) of Figure 2–14). On the other hand, as the well distance increases to 1000 m, Figure 2–12 shows that the CO_2 production flow rate presents a gradual increase trend, which also can be seen as the undesirable transient process for the steady power generation. In addition, there is also a huge increase for the water production at the larger well distance, which potentially increases the cost of sCO_2 and water separation. Another phenomenon can be observed in the right hand side (RHS)

of Figure 2–13 is a great pressure drop occurring after the production well is fully opened. It is because a considerable amount of water suddenly is produced for the large well distance case which is yielded to a sudden pressure drop at the production well head. Furthermore, well head pressure difference decreases as the well distance increases.

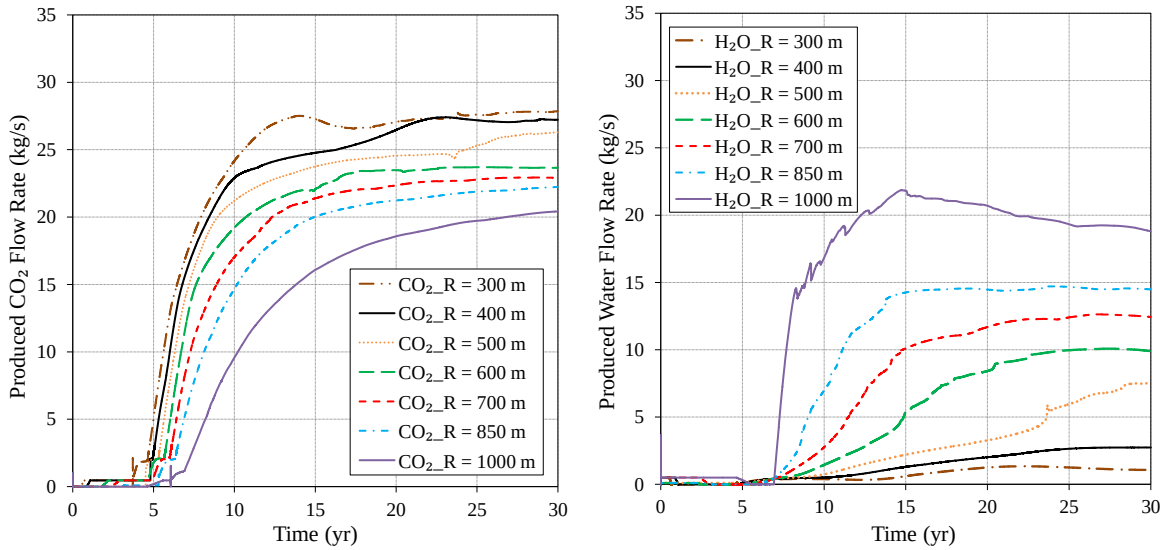

Figure 2–12 Produced CO_2 and water flow rate over 30 years for different well distances.

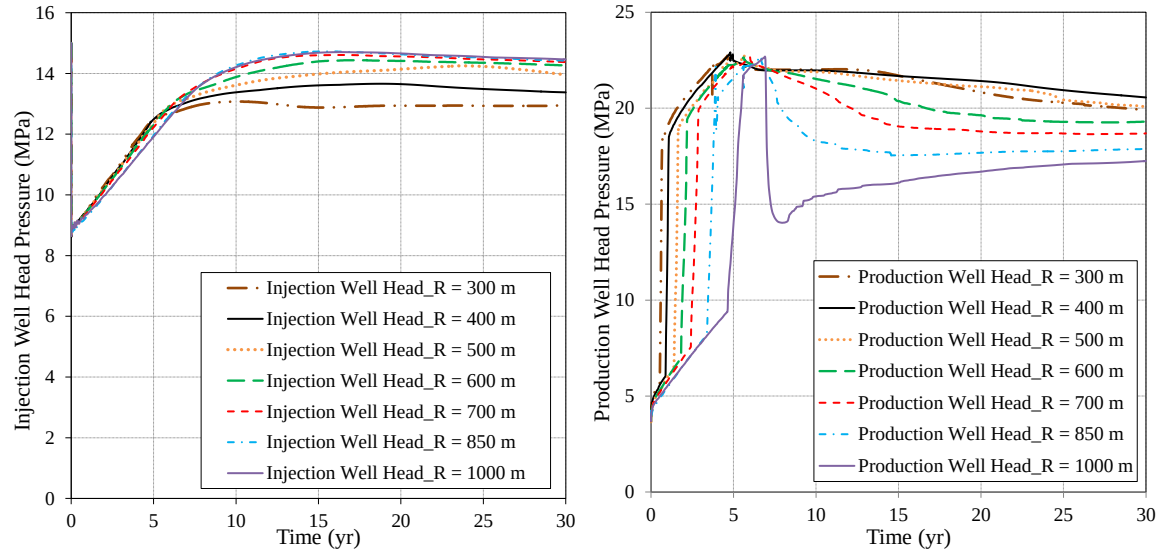

Figure 2–13 Well head pressures over 30 years for different well distances.

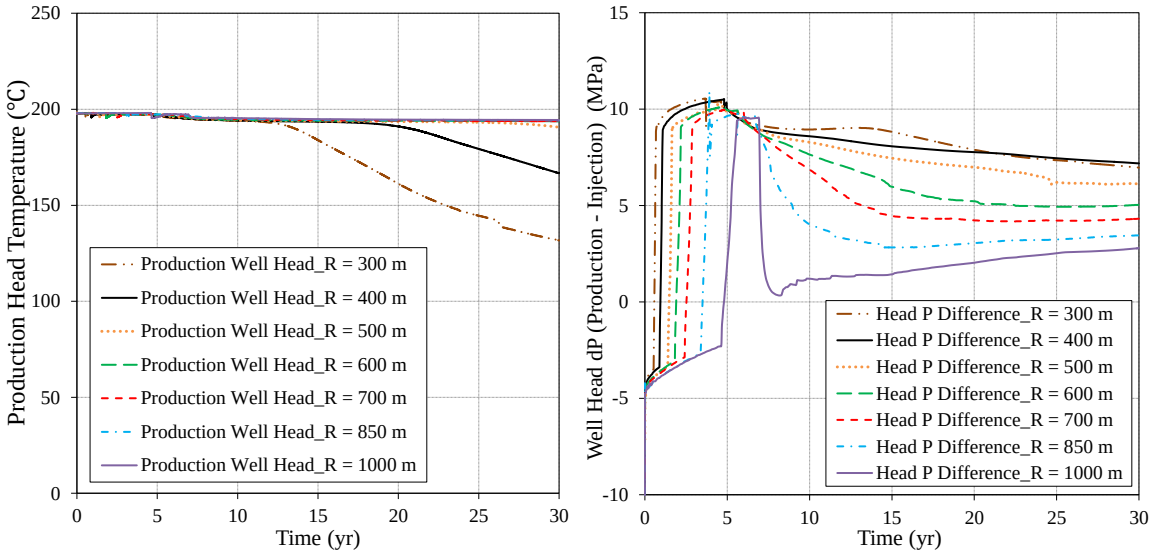

Figure 2–14 Production well head temperature (LHS) and well head pressure difference (RHS) over 30 years for different well distances.

The well distance between production well and injection well affects production temperature, CO_2 fraction, and CO_2 total production rate. The larger distances where the production well locates more CO_2 escaping will result in a lower CO_2 production rate and a larger amount of water eruption. An optimal well distance exists in which the production temperature won't go down, the CO_2 production rate keeps steady, and CO_2 thermosiphon effect is not compromised.

It can be seen in LHS of Figure 2–14, a well distance of 500 m is the smallest well distance to sustain the production temperature without dropping off. Additionally, the CO_2 production flow rate and the well head pressure difference make it qualified for a long term steady power generation application. Furthermore, it is also proven that the base case conditions are reasonable for power generation systems thermodynamic analyses.

2.3.2.2 CO_2 Injection Flow Rate

The injection flow rate of CO_2 is another critical parameter for the heat mining simulations. 1.5, 2 and 3 times of base case CO_2 injection flow rate are used to perform the study. As the CO_2 injection flow rate becomes 3 times of it for the base case, the produced CO_2 through the production well are more than 3 times larger than it is for the base case, which indicates that the higher CO_2 concentration is achieved (Figure 2–15). Meanwhile, the changes of CO_2 injection rate have a negligible impact on the water production for the cases with CO_2 injection flow rate larger than 180 kg/s. However, the water concentration of the produced mixture can be up to 35%, especially after 20 years production for the 120 kg/s CO_2 injection flow rate case, which requires to be considered in the sCO_2-water separator design. Nevertheless, the CO_2 production rate stays steady over this CO_2 injection flow rate range.

As discussed in Section 2.3.2.1, at the CO_2 injection flow rate of 120 kg/s, 500 m is the smallest feasible well distance with no dramatic temperature drop. As the CO_2 injection flow rate increases, the larger depletion of the geothermal energy reserve in the reservoir occurs with the larger CO_2 injection flow rate. The LHS of Figure 2–17 shows a premature temperature drop can happen as early as year 10 for a 360 kg/s CO_2 injection. Eventually at year 30, the production head temperature drops as low as 130 ℃. As expected, a larger CO_2 injection flow rate results in requiring larger injection pressure to overcome the resistance through the reservoir which is positively correlated to the fluid mass flow rate. Since the strategy used in the simulation is pressure control production, the production well head pressure is not affected by CO_2 mass flow rate increasing (Figure 2–16). It is

important to mention that, different from the results of varying the well distance, there is no dramatic change of water production for changing CO_2 injection flow rate. Therefore, the production well head pressure does not behave the same between changing well distances and changing CO_2 injection flow rates, although, they all have step changing CO_2 production rates.

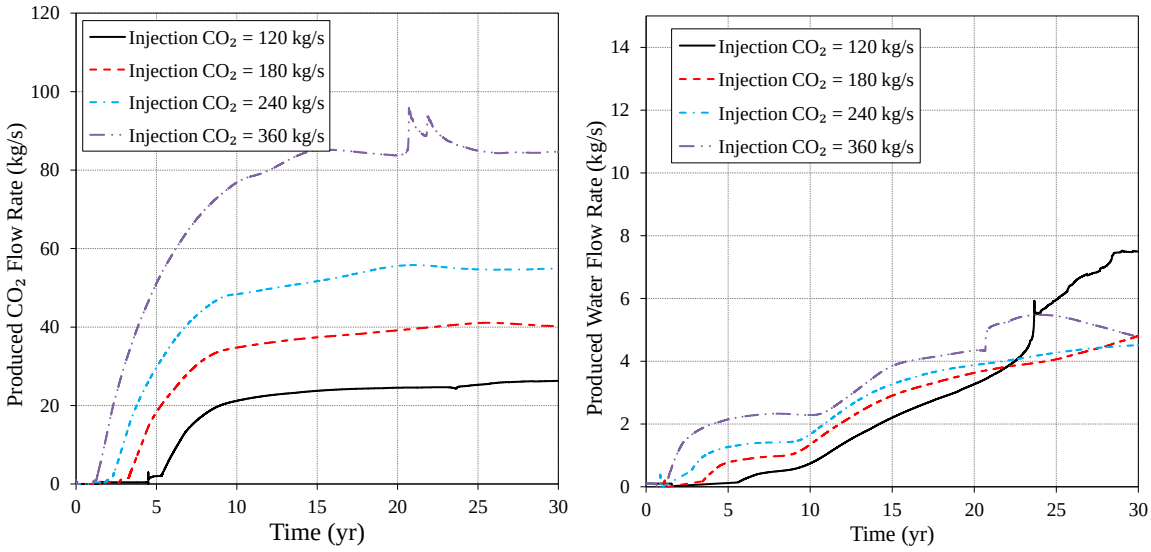

Figure 2–15 Produced CO_2 and water flow rate over 30 years for different injection CO_2 flow rates.

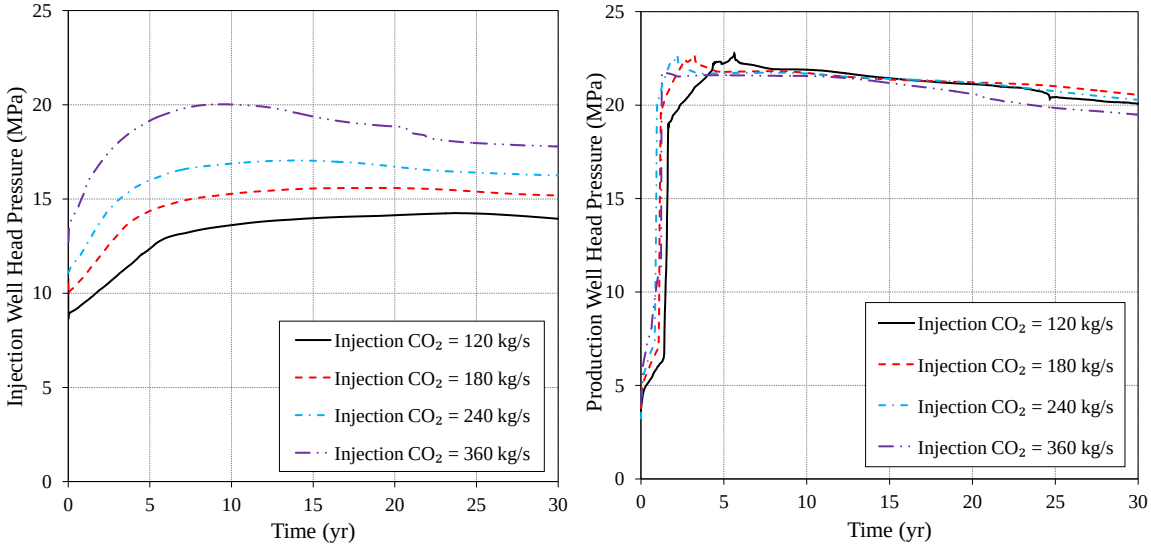

Figure 2–16 Well head pressures over 30 years for different CO_2 flow rates.

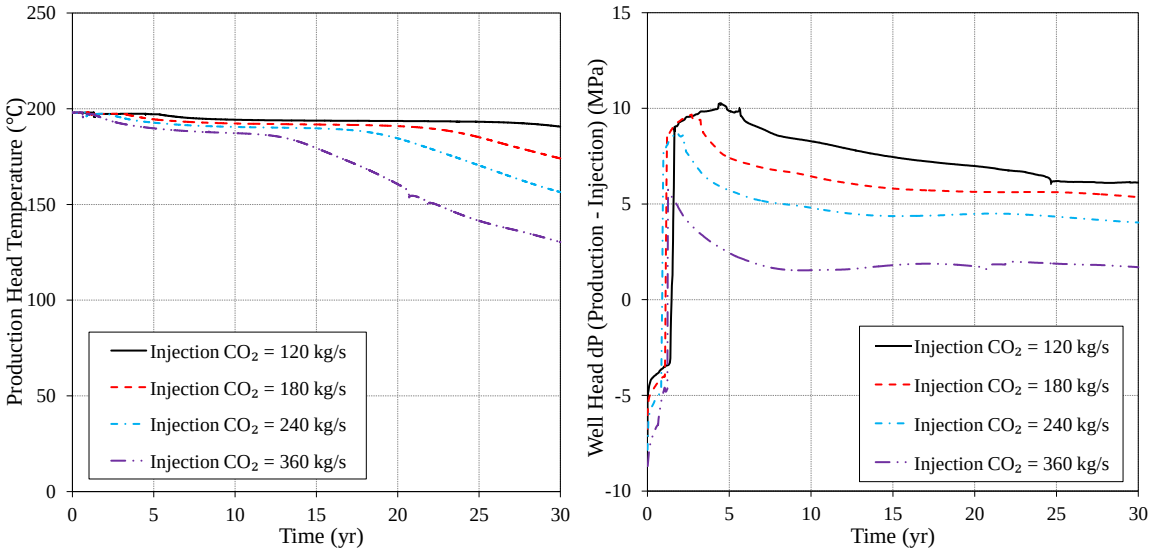

Figure 2–17 Production well head temperature (LHS) and well head pressure difference (RHS) over 30 years for different co_2 flow rates.

Furthermore, it is found that a minimum feasible or optimal well distance is corresponding to a CO_2 injection flow rate to ensure a 30 years life of steady geothermal energy exploitation.

2.3.2.3 Reservoir Permeability

A range of permeabilities from 15 to 60 mD has been considered in the simulation. It can be seen in Figure 2–18, that the transient process of reaching a steady CO_2 production for the high permeability case (60 mD) is extremely short. However, considerable amount of water is also produced. On the contrary, small reservoir permeability brings the difficulty for CO_2 diffusing through the reservoir which leads to the large pressure drop, then it requires the larger injection well head pressure to overcome this pressure drop (see LHS of Figure 2–19). However, the less water production compensates this resistance in the reservoir due to the less pressure drop occurring in the production well. It is reflected from the RHS of Figure 2–20 that the well head pressure differences are quite close. In this

permeability range, the production well head pressure is still about more than 5 MPa over the injection well head pressure which indicates the elimination of recompression for CO_2 reinjection can be applied to this reservoir permeability range. In addition, the production temperature is almost unaffected by the change of reservoir permeability over 30 years.

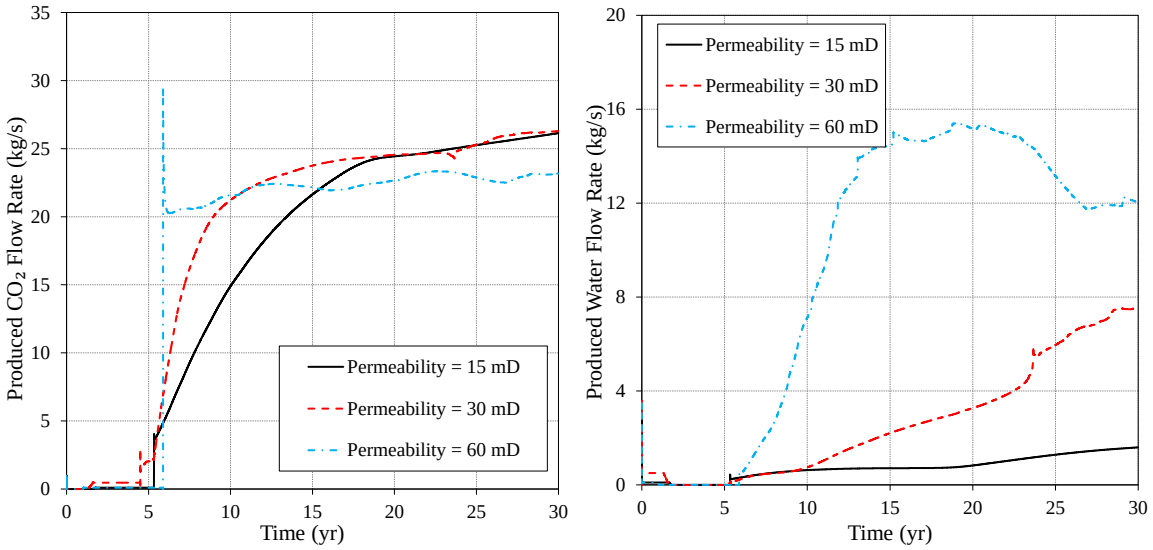

Figure 2–18 Produced CO_2 and water flow rate over 30 years for different permeabilities.

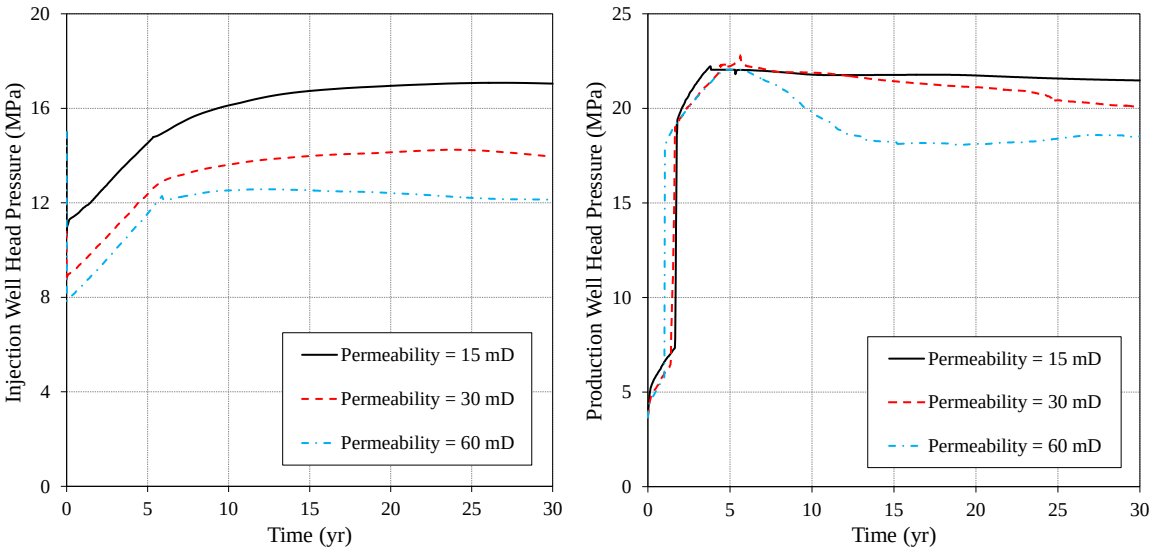

Figure 2–19 Well head pressures over 30 years for different permeabilities.

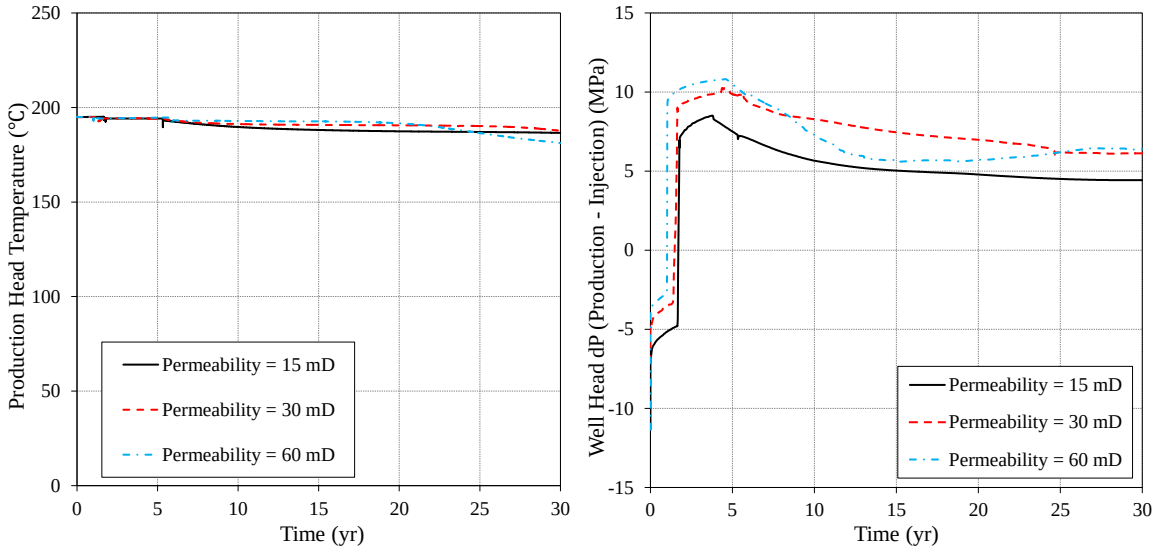

Figure 2–20 Production well head temperature (LHS) and well head pressure difference (RHS) over 30 years for different permeabilities.

As discussed above, the reservoir permeability can have considerable effect on the circuit pressure and the water production. However, the reservoir permeability belongs to an inherent natural property which only changes along with the site location. To simplify the optimization, 30 mD is designated and fixed in this study.

2.3.2.4 CO_2 injection Temperature

The simulations have been carried out for the CO_2 injection temperatures of 30, 50 and 80 ℃. It is obvious that the CO_2 and water production flow rates, the production well heat pressure and temperature are barely affected by the changes in injection temperatures over the range mentioned above, this is presented in Figure 2–21, RHS of Figure 2–22 and LHS of Figure 2–23. Due to the larger density of CO_2 at lower temperatures, the pressure change through the injection well is substantial for the CO_2 at lower temperatures. Thus, smaller injection well head pressure is needed to maintain the fixed production well bottom

pressure. This phenomenon almost diminishes the thermosiphon effect at CO_2 injection temperature of 80 ℃ (see RHS of Figure 2–23). To enhance the benefit of CO_2 thermosiphon, the low CO_2 injection temperature is preferable.

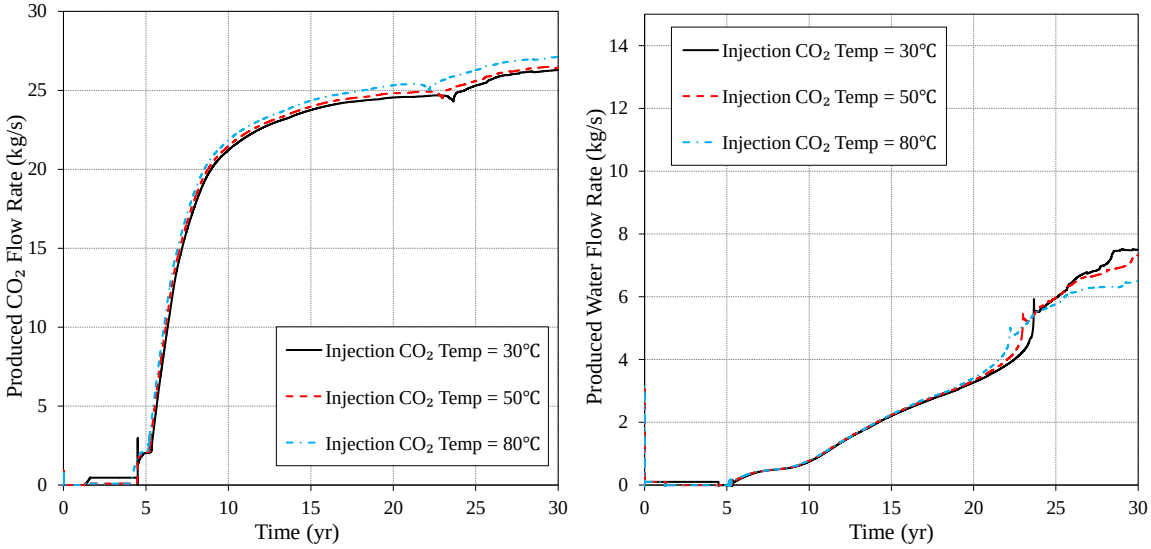

Figure 2–21 Produced CO_2 and water flow rate over 30 years for different CO_2 injection temperatures.

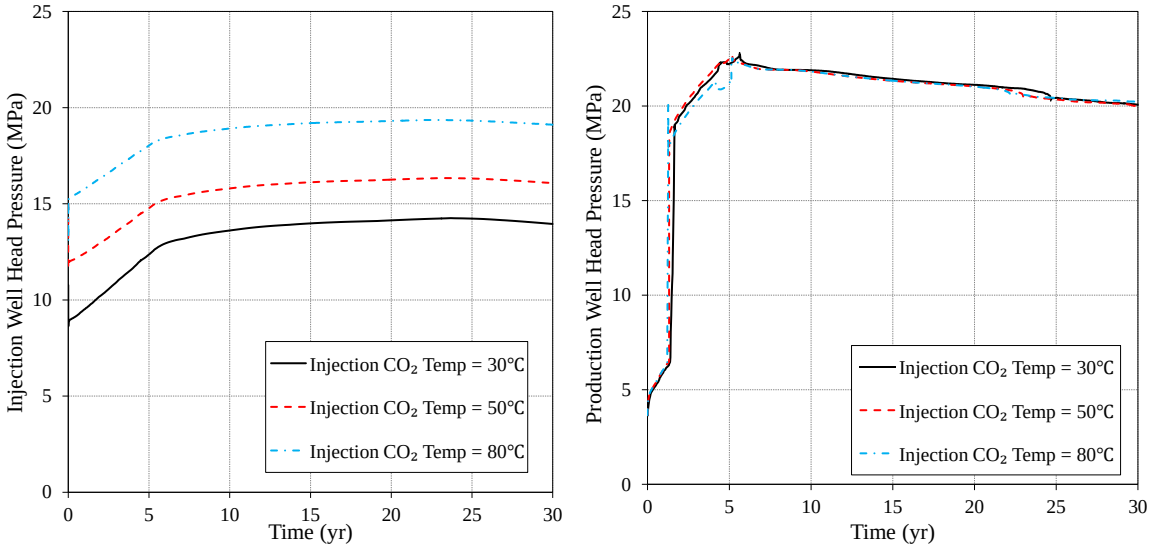

Figure 2–22 Well head pressures over 30 years for different CO_2 injection temperatures.

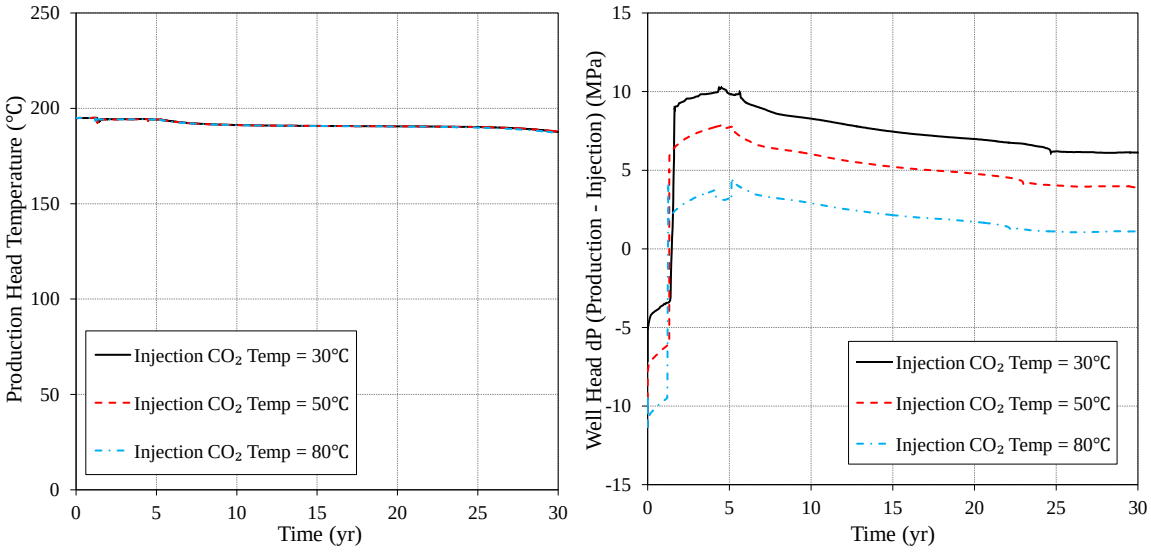

Figure 2–23 Production well head temperature (LHS) and well head pressure difference (RHS) over 30 years for different CO_2 injection temperatures.

2.3.2.5 Production Well Bottom Pressure

As mentioned previously, the full production starts at the time when the production well bottom pressure reaches 27 MPa for the base case. However, this pressure can be set to different values which may affect the time to start production and also the injection and production pressures.

The production well bottom pressures of 24 MPa, 27 MPa and 30 MPa have been selected to carry out simulations. The 3 MPa pressure difference at the production well bottom caused 2.5 years of time difference for the start of the production (Figure 2–24). When the lower production well bottom pressure is reached, more water is produced since the CO_2 plume was not big enough to push the water outwards to achieve higher CO_2 fraction streams of production. However, the CO_2 production mass flow rates are in very similar magnitude during steady production after 15 years which is shown in Figure 2–24.

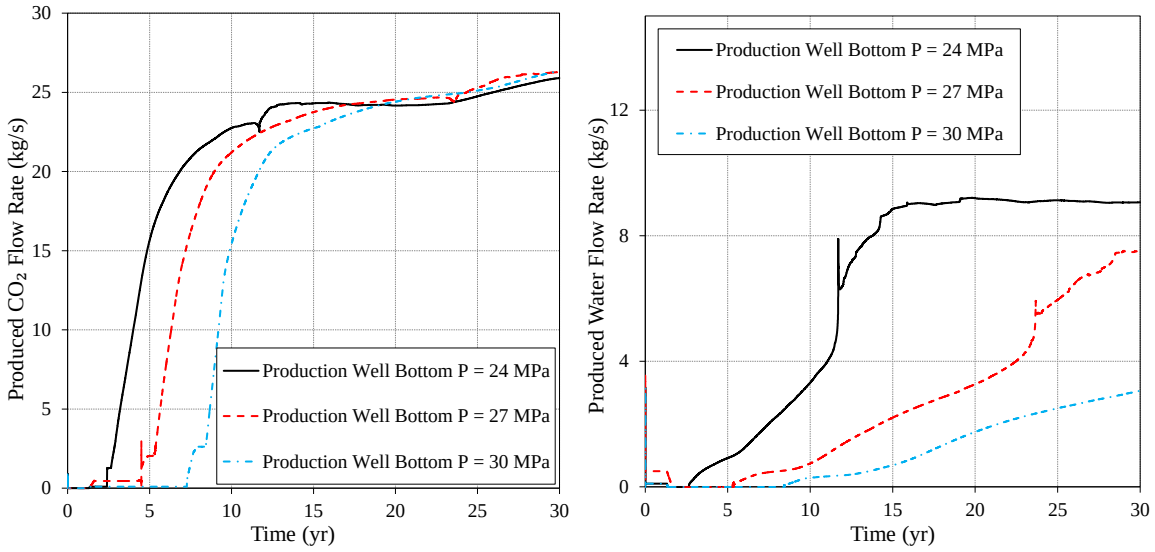

Figure 2–24 Produced CO_2 and water flow rate over 30 years for different production well bottom pressures.

Obviously, different production well bottom pressures affected well head pressures of this thermosiphon system. The whole circuit pressure increased along with the increase of production well bottom pressure (Figure 2–25). However, the production temperature stays the same during the whole production process (LHS of Figure 2–26). Although both the injection well head pressure and the production well head pressure increase as the production well bottom pressure increases, it still results in a stronger thermosiphon effect, when the larger well head pressure difference is obtained (RHS of Figure 2–26). However, it needs to carefully examine the influence of the augment of the thermosiphon effect on the cycle performance since the injection well head pressure is also increasing which leads to the larger compression work.

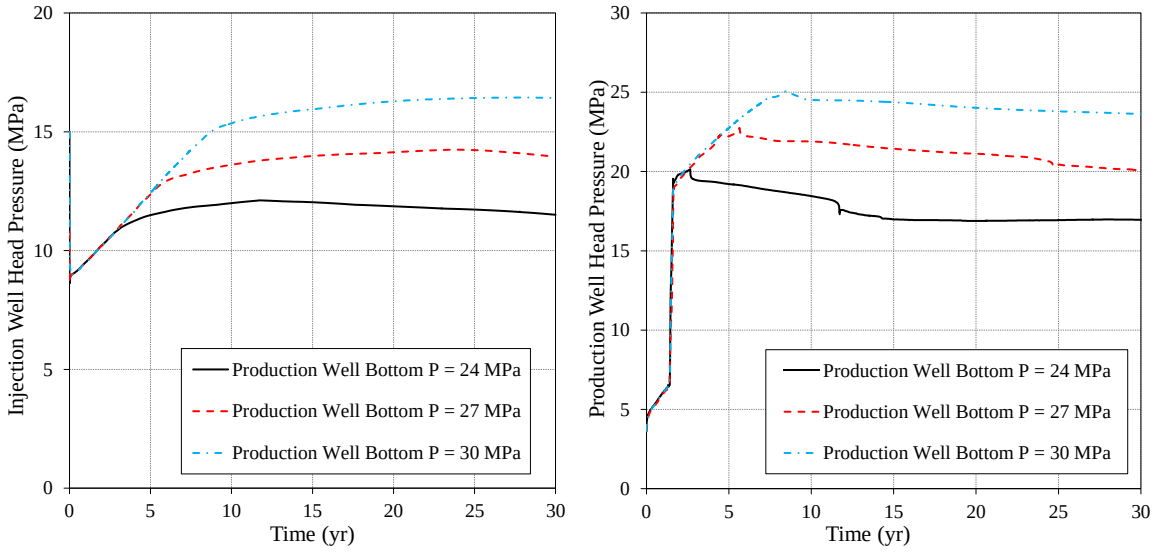

Figure 2–25 Well head pressures over 30 years for different production well bottom pressures.

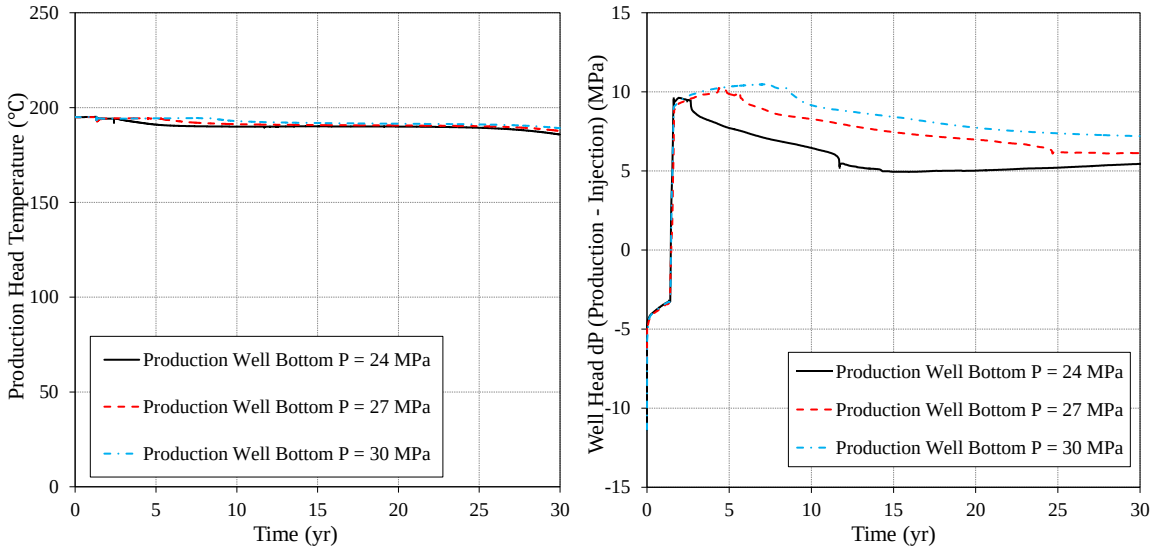

Figure 2–26 Production well head temperature (LHS) well head pressure difference (RHS) over 30 years for different CO_2 injection temperatures.

2.4 Summary and Conclusion for Geothermal Heat Mining Modeling

A fully coupled wellbore-reservoir system has been modeled using a high temperature and research version of T2Well/ECO2N software provided by the LBNL. The parametric analyses for well distance, CO_2 injection flow rate, reservoir permeability, CO_2 injection temperature, and production well bottom pressure have been performed. The impacts on well head pressure, produced H_2O flow rate, produced CO_2 flow rate and temperature are discussed and presented in this chapter. In addition, the well head pressure difference which reflects the strength of CO_2 thermosiphon effect has been calculated.

These results indicate the well distance, as well as the injection flow rate are two dominated parameters in the power generation applications using hot produced sCO_2 discussed in this study. These two parameters would be subject to optimization, so that the consistent temperature and flow rate of hot produced sCO_2 are able to be provided to the power generation systems for a stable electric power generation. As expected, it has been also found from the parametric study for CO_2 injection flow rate that this variable has a first order impact on and production flow rate. However, a larger injection flow rate results in a faster depletion of the geothermal energy reserve in the reservoir. It is identical to the well distance. A smaller well distance also leads to an earlier and undesirable reduction of the production temperature even if a larger production rate is obtained.

It needs to be mentioned that the TOUGH2 calculation is extremely time intensive for the time period of 30 years in simulations. To avoid spending an unreasonable amount of time, the CO_2 injection temperature, the reservoir permeability and the production well bottom pressure are fixed to the optimal or typical values. The data set has been generated

throughout the ranges of well distance from 500 m to 900 m and injection mass flow rate from 120 kg/s to 360 kg/s. Table 2–4 shows the average values of produced CO_2 flow rate, CO_2 production temperature, CO_2 production pressure, and required injection pressure from 10 to 30 years in which can be considered a time period for steady production. However, for the well distance of 500 m with 240 kg/s injection rate, as well as the well distances of 500 and 600 m with 360 kg/s injection rate, the CO_2 production temperatures decrease significantly. Moreover, those falling processes lasting for more than 5 years would affect the power generation greatly which is unacceptable. Therefore, the cases of 500 m with 240 kg/s and 360 kg/s injection rates, and 600 m with 360 kg/s are removed from the data set for the global optimization analysis.

Table 2–4 Geothermal heat mining using CO_2 simulation results.

Geothermal Heat Mining Simulation Results (Average from 10 Years to 30 Years)					
Injection Flow Rate (kg/s)	Well Distance (m)	Produced $\dot{m}_{CO_2}$ (kg/s)	Production T (℃)	Production P (MPa)	Injection P (MPa)
120	500	98.17	190.32	20.83	14.08
	600	92.48	194.02	19.75	14.34
	700	87.67	194.21	19.00	14.50
	800	75.63	194.51	18.69	14.45
	900	68.26	194.74	18.09	14.67
240	500	211.87	178.32*	21.15	16.73
	600	204.53	188.95	20.71	17.75
	700	192.83	190.92	19.77	18.02
	800	183.90	192.00	19.19	18.32
	900	173.12	192.91	18.36	18.61
360	500	338.05	157.71*	20.55	18.77
	600	320.30	178.41*	20.94	20.64
	700	305.77	185.91	20.46	21.81
	800	292.17	188.33	19.68	22.19
	900	277.98	189.09	19.21	22.54

Note: * - Production Temperature Decreases Significantly Over 5 Years.

Chapter 3 sCO_2-based Power Cycles Using Hot Produced sCO_2 from Geothermal Reservoirs and High Temperature Heat Sources

Figure 3–1 presents the concept of using sCO_2 produced from a geothermal reservoir through sCO_2 power cycles to generate electric power. sCO_2-based power cycles can consist of a supercritical cycle where the whole cycle lies above the CO_2 critical point as well as a transcritical cycle where the cycle partially remains in the supercritical region. From another perspective, sCO_2-based cycles can be divided into a direct turbine expansion cycle and closed sCO_2 cycle depending on if the working fluid is recirculated or not at the end of the cycle.

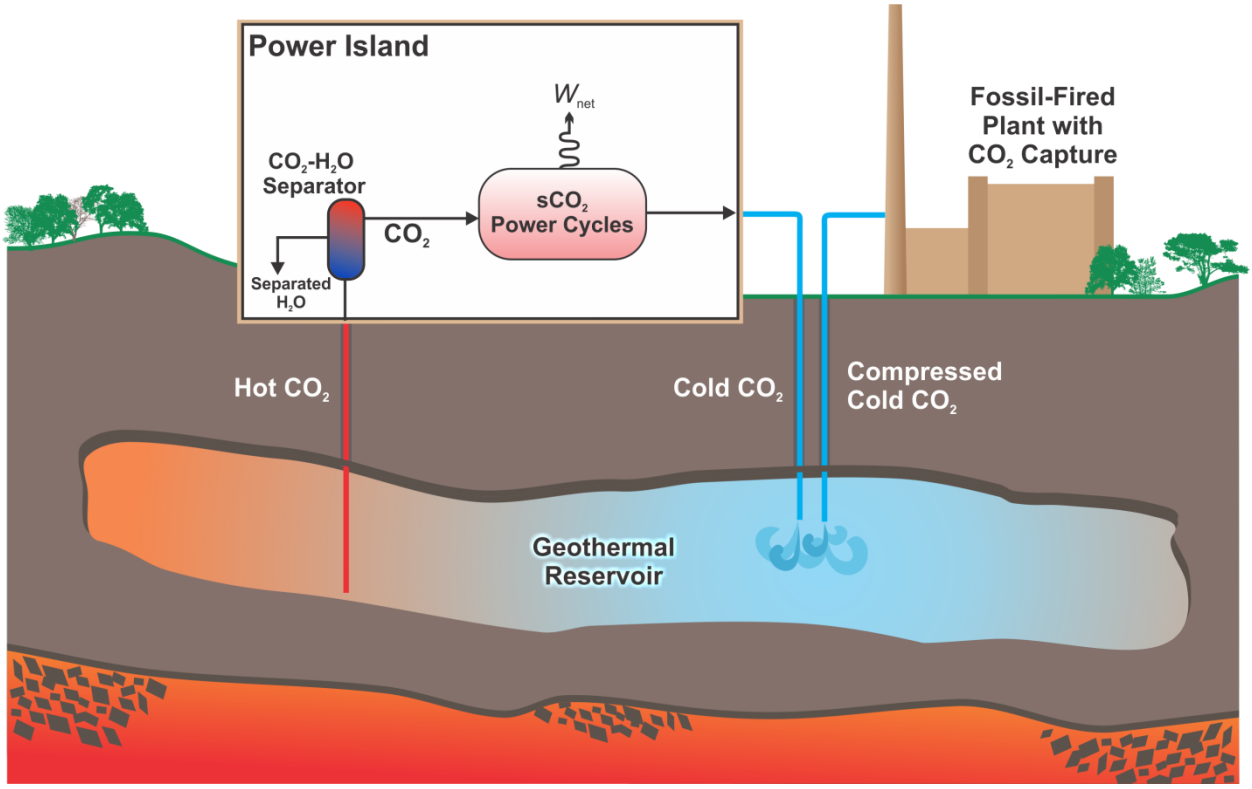

Figure 3–1 Sketch of CO_2 direct expansion approach using hot produced CO_2 from geothermal reservoir.

In this study, three major types of power cycles are used to convert the geothermal heat into electricity using the hot produced sCO_2 from geothermal reservoirs: 1). direct turbine expansion, 2). closed sCO_2 Brayton cycle, and 3). transcritical sCO_2 cycle. Particularly, for the closed sCO_2 Brayton cycle, the cycle performance improvement methods including recuperating, pre-compression, inter-cooling, and reheating are considered. The baseline conditions of hot produced CO_2 using in the cycle thermodynamic analysis have been obtained in Chapter 2.

Before more detailed sCO_2 power cycle analyses are carried out, it is necessary to have a better understanding of CO_2 physical properties which provide theoretical fundamentals to design and develop sCO_2-based power cycles. In addition, examining CO_2 physical properties is also helpful to demonstrate the advantages of using CO_2 as the working fluid for power cycles.

It is assumed that the pressure drops are neglected for CO_2 and the cooling water passing through the HX, as well as passing through the CO_2-H_2O separator. The detailed thermodynamic models for all approaches have been developed using ASPEN Plus, which is a well-validated commercial software for process modeling. The objective for the optimization analysis is maximizing the net power output, or in another word, maximizing the conversion rate from geothermal energy to electricity. However, evaluation parameters such as system thermal efficiency, system exergy efficiency, and specific net power output are considered as well to determine the most feasible design on a thermodynamic perspective. Moreover, sensitivity analyses regarding critical parameters affecting cycle performance have been carried out.

The results presented in this chapter are only focusing on the thermodynamic performance. The layout of sCO_2-power cycle with the best cycle performance is selected to be compared to other power generation options subsequently to determine the most cost-effective one.

3.1 CO_2 Properties

CO_2 with relatively low critical pressure and temperature potentially could be easily compressed and heated up to a supercritical state. The physical properties of CO_2 near its critical point (31.1 ℃, 7.38 MPa from REFPROP [90]) such as liquid-like large density and gas-like low dynamic viscosity offer advantages to reduce the cycle compression power which is the main contributor to increase the cycle efficiency.

Figure 3–2 shows specific heat, density, viscosity and thermal conductivity of CO_2 change with temperature at the pressure range from 6 to 9 MPa where the critical point is covered. It can be seen the dramatic changes of physical properties occur near the CO_2 critical point. Particularly for the specific heat, when the pressure is above the critical pressure, the temperature for the peak value of the specific heat is known as the pseudo-critical temperature. Near the pseudo-critical temperature, density, viscosity and thermal conductivity changes dramatically. The parameters plotted in Figure 3–2 directly affect the heat transfer efficiency and pressure drop behavior of CO_2 in heat exchangers. The specific heat significantly increases when the CO_2 temperature approaches the pseudo-critical temperature which allows CO_2 can absorb more heat from heat sources. Additionally, after the pseudo-critical temperature, the dynamic viscosity drops dramatically resulting in the low flow resistance. However, the thermal conductivity decreases at a higher temperature

region which leads to the deterioration of heat transfer. Especially near the critical region, these characteristics can offer the benefits such as compact turbomachinery size, low friction loss and relatively high heat transfer coefficient for sCO_2-based cycles. In addition, no phase change occurs when CO_2 expands through a turbine in a sCO_2 power cycle eliminates the blade erosion risk.

All the physical property data presented in this dissertation are based on the REFFPROP by NIST in this study [90].

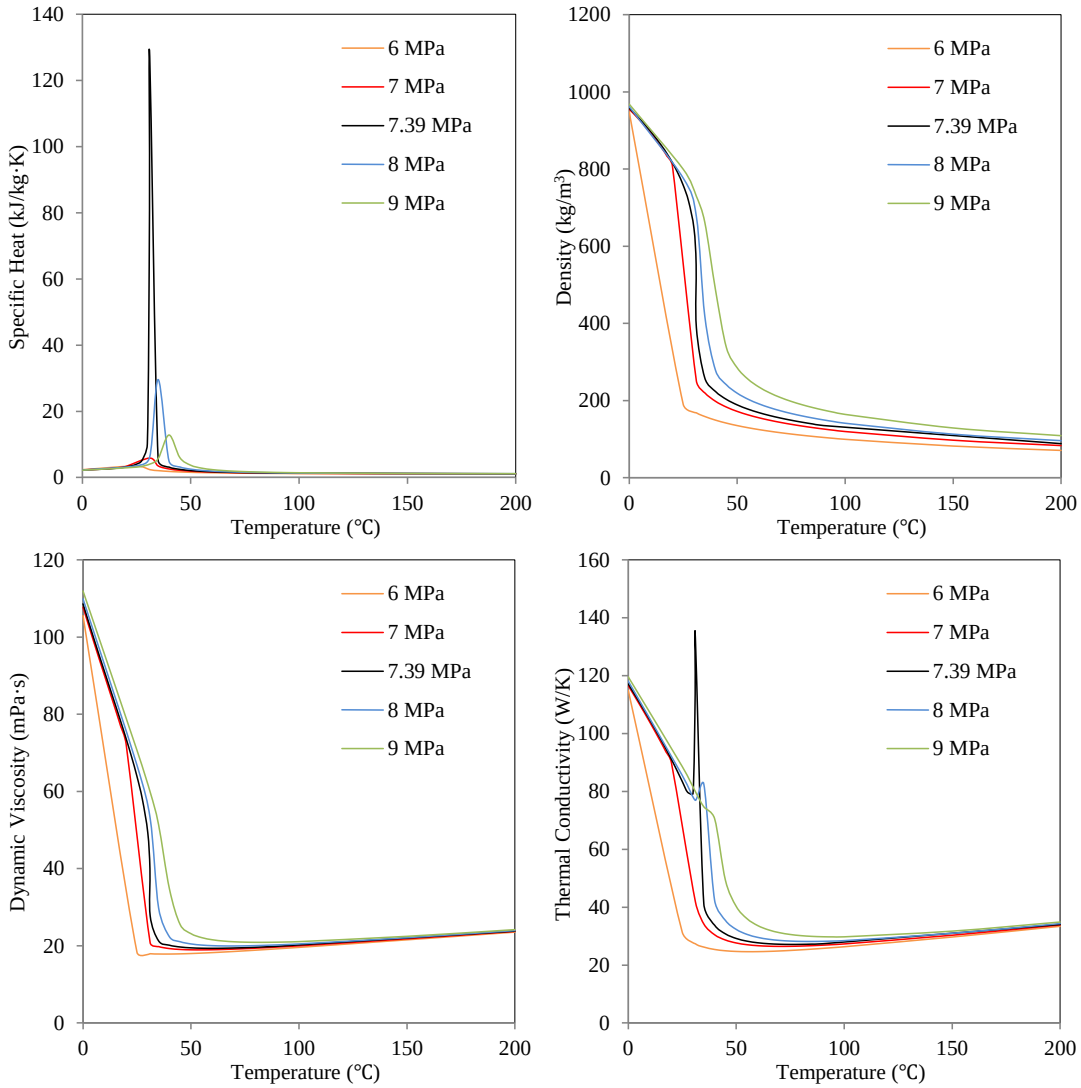

Figure 3–2 CO_2 physical properties near its critical point.

Figure 3–3 shows the phase diagram for CO_2 in the range of pressure and temperature conditions that are of interest for the geothermal heat mining simulation as well as the sCO_2 power cycles. The supercritical region has no phase boundaries either to gas CO_2 or liquid CO_2, which CO_2 can change continuously from a gaseous sate or liquid state to a supercritical state. The main advantage of sCO_2 power cycle is due to the dramatically low compression work near the critical point. To demonstrate this dominance, the compressibility factor is discussed as follows.

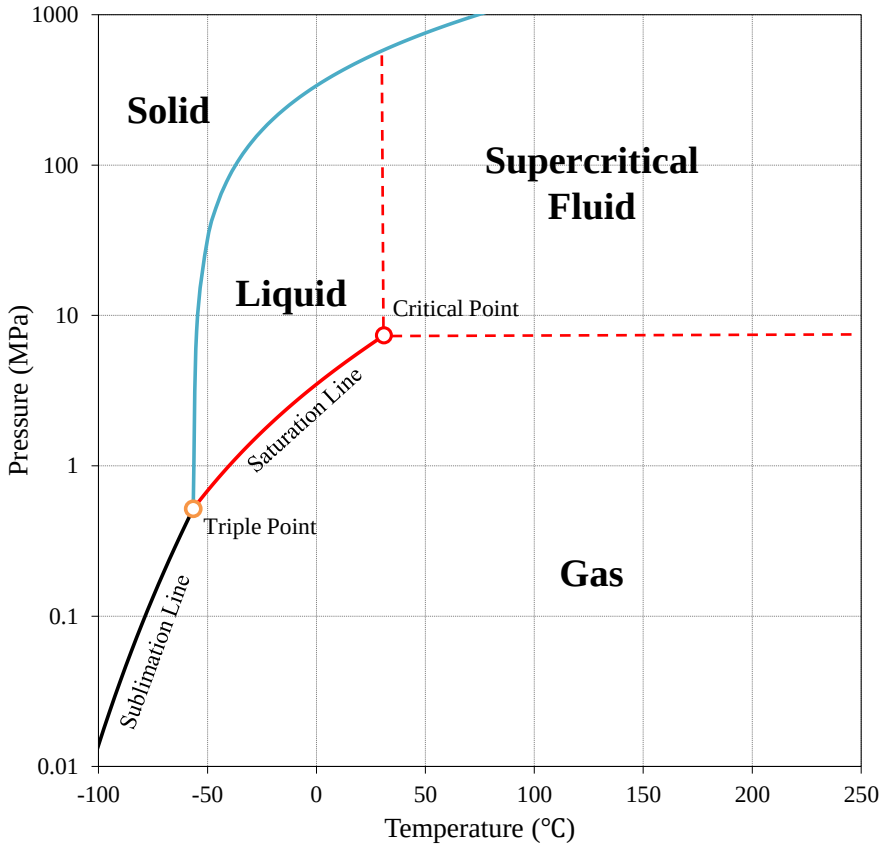

Figure 3–3 Phase diagram of CO_2.

The compressibility factor is defined as:

$$Z = \frac{pM}{\rho RT} \tag{3.1}$$

where p is the pressure, ρ is the density in kg/m^3, M is the molar mass in g/mol, R is the gas constant which is 8.314 J/mol·K and T is the absolute temperature in K. For ideal gas, $Z = 1$.

If we roughly consider CO_2 near critical point as incompressible, the compressor specific work can be written as:

$$w_{comp} = h_{out} - h_{in} = \gamma(p_{out} - p_{in}) = \frac{p_{out} - p_{in}}{\rho} \tag{3.2}$$

Substitute Equation (3.1) into Equation (3.2):

$$w_{comp} = \frac{R}{M}(Z_{out}T_{out} - Z_{in}T_{in}) \tag{3.3}$$

In Figure 3–4, it can be seen that if CO_2 at compressor inlet is near its critical point, especially at the pressure within the range of 7 to 8 MPa and the temperature below 35 ℃, the compression work would be considerably lower based on Equation (3.3). However, it has to be declared that although CO_2 has liquid like density in supercritical state, it is still a compressible substance practically. The imperfect method derived by Equation (3.3) is only used to demonstrate a main advantage of sCO_2-based power cycle expediently.

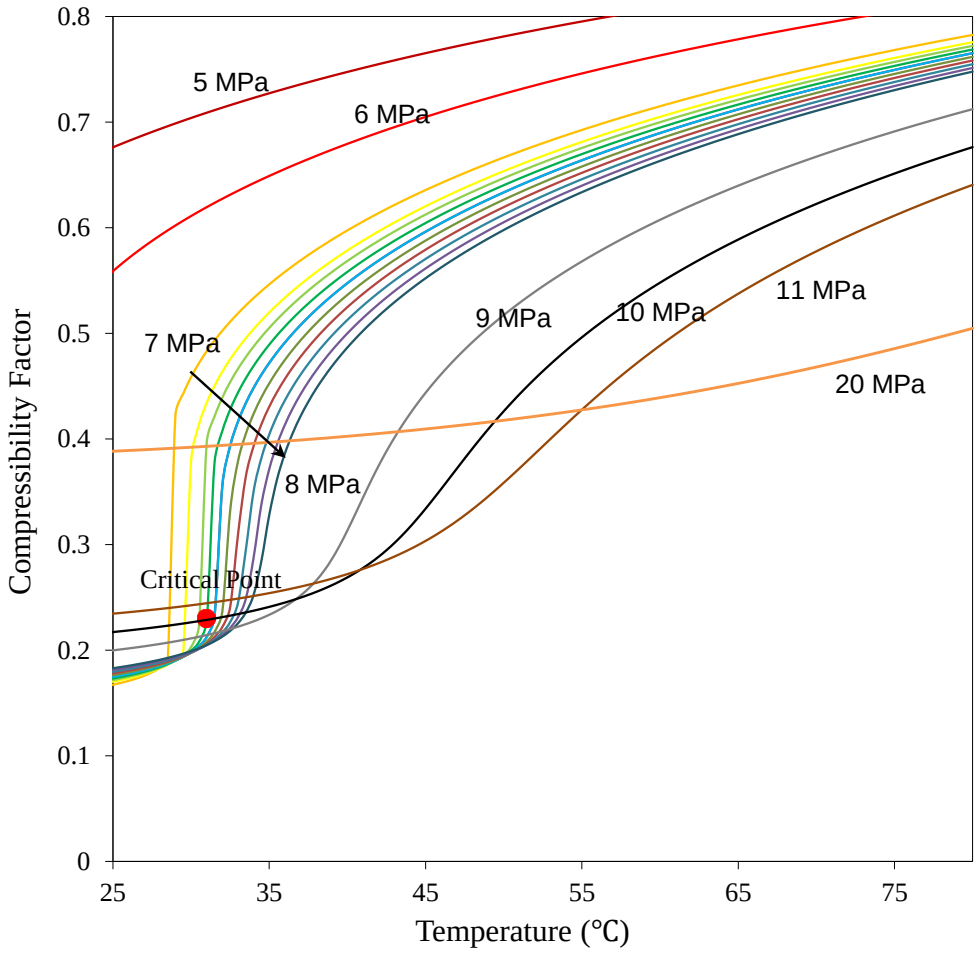

Figure 3–4 Compressibility factor of CO_2 vs. temperature in the pressure range of 5 to 11 MPa.

Additionally, if CO_2 is compressed isentropically from its critical point to 20 MPa which is represented by the red arrow line in Figure 3–5, the temperature and enthalpy increases are prominently small. Based on Equation (3.2), a remarkable low compression work is obtained.

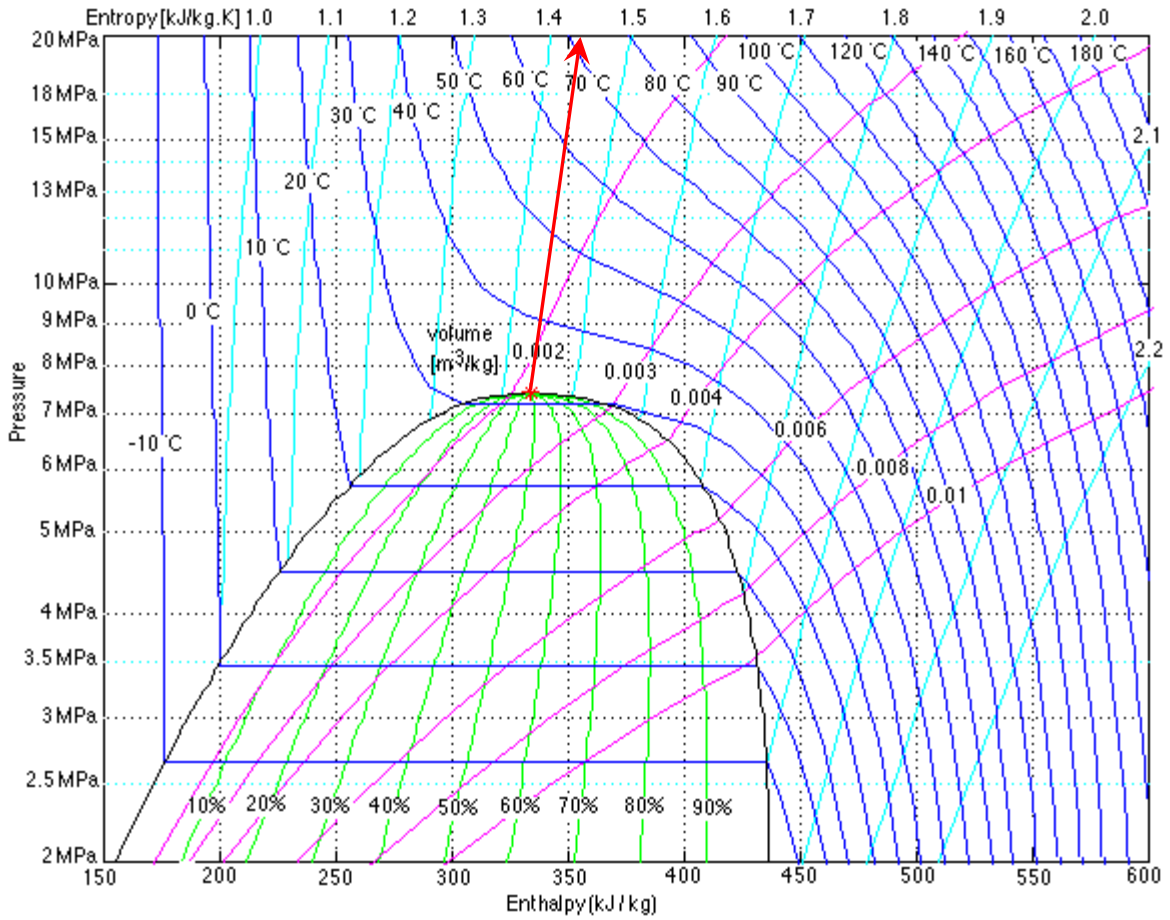

Figure 3–5 *P-h* diagram of CO_2.

The point where the minimum temperature approach in the heat exchanger is observed and referred to as the "pinch point". Figure 3–6 shows the *T-Q* diagrams for the heat source curves and the working fluid curves in a counter-current way. The LHS of Figure 3–6 presents the phase change occurs during the heat transfer process for a working fluid. The pinch point happens at the bubbling point where the working fluid starts to evaporate. On the RHS of Figure 3–6, the working fluid with no phase change takes place and the pinch point locates at the end of the heat transfer process. This situation demonstrates one of the main advantages of closed sCO_2-based power cycles using hot produced sCO_2.

The exergy destruction is the irreversible energy loss generated in heat transfer. Generally speaking, the working fluid with no phase change in heat transfer potentially has less exergy destruction than it has with phase change (see Figure 3–6). Therefore, closed sCO_2-based power cycles are worth being investigated although the majority of researches are focused on utilizing high temperature heat sources.

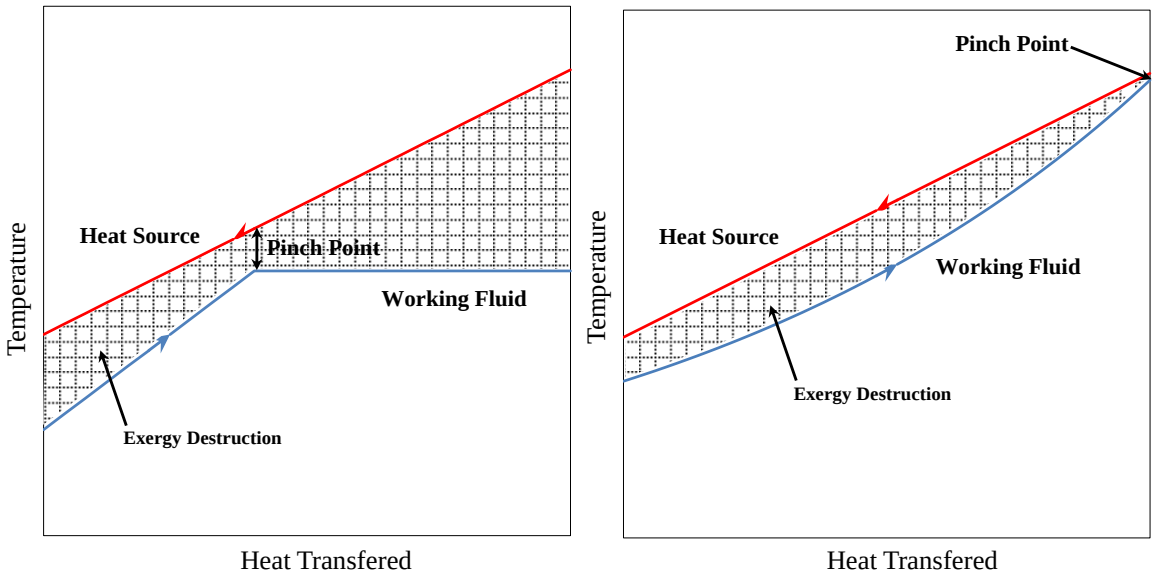

Figure 3–6 Pinch temperature in HXs.

On the other hand for working fluids used in ORCs which are discussed in Chapter 4, the pinch points are much more likely to occur in the IHX since the working fluids used in ORC have higher critical temperatures than CO_2 (see Figure A–1 and Figure A–2), which needs more detailed studies.

3.2 Model Description of sCO_2 Power Cycles

The baseline conditions for sCO_2 power cycle thermodynamic analysis are presented in Table 3–1. The heat source conditions obtained in Chapter 2, as well as the turbine and compressor efficiencies are fixed. It should be mentioned that, for the direct expansion and sCO_2 Brayton cycles, the lowest limit of turbine discharger pressure is selected as 7.8 MPa which is right above the critical pressure of CO_2. For the transcritical sCO_2 cycle, the lowest limit of turbine discharger pressure is set to be 0.5 MPa higher than the saturated pressure also corresponding to the cycle cooler temperature. The CO_2 at the turbine outlet should be in the liquid phase region where it is above the saturation line in Figure 3–3.

In addition, the IHX design objective is specified to the hot stream outlet temperature and cold stream inlet temperature difference of 5 ℃ in ASPEN Plus modeling. Furthermore, the minimum temperature approach, also known as pinch temperature is set to be 3 ℃. For both sCO_2 Brayton cycle and transcritical sCO_2 cycle, the cycle compressor discharger pressure is initiated to be 20 MPa.

As the optimization analysis has been performed with varying design parameters, it is necessary to mention that the values of parameters marked with * listed in Table 3–1 are fixed in the thermodynamic and optimization analyses.

Table 3–1 Baseline conditions for sCO_2 power cycle thermodynamic analysis.

Parameters	Units	Values
Hot Produced CO_2 Flow Rate *	kg/s	90
Hot Produced CO_2 Temperature *	℃	195
Hot Produced CO_2 Pressure *	MPa	22.5
CO_2 Reinjection Pressure *	MPa	14.5
Turbine Isentropic Efficiency *	%	0.88
Compressor Isentropic Efficiency *	%	0.85
Lowest Pre-cooler Outlet Temperature	℃	31.5
Post-cooler Outlet Temperature *	℃	30
Cooling Water Inlet Temperature *	℃	20
Cooling Water Pressure *	MPa	0.2
Direct Turbine Expansion		
Turbine Outlet Pressure	MPa	7.8
sCO_2 Brayton Cycle		
HP Turbine Outlet Pressure	MPa	15
(LP) Turbine Outlet Pressure	MPa	7.8
Lowest Cycle Cooler Outlet Temperature	℃	31.5
Cycle Main Compressor Outlet Pressure	MPa	20
Pre-Compressor Outlet Pressure	MPa	12.5
Recuperator Cold Inlet and Hot Outlet ΔT *	℃	10
IHX Cold Inlet and Hot Outlet ΔT *	℃	5
Minimum Temperature Approach in HX (Pinch) *	℃	3
Transcritical sCO_2 Cycle		
Turbine Outlet Pressure	MPa	$P_{sat,,liq}$ + 0.5
IHX Cold Inlet and Hot Outlet ΔT *	℃	5
Minimum Temperature Approach in HX (Pinch) *	℃	3
Lowest Cycle Cooler Outlet Temperature	℃	23
Cycle Compressor Outlet Pressure	MPa	20

Note: * - Fixed Value Parameter

3.2.1 Direct Turbine Expansion

In a CO_2 direct turbine expansion system, the hot produced CO_2 stream through the production well enters into a CO_2-H_2O separator on the surface illustrated in Figure 3–7. The purified sCO_2 at State 1 goes into a turbine and is expanded to a pressure above the CO_2 critical pressure (State 2). The hot discharged sCO_2 then cooled down by a water cooler, called a pre-cooler here, at State 3. To avoid phase change in a compressor, CO_2 temperature at State 3 should be above the critical temperature as well. Then, CO_2 at State 3 is compressed to the required injection well head pressure for re-injection back to the geothermal reservoir. Based on the geothermal heat mining simulation results presented in Chapter 2, pressurized hot CO_2 is cooled again by a water cooler (post-cooler in Figure 3–7) to 30 ℃ which is the preferable re-injection temperature of CO_2. The CO_2 at State 5 is injected to a geothermal reservoir where it is transitioning to a supercritical fluid. Finally, sCO_2 is heated up and pressurized then reaches the production well head, and a cycle is completed.

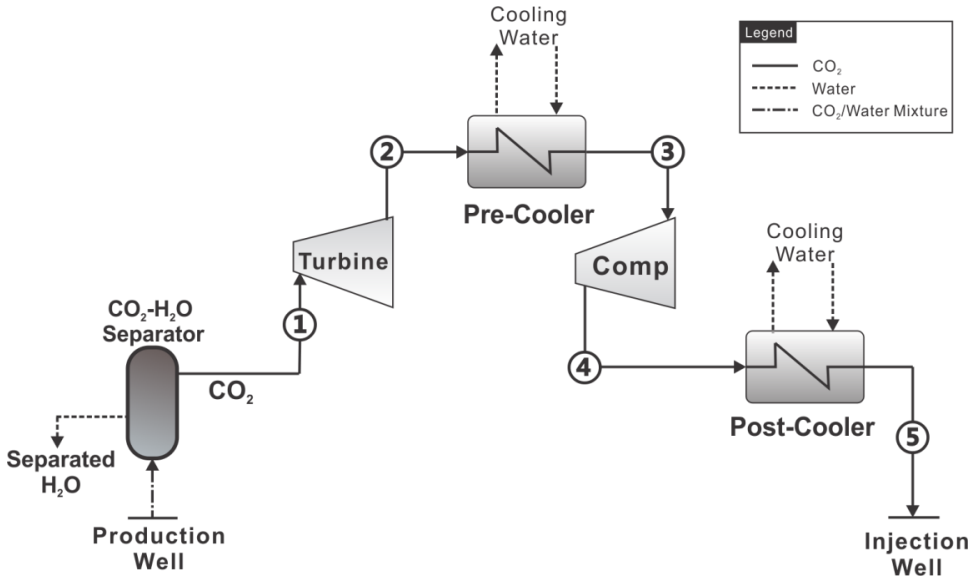

Figure 3–7 Schematic of direct turbine expansion system.

The thermodynamic analysis is critical to determining the system performance and performing the optimization study under different operation conditions. The mathematical equations expressing the models of the turbine and the compressor are presented. In addition, the system thermal efficiency, the system exergy efficiency, and the system specific net power output are used to evaluate the system thermodynamic performance.

Turbine

The isentropic expansion work and efficiency (States 1 to 2 in Figure 3–7) in the turbine can be obtained by:

$$W_t = \dot{m}_{geo,\,CO_2}\left(h_1 - h_2\right) \tag{3.4}$$

$$\eta_{t,s} = \frac{h_1 - h_2}{h_1 - h_{2s}} \tag{3.5}$$

Compressor

The isentropic compression work and efficiency (States 3 to 4 in Figure 3–7) are defined as:

$$W_{comp} = \dot{m}_{geo,\,CO_2}\left(h_4 - h_3\right) \tag{3.6}$$

$$\eta_{comp,s} = \frac{h_{4s} - h_3}{h_4 - h_3} \tag{3.7}$$

System Performance

The net power output can be calculated by:

$$W_{net} = W_t - W_{comp} \tag{3.8}$$

The system thermal efficiency can be obtained with the control volume shown in Figure 3–8:

$$\eta_{th,sys} = \frac{W_{net}}{\dot{m}_{CO_2}\left(h_1 - h_5\right)} \tag{3.9}$$

The thermal efficiency, also known as the 1st law efficiency, does not evaluate the quality of the energy conversion process and does not reflect the potential for improvement. The exergy efficiency, which accounts for this and can be defined as:

$$\eta_{ex,sys} = \frac{W_{net}}{\dot{m}_{CO_2}\left(e_{in} - e_{out}\right)} \tag{3.10}$$

where

$$e = \left(h - h_0\right) - T_0\left(s - s_0\right) + \frac{V^2}{2} + g\Delta H \tag{3.11}$$

In this analysis, there are no changes in kinetic and potential energy, and Equation (3.11) then can be reduced to

$$e = \left(h - h_0\right) - T_0\left(s - s_0\right) \tag{3.12}$$

where T_0, h_0, s_0 are the temperature, enthalpy and entropy of the CO_2 and cooling water at the reference state which is 0.1 MPa, 25 ℃ in this analysis.

The system specific net power output can be calculated from:

$$w_{net,sys} = \frac{W_{net}}{\dot{m}_{CO_2}} \tag{3.13}$$

The cooing water flow rates are selected as:

$$\dot{m}_{H_2O,pre-cooler} = \frac{175\ \text{kg/s}}{90\ \text{kg/s}}\dot{m}_{CO_2}$$
$$\dot{m}_{H_2O,post-cooler} = \frac{150\ \text{kg/s}}{90\ \text{kg/s}}\dot{m}_{CO_2} \quad (3.14)$$

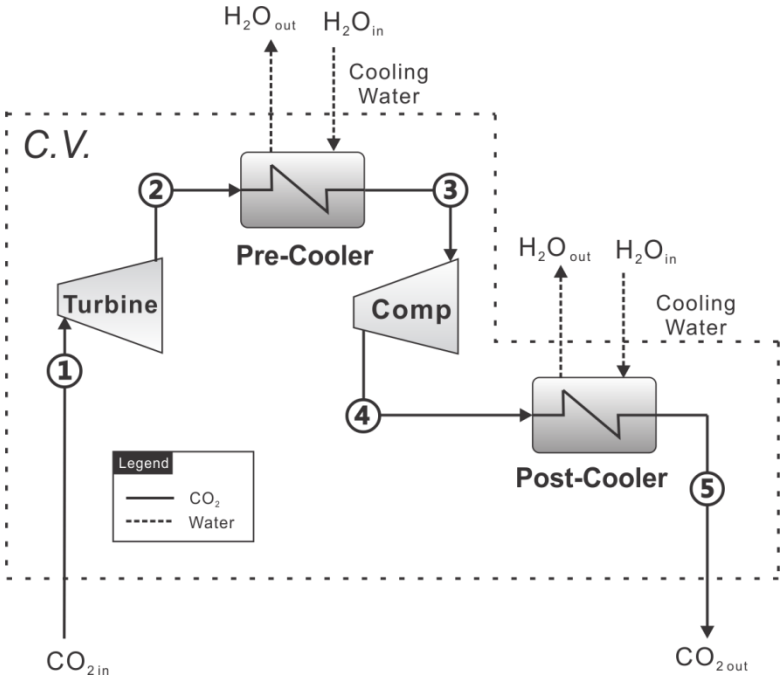

Figure 3–8 Control volume for direct expansion performance evaluation.

Figure 3–9 shows the temperature-entropy (*T*-*s*) diagram for the direct turbine expansion system, where it is assumed CO_2 from the production well head enters the turbine at 22.5 MPa and 195 ℃ directly, and expands in the turbine to 7.8 MPa (States 1 to 2 in Figure 3–9) which is right above the critical point. Subsequently, the CO_2 is cooled to 31.5 ℃ (States 2 to 3 in Figure 3–9) and compressed to the injection well head pressure of 14.5 MPa (States 3 to 4 in Figure 3–9) which the parameter values are shown in Table 3–1. Then, the pressurized CO_2 is cooled to 30 ℃ prior to re-injection into the geothermal reservoir

(States 4 to 5 in Figure 3–9). It can be seen from the *T*-*s* diagram that the direct turbine expansion cycle is an open cycle. The produced CO_2 from the geothermal reservoir potentially contains minerals directly in contact with the turbine and the heat exchangers even though the separation facility is included and CO_2 is a poor solvent for minerals. As a consequence, it is necessary to manufacture the components with anti-corrosive materials which lead to a higher plant capital cost. The detailed cost analyses considering material effects have been performed and are presented in Chapter 5.

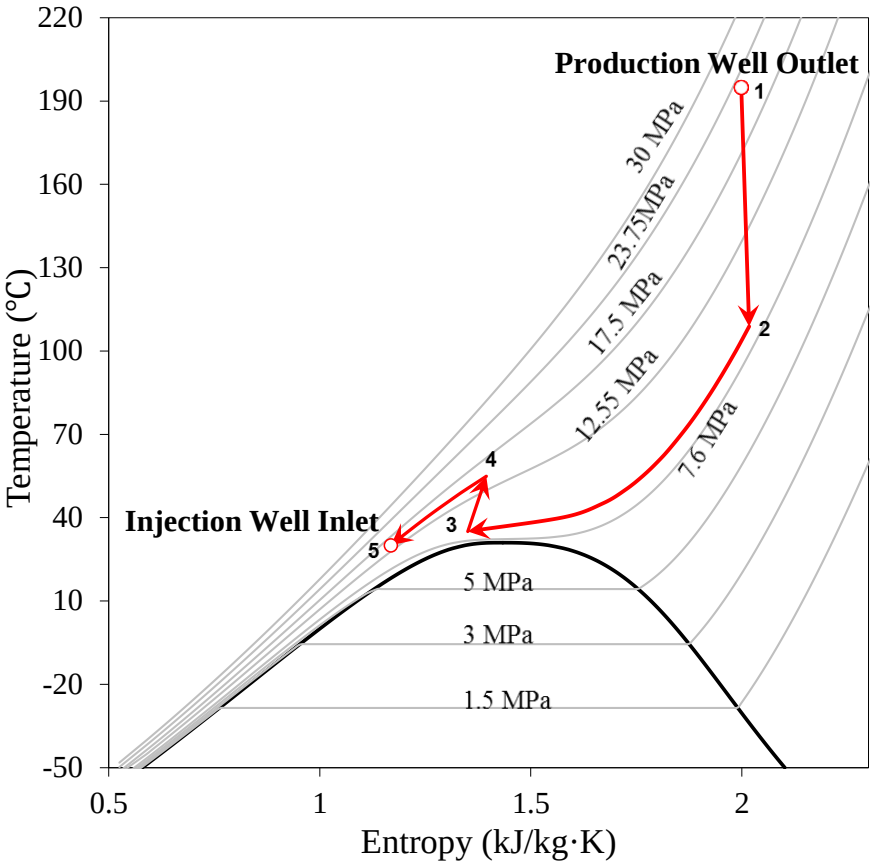

Figure 3–9 *T*-*s* diagram of direct turbine expansion.

In this analysis, prior to the injection well head, the whole cycle is above the critical point of CO_2. Nevertheless, the compressor inlet temperature as low as 23 ℃ has been

investigated shown in Figure 3–10. It is found that a maximum net power output of 4.253 MW_e as well as maximum cycle efficiencies are achieved at 31.1 ℃ which is the pseudo-critical temperature of CO_2 at a pressure of 7.8 MPa (also see Figure 3–10). The system optimal efficiencies are obtained at the same time, with the system thermal efficiency of 14.67% and the system exergy efficiency of 66.92%. However, the compressor inlet temperature of 31.5 ℃ is the lowest limit to ensure no phase change occurring in the compressor. Consequently, the allowed maximum net power output is achieved at the pre-cooler outlet temperature of 31.5 ℃.

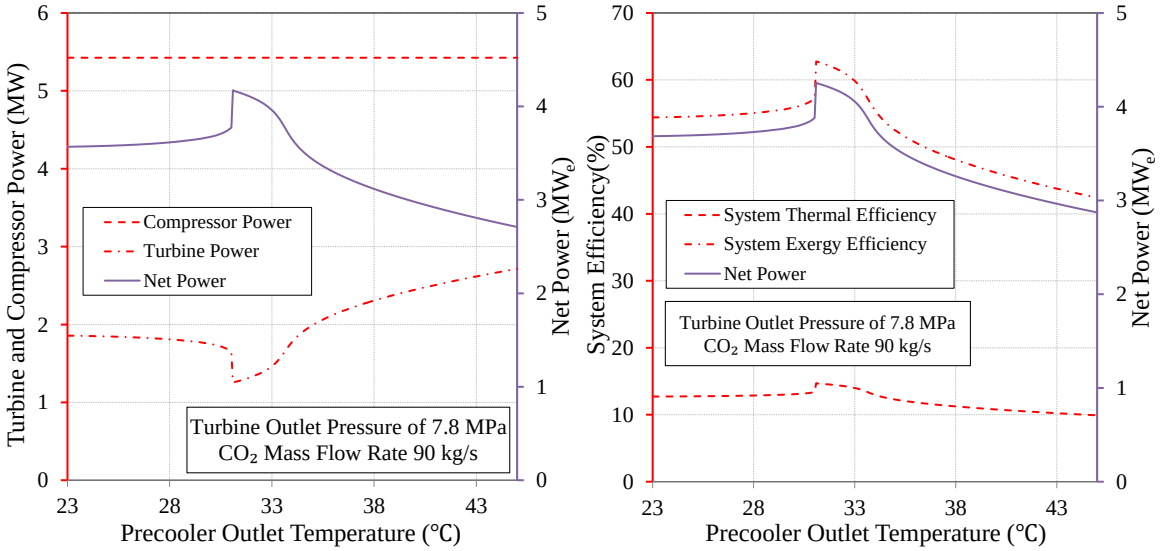

Figure 3–10 Turbine power, compressor power, net power output and system efficiencies vs. pre-cooler outlet temperature of direct expansion.

Another parameter to be considered for the system performance optimization is the turbine outlet pressure. Similarly to the sensitivity analysis for pre-cooler outlet temperature, although the lowest limit for the turbine outlet pressure is 7.8 MPa, a range of 5 to 13 MPa is selected to perform the analyses. It is found that the maximum net power output of 4.231 MWe and the maximum system thermal efficiency of 14.60% are obtained at the turbine

outlet pressure of 7.69 MPa, which is corresponding to the pseudocritical temperature of 31.5 ℃ (see RHS of Figure 3–11). In addition, the system optimal exergy efficiency of 62.45% is also achieved at the same conditions.

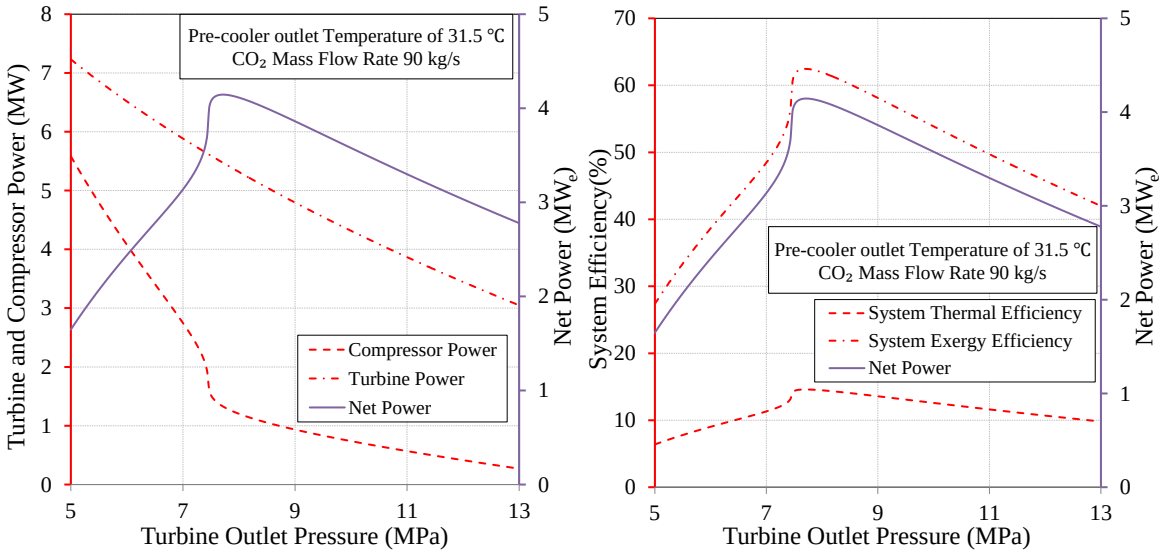

Figure 3–11 Turbine power, compressor power, net power output and system efficiencies vs. turbine outlet pressure of direct turbine expansion.

The optimization analyses have been performed over ranges of turbine exhaust pressures from 7.8 MPa to 15 MPa and compressor inlet temperatures or pre-cooler outlet temperatures from 31.5 ℃ to 45 ℃. Net power output is used as the optimization objective and the Sequential Quadratic Programming (SQP) method is employed to obtain the optimal results. The maximum power output is 4.226 MW_e which is obtained at the turbine outlet pressure of 7.8 MPa and the pre-cooler outlet temperature of 31.5 ℃. The system thermal efficiency is 14.58% and the exergy efficiency is 62.37% respectively. For the direct turbine expansion power system, the CO_2 thermosiphon effect is the main reason to contribute to high power generated but low compression work needed for re-injection.

If the higher temperature heat sources are available, the hot produced CO_2 from geothermal can be heated up to a higher temperature to generate more power with taking advantages of the CO_2 thermosiphon effect and the existing infrastructure.

It also needs to be mentioned that the maximum net power output is not necessary always to be obtained at the allowable lowest compressor inlet temperature. Figure 3–12 shows the higher net power output is achieved at the compressor inlet temperature of 31.5 ℃ and 25 ℃ respectively for the turbine inlet temperature of 195 ℃ and 595 ℃. It appears that relatively higher compressor inlet temperature and turbine output pressure are preferable for the low temperature heat source to achieve optimal net power output for the direct turbine expansion cycle.

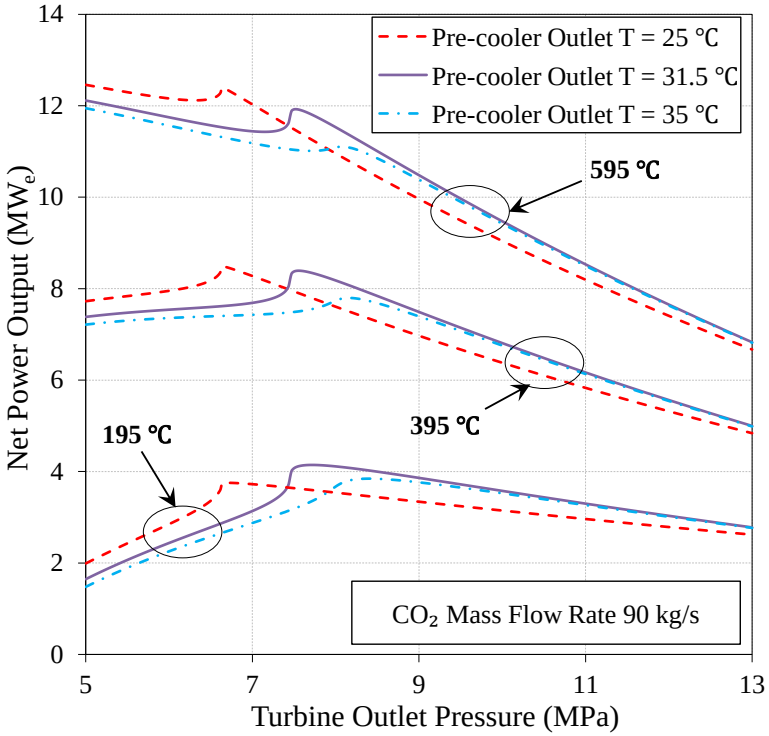

Figure 3–12 Net power output vs. turbine outlet pressure with different pre-cooler outlet temperature direct turbine expansion for different turbine inlet temperatures.

3.2.2 Closed sCO_2 Power Cycle

A closed sCO_2-based power cycle is driven by the geothermal heat from the hot produced sCO_2 in an outside geothermal loop through an IHX. It may have smaller net power output than the direct expansion system due to energy losses, but no contact with the geothermal fluid is its primary advantage. As discussed earlier in this chapter, closed sCO_2-based power cycles are using CO_2 as the working fluid, which has the similar temperature profile as the hot produced sCO_2 from geothermal reservoirs. This potentially increases the IHX efficiency to gain more geothermal heat. Furthermore, the closed sCO_2 power cycle eventually can have higher efficiencies than using other working fluids possibly. As one of the key components, the IHX plays an important role to transfer the geothermal heat from one loop to the closed power cycle loop. For each proposed configuration, the optimization analysis has been conducted. The optimal cycle CO_2 flow rate has also been obtained.

Figure 3–13 shows the two loops are connected through the IHX. Compared to the direct expansion system, the turbine is replaced by the IHX to connect the closed sCO_2 Brayton cycle and other components in the geothermal loop stay the same. However, negligible pressure drops passing through the HXs as well as the positive pressure difference between the production and the injection well heads, can eliminate using the compressor and post-cooler for the geothermal loop. Unlike the direct expansion system significantly benefiting from the CO_2 thermosiphon effect, the binary sCO_2 power cycle is relatively independent from the geothermal loop. However, there are still some advantages from the positive pressure difference between the production well head and the injection well head. When

the pressure of geothermal sCO_2 is higher than the required injection well head pressure after it passes through the IHX, a valve is used in place of a pre-cooler and a compressor. This process is an adiabatic expansion process which the CO_2 temperature drops to eliminate a portion of cooling loads. Meanwhile, equipment costs decrease since a costly pre-cooler and a compressor are replaced by an inexpensive valve, which also makes the system simple and easy to maintain. Furthermore, corrosive substances can hardly invade the closed cycles plus another superiority as the components can be built with lower grade materials, which make the closed cycles potentially could be more cost-effective than the direct expansion cycle.

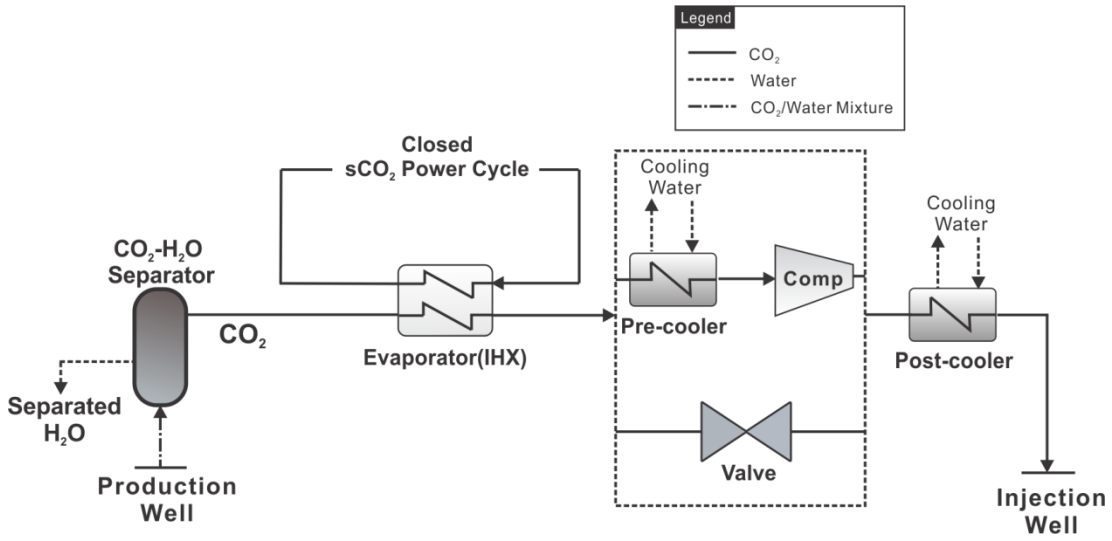

Figure 3–13 Schematic of closed sCO_2 power cycle.

The mathematical equations for evaluating the cycle and system performances are presented as follows. The cooling water flow rates of the pre-cooler and post-cooler of the geothermal loop are also specified here. Components like turbines and compressors for closed sCO_2 cycles are identical with direct expansion cycle, which are already described in Section 3.2.1.

Cycle Performance

Figure 3–14 shows the control volume considered for the closed sCO_2 power cycle thermodynamic analyses.

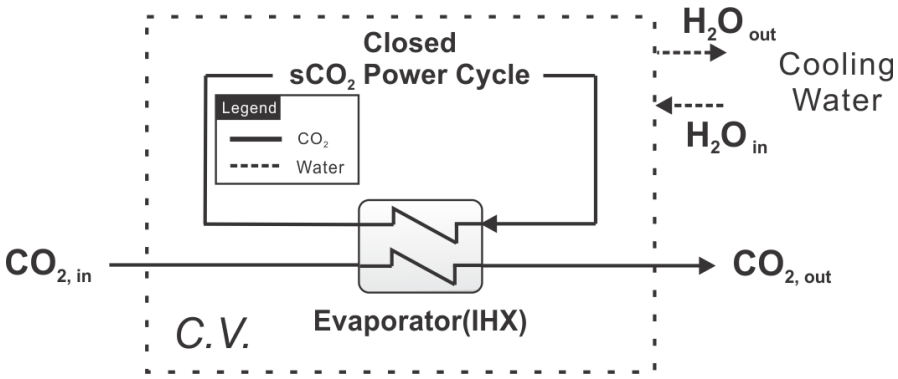

Figure 3–14 Control volume for closed sCO_2 Brayton cycle analysis.

The cycle net power output can be calculated by:

$$W_{sCO_2,net,cyc} = \sum W_t - \sum W_{comp} \tag{3.15}$$

Similarly, the turbine and compressor model are defined as same as the direct expansion analysis. The cycle thermal efficiency is defined as:

$$\eta_{sCO_2,th,cyc} = \frac{W_{sCO_2,net,cyc}}{\sum Q_{IHX}} \tag{3.16}$$

$$\eta_{sCO_2,ex,cyc} = \frac{W_{sCO_2,net,cyc}}{\dot{m}_{geo,CO_2}(e_{in} - e_{out})} \tag{3.17}$$

The cooling water flow rate for a cycle cooler after the turbine is:

$$\dot{m}_{H_2O,cyc\ cooler} = \frac{175\ \text{kg/s}}{90\ \text{kg/s}} \dot{m}_{cyc,\ CO_2} \tag{3.18}$$

If another cooler is needed for inter-cooling, the cooling water flow rate is:

$$\dot{m}_{H_2O,cyc\ \text{intercooling}} = \frac{150\ \text{kg/s}}{90\ \text{kg/s}} \dot{m}_{cyc,\ CO_2} \tag{3.19}$$

System Performance

The system net power output can be expressed as:

$$W_{sCO_2,net,sys} = W_{sCO_2,net,cyc} - W_{comp,geo\ loop} \tag{3.20}$$

The system efficiencies can be obtained by:

$$\eta_{sCO_2,th,sys} = \frac{W_{sCO_2,net,sys}}{\dot{m}_{CO_2,prod}\left(h_{CO_2,prod} - h_{CO_2,inj}\right)} \tag{3.21}$$

$$\eta_{sCO_2,ex,sys} = \frac{W_{sCO_2,net,cyc}}{\dot{m}_{geo,CO_2}(e_{in,sys} - e_{out,sys})} \tag{3.22}$$

The system specific net power output is defined as:

$$w_{sCO_2,net,sys} = \frac{W_{sCO_2,net,sys}}{\dot{m}_{geo,\ CO_2}} \tag{3.23}$$

The cooing water flow rates for geothermal loop coolers are selected to:

$$\begin{aligned} \dot{m}_{H_2O,pre-cooler} &= \frac{75\ \text{kg/s}}{90\ \text{kg/s}} \dot{m}_{geo,\ CO_2} \\ \dot{m}_{H_2O,post-cooler} &= \frac{75\ \text{kg/s}}{90\ \text{kg/s}} \dot{m}_{geo,\ CO_2} \end{aligned} \tag{3.24}$$

3.2.2.1 Simple sCO_2 Brayton Cycle

Figure 3–15 illustrates a simple sCO_2 Brayton cycle consisting of a turbine, a compressor, an IHX and a cycle water cooler. Cold sCO_2 in State 1 is compressed to State 2, and then geothermal energy is transferred through an IHX from geothermal produced CO_2 to cycle CO_2. Pressurized and hot cycle CO_2 expands at a turbine to generate electric power. From States 4 to 1, heat is then rejected by a water cooler and a Brayton cycle is completed.

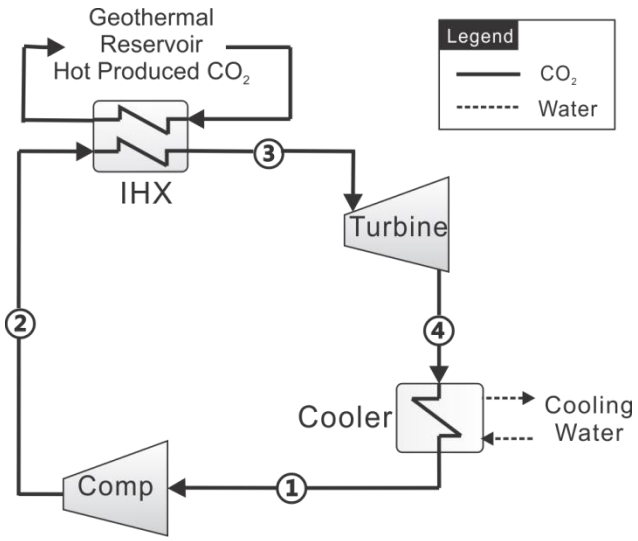

Figure 3–15 Schematic of simple sCO_2 Brayton cycle.

An ASPEN Plus model has been developed and the baseline conditions are listed in Table 3–1.

The *T-s* diagram of a simple sCO_2 Brayton cycle is illustrated in Figure 3–16. This typical Brayton cycle lies above CO_2 critical point and runs at the supercritical region of CO_2.

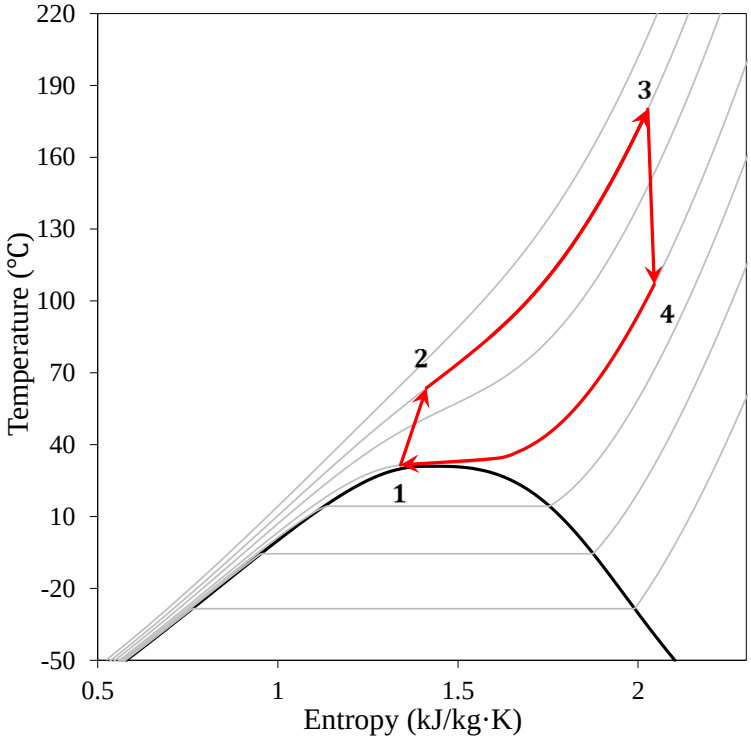

Figure 3–16 *T-s* diagram of simple sCO_2 Brayton cycle.

The compressor outlet pressure and the cooler outlet temperature are two major parameters impacting on the cycle performance. It is restricted for a Brayton cycle to have no phase change during any stages of the whole cycle. Therefore, 31.5 ℃ and 7.8 MPa are the lowest limit temperature and pressure for the whole cycle. Figure 3–17 presents that the net power and system efficiencies change with the compressor outlet pressure. The LHS of Figure 3–17 shows the compressor power constantly increases with the compressor outlet pressure. However, the increasing rate of turbine power output decreases when the compressor discharger pressure is over 22.09 MPa. The reason is the specific heat of CO_2 increases rapidly at the pressure range of 13 to 22.09 MPa. After 22.09 MPa, the power

gains due to the pressure increase starts to drop but the compression work keeps increasing which indicates an optimal compressor outlet pressure exists. The optimal net power output of 2.73 MPa is achieved at this compressor discharger pressure. However, the cycle efficiencies affected by the IHX heat duty and the irreversibility generated in the IHX, reach peak values at higher compressor outlet pressures. Therefore, an objective for selecting the suitable layouts is necessary. In this study, the primary goal is to achieve a higher net power output as possible. However, to assure the selected layouts are feasible and realistic, cycle thermal efficiency, cycle exergy efficiency, and specific net power output are calculated as well for comparing different layouts of sCO_2 Brayton cycles. This criterion is applied to other cycle thermodynamic analyses in this dissertation, including the transcritical sCO_2 cycle and ORCs.

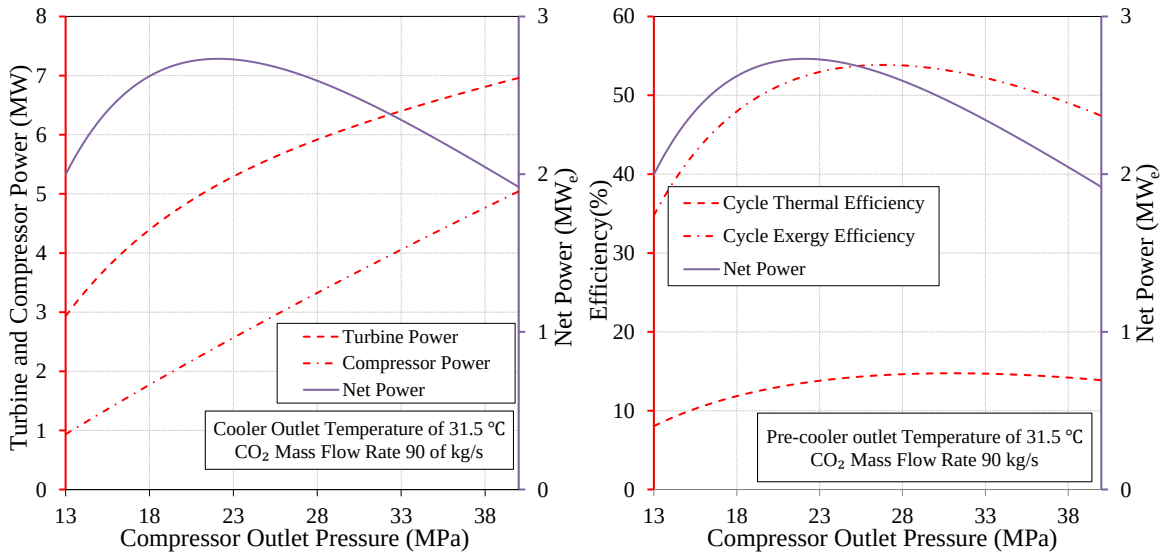

Figure 3–17 Net power output, turbine and compressor power, cycle efficiencies vs. compressor outlet pressure for simple sCO_2 Brayton cycle.

In regard to the compressor inlet temperature, or the cooler outlet temperature, the maximum net power output and cycle efficiencies appear at the required lowest cooler output temperature of 31.5 ℃ at the same time.

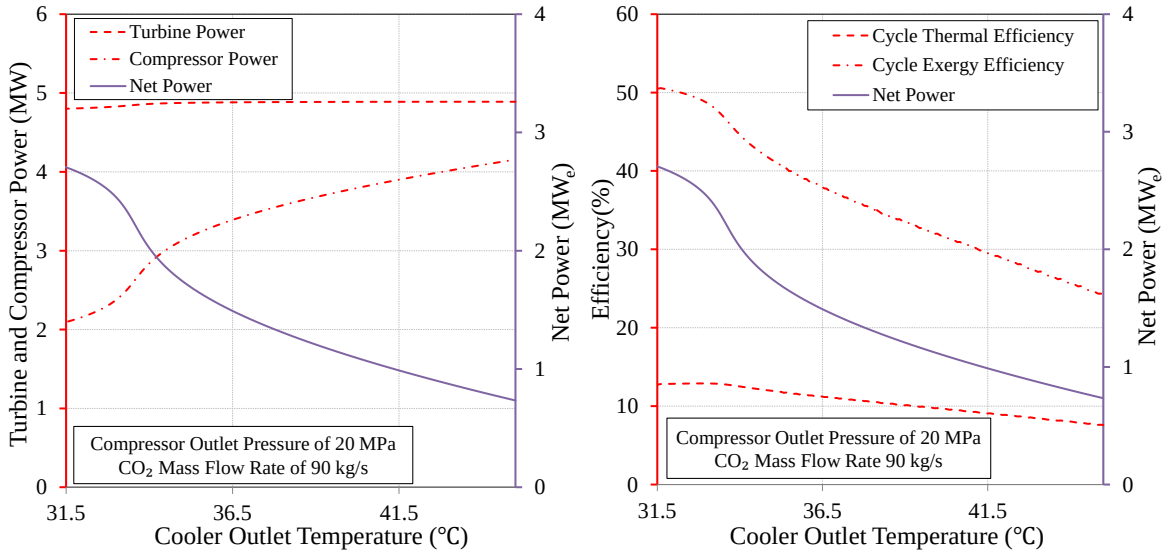

Figure 3–18 Net power output, turbine and compressor power, cycle efficiencies vs. cooler outlet temperature for simple sCO_2 Brayton cycle.

The optimization has been performed with constrains of compressor outlet pressure ranging from 13 to 40 MPa and cooler outlet temperature ranging from 31.5 to 45 ℃. Meanwhile, the optimal cycle CO_2 flow rate can be determined. In this analysis, the optimal design is achieved at the cooler outlet temperature of 31.5 ℃ and the compressor outlet pressure of 22.88 MPa. Under these conditions, the net power output, cycle thermal efficiency and cycle exergy efficiency are 2.76 MW_e, 13.92% and 53.47% respectively. The optimal cycle CO_2 mass flow rate is 87.58 kg/s.

3.2.2.2 Recuperative sCO_2 Brayton Cycle

The recuperative sCO_2 Brayton cycle adds a recuperator on the basis of the simple sCO_2 Brayton cycle. Figure 3–19 shows the stream at State 2 leaving the compressor passes through the recuperator where it gets the hotter stream (State 5) exhausted from the turbine. Therefore, the cooling load in the cooler and the heat needed through the IHX decrease which potentially leads to higher cycle efficiency. The recuperator is specified as hot outlet and cold inlet temperature difference of 10 ℃. Due to sCO_2 streams are on both sides of the recuperator, no phase change takes place in the recuperator.

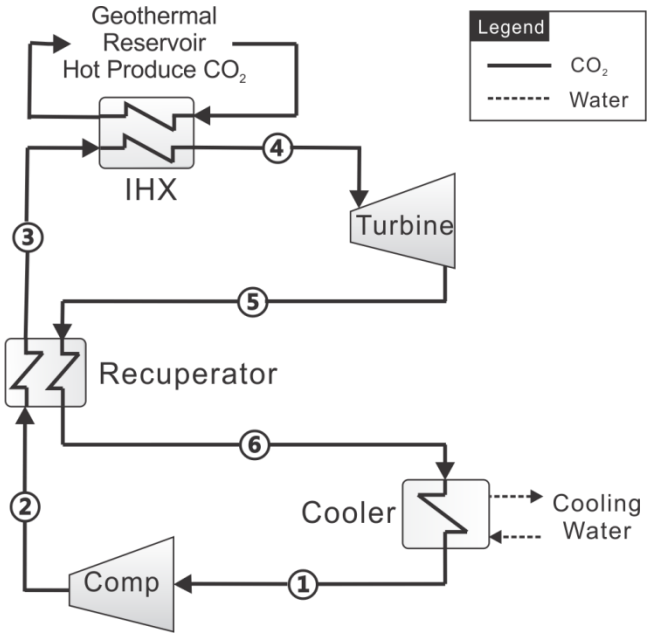

Figure 3–19 Schematic of recuperative sCO_2 Brayton cycle.

The heat from the process of States 5 to 6 is obtained from the process of States 2 to 3 shown in Figure 3–20, which happens in the recuperator. Despite the recuperator, the *T*-*s* diagrams are exactly the same for both the recuperative and simple sCO_2 Brayton cycles. This indicates that the recuperator only increases the cycle thermal efficiency "internally".

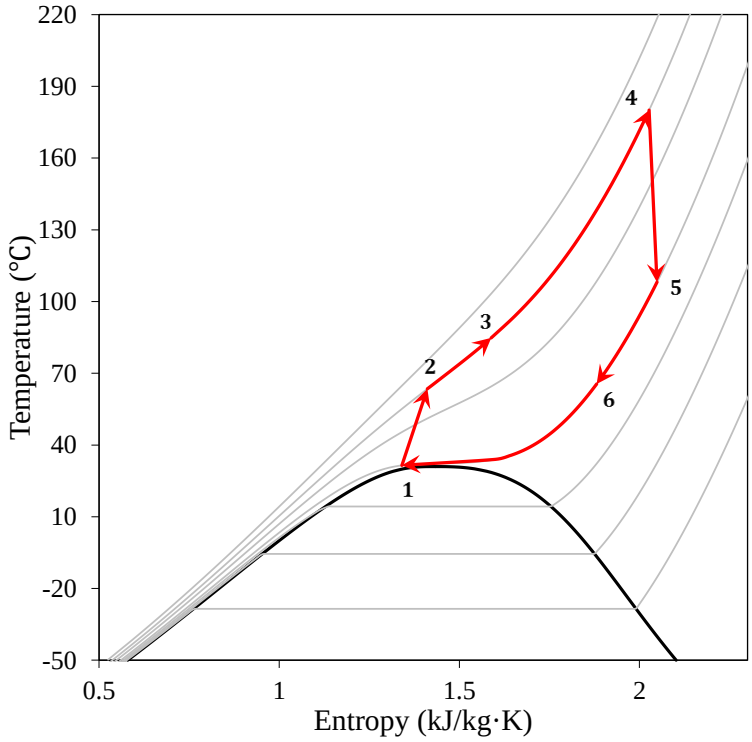

Figure 3–20 *T-s* diagram of recuperative sCO_2 Brayton cycle.

The thermodynamic analysis and optimization method used are identical to the simple sCO_2 Brayton cycle, with the same lowest temperature and pressure limits, the optimal results can be obtained. Differ from the simple sCO_2 cycle, the maximum cycle thermal efficiency as well as the cycle exergy efficiency appears not to reach optimal value at the same time as the net power output. The recuperator eliminates the heat rejection and utilizes this portion of energy to heat up the CO_2 at the compressor output. However, the temperature entering the IHX rises which reduces the amount of heat obtained from the hot sCO_2. This directly leads to the net power output reduction. On the other hand, the higher compressor outlet pressure has a higher outlet temperature as well, which impairs the impact of the recuporator. Due to this interaction, the net power output, cycle thermal

efficiency and cycle exergy efficiency are not necessary to be obtained at the same conditions as the simple sCO_2 Brayton cycle (see Figure 3–21).

Figure 3–22 shows the net power output as well as cycle efficiencies decrease with the increasing cooler output temperature. Moreover, the maximum reduction rate occurs at the pseudo-critical temperature of CO_2 at a pressure of 7.8 MPa which is the turbine outlet pressure. It is because the compression work increases significantly if the compressor inlet temperature is over the pseudo-critical temperature of CO_2. In practicality, the cooler outlet temperature is not necessary to be as low as possible since a large cooling load may cause considerable O&M cost. Furthermore, the fixed turbine outlet pressure in this analysis is also necessary to be considered for a techno-economic optimization to come up with the most cost-effective design. However, as a very huge and complex system is investigated here, it is impractical to include all parameters in the global optimization. Nevertheless, the parametric study conducted and discussions made here are significant for the future work and are also the consequential recommendations.

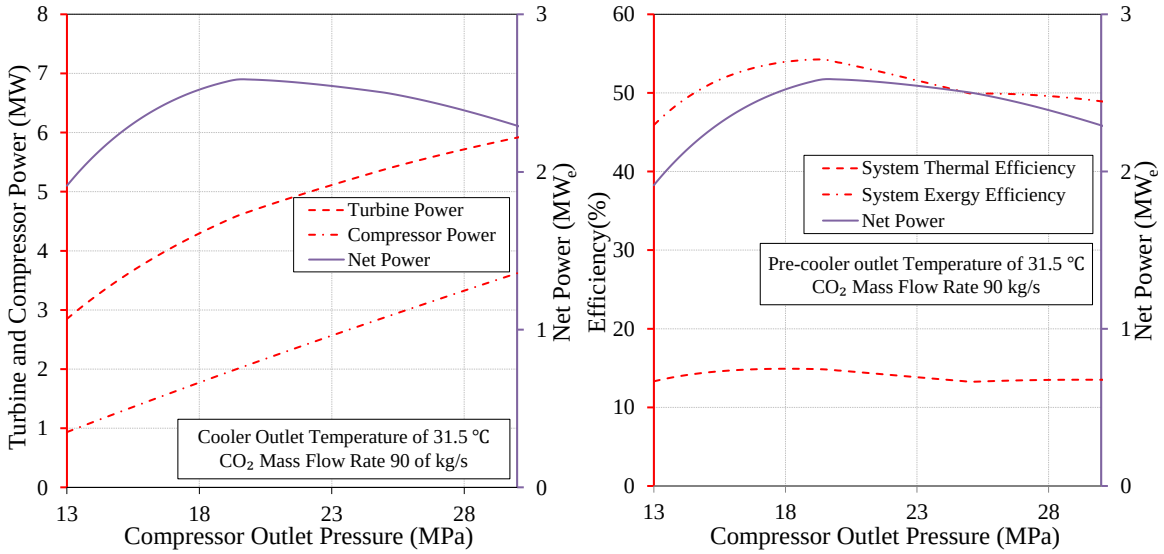

Figure 3–21 Net power output, turbine and compressor power, cycle efficiencies vs. compressor outlet pressure for recuperative sCO_2 Brayton cycle.

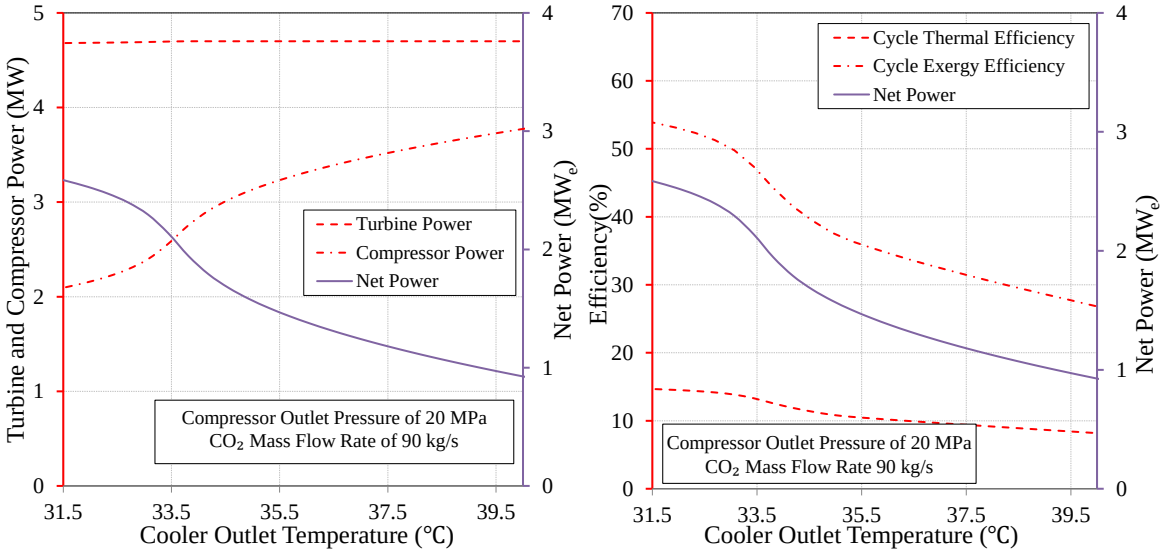

Figure 3–22 Net power output, turbine and compressor power, cycle efficiencies vs. cooler outlet temperature for recuperative sCO_2 Brayton cycle.

For the recuperative sCO_2 Brayton cycle, the optimal design is achieved at the cooler outlet temperature of 31.5 ℃ and the compressor outlet pressure of 20.01 MPa. Under these conditions, the net power output, cycle thermal efficiency and cycle exergy efficiency are 2.584 MW_e, 14.64% and 53.75% respectively. The optimal cycle CO_2 mass flow rate is

90.26 kg/s. It needs to be mentioned that, less heat is transferred from the produced CO_2 from geothermal reservoirs to the cycle CO_2 in the recuperative cycle than the simple cycle, since the temperature of cycle CO_2 at the inlet of IHX is higher after obtaining the heat from the recuperator. Although the cycle thermal efficiency increases, the net power output and system exergy efficiency slightly decrease.

3.2.2.3 sCO_2 Brayton Cycle with Pre-compression and Inter-cooling

In the sCO_2 Brayton cycle with pre-compression and intercooling configuration shown in Figure 3–23, an additional cooler and a pre-compressor help to split the compression work, which intends to make the compression process happen near CO_2 critical point. These improvements further decrease the compression work and eventually more net power can be generated. However, more components added potentially raise the system capital cost and complexity. Furthermore, the instability of the system also increases.

The concerns regarding the cost effectiveness and feasibility are going to be addressed later in the global optimization and cost analyses in Chapter 5. As already discussed at the beginning of this chapter, thermodynamic performance is the primary objective of selecting the most promising layout for each type of power generation system. At this stage of the analysis, the improvement methods are considered simply to identify their contributions on the cycle thermodynamic performance.

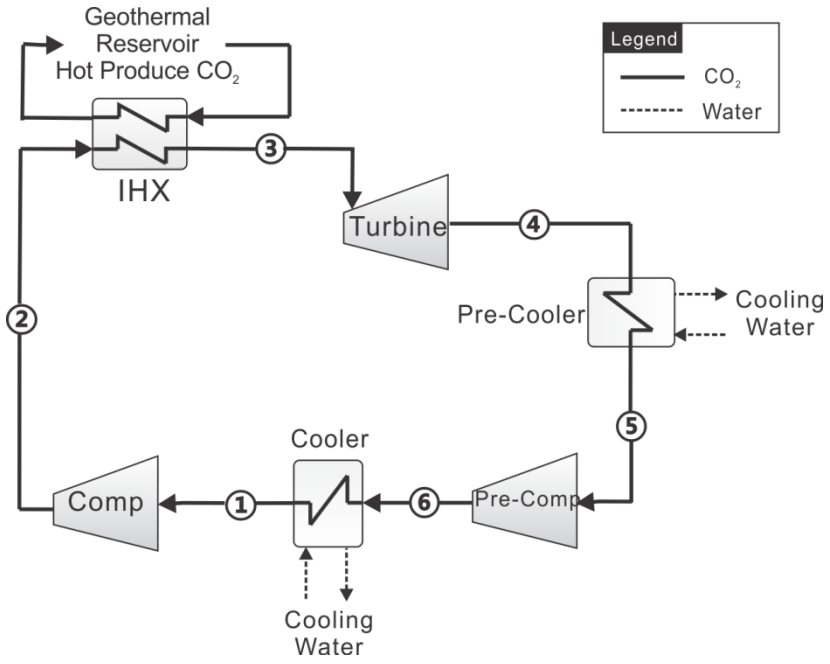

Figure 3–23 Schematic of sCO_2 Brayton cycle with pre-compression and inter-cooling.

Figure 3–24 presents the whole process in *T-s* diagram. Start from State 1, CO_2 near critical point is compressed and gets heated in the IHX (States 2 to 3). At State 3, CO_2 expands through the turbine to produce power. The exhausted CO_2 at Stage 4 is cooled down to State 5 before enters into the pre-compressor. States 5 to 6 is the pre-compression process. The pre-compressor discharger pressure is an intermediate pressure between the turbine inlet and outlet pressures. Then, it is cooled down again (States 6 to 1) and subsequently compressed to the turbine inlet pressure (States 1 to 2). The cycle CO_2 is circulating in this closed system continuously above its critical point.

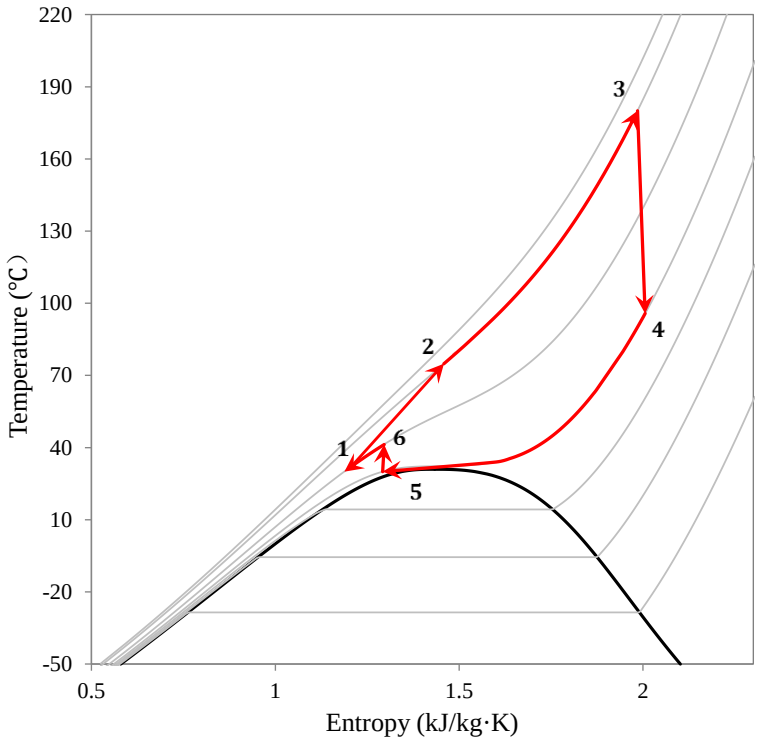

Figure 3–24 *T-s* diagram of sCO_2 Brayton cycle with pre-compression and inter-cooling.

There are five parameters that need to be investigated for their impacts on the cycle performance: compressor outlet pressure, cooler outlet temperature, pre-compressor outlet pressure, pre-cooler outlet temperature, and cycle CO_2 flow rate. In order to make the whole cycle above CO_2 critical point, again, the bottom boundaries for temperature and pressure are 31.5 ℃ and 7.8 MPa. In Figure 3–25, the compressor outlet pressure ranging from 12.5 to 40 MPa is used to investigate its impacts on the cycle performance due to the pre-compressor outlet pressure is fixed to 12.5 MPa. After the pre-compressor and pre-cooler, the cooled and pre-compressed CO_2 enters into the main compressor. The cycle performances behave very similarly to the simple sCO_2 cycle and an optimal compressor outlet pressure exists at 28.48 MPa which leads to a maximum net power output of 3.193 MW_e.

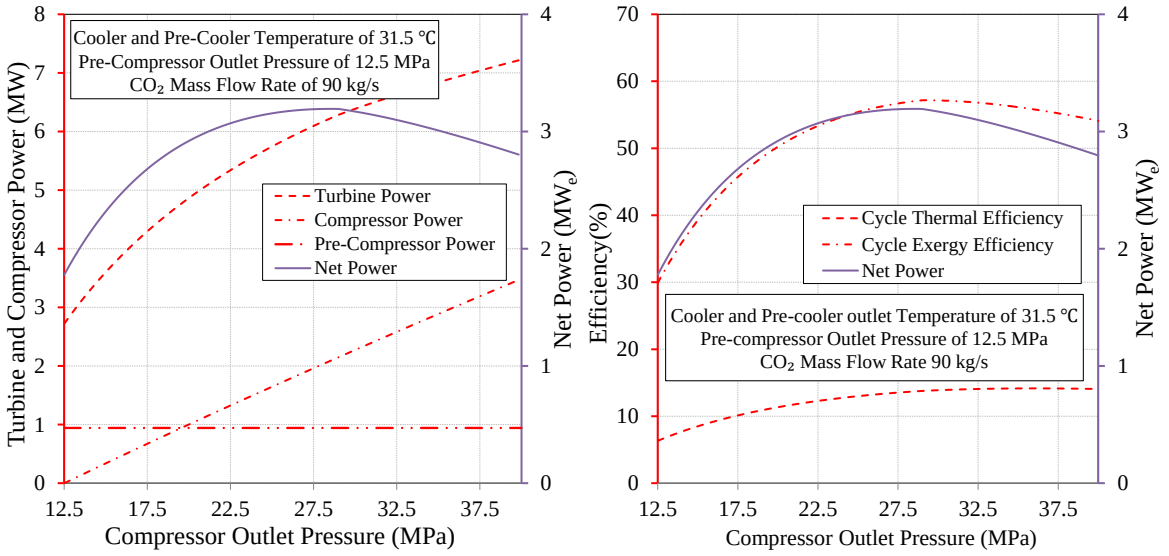

Figure 3–25 Net power output, turbine and compressor power, cycle efficiencies vs. compressor outlet pressure for sCO_2 Brayton cycle with pre-compression and inter-cooling.

The cycle performance is not affected by the cooler outlet temperature significantly for this cycle configuration. Figure 3–26 illustrate that the compressor work slightly increases due to the compressor inlet temperature rise. It indicates if the cooling capability is very critical to the system design and cost, the cooler outlet temperature is not necessary to be as low as possible. The net power output changes from 2.992 to 2.734 MW_e throughout the cooler outlet temperature ranging from 23 to 45 ℃. In addition, the cycle exergy efficiency is around 53% and the cycle thermal efficiency even increases approximately 3% with the increase of cooler outlet temperature. The reason is that the heat transferred in the IHX decreases more than the reduction of net power output. The thermal efficiency can be expressed as:

$$\eta_{th,cyc} = \frac{h_4 - h_3}{h_3 - h_2} \tag{3.25}$$

where the states point of the enthalpies can be found in Figure 3–23. Therefore, when the enthalpy at State 2, which is related to the compressor outlet temperature, increases, the cycle thermal efficiency increases too.

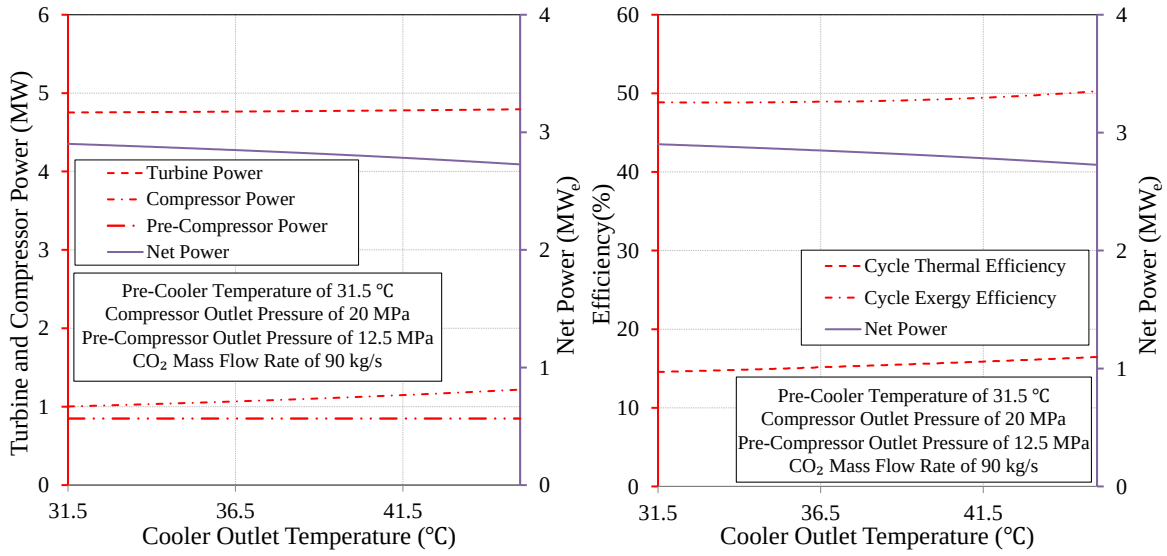

Figure 3–26 Net power output, turbine and compressor power, cycle efficiencies vs. cooler outlet temperature for sCO_2 Brayton cycle with pre-compression and inter-cooling.

The sensitivity analysis results of pre-compressor outlet pressure are presented in Figure 3–27. The compression work is shared by the pre-compressor and the main compressor. The pre-compressor work increases with the increasing pre-compressor outlet pressure. Meanwhile, the main compression work gets less. There is an optimal pre-compressor outlet pressure of 9.60 MPa to obtain the maximum net power output of 2.974 MW_e. The cycle efficiencies are almost unaffected by the change of pre-compressor outlet pressure.

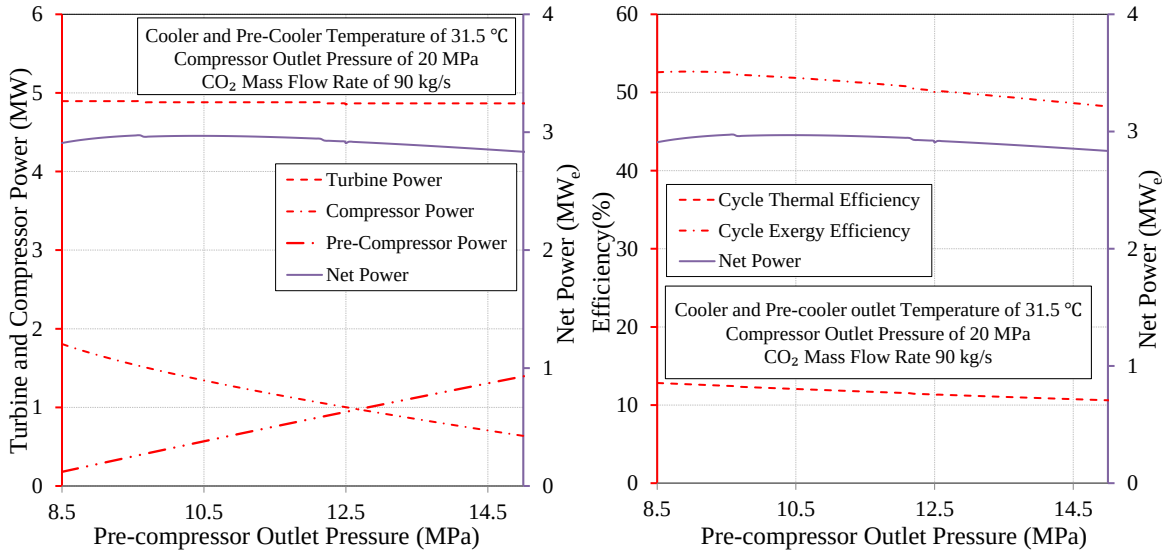

Figure 3–27 Net power output, turbine and compressor power, cycle efficiencies vs. pre-compressor outlet pressure for sCO_2 Brayton cycle with pre-compression and inter-cooling.

Subsequently, the pre-cooler outlet temperature is investigated. Among the turbine and compressors, only the pre-compressor is affected by the change of pre-cooler outlet temperature. Compared to the impact of the cooler outlet temperature on the main compressor, the pre-compressor inlet temperature can have significant effect of the pre-compression work. Obviously, due to dramatic change of CO_2 near its critical point, the pre-compressor performance can vary greatly, since the pre-compressor inlet conditions are much closer to CO_2 pseudo-critical temperature at pressure of 7.8 MPa. Furthermore, the net power output and cycle efficiencies are showing the exact tendency over the pre-compressor outlet temperature range of 31.5 to 45 ℃ (see RHS of Figure 3–28).

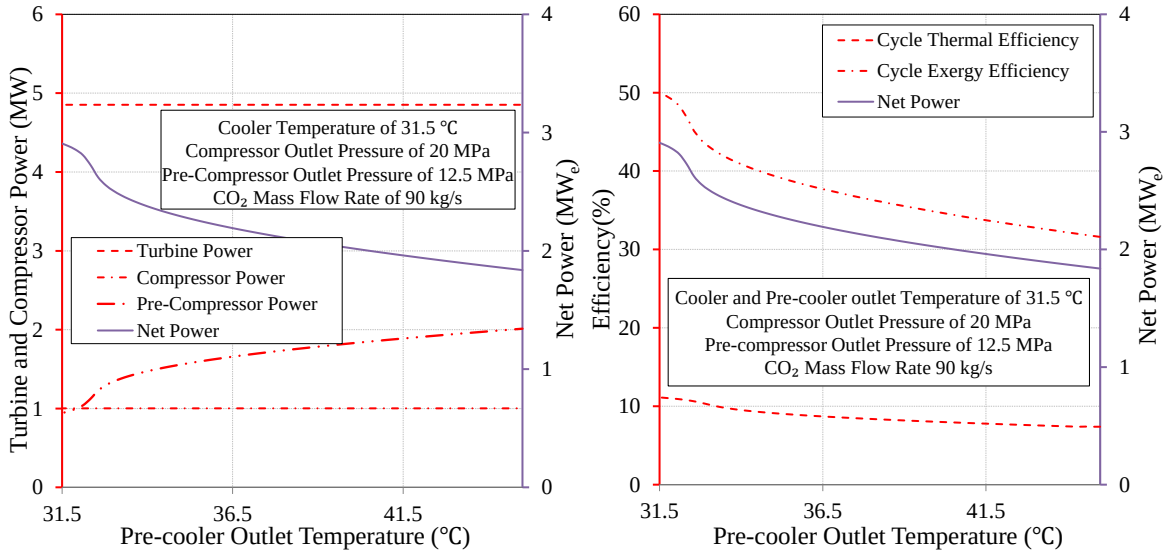

Figure 3–28 Net power output, turbine and compressor power, cycle efficiencies vs. pre-cooler outlet temperature for sCO_2 Brayton cycle with pre-compression and inter-cooling.

Finally, the optimal results are obtained with the parameter ranges used in the sensitivity analysis. The optimal net power output, cycle thermal efficiency and cycle exergy efficiency are 3.194 MWe, 13.28% and 56.32% respectively. The optimal cycle CO_2 flow rate is 90.44 kg/s. In addition, the optimal design conditions are the cooler outlet temperature of 31.5 ℃, the pre-cooler outlet temperature of 31.5 ℃, pre-compressor outlet pressure of 13.87 MPa and the compressor outlet pressure of 28.47 MPa.

3.2.2.4 sCO_2 Brayton Cycle with Reheat

If an additional heat source is available, to take advantage of the existing infrastructure, a set of extra turbine and IHX can be installed to generate more power. The hot produced CO_2 from a geothermal reservoir is considered as the first heat source. Since geothermal energy is typically recognized as a low grade heat source, the reheat heat source with higher temperature is used in this study. Figure 3–29 and Figure 3–30 generally show the

sCO_2 Brayton cycle with a higher temperature heat source of 300 ℃ as the reheat heat source. For convenience, the higher heat source is assumed to be sufficient to heat the cycle CO_2 to the temperature of 5 ℃ lower than the heat source temperature.

The LP turbine outlet pressure is fixed to 7.8 MPa which is the same as the previous analyses. The compressor outlet pressure, cooler outlet temperature and HP turbine discharge pressure are three variables considered for the sensitivity analysis and optimization (see Figure 3–29).

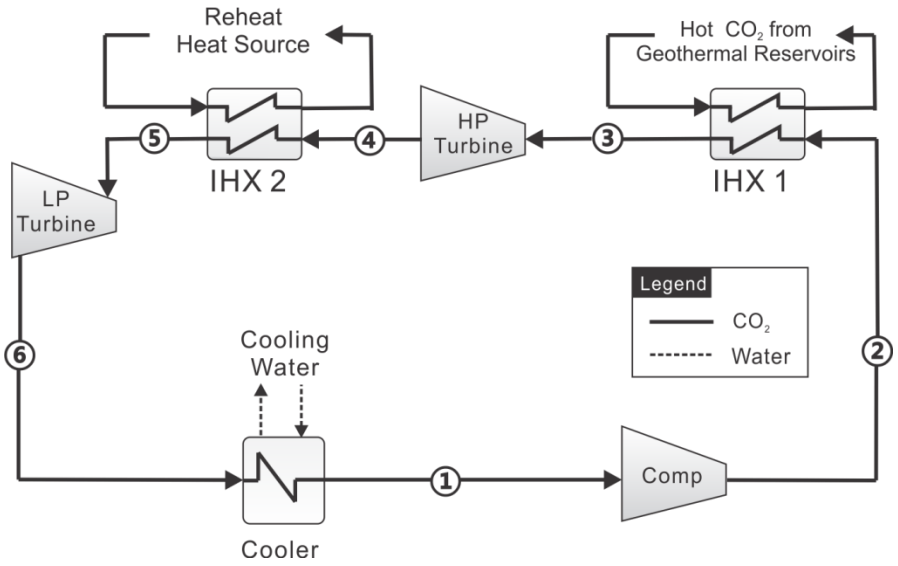

Figure 3–29 Schematic of sCO_2 Brayton cycle with reheat.

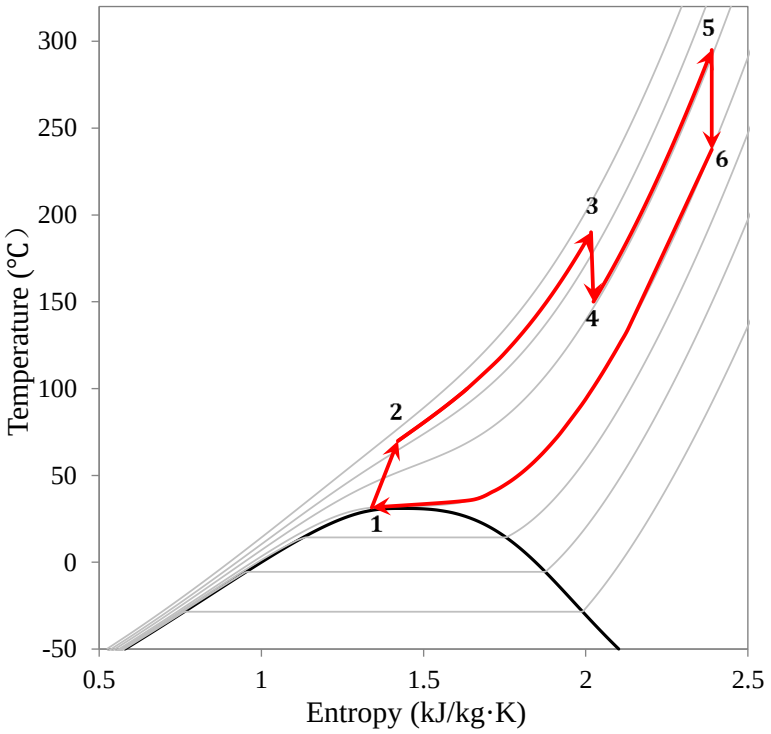

Figure 3–30 *T-s* diagram of sCO_2 Brayton cycle with reheat.

Since the reheat heat source is assumed to simply heat up the CO_2 to a specified temperature, the cycle exergy efficiency is not available to be calculated. However, the heat duty for the reheat process is obtained for getting the cycle thermal efficiency.

Figure 3–31 presents the effects of the compressor outlet pressure on the cycle performance. For the LP turbine, the inlet and outlet pressures are fixed and the power output is kept constant. However, the HP turbine power and the compressor power increase when the compressor outlet pressure gets larger. An optimal net power output appears when the growth rate of compressor power is greater than the growth rate of turbine power. The cooler outlet temperature or the compressor inlet temperature is also investigated and the results are shown in Figure 3–32. It can be seen that the maximum net power output and cycle thermal efficiency both are achieved at the cooler outlet temperature of 31.5 ℃.

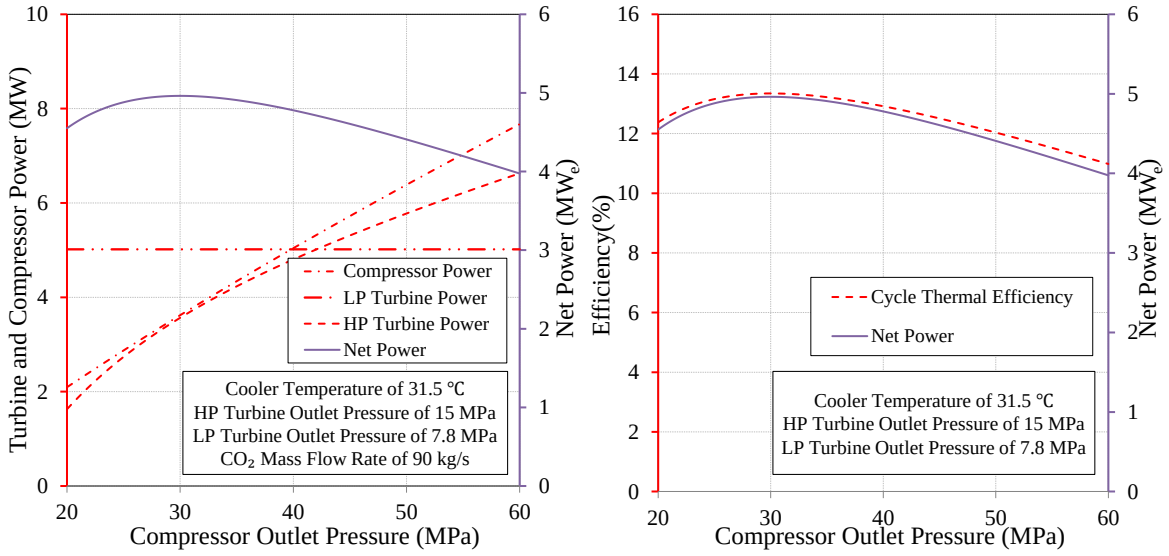

Figure 3–31 Net power output, turbine and compressor power, cycle thermal efficiency vs. compressor outlet pressure for sCO_2 Brayton cycle with reheat.

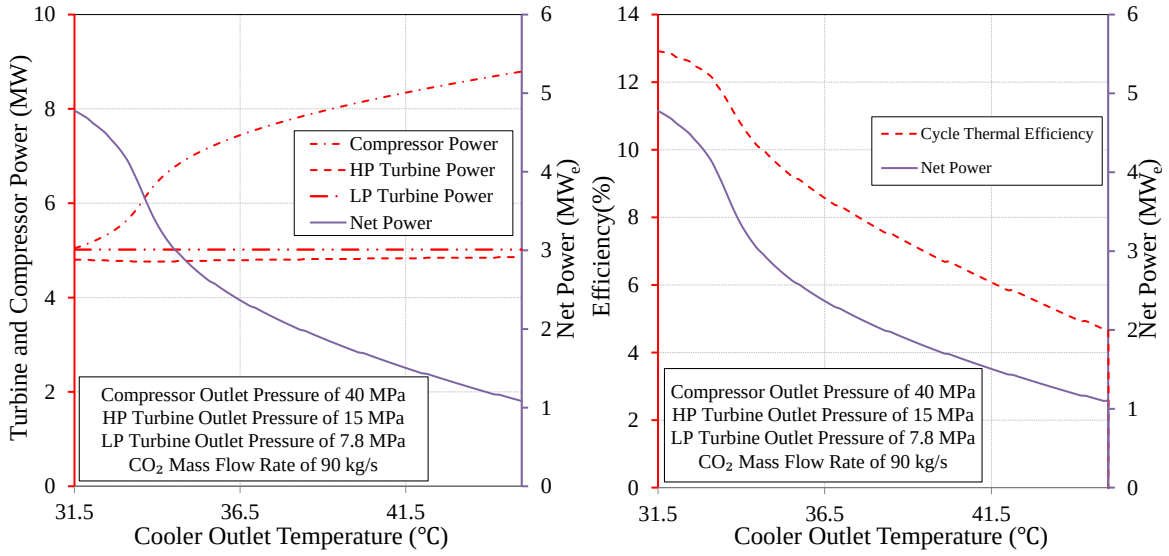

Figure 3–32 Net power output, turbine and compressor power, cycle thermal efficiency vs. cooler outlet temperature for sCO_2 Brayton cycle with reheat.

The HP turbine discharge pressure is another important parameter to be considered for efficiently using the reheat source. The cycle tends to obtain more energy from the high temperature heat source to achieve better performance. Figure 3–33 shows the highest cycle efficiency even requires to get rid of the HP turbine, since the HP turbine outlet

pressure is the same as the compressor outlet pressure at the highest cycle thermal efficiency. Nevertheless, the objective in this study for the optimal design is maximizing the net power output. Although the sensitivity analysis in Figure 3–33 shows the maximum net power output is obtained almost at the upper limit of the HP turbine outlet pressure, the parameters with the integration effects which may show different behaviors in the final optimization analysis.

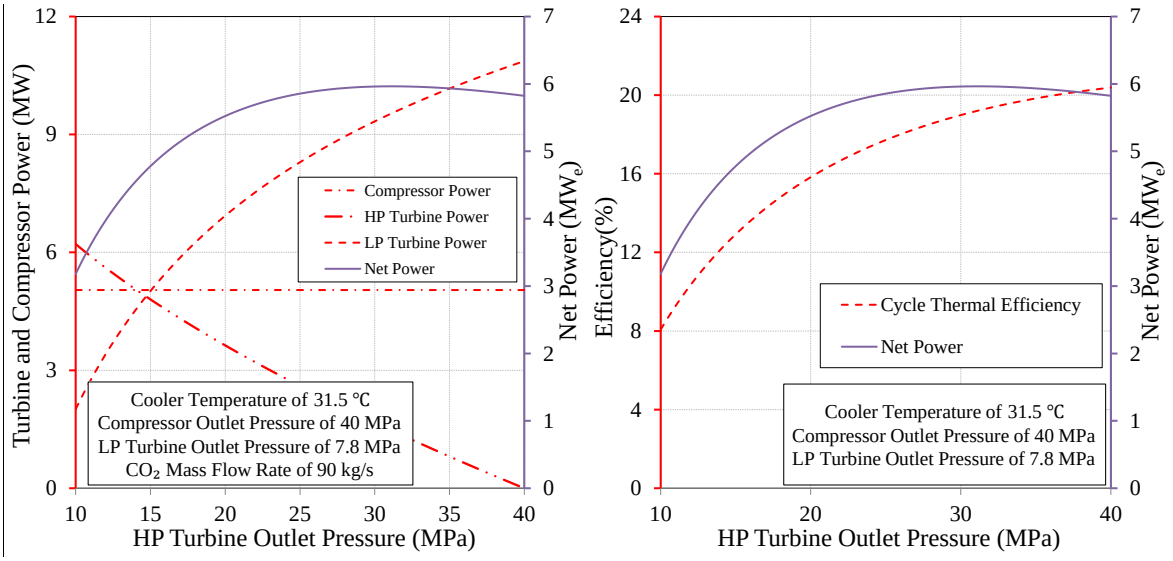

Figure 3–33 Net power output, turbine and compressor power, cycle thermal efficiency vs. HP turbine outlet pressure for sCO_2 Brayton cycle with reheat.

Different from the previous layouts, with a generic heat source of a specific heating temperature to provide enough thermal energy in this configuration, the cycle CO_2 flow rate is fixed to 90 kg/s based on the optimal results of other sCO_2 Brayton cycles. However, if a reheat source can be classified with a specific amount as well as the heat transfer fluid is determined, a more accurate and detailed optimization analysis can be performed. The optimal power output and cycle thermal efficiency are 5.970 MW_e and 19.28%

respectively, under the conditions of the cooler outlet temperature of 31.5 ℃, the compressor outlet pressure of 42.25 MPa and the HP turbine outlet pressure of 31.59 MPa.

In addition, it is necessary to examine the performance of the stand-alone simple sCO_2 Brayton cycle with the same amount of energy used for reheat. From the analysis above, 17.72 MW_{th} as the amount of thermal energy for reheat in a temperature of 295 ℃ can be calculated. With this amount of heat and its temperature, the optimization analysis for a stand-alone simple sCO_2 Brayton cycle has been performed. The optimal maximum net power output is 3.813 MW_e presented in Table 3–2.

To demonstrate the benefits with a reheat option, the simple sCO_2 Brayton cycle system discussed in Section 3.2.2.1 and the sCO_2 Brayton cycle with reheat which is on the basis of the simple sCO_2 Brayton cycle but adding reheat. The results in Table 3–2 indicate the total net power output of two different systems with the hot sCO_2 and the 295 ℃ reheat source is 6.571 MW_e, which is about 10% higher than the reheat system using both heat sources. However, this integrated reheat system has higher specific net power output, as well as the same magnitude of cycle thermal efficiency to the stand-alone system using only 295 ℃ heat source. Plus, to achieve the optimal net power output, the integrated reheat system has lower operating pressure than the system with 295 ℃ heat source for the desired power output of 3.813 MW_e.

Table 3–2 Cycle performance comparisons for reheating evaluation.

Parameter	Simple sCO_2 Brayton Using Produced CO_2	sCO_2 Brayton Using Produced CO_2 with Reheat	Simple sCO_2 Brayton with amount of heat used in Reheat
Net Power (MW_e)	2.758	5.970	3.813
Cycle Thermal Eff (%)	9.52	19.28	21.50
Cycle $\dot{m}_{CO_2,cyc}$	87.58	90*	65.83
Specific Net Power (kW_e/(kg/s))	31.49	66.33	57.92

Note: * - Not the Optimal Value

3.2.2.5 sCO_2 Brayton Cycle with Pre-compression, Inter-cooling and Reheat

It can be seen from the results of sCO_2 Brayton cycle with reheat only in Section 3.2.2.4, a significantly higher compression work is needed to achieve the optimal objective. Obviously, the option of splitting compression work with inter-cooling is worth being investigated. The configuration shown in Figure 3–34 can be seen as the combination of the layouts presented in Figure 3–23 and Figure 3–29. The same reheat conditions used in Section 3.2.2.4 are considered here. Figure 3–35 shows the cycle CO_2 at the HP turbine outlet is reheated to 295 ℃. The cooler, pre-cooled outlet temperatures of 31.5, pre-compressor outlet pressure of 12.5 MPa and HP turbine outlet pressure of 15 MPa are selected for the parametric study. The cycle CO_2 flow rate is also fixed to 90kg/s both for the sensitivity analysis and the final optimization, which is same as the reheat only case.

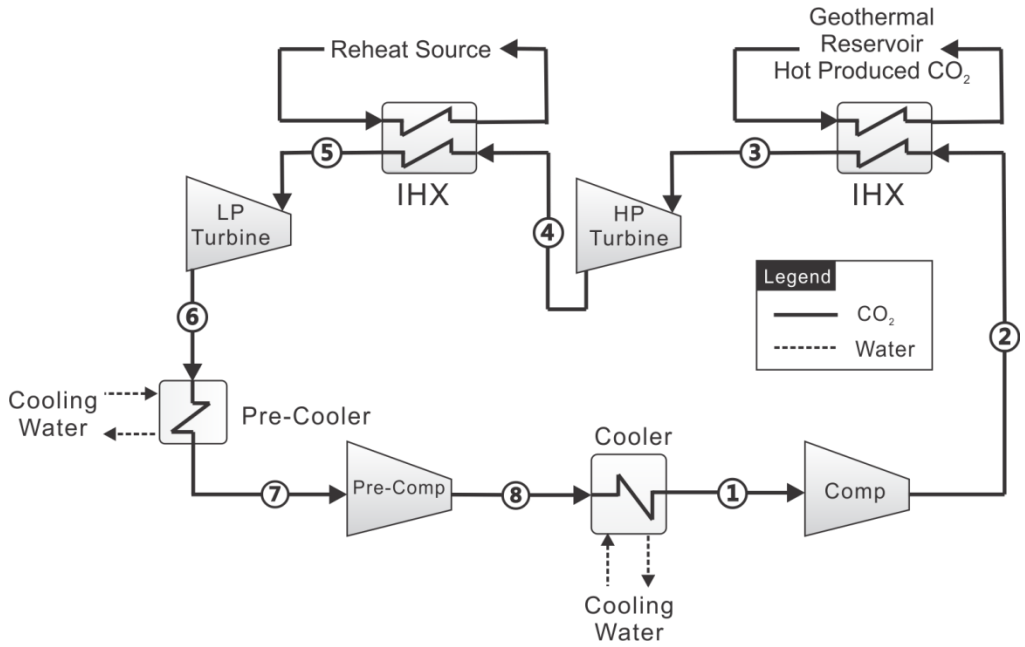

Figure 3–34 Schematic of sCO_2 Brayton cycle with pre-compression, inter-cooling and reheat.

Processes of States 7 to 8 and States 1 to 2 in Figure 3–35 represent the pre-compression and main compression respectively. Compared to the *T-s* diagram in Figure 3–30, it is clear that these two stage compression process have less enthalpy change and lower outlet temperature. Therefore, it is helpful to obtain more heat from the geothermal heat source which increases the utilization of geothermal energy and decrease the cooling load for CO_2 being cooled before it is re-injected back to geothermal reservoirs.

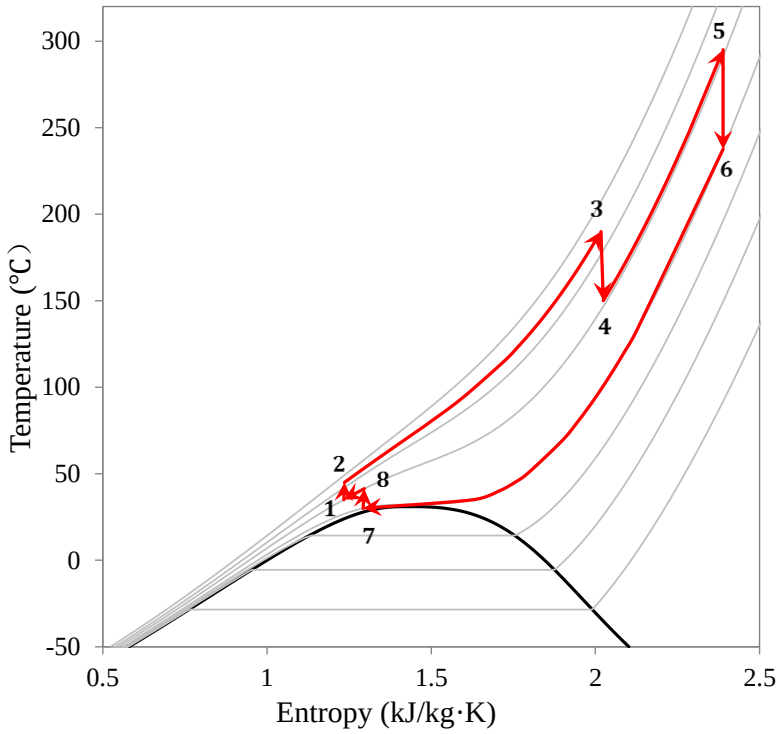

Figure 3–35 *T-s* diagram of sCO_2 Brayton cycle with pre-compression, inter-cooling and reheat.

The pre-cooler outlet temperature and the pre-compression outlet pressure are two additional parameters to be considered in parametric study and optimization analysis, compared to the case of sCO_2 Brayton cycle with reheat only. Figure 3–36 shows the HP and LP turbine powers keep constant while the pre-compressor outlet pressure increases. The pre-compressor outlet pressure determines the portions of compression work for the pre-compressor and the main compressor. The maximum net power output of 5.570 MW_e is obtained at the pre-compressor outlet pressure of 14.39 MPa. However, the optimal cycle thermal efficiency appears at the pre-compressor outlet pressure of 9.14 MPa. This difference indicates the optimal cycle efficiency and net power output are not necessary to occur at same time. Due to the inter-cooler outlet temperature is fixed, the cooling load in the inter-cooler changer as well as the CO_2 temperature at the main compressor outlet

varies with the changes of pre-compressor outlet pressure. Moreover, the heat obtained through the IHX also changes. These non-linear behaviors of the power and the heat duty lead to the different trends shown in RHS of Figure 3–36.

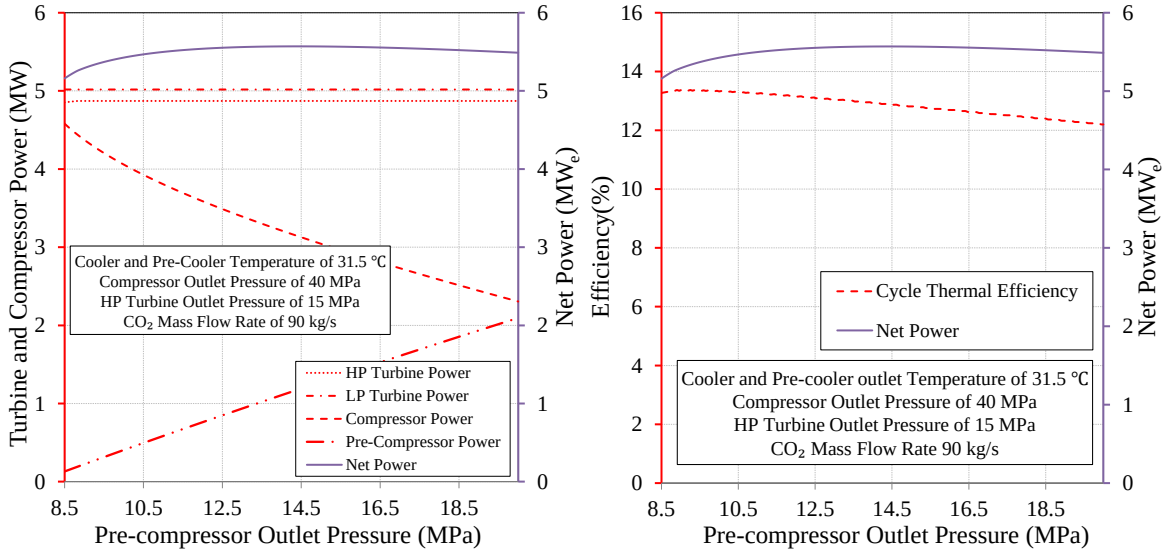

Figure 3–36 Net power output, turbine and compressor power, efficiencies vs. pre-compressor outlet pressure for sCO_2 Brayton cycle with pre-compression, inter-cooling and reheat.

The pre-cooler outlet temperature affects the pre-compressor work only (see Figure 3–37). This intermediate process will not have an impact on the heat transfer process both in the IHX1 and IHX2. Therefore, the system thermal efficiency shows exactly the same trend with the net power output.

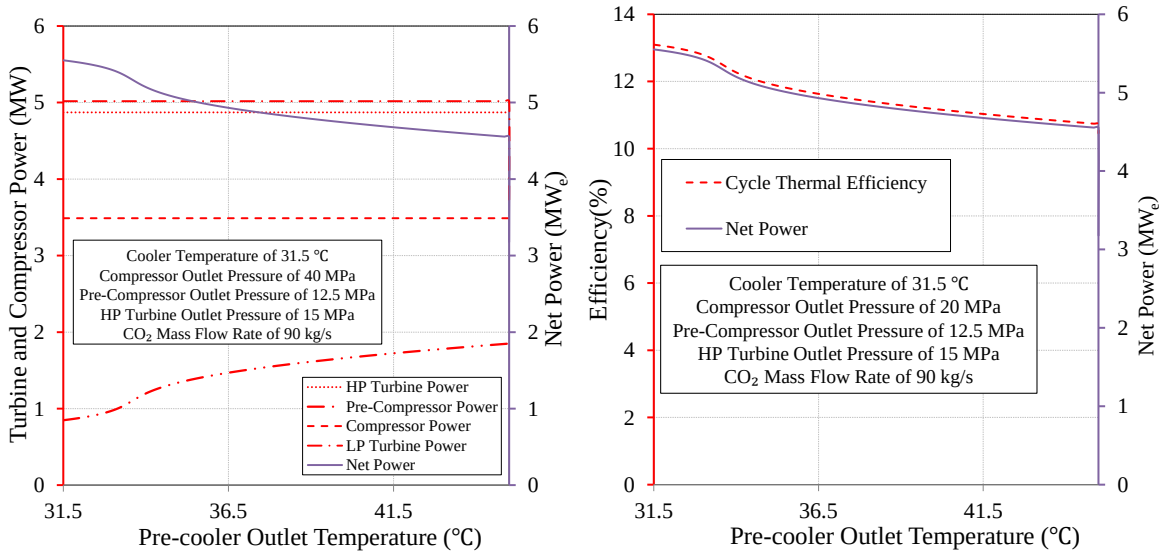

Figure 3–37 Net power output, turbine and compressor power, efficiencies vs. pre-cooler outlet temperature for sCO_2 Brayton cycle with pre-compression, inter-cooling and reheat.

The HP turbine power increases as the compressor outlet pressure goes up. However, the main compression power increases with constant rate and the HP turbine power increases with a slowing down changing rate, which leads to a peak value occurring when the second durative of HP turbine power curve in LHS of Figure 3–38 equals to 0. The cycle thermal efficiency behaves similarly to the net power output when the compressor outlet pressure changes. A maximum value for the cycle thermal efficiency is obtained at the same time when the maximum net power of 5.580 MW_e is achieved.

The impact of cooler outlet temperature on the cycle performance is unremarkable (see Figure 3–39). The net power output drops from 5.508 to 4.876 MW_e throughout the range of the cooler outlet temperature from 31.5 to 45 ℃. Moreover, the cycle thermal efficiency varies only about 0.2% with this considerable change of cooler outlet temperature. It is because CO_2 at the compressor inlet is far from the critical point where properties don't change dramatically. This indicates that the cooler is possible to be removed or has higher

outlet temperature if the penalty of net power loss can be compensated by the cost of electricity decreases due to eliminating the cooler. To make this decision, a cost estimation is needed.

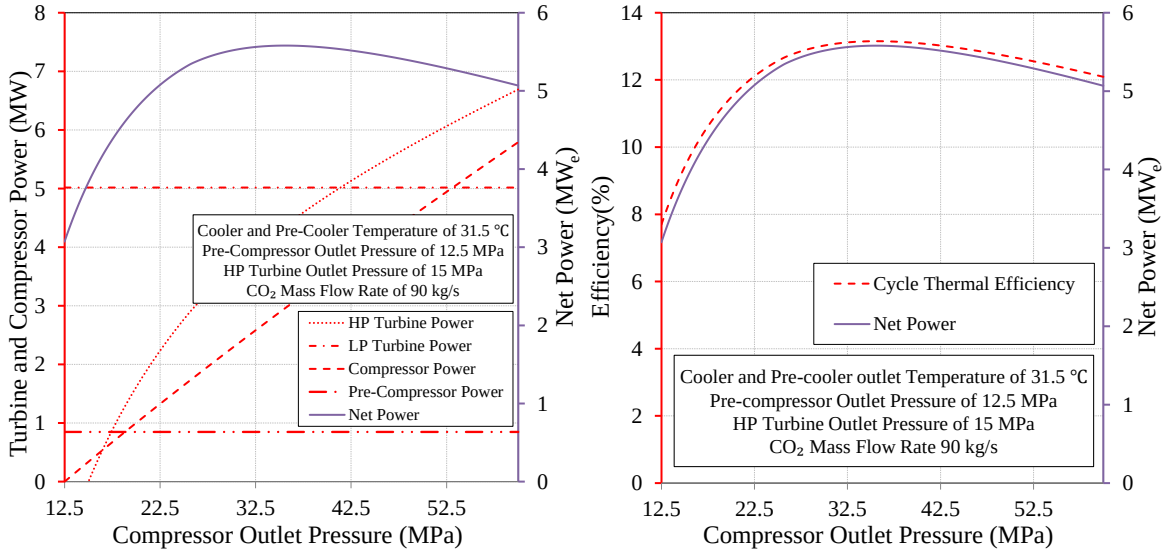

Figure 3–38 Net power output, turbine and compressor power, efficiencies vs. compressor outlet pressure for sCO_2 Brayton cycle with pre-compression, inter-cooling and reheat.

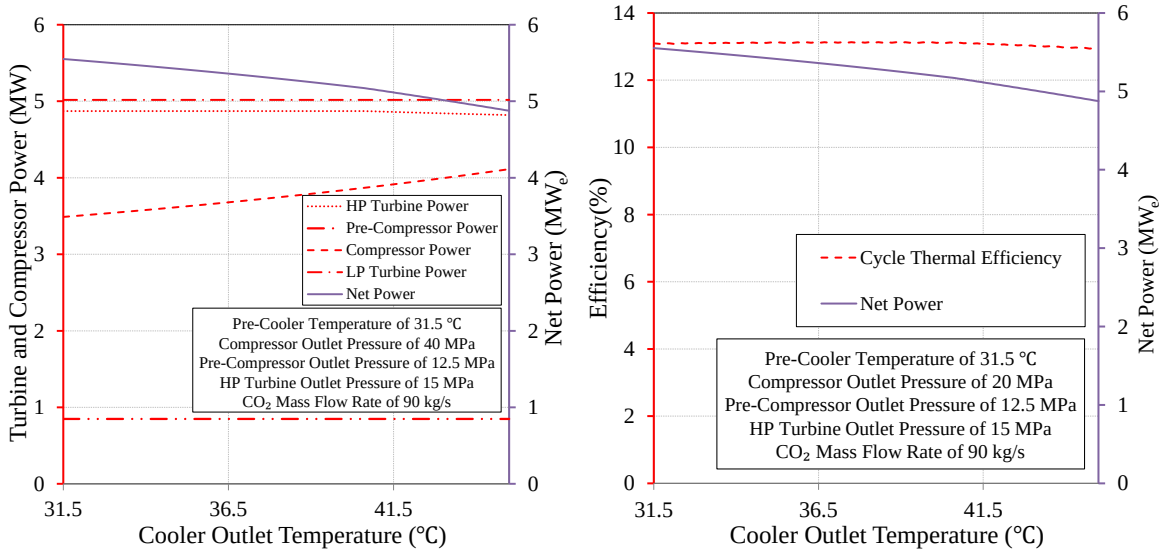

Figure 3–39 Net power output, turbine and compressor power, efficiencies vs. cooler outlet temperature for sCO_2 Brayton cycle with pre-compression, inter-cooling and reheat.

The system tends to have better performance at higher HP turbine outlet pressure. It means the cycle tends to obtain more heat from the reheat process due to a high grade heat source. However, the tendency of achieving larger net power output is getting moderated with the increase of HP turbine outlet pressure. Increasing the main compressor outlet pressure would more efficiently utilize the geothermal energy. Eventually, an optimal HP turbine outlet pressure appears with the compressor outlet pressure raises.

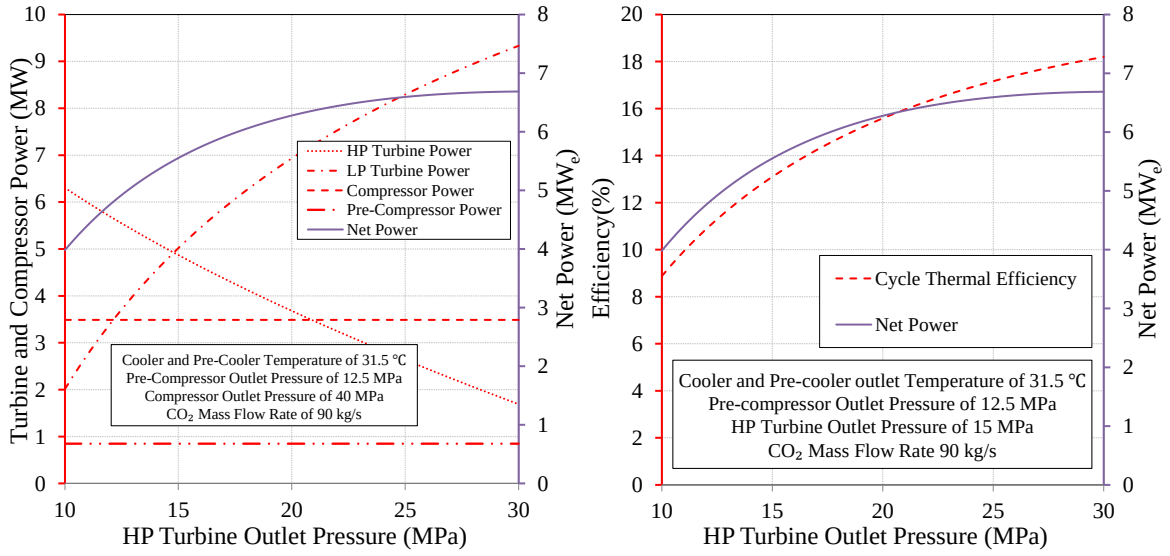

Figure 3–40 Net power output, turbine and compressor power, efficiencies vs. HP turbine outlet pressure for sCO_2 Brayton cycle with pre-compression, inter-cooling and reheat.

As a consequence, despite the capability of the compressor, the optimal net power as high as 6.904 MW_e has been achieved with a cycle thermal efficiency of 18.76% at the compressor outlet pressure of 57.24 MPa. In addition, the optimal pre-compressor outlet pressure is 16.36 MPa and the optimal HP turbine outlet pressure is 36.29 MPa. Both the pre-cooler and cooler optimal outlet temperatures are 31.5 ℃. The CO_2 flow rate as the cycle working fluid is fixed to 90.00 kg/s. The thermal heat of 19.24 MW_{th} is added for the

reheat process which is slightly higher than the reheat only case. However, the power gained is almost 1 MW_e.

3.2.2.6 Transcritical sCO_2 Power Cycle

A simple transcritical sCO_2 power cycle with no other improvement methods is considered in this section. The only difference between the simple Brayton cycle and the transcritical sCO_2 cycle is the part of the cycle running below CO_2 critical point (see Figure 3–41 and Figure 3–42). The phase change occurs at the cooler, where CO_2 is transitioning from a supercritical state to liquid state. The turbine outlet pressure is designed as a function of the cooler outlet temperature, which can be expressed as:

$$P_{t,out} = (0.0013 \times T_{cooler,out}^2 + 0.0827 \times T_{cooler,out} + 3.5474) + 0.5 \quad (3.26)$$

where T is in ℃, P is in MPa. The value of 0.5 at the RHS of this curve fitting equation is the pressure difference above the CO_2 saturation line (see Figure 3–4). The pressure of the turbine outlet would be right above the saturation line corresponding to the cooler temperature. In addition, a compressor/pump working both at liquid and supercritical regions is required. Since the cycle partially works outside of CO_2 supercritical region, the lowest temperature at the cooler is determined by the cooling water temperature which is 20 ℃. Considering the minimum temperature approach of 3 ℃ assumed in this study, it then comes up with 23 ℃ as the lowest cooler outlet temperature for CO_2.

The transcritical sCO_2 power cycle can generate more power due to the lower discharge pressure of the turbine. However, it needs much lower temperature at the turbine outlet than typical power cycles, which require the greater cooling capability and lower heat sink

temperature due to the considerable low critical temperature of CO_2. In addition, there is not much flexibility of the cycle CO_2 outlet temperature in the cooler with this low critical temperature.

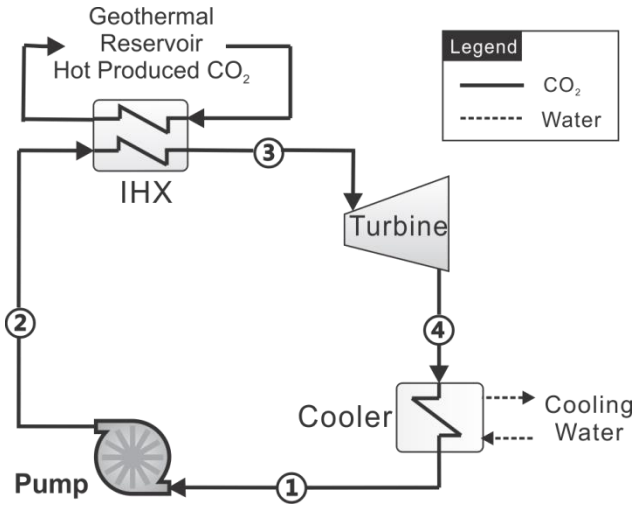

Figure 3–41 Schematic of Transcritical sCO_2 power cycle.

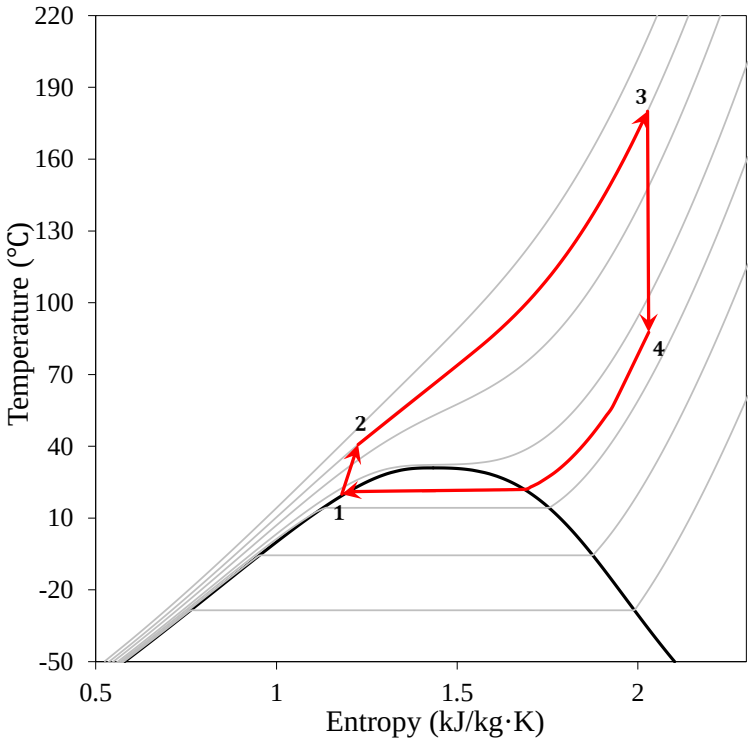

Figure 3–42 *T-s* diagram of Transcritical sCO_2 power cycle.

Figure 3–43 shows the net power output changes from 2.148 MW_e to 3.892 MW_e for the compressor outlet pressure ranging from 10 to 40 MPa, with the cooler outlet temperature of 23 ℃, and the cycle CO_2 mass flow rate of 90 kg/s. The cycle performance dose not increase continuously with the increase of compressor outlet pressure, since it is further from the critical point, the less benefit can obtained for gaining expanding power.

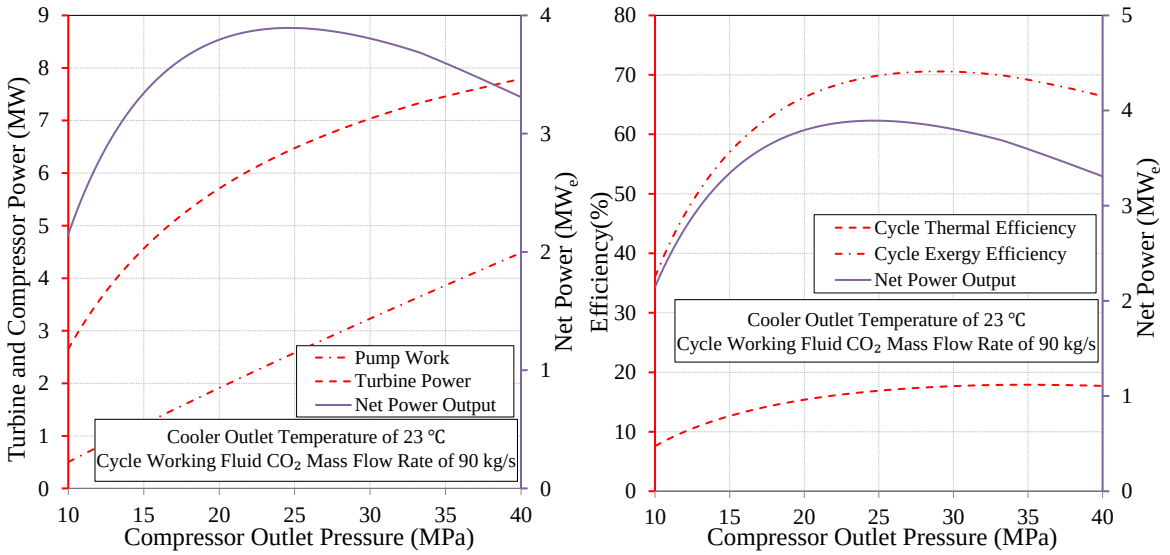

Figure 3–43 Net power output, turbine and compressor power, efficiencies vs. compressor outlet pressure for Transcritical sCO_2 cycle.

For the cooler outlet temperature or the compressor inlet temperature, the lower it goes, the lower turbine discharge pressure can be achieved. Consequently, more power can be generated. The compressor power is almost constant since CO_2 is in the liquid region which can be treated as incompressible flow, and the compression work won't change significantly with compressor inlet temperature change. Therefore, Figure 3–44 shows the maximum power output, cycle thermal efficiency, and cycle exergy efficiency happen at the cooler output temperature of 23 ℃. If the possible lower cooler output temperature can be reached, more net power output and higher cycle exergy efficiency will be obtained.

However, the cycle thermal efficiency won't shift too much due to the load of IHX increases together with the net power output. It is because that the cycle CO_2 temperature at the IHX inlet decreases as the cooler outlet temperature decreases.

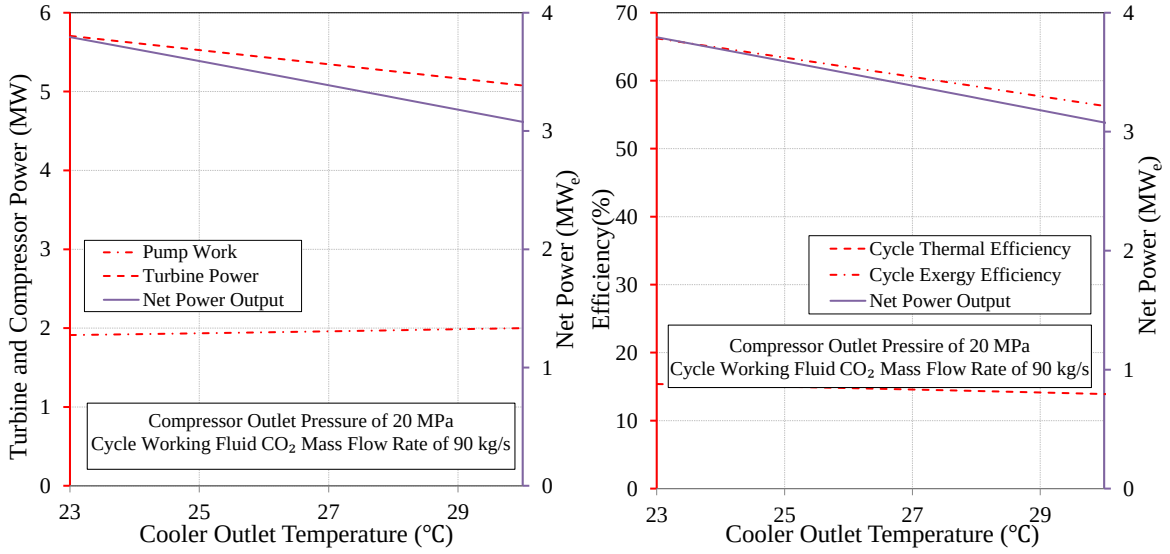

Figure 3–44 Net power output, turbine and compressor power, efficiencies vs. cooler outlet temperature for Transcritical sCO_2 cycle.

Same as the previous optimization analysis, the SQP method is employed. The optimal results and design conditions are presented below. The maximum net power output of 3.922 MW_e is achieved at the cooler outlet temperature of 23.00 ℃, the compressor outlet pressure of 24.08 MPa and the turbine outlet pressure of 6.24 MPa. In these conditions, the cycle thermal efficiency and cycle exergy efficiency are, 16.80% and 70.02% respectively. The optimal CO_2 flow rate as the cycle working fluid is 88.38 kg/s. Although, substantial gains of the net power output makes the transcritical sCO_2 cycle competitive, there are still difficulties in terms of component designing and cycle control. For instance, a crossing phase region compressor/pump is required. It is also challenging to manage the cooler outlet temperature as well as the turbine discharger pressure since the cooler is running

below CO_2 critical temperature which is a low heat rejecting temperature for a power cycle. Additionally, due to CO_2 cooling down to the liquid region, where it passes over the pseudocritical point, a potential large cooling load is needed.

3.3 Results Summary and Comparisons

Five different layouts of sCO_2 Brayton cycle have been examined carefully through parametric study. Using baseline heat source conditions, the optimization analyses have also been performed for each cycle configuration. Both system and cycle efficiencies have been calculated.

Table 3–3 presents the optimal thermodynamic results of the different sCO_2 Brayton cycles. In order to select the most suitable layouts to perform the further cost estimation and optimization analyses, the cases with reheating are not included since extra high temperature heat sources are needed.

Table 3–3 Optimal results of different sCO_2 Brayton cycles.

Case with Optimization	Net Power Output [MW_e]	$\dot{m}_{CO_2}$ CO_2 as Working Fluid [kg/s]	System/Cycle Thermal Eff [%]	System/Cycle Exergy Eff [%]	Specific Net Power Output [kW_e/kg·s]
Simply sCO_2 Cycle	2.758	87.58	13.92/9.52	40.71/53.47	31.49
Recuperative sCO_2 Cycle	2.584	90.26	8.92/14.64	38.14/53.75	28.63
sCO_2 Cycle with Pre-compression and Inter-cooling	3.194	90.44	11.02/13.28	47.15/56.32	35.32
sCO_2 Cycle with Reheat	5.970	90.00*	10.30/19.28	N.A.	66.34
sCO_2 Cycle with Pre-compression, Inter-cooling and Reheat	6.904	90.00*	11.91/18.76	N.A.	76.71

Note: * - Not Optimal Value

The results indicate that recuperative sCO_2 Brayton cycle generated less power even than the simple sCO_2 Brayton but it has the highest cycle thermal efficiency excluding cases with reheating. However, its system efficiencies are significantly lower than other two cases. Accordingly, for the application with fixed heat source conditions, such as with given heat source temperature, pressure and flow rate, the recuperator cannot help to gain power output. Especially when maximizing net power output as the objective of optimization, it reduces the net power output for obtaining less heat from the heat source.

To take the advantage of low compression work near critical point of CO_2, sCO_2 Brayton cycle with pre-compression and inter-cooling generates 15.81% more power than the simple sCO_2 Brayton cycle. In addition, pre-compression and inter-cooling are the widely considered means to improve sCO_2 Brayton cycle performance. Therefore, the sCO_2 Brayton cycle with pre-compression and inter-cooling is selected for comparisons and further analyses. When the additional thermal energy is available, such as solar thermal energy and waste heat, reheating can be used to generate more power benefiting from the existing infrastructure. However, since more specific heat source conditions are needed to conduct further cost and optimization investigation, the reheating option with generic heat source in this study would not be taken into account.

Table 3–4 presents the three selected sCO_2-based power cycles. The net power output ranges from 3.194 to 4.226 MW_e. However, these three cycles can behave differently when the geothermal heat mining conditions vary. Different levels of CO_2 thermosiphon effect can lead to distinct cycle performances. Therefore, as three types of sCO_2-based power

cycles, the direct turbine expansion, the sCO_2 Brayton cycle with pre-compression and inter-cooling, and the transcritical sCO_2 cycle are selected.

Table 3–4 The Selected sCO_2 power cycles for cost and global optimization.

Case with Optimization	Net Power Output [MW_e]	$\dot{m}_{CO_2}$ Cycle CO_2 Flow Rate [kg/s]	System Thermal Efficiency [%]	System Exergy Efficiency [%]	Specific Net Power Output [kW_e/kg·s]
Direct Expansion	4.226	90	14.58	62.37	46.95
sCO_2 Cycle with Pre-compression and Inter-cooling	3.194	90.44	11.02	47.15	35.32
Transcritical sCO_2 Cycle	3.922	88.34	13.53	57.89	44.38

Chapter 4 ORC Applications Using Hot Produced CO_2 from Geothermal Reservoirs

An organic working fluid is used in a Rankine cycle, in place of using water in a conventional steam Rankine cycle, this is known as an ORC. Typically, organic working fluids have low phase change temperatures as well as low critical points (see Table A–1). Therefore, it is potentially a promising choice for recovering waste heat or utilizing low temperature heat sources. As geothermal energy is widely recognized as the low grade heat, ORC power generation systems are considered to convert the geothermal heat into electricity in this study. As a closed power cycle, an ORC power generation system is similar to a closed sCO_2 cycle discussed in Chapter 3 which needs an IHX (see Figure 4–1) to connect it to the geothermal loop.

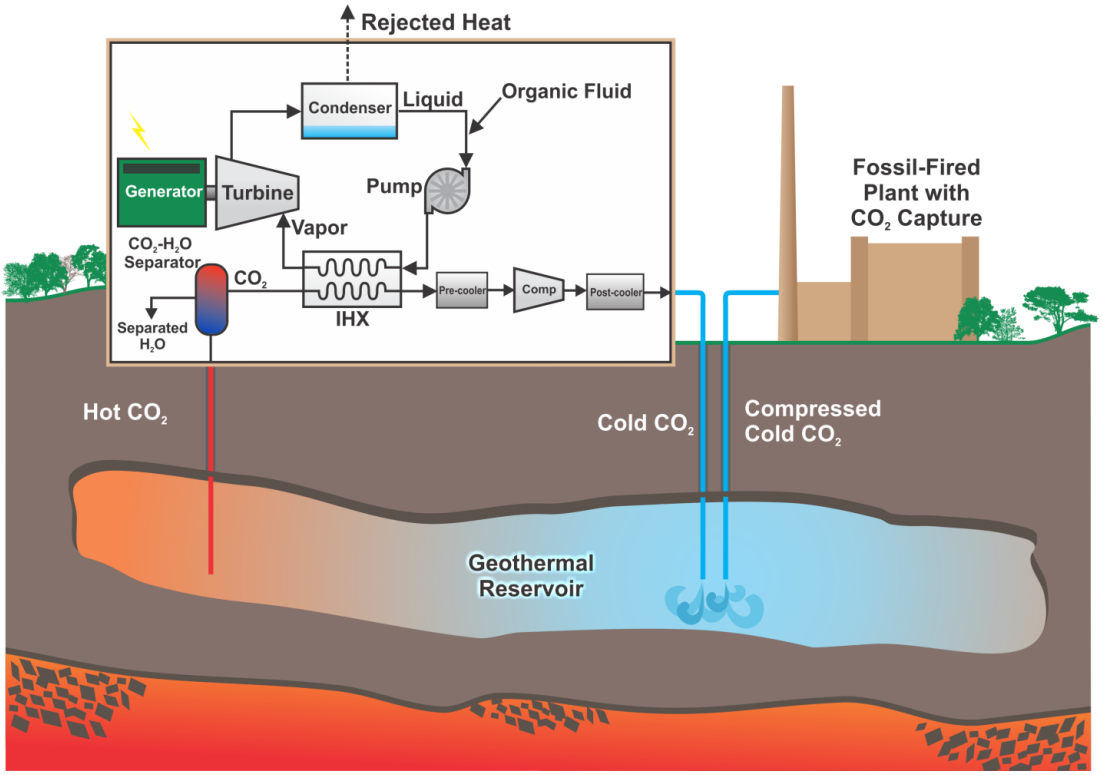

Figure 4–1 Sketch of ORC application using hot produced CO_2 from geothermal reservoir.

The IHX is a critical component in this analysis since it obtains heat from hot sCO_2 which directly affects the cycle performance. Consequently, how to design the IHX to efficiently utilize geothermal thermal energy carried by sCO_2 with various organic working fluid candidates has to be carefully considered to obtain the optimal ORC design. Furthermore, the heat transfer process between sCO_2 and organic working fluid candidates are necessary to be investigated. Particularly, the pinch point analyses in the IHX should also be performed with different working fluids.

Finally, proper working fluids are selected following the working fluid selection criteria proposed in this study. The most appropriate cycle layouts and working fluids are determined to perform the cost estimation and optimization analyses.

In this chapter, the baseline conditions obtained from Chapter 2 are used for the working fluid selection analyses and the cycle performance calculations, which are presented in Table 4–1.

Table 4–1 Hot produced CO_2 baseline conditions.

Parameters	Units	Values
Hot Produced CO_2 Flow Rate	kg/s	90
Hot Produced CO_2 Temperature	℃	195
Hot Produced CO_2 Pressure	MPa	22.5
System Pre-cooler Outlet Temperature	℃	31.5
System Post-cooler Outlet Temperature	℃	30
Turbine Isentropic Efficiency	%	0.88
Pump Isentropic Efficiency	%	0.85

4.1 Model Description

The simple ORC system, consisting of an evaporator, a turbine, a condenser and a pump, which is illustrated in Figure 4–2, is used to perform the working fluid selection analyses. For this particular case, hot produced sCO_2 transfers heat to the ORC working fluid in the evaporator, then it is cooled and re-injected back to the geothermal reservoir. The working fluid starts to be pumped at State 1 in Figure 4–2. The pressurized working fluid then passes through the evaporator to be heated up and expands through the turbine to generate power. The working fluid is finally cooled down from State 4 by cooling water. The geothermal loop is similar to the closed sCO_2-based cycle system.

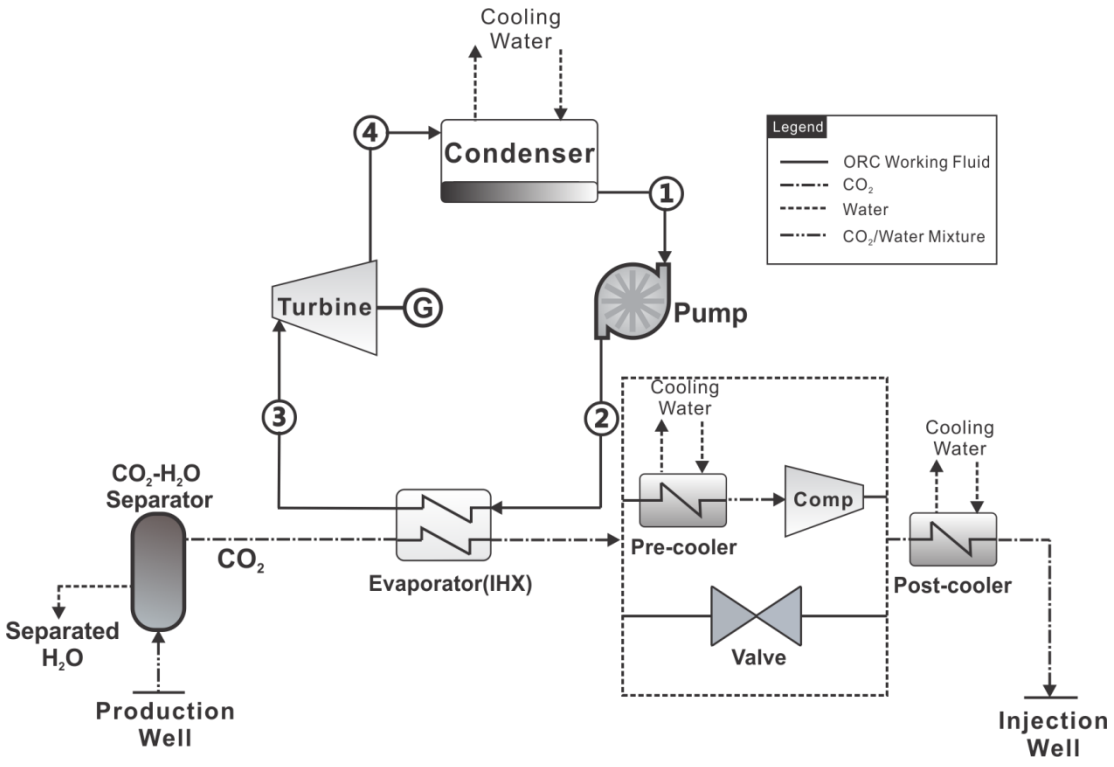

Figure 4–2 Schematic of ORC power generation system using hot produced sCO_2 from geothermal reservoir.

The model and mathematic equations for each component used for the ORC thermodynamic analysis are as follows:

Evaporator (IHX)

The evaporator is the main component in this analysis, connecting hot produced sCO_2 and the working fluid. Since the evaporator outlet pressure and mass flow rate of the working fluid are undetermined, a model has been developed to obtain the optimal working fluid mass flow rate.

The energy balance for the evaporator is:

$$\dot{m}_{WF}\left(h_3 - h_2\right) = \dot{m}_{CO_2}\left(h_{CO_2,in} - h_{CO_2,out}\right) \tag{4.1}$$

$h_{out,evp}, h_{in,evp}$ are the enthalpies corresponding to the evaporator outlet temperature and condenser temperature of the working fluid. The CO_2 temperature at the evaporator outlet is calculated by Equation (4.1) with an assumed working fluid mass flow rate. In the heat transfer process, the temperature distribution in the evaporator can be obtained by:

$$\dot{m}_{WF}\left(h_{WF,i+1} - h_{WF,i}\right) = \dot{m}_{CO_2}\left(h_{CO_2,i+1} - h_{CO_2,i}\right) \tag{4.2}$$

where $\sum_i \left(h_{WF,i+1} - h_{WF,i}\right) = h_3 - h_2$, $\sum_i \left(h_{CO_2,i+1} - h_{CO_2,i}\right) = h_{CO_2,in} - h_{CO_2,out}$, and i is the location point in the evaporator. Subsequently, the pinch temperature in the evaporator can be obtained. The optimal working fluid mass flow rate is calculated through iteration.

Finally, the heat transferred from sCO_2 to the working fluid can be calculated by:

$$Q_{evp} = \dot{m}_{WF}\left(h_3 - h_2\right) \tag{4.3}$$

Pump

The process 1 – 2 in Figure 4–2 is the isentropic compression. The pump work and isentropic efficiency are defined as:

$$W_{pump} = \dot{m}_{WF}\left(h_2 - h_1\right) \tag{4.4}$$

$$\eta_{pump,s} = \frac{h_{2s} - h_1}{h_2 - h_1} \tag{4.5}$$

Turbine

The isentropic expansion work and efficiency (States 3 to 4 in Figure 4–2) in the turbine can be obtained by:

$$W_t = \dot{m}_{WF}\left(h_3 - h_4\right) \tag{4.6}$$

$$\eta_{t,s} = \frac{h_3 - h_4}{h_3 - h_{4s}} \tag{4.7}$$

Condenser

The heat ejected by the condenser is:

$$Q_{cond} = \dot{m}_{WF}\left(h_4 - h_1\right) \tag{4.8}$$

Cycle Performance

The cycle net power output can be obtained from:

$$W_{ORC,net} = W_t - W_{pump} \tag{4.9}$$

The ORC thermal efficiency can be calculated by Equation (4.10) with a control volume as shown in Figure 4–3:

$$\eta_{ORC,th,cyc} = \frac{W_{ORC,net,cyc}}{Q_{evp}} \tag{4.10}$$

The exergy efficiency, which accounts for this and can be defined as:

$$\eta_{ORC,ex,cyc} = \frac{W_{ORC,net,cyc}}{\dot{m}_{CO_2}(e_{CO_2,in} - e_{CO_2,out})} \tag{4.11}$$

where

$$e = (h - h_0) - T_0(s - s_0) + \frac{V^2}{2} + g\Delta H \tag{4.12}$$

In this analysis, there are no changes in kinetic and potential energy, and Equation (4.13) can be reduced to:

$$e = (h - h_0) - T_0(s - s_0) \tag{4.13}$$

where T_0, h_0, s_0 are the temperature, enthalpy and entropy of the working fluid at the reference state which is 0.1 MPa, 25 ℃ in this paper.

The cycle specific net power output can be calculated by:

$$w_{ORC,net,cyc} = \frac{W_{ORC,net,cyc}}{\dot{m}_{WF}} \tag{4.14}$$

System Performance

The system net power output can be obtained from:

$$W_{ORC,net,sys} = W_{ORC,net,cyc} - W_{comp,inj} \tag{4.15}$$

The system efficiencies can be obtained by:

$$\eta_{ORC,th,sys} = \frac{W_{ORC,net,sys}}{\dot{m}_{CO_2}\left(h_{CO_2,prod} - h_{CO_2,inj}\right)} \tag{4.16}$$

$$\eta_{ORC,ex,sys} = \frac{W_{ORC,net,sys}}{\dot{m}_{CO_2}\left(e_{CO_2,prod} - e_{CO_2,inj}\right)} \tag{4.17}$$

The system specific net power output is defined as:

$$w_{ORC,net,sys} = \frac{W_{ORC,net,sys}}{\dot{m}_{CO_2}} \tag{4.18}$$

The cooling water flow rates are selected as:

$$\begin{aligned} \dot{m}_{H_2O,condenser} &= \frac{150\text{kg/s}}{90\text{ kg/s}}\dot{m}_{CO_2} \\ \dot{m}_{H_2O,pre-cooler} &= \frac{75\text{ kg/s}}{90\text{ kg/s}}\dot{m}_{CO_2} \\ \dot{m}_{H_2O,post-cooler} &= \frac{75\text{ kg/s}}{90\text{ kg/s}}\dot{m}_{CO_2} \end{aligned} \tag{4.19}$$

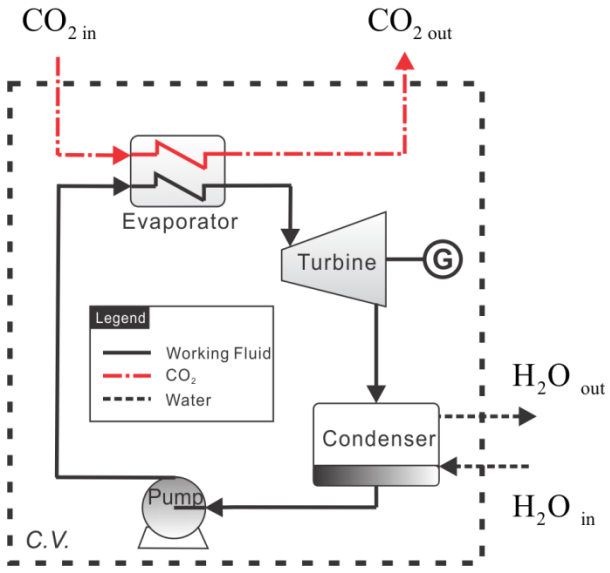

Figure 4–3 Control volume for ORC exergy and thermal efficiency calculation.

4.2 Different Layouts of ORC

In this study, three different types of ORCs are discussed: subcritical, superheated and supercritical ORCs (see Figure 4–4, Figure 4–5 and Figure 4–6). The input parameter values and assumptions are listed in Table 4–2. R600 with critical temperature of 151.975 ℃ and critical pressure of 3.796 MPa is selected as the instanced working fluid to elucidate the difference of the three ORC layouts. For the subcritical ORC with R600 as working fluid, the maximum evaporative pressure is corresponding to its "turning point" temperature which is discussed in Section 4.3.2. As the evaporating process of superheated ORC also occurs below the critical point, the maximum evaporating temperature is limited to 5 ℃ below the critical temperature of working fluid that is R600 discussed in this section. Moreover, the supercritical ORC pressure is confined as 0.5 MPa higher than the critical pressure of working fluid, but the upper limit is 20 MPa.

Additionally, all property data used in this analysis are obtained from the NIST REFPROP data base [90].

Table 4–2 Assumptions of base case ORC analysis.

Parameters	Units	Values
Organic WF for Model Description	-	R600
Subcritical Evaporative Pressure	MPa	P_{sat} (at $T \leq T_{tn}$)
Supercritical Pressure Range	MPa	$P_{cr} + 0.5$ to 20 MPa
Condensing Temperature	℃	25
IHX Cold Outlet and Hot Inlet ΔT	℃	5
Recuperator Cold Inlet and Hot Outlet ΔT	℃	10
Minimum Temperature Approach in HTX	℃	3
Turbine Isentropic Efficiency	%	0.88
Pump Isentropic Efficiency	%	0.85
Cooling Water Inlet Temp	℃	20
Cooling Water Inlet Pressure	MPa	0.2

The generic *T-s* and *P-h* diagrams of R600 are illustrated in Figure 4–4, Figure 4–5 and Figure 4–6. In ideal cycles, the processes can be identified as:

- Isentropic pumping (States 1 to 2s). The isentropic pumping process cannot be seen in the *T-s* diagram due to no entropy change occurs.

- Isobaric heat absorption (States 2s to 3). The working fluid absorbs heat from heat source. For subcritical ORC, State 3 is at a saturated vapor state (see Figure 4–4). For superheated ORC, State 3 is at a superheated vapor state (see Figure 4–5). For supercritical ORC, State 3 is at a supercritical state (see Figure 4–6).
- Isentropic expansion (States 3 to 4s). This process is adiabatic.
- Isobaric condensation (States 4s to 1). From State 4s to the saturated vapor state, the working fluid is cooled down from a superheated state. Then, the saturated vapor condensates to State 1 which is a saturated liquid state.

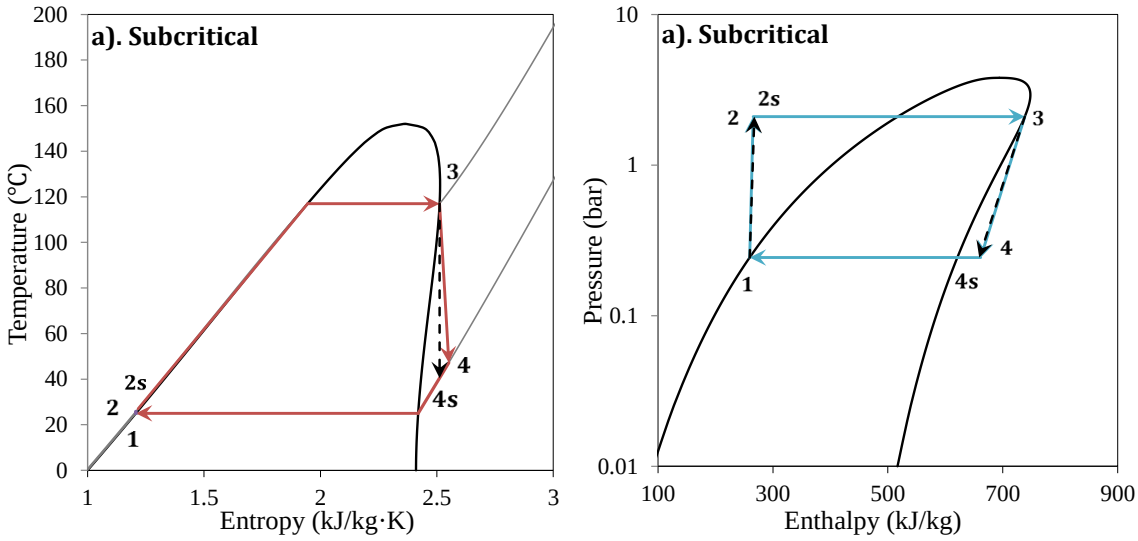

Figure 4–4 *T-s* and *p-h* diagrams of base case Subcritical ORC with R600 as working fluid.

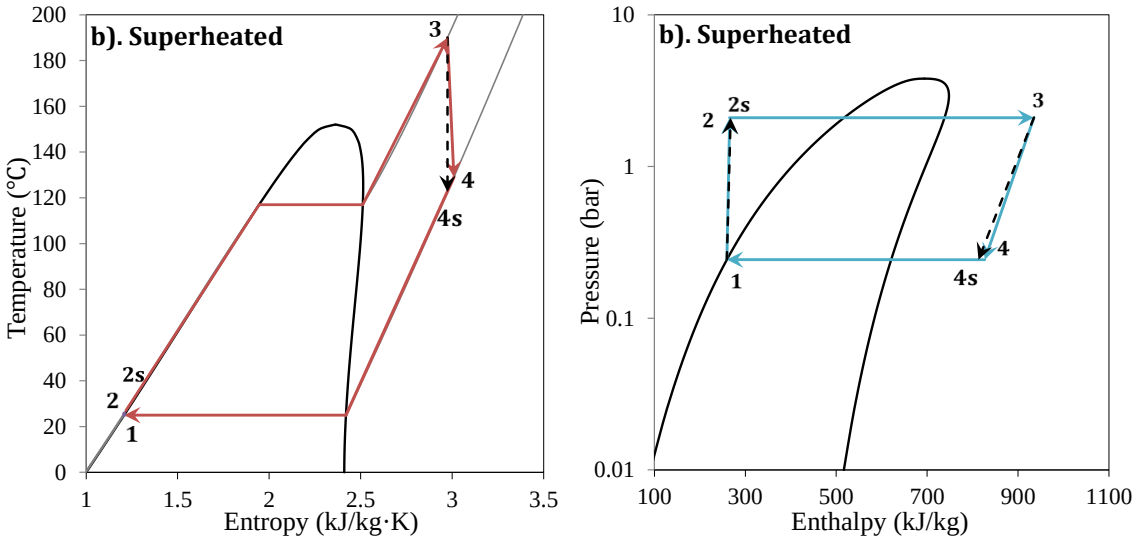

Figure 4–5 *T-s* and *p-h* diagrams of base case Superheated ORC with R600 as working fluid.

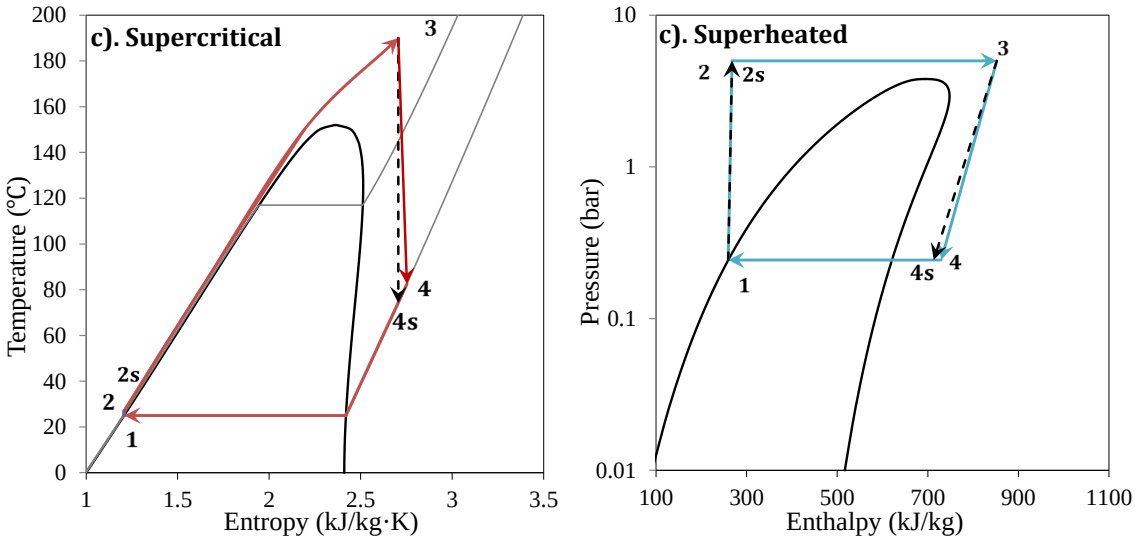

Figure 4–6 *T-s* and *p-h* diagrams of base case Supercritical ORC with R600 as working fluid.

For the actual processes taking into account the turbine and pump isentropic efficiencies shown in Table 4–2, the state points are represented without "s".

4.3 Organic Fluid Selection

4.3.1 Type of Organic Working Fluid

Working fluids for ORCs can be classified based on the slope of their saturated vapor curves as: dry fluid, isentropic fluid and wet fluid (see Figure 4–7).

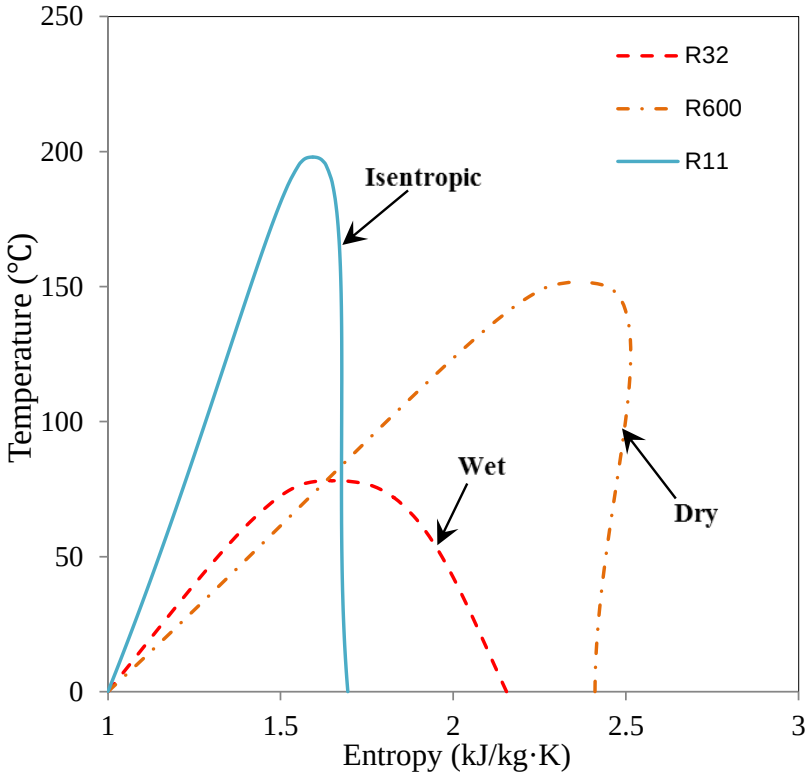

Figure 4–7 Three types of organic working fluids.

A method used to determine the type of working fluids was first proposed by Liu et al. [91]. An equation was derived for ξ, the slope of saturation vapor curve, as:

$$\xi = \frac{ds}{dT_H} \tag{4.20}$$

When $\xi > 0$, the fluid is a dry fluid; when $\xi < 0$, the fluid is a wet fluid and if $\xi \approx 0$, the working fluid is an isentropic fluid. In this analysis, Liu et al. [91] used ideal gas relations to derive an equation to predict ξ as follows :

$$\begin{aligned} \xi &= \frac{ds}{dT_H} \\ &= \frac{c_p}{T_H} - \frac{\frac{n \cdot T_{rH}}{1 - T_{rH}} + 1}{T_H^2} \Delta h_H \end{aligned} \tag{4.21}$$

where T_H is the normal boiling point; Δh_H is the evaporation enthalpy change; c_p is the specific heat; and $T_{rH} = T_H / T_{cr}$.

Another parameter σ called molecular complexity was introduced and defined as:

$$\sigma = \frac{T_{cr}}{R} \left(\frac{\partial s}{\partial T} \right)_{sv, T = 0.7 T_{cr}} \tag{4.22}$$

The value of σ by adopting the ideal gas law was also calculated by Liu. et al. [91]. Equation (4.23) was derived to predict the slope of the saturated vapor curve [92]:

$$\begin{aligned} \sigma &= \frac{T_{cr}}{R} \left[\left(\frac{\partial s}{\partial p} \right)_T \left(\frac{\partial p}{\partial T} \right)_{sv} + \left(\frac{\partial s}{\partial T} \right)_p \right]_{sv, T = 0.7 T_{cr}} \\ &= \frac{T_{cr}}{R} \left[-\frac{R}{p} \left(\frac{\partial p}{\partial T} \right)_{sv} + \frac{C_p}{T} \right]_{sv, T = 0.7 T_{cr}} \\ &= \left[-\frac{1}{p_R} \left(\frac{\partial p_r}{\partial T_r} \right)_{sv} + \frac{\gamma}{\gamma - 1} \frac{1}{T_r} \right]_{sv, T = 0.7 T_{cr}} \end{aligned} \tag{4.23}$$

Equations (4.21) and (4.23) were widely used to classify the types of working fluids for ORCs studies and applications. However, the ideal gas law would fail near the saturated vapor curve, especially close to the critical point of the working fluid. Therefore Equations (4.21) and (4.23) are not accurate enough to classify working fluid type. Calculations of specific volume of R600 using the ideal gas law and directly using saturated vapor properties respectively are then performed in this study. For the ideal gas, the specific volume can be calculated by:

$$\upsilon = \frac{RT}{pM} \tag{4.24}$$

where υ is the specific volume in m^3/kg; T is the ideal gas temperature in K; p is the ideal gas pressure in kPa; M is the molecular weight in unit of kg/kmol; and R is the gas constant.

The specific volume of R600 at pressures of 0.25 MPa, 0.5 MPa, 1 MPa and 3MPa at the saturated vapor conditions are calculated by Equation (4.24). The error between the calculated value by the ideal gas law and the more realistic real value is estimated as:

$$\upsilon_{err} = \frac{\upsilon_{cal} - \upsilon_{real}}{\upsilon_{real}} \times 100\% \tag{4.25}$$

Calculated errors are shown in Figure 4–8. If the saturated vapor pressure is lower than 0.1 MPa, the error is 8.37% which is already a significant shift. If the working fluid pressure is at the ORC operation conditions (for example $0.7\,p_{cr}$), the error is too big to assume these two values are the same. The region that the vapor can be treated as ideal gas is far from

the saturated vapor curve. Thus, the ideal gas law will fail to calculate ξ and σ for working fluid classification. The more realistic method to calculate the slop of saturated vapor curve would be using the actual physical properties.

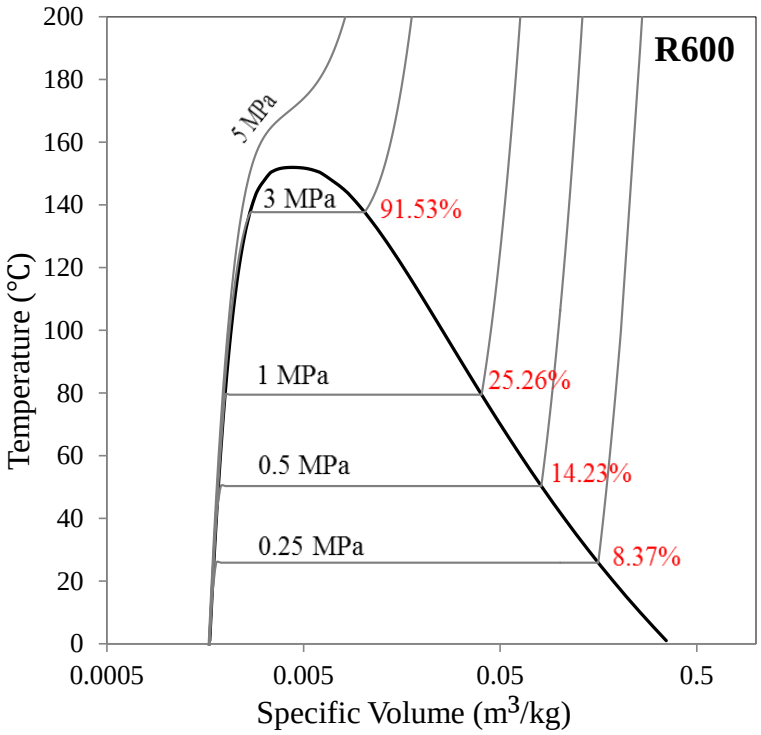

Figure 4–8 $T-\upsilon$ diagram of R600 and specific volume error on saturated vapor curve of different pressure.

A method to classify working fluids for ORC is proposed in this study. To illustrate the method, an evaporator outlet temperature of $0.7T_{cr}$ at State 3 in Figure 4–9 is selected to perform the analysis. State 3 to 4s is an isentropic process; State 3 to 4 is a turbine expansion process with an isentropic efficiency of 95%. State 4' is saturated vapor at condenser temperature. An equation is defined to determine the working fluid type:

$$\varepsilon = \frac{s_{4s} - s_{4'}}{s_4 - s_{4s}} \tag{4.26}$$

where ε is defined as the working fluid type factor in this paper. $s_4, s_{4'}, s_{4s}$ are the entropy values of State 4, 4s and 4'. If $-1 \le \varepsilon \le 1$, the working fluid is an isentropic fluid; If $\varepsilon < -1$, the working fluid is a wet fluid; If $\varepsilon > 1$, it is a dry fluid. Employing this method, thirty fluids types are determined and listed in Table A–1.

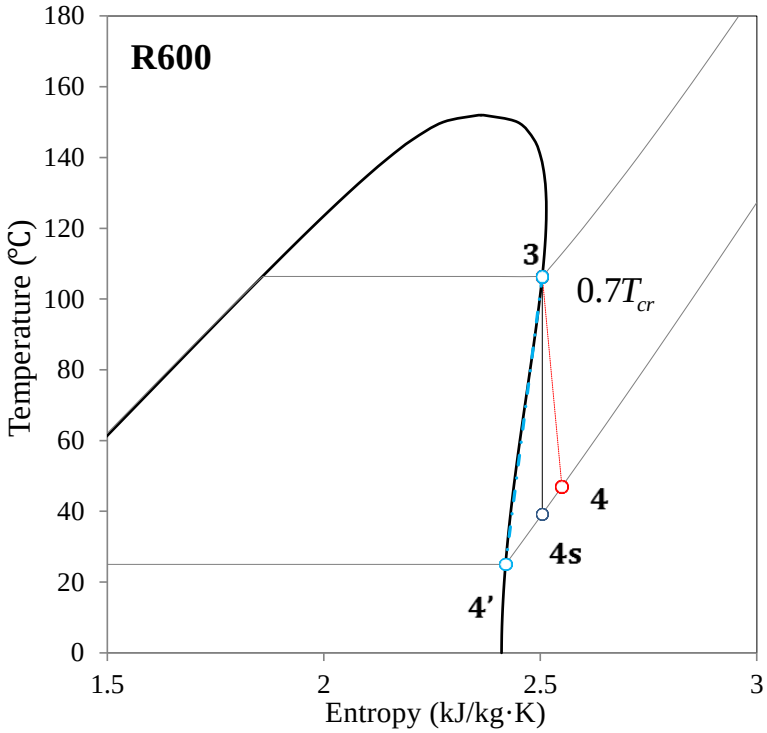

Figure 4–9 *T-s* diagram of illustration of fluid type classification.

4.3.2 Turning Points of Isentropic and Dry Working Fluids

Rayegan et al. [64] stated that a practical limit for a working fluid in ORC should be considered to avoid the presence of liquid in the turbine. Potentially, for dry fluids and isentropic fluids, the liquid is also possible to be formed during the isentropic expansion for subcritical ORC, superheated ORC and supercritical ORC shown in Figure 4–10.

Accordingly, the turbine inlet conditions have to be examined more carefully during the calculation.

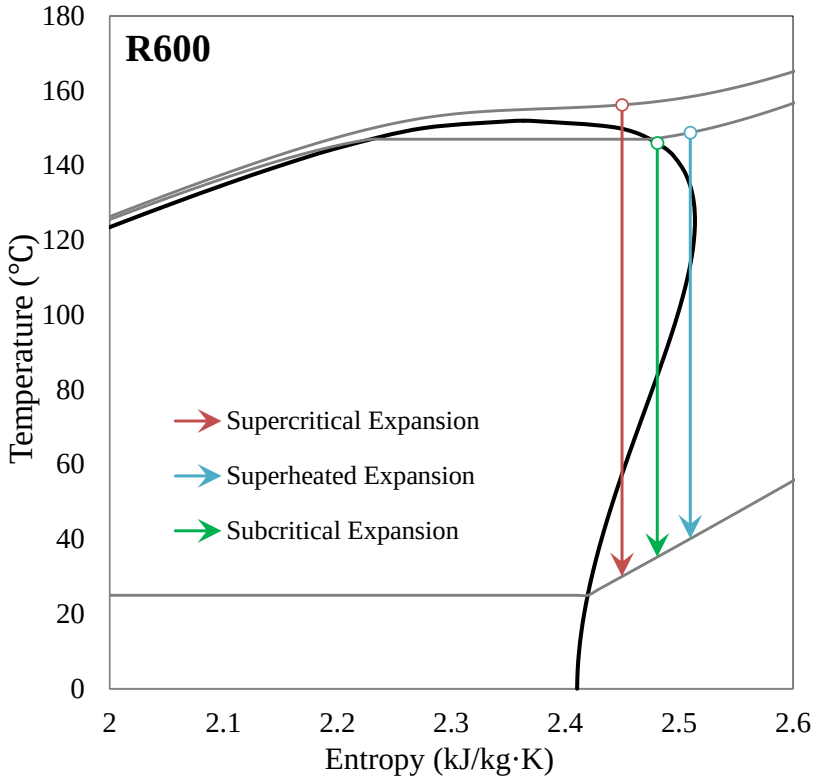

Figure 4–10 Isentropic expansion process for three ORC approaches.

To find a proper turbine inlet condition that prevents erosion of turbine blades, the concept of "turning point" has been proposed. As mentioned in Section 4.3.1, the slope of saturated vapor curve can be expressed by Equation (4.18). The turning point T_{tn} can be calculated by:

$$\xi = \left(\frac{\partial s}{\partial T} \right)_{sv, T=T_{tn}} = 0 \tag{4.27}$$

The turning point of R600 is 125.23 ℃ (see Figure 4–11). For the subcritical ORC, when the entropy value of the working fluid is smaller than $s_{sv,T=125.23℃}$ and the working fluid

temperature is larger than 125.23 ℃ at the turbine inlet, it is highly possible that fluid will be formed during expansion (see Figure 4–11). However, if the entropy value of the working fluid is smaller than $s_{sv,T=125.23℃}$ and the working fluid temperature is also smaller than 125.23 ℃ at the turbine inlet, there is no chance of turbine blade erosion. Therefore, for a subcritical ORC, the turbine inlet temperature should be smaller than the turbine point temperature. Furthermore, when the working fluid entropy at the turbine inlet is larger than the entropy value corresponding to its turning point, the turbine will be in a safe operating mode for superheated ORC and supercritical ORC with isentropic and dry working fluids.

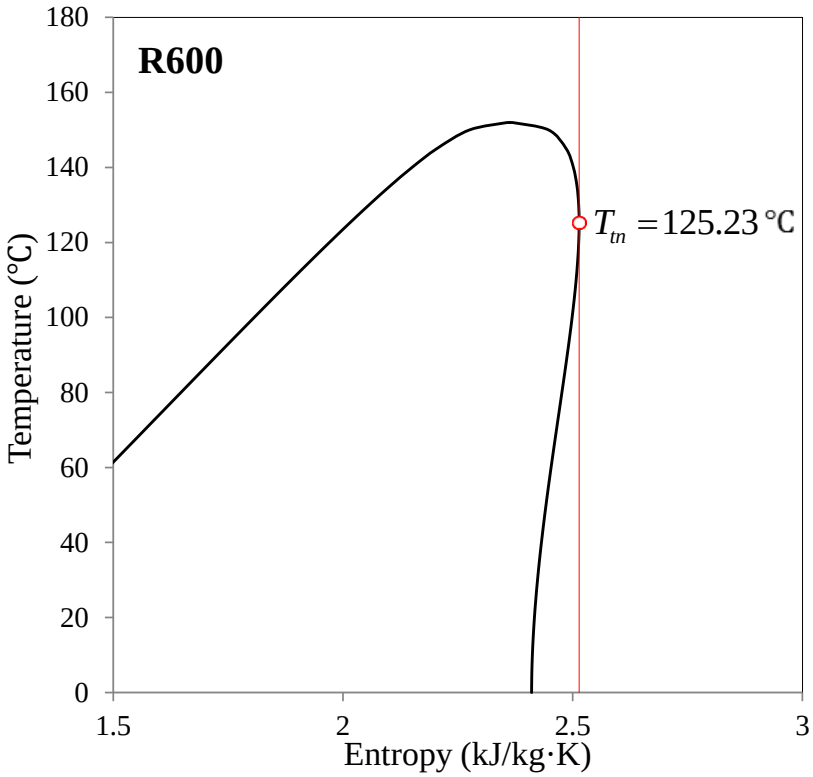

Figure 4–11 Illustration for turning point of R600.

For the supercritical ORC, if the turbine inlet pressure is too high and the working fluid temperature is not high enough, the turbine expansion process is possible to access the two

phase region which is also potentially harmful for the turbine blades (see Figure 4–10). Therefore, a maximum turbine inlet temperature can be obtained considering the turning point and the minimum supercritical pressure of 0.5 MPa higher than the critical pressure of the working fluid.

It can be calculated by the entropy value corresponding to the turning point temperature and the minimum supercritical pressure at the turbine inlet. The minimum allowable turbine inlet temperature can be expressed as:

$$T_{\min,scrit} = T\left(s_{sv,tn}, P_{cr,WF} + 0.5\ \text{MPa}\right) \tag{4.28}$$

4.3.3 Minimum Turbine Inlet Temperatures of Wet Working Fluids for Fixed Condenser Temperatures

Besides the isentropic and dry working fluids selection criteria, a concept of minimum turbine inlet temperature of the wet working fluid is necessary to be defined and applied in the selection of wet working fluids. Similarly, to avoid fluid forming in the turbine expansion process, there should be a minimum turbine inlet temperature corresponding to the condenser temperature with a given evaporator pressure:

$$T_{t,in,\min} = T\left(s_{sv,cond}, p_{evp} / p_{scrit}\right) \tag{4.29}$$

In these analyses, the condenser temperature is fixed to 25 ℃. The corresponding minimum turbine inlet temperature, $T_{t,in,\min}$, can be calculated to make sure the turbine inlet temperatures of ORCs with wet working fluids safe.

4.3.4 Potential Working Fluid Screening and Pre-selection

There are a great many refrigerants and organic fluids can work well with the Organic Rankine Cycle (ORC) for low temperature heat source power generation. In the applications using hot produced CO_2 as heat source which the temperature is 195 ℃, potential working fluids with critical temperatures in the range of 50 to 225 ℃ are listed in Table A–1. Environmental impacts, Ozone Depletion Potential (ODP) and Global Warming Potential (GWP) values for those fluids are also included in Table A–1. The ODP is a parameter that refers to the level of ozone depletion caused by a substance. R11 is defined to have the ODP value of 1.0. The ODP for other substances are compared to R11 based on their abilities to deplete ozone. High ODP working fluids like R11 and R114 have been targeted to be phased out by the Montreal and the Kyoto Protocols. In addition, R11 and R114 production have been stopped in the U.S. since 1996. In consequence, the high ODP working fluids (ODP > 0.5) will not be considered in this study.

GWP is a factor reflecting the relative radiative effect of a substance. Similarly as for the ODP, CO_2 is assigned a GWP value of 1 and used for comparison with other substances. Typically, a time period of 100 years is considered for evaluating the effect on global warming over time. Although the working fluids shown in Table A–1 have GWPs that are thousands times of CO_2, ORC working fluids are rarely exhausted to the atmosphere, thus GWP will be a minor factor in working fluid selection.

NFPA 704 is a standard system maintained by the American National Fire Protection Association which is widely used to identify the flammability, health impact and chemical reactivity of a substance. NFPA 704 codes for all potential working fluids in this paper are

also presented in Table A–1. In this analysis, regarding health impact and chemical reactivity which is a part of safety impacts, the substances with blue and yellow codes of equal or larger than 3 are removed from the list. Although flammability is also one aspect of safety, the substances with NFPA 704 red code 3 and 4 are still considered since that flammable working fluids like R600/R601 are widely considered as ORC working fluids.

Based on the discussion above, the considerations for ORC working fluid pre-selection are as follows:

a. High ODP (>0.5) fluids should be avoided, which are R11, R113, R114, R115, R12;
b. Toxic fluids which have a NFPA 704 blue code of more than 2 should be avoided; Therefore, R245ca was removed from the list;
c. Unstable fluids which have the NFPA 704 yellow code of more than 2 should be avoided; as a consequence, R125 is removed;
d. Wet fluids do not work reliably due to liquid forming during expansion in the turbine for subcritical ORCs;
e. For subcritical ORCs, to avoid liquid forming during the turbine expansion process:

$$T_{WF,IHX\ outlet} \leq T_{tn} \tag{4.30}$$

f. For superheated ORCs, the smallest degree of superheat is 10 ℃ higher than the evaporative temperature. To avoid liquid forming during the turbine expansion process:

$$s_{T_{t,inlet}} > \begin{cases} s_{T_{tn}} & \text{Dry and Isentropic Fluids} \\ s_{sv,cond} & \text{Wet Fluids} \end{cases} \tag{4.31}$$

g. For superheated and supercritical ORCs, the turbine inlet temperature should be larger than the minimum turbine inlet tempreature discussed in Section 4.3.3 of all wet working fluids in Table A–1. To avoid liquid forming during the turbine expansion process:

$$s_{T_{t,inlet}} > \begin{cases} s_{T_{tn}} & \text{Dry and Isentropic Fluids} \\ s_{sv,cond} & \text{Wet Fluids} \end{cases} \tag{4.32}$$

4.3.5 Demonstration of the Model with R600 as the Working Fluid

To demonstrate the calculation and optimization process of working fluid selection, R600 ($T_{cr} = 151.98$ ℃, $p_{cr} = 3.796$ MPa) is selected, since it is classified as a dry working fluid which would be feasibly applied to all three ORC approaches. In this analysis, enthalpy change in the working fluid pump is ignored. The pressure drops on both the working fluid side and the sCO_2 side are also neglected in the evaporator.

The heat source conditions for all three ORC approaches, which are the produced sCO_2 mass flow rate, temperature and pressure from the geothermal reservoir as shown in Table 4–1, can be obtained from Chapter 2 and fixed in the following analyses and calculations.

For the subcritical and superheated approaches, the evaporator outlet temperature and working fluid mass flow rate need to be determined in the optimization analysis; In addition for the superheated approach, the superheating temperature of working fluid is

also a variable should be considered. For the supercritical approach, the supercritical pressure, i.e. the working fluid pressure at pump outlet, the evaporator outlet temperature, as well as the working fluid mass flow rate need to be determined to obtain the optimal design. The constraint for the optimization calculation is the pinch temperature in the evaporator. As a consequence, the optimal conditions can be obtained through the procedure presented in Figure 4–18.

The different evaporator outlet temperatures in the range from the condenser temperature of 25 ℃ to 5 ℃ below the critical temperature of working fluids for the subcritical ORC and superheated ORC were considered. Regarding the supercritical ORC, supercritical pressures of 0.5 MPa over the critical pressure and up to 20 MPa have been considered in the simulation.

The net power output, optimal working fluid flow rate, ORC thermal efficiency, ORC exergy efficiency and specific net power output are the factors that are considered for working fluid selection. Since ORC thermodynamic performance is related to many factors, such as physical properties of working fluids, heat source types and heat sink conditions, it is not practical to get the most optimal design considering for all factors for the working fluid selection. Therefore, the flow rate, temperature and pressure of the hot produced sCO_2 are considered to be constant. It means that the total thermal energy mined from geothermal reservoir is fixed. Accordingly, the maximum net power output is selected as the objective to evaluate the ability of each working fluid to convert thermal energy to electricity.

4.3.5.1 Subcritical ORC

The *T-s* diagram of a subcritical ORC (Figure 4–4) shows the whole cycle is operating below the critical point. Meanwhile, at the evaporator outlet, the working fluid is at the saturated vapor state. The maximum evaporative temperature is assumed to be 5 ℃ below the critical temperature in this analysis. As presented in Table A–1, the turning point of R600 is 125.23 ℃. The evaporator outlet temperatures of 125.23, 100.23 and 75.23 ℃ for R600 are selected to calculate the optimal working fluid mass flow rates. Figure 4–12 shows that optimal working fluid mass flow rates of 49.51, 56.50 and 66.19 kg/s are obtained at evaporator outlet temperatures of 125.23, 100.23 and 75.23 ℃, respectively. In addition, it can be seen that the pinch points occur at the evaporator bubble point which the working fluid starts to evaporate. The calculation results for subcritical ORC presented in Table 4–3 show that the higher turbine inlet temperatures lead to the larger net power outputs although the working fluid mass flow rates increase. Hence, it is necessary to conduct an optimization analysis to get the optimal design conditions.

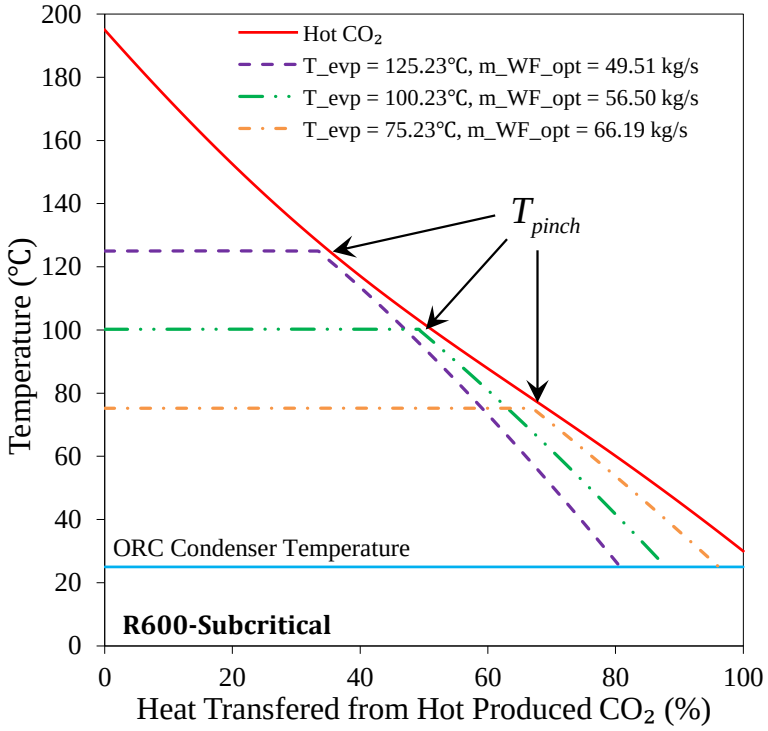

Figure 4–12 Subcritical ORC optimal WF mass flow rates with R600 at different evaporative temperatures with showing T_{pinch}.

4.3.5.2 Superheated ORC

Similarly to the subcritical ORC, the evaporating process of the superheated ORC is also below the critical point (Figure 4–5). The maximum evaporative temperature for superheated ORC is also assumed to be 5 ℃ below the critical temperature similar to the subcritical ORC. Differ from the subracial ORC, the saturated working fluid vapor will be continuously superheated before it enters the turbine to generate electric power. The largest superheated temperature of working fluids is 5 ℃ below the hot produced sCO_2 temperature of 195 ℃ in this demonstration analysis. The minimum superheating temperature is specified to 10 ℃ higher than the evaporative temperature mentioned above. Potentially, the superheated ORC will achieve larger net power output due to the higher

turbine inlet temperature compared to the subcritical ORC. However, the optimal working fluid flow rate is relatively smaller compared to the subcritical case. It can be seen from Table 4–3 that at the same magnitude of evaporator outlet temperature and pressure, the subcritical ORC will generate more power than superheated ORC with R600 as working fluid. However, it is too early to conclude that superheated ORCs have better thermal performance than subcritical ORCs since the thermal performance significantly depends on physical properties of working fluids. On the other hand, the superheating temperatures of working fluids are varying in the further optimization analysis which will result in different net power outputs.

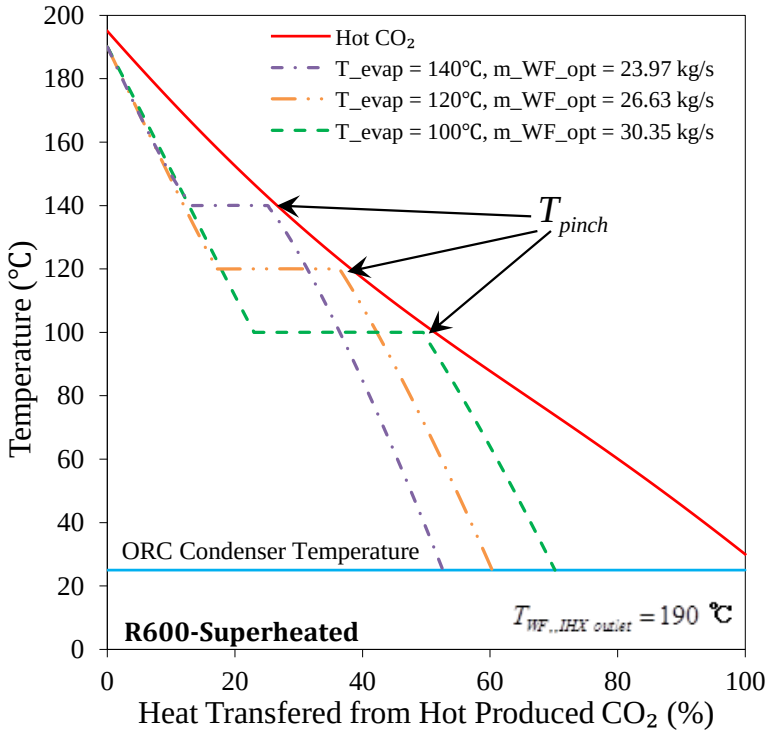

Figure 4–13 Superheated ORC optimal WF mass flow rates with R600 at different evaporative temperatures with showing T_{pinch}.

4.3.5.3 Supercritical ORC

The evaporator pressure on the ORC working fluid side of supercritical ORC cases above the critical point, thus the working fluid does not have the phase change during the heat transfer process (Figure 4–6). Figure 4–14 shows that the optimal mass flow rate of R600 increases when the pressure at the pump outlet increases. When the supercritical pressure is near critical point, the properties of working fluid will dramatically change where the pinch point occurs (see Figure 4–14). The more "parallel" temperature distribution curves of both working fluid and hot CO_2 appear at a larger supercritical pressure for R600, which is the region far away from the critical point. In Table 4–3, it presents that more power is generated at higher supercritical pressures. Nevertheless, high system pressure requires a higher pressure bearing infrastructure which will significantly affect cost of the system. Thermal performance and optimization analyses are also conducted for supercritical ORCs with the supercritical pressure range from 0.5 MPa above the critical pressure of working fluid to 20 MPa. Similar to superheated ORC analysis, the maximum R600 evaporate outlet temperature is fixed to 190 ℃ particularly in this demonstration analysis.

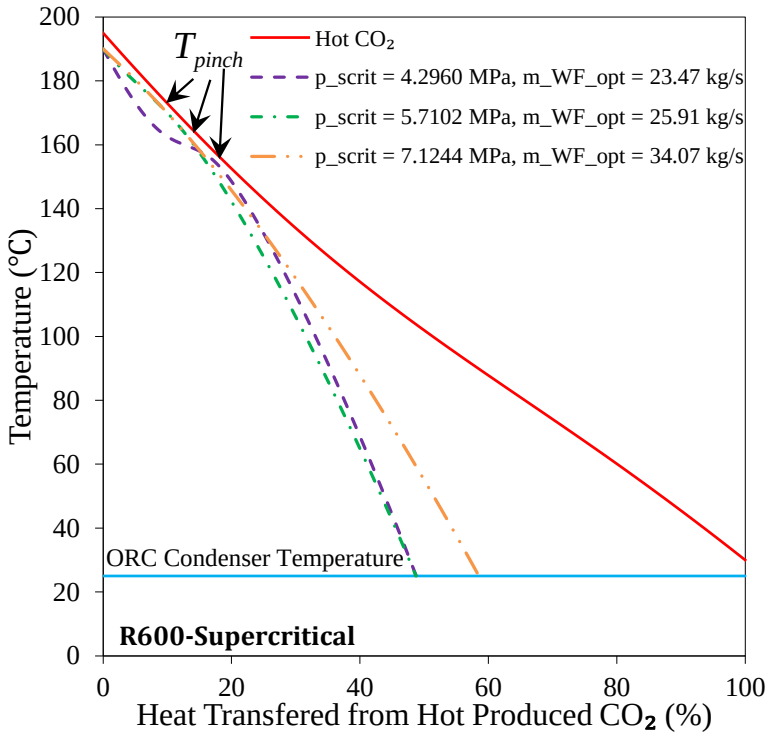

Figure 4–14 Supercritical ORC optimal WF mass flow rates with R600 at different supercritical pressures with showing T_{pinch}.

Table 4–3 Thermodynamic results corresponding to Figure 4–12, Figure 4–13 and Figure 4–14.

	T_{evp} (°C)	$\dot{m}_{WF,opt}$ (kg/s)	W_{net} (MW_e)	$\eta_{ORC,th,cyc}$ (%)	$\eta_{ORC,ex,cyc}$ (%)	w_{net} (kW_e/(kg/s))
Subcritical	125.23	49.51	3.9578	16.6	70.4	79.95
	100.23	56.50	3.6948	14.2	63.6	65.40
	75.23	66.19	3.1001	10.9	52.1	46.84
Superheated	140.00	23.97	2.7628	17.8	63.3	115.27
	120.00	26.63	2.8310	15.9	59.1	106.30
	100.00	30.35	2.8127	13.5	53.6	92.69
	p_{scrit} (MPa)	$\dot{m}_{WF,opt}$ (kg/s)	W_{net} (MW_e)	$\eta_{ORC,th,cyc}$ (%)	$\eta_{ORC,ex,cyc}$ (%)	w_{net} (kW_e/(kg/s))
Supercritical	4.2960	23.47	2.7666	19.2	47.8	117.89
	5.7102	25.91	2.8485	19.9	69.2	109.93
	7.1244	34.07	3.3753	19.6	72.1	99.06

4.3.5.4 Model Validation and Optimized Results

An ASPEN Plus model has been developed to validate the three ORC models. The ORC thermal efficiency and net power output presented in Figure 4–19 show a very good agreement between the ASPEN Plus model and the ORC thermodynamic model results [93].

The results plotted in Figure 4–19 indicate maximum net power output and cycle thermal efficiency for the subcritical ORC are achieved at the possible largest evaporator outlet temperature which is 125.23 ℃ for R600. The predicted optimal net power output of 3.9578 MW_e is obtained. Maximum net power output of 3.6654 MW_e for superheated ORC is predicted at the evaporator outlet temperature of 116.98 ℃. Regarding the supercritical ORC with R600, maximum net power output of 4.0031 MW_e is obtained at the supercritical pressure of 4.2960 MPa (see Table 4–4). It indicates that the supercritical ORC with R600 has the largest net power output as well as highest cycle efficiencies. However, the subcritical ORC has the comparable net power output but with a considerably lower operating pressure than the supercritical ORC.

Based on the thermodynamic results, the maximum net power output of ORC is achieved at a specific evaporative temperature (or supercritical pressure for supercritical ORC) with an optimal organic fluid mass flow rate. Figure 4–15 presents the optimal net power output changes with evaporative temperature for subcritical ORC with R600 as working fluid. Obviously for R600 subcritical ORC, the higher evaporative temperature, the larger net power output is generated. For both superheated ORC and supercritical ORC, the working fluid temperature at the IHX outlet is another variable should be considered. Figure 4–16

and Figure 4–17 indicate the largest net power outputs won't occur at the highest IHX outlet temperature for R600. It is because the working fluid flow rate varies with the evaporative temperature as well which also significantly affect the net power output in both subcritical ORC systems and superheated ORC systems. Accordingly, the working conditions for all types of ORCs can be obtained through the procedure shown in Figure 4–18 with working fluid selection criteria disguised above.

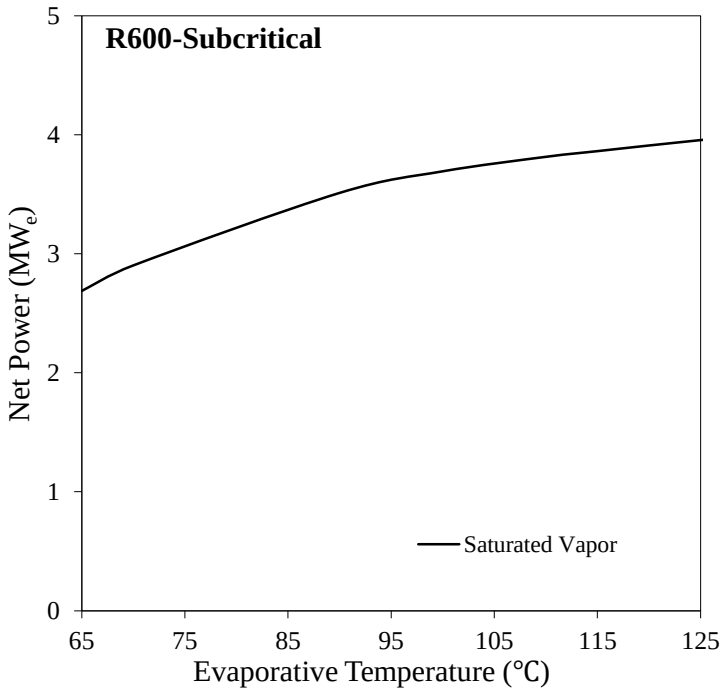

Figure 4–15 Net power output vs. evaporative temperature of Subcritical ORC with R600 as working fluid.

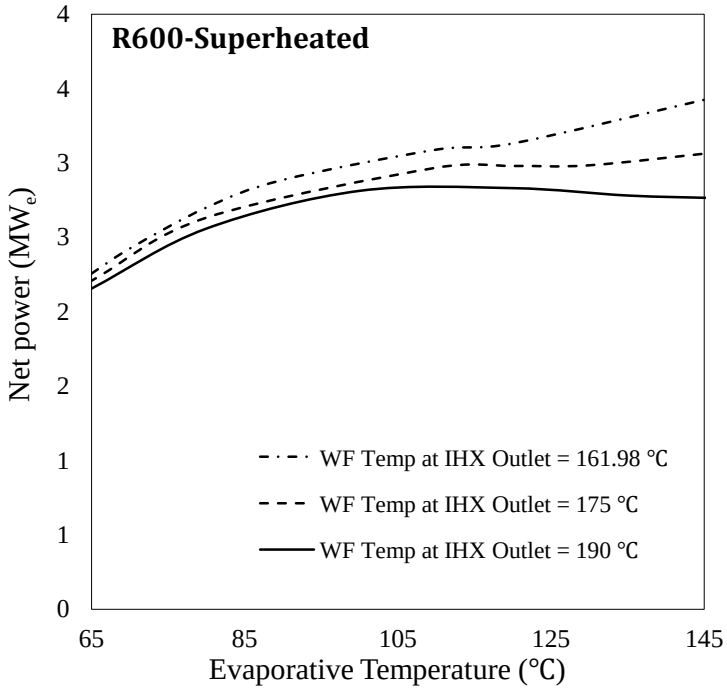

Figure 4–16 Net power vs. evaporative temperature for Superheated ORC with R600 as the working fluid.

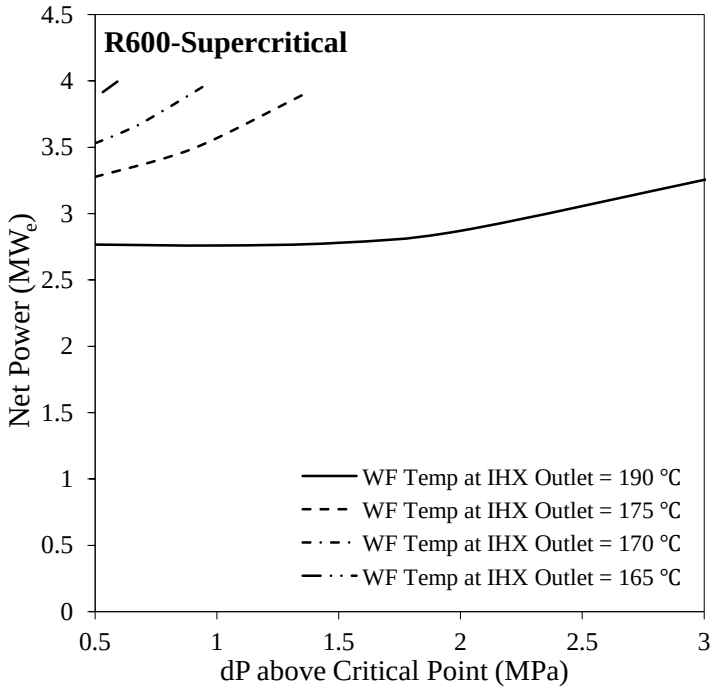

Figure 4–17 Net power vs. evaporative temperature for Supercritical ORC with R600 as the working fluid.

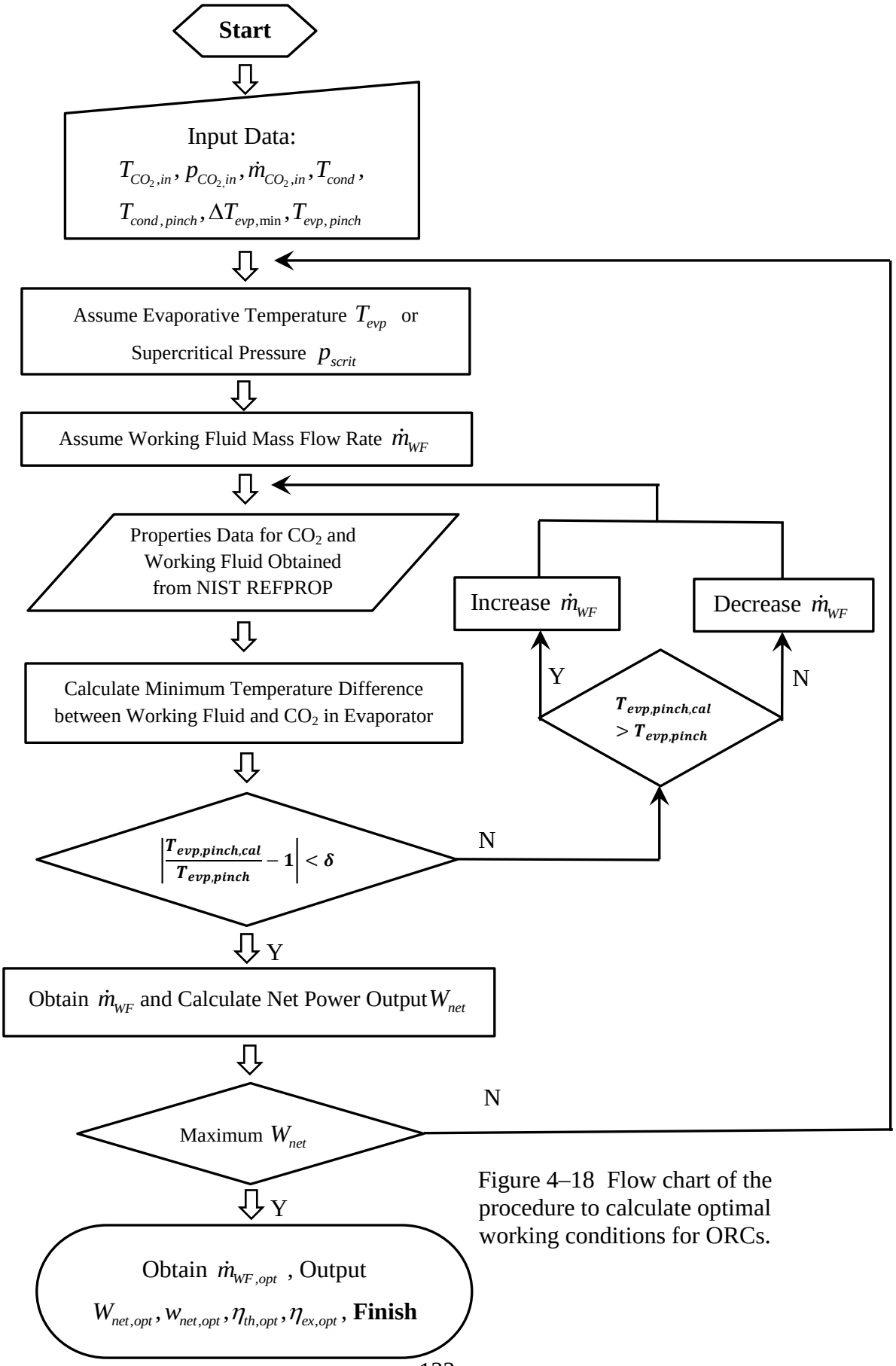

Figure 4–18 Flow chart of the procedure to calculate optimal working conditions for ORCs.

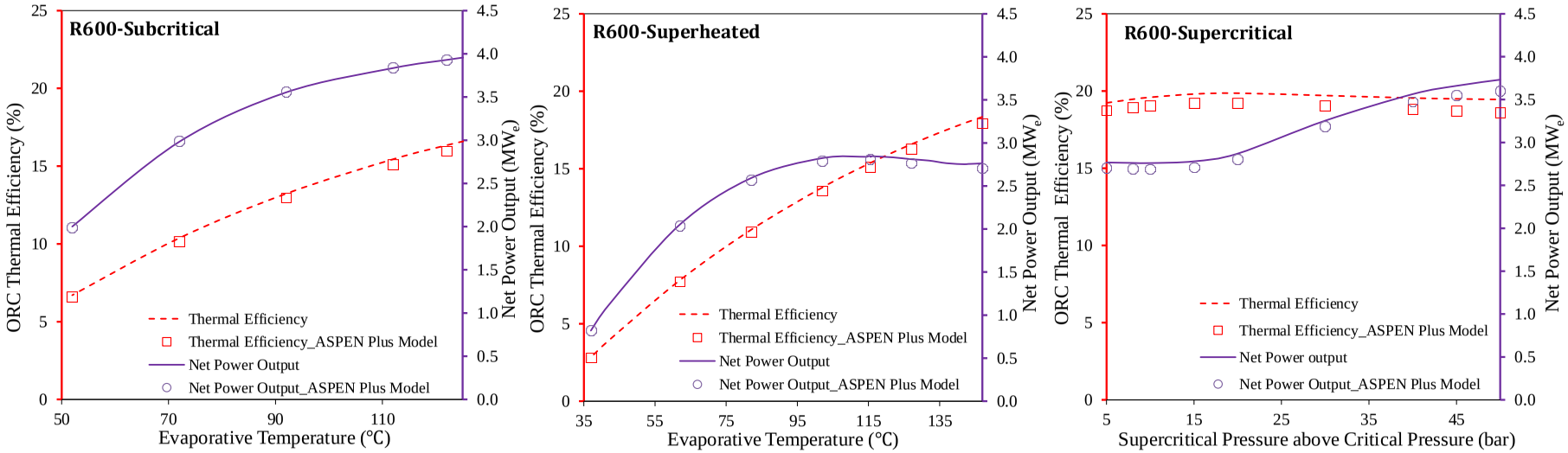

Figure 4–19 Thermodynamic Results for
a). Subcritical, b). Superheated, and c). Supercritical approaches with R600 as working fluid.

Table 4–4 Optimal calculation results for R600.

Subcritical	$T_{evp,opt}$ **(℃)**	$\dot{m}_{WF,opt}$ **(kg/s)**	W_{net} **(MW_e)**	$\eta_{ORC,th,cyc}$ **(%)**	$\eta_{ORC,ex,cyc}$ **(%)**	w_{net} **(kW_e/(kg/s))**	
	125.23	49.51	3.9578	16.6	70.4	79.95	
Superheated	$T_{evp,opt}$ **(℃)**	$T_{SH,opt}$ **(℃)**	$\dot{m}_{WF,opt}$ **(kg/s)**	W_{net} **(MW_e)**	$\eta_{ORC,th,cyc}$ **(%)**	$\eta_{ORC,ex,cyc}$ **(%)**	w_{net} **(kW_e/(kg/s))**
	135.01	145.01	40.19	3.6654	17.5	69.5	91.21
Supercritical	$T_{WF,IHX\ outlet}$ **(℃)**	$p_{crit,opt}$ **(MPa)**	$\dot{m}_{WF,opt}$ **(kg/s)**	W_{net} **(MW_e)**	$\eta_{ORC,th,cyc}$ **(%)**	$\eta_{ORC,ex,cyc}$ **(%)**	w_{net} **(kW_e/(kg/s))**
	163.58	4.2960	43.39	4.0031	18.6	74.8	92.27

4.4 Organic Working Fluid Selection Results

Maximum net power output values are calculated for all possible working fluids and optimal design conditions are obtained as well. The ranges of evaporative temperature and supercritical pressure for three ORC analyses are expressed by Equations (4.33), (4.34), (4.35) and (4.36).

The range of evaporative temperature for the subcritical cycle analysis is:

$$T_{evp} \in (T_{cond}, T_{tn}] \tag{4.33}$$

The range of evaporative temperature for the superheated cycle analysis is:

$$T_{evp} \in (T_{cond}, T_{cr} - 5] \tag{4.34}$$

$$T_{SH} \in [T_{evp} + 10, 190] \tag{4.35}$$

The range of supercritical pressure for the supercritical cycle analysis is:

$$p_{scrit} \in [p_{cr} + 0.5, 20] \tag{4.36}$$

The optimal design conditions and thermodynamic results are presented in Table 4–5, Table 4–6 and Table 4–7. Additionally, Figure 4–20, Figure 4–22, and Figure 4–24 show that the net power output and specific net power output for subcritical, superheated and supercritical respectively, ordered in terms of optimal net power output for different working fluids from high to low. Similarly, Figure 4–21, Figure 4–23 and Figure 4–25 present the cycle thermal efficiency and cycle exergy efficiency with working fluid net power output ranking from high to low.

The net power output, specific net power output, cycle thermal efficiency and cycle exergy efficiency are the factors used to compare the thermodynamic performance of different working fluids. In Figure 4–20 and Figure 4–22, it is obvious that R218 has the lowermost net power output and specific net power output in subcritical ORC and superheated ORC due to its relatively low critical temperature as well as low critical pressure. It is obviously that the thermodynamic performance of working fluids for subcritical and superheated ORCs is highly related to its critical temperature and pressure. For instance, superheated ORC with R32 with a comparable low critical temperature as R218 generates 3.5320 MW_e which is considerably larger than it for R218. The reason is that R32 has the highest critical pressure among all working fluids included in this study. However, the specific net power output and efficiencies of R32 with superheated ORC are lower compared to working fluids with similar net power output as shown in Figure 4–23. Therefore, the high net power output, specific net power output and cycle efficiencies are achieved with working fluids having both high critical temperatures and pressures in subcritical and superheated ORCs. Besides R218, the net power outputs of other working fluid candidates for the subcritical ORC are in the range from 3.0 to 4.3 MW_e and for the superheated ORC in the range from 2.7 to 4.1 MW_e. However, the specific net power output varies significantly with the working fluids having similar net power outputs and cycle efficiencies. Meanwhile, the cycle efficiencies are not completely correlated with the net power output. Regarding supercritical ORC systems, the wet working fluids have relatively high net power outputs. However, the large mass flow rates are needed for wet working fluids leading to lower specific net power outputs. In general, the net power output and efficiencies of supercritical ORCs are larger than subcritical and superheated ORCs.

As discussed above, the selection decision of the working fluids cannot be made based on a single factor. It is necessary to come up with a procedure to compare the working fluid thermodynamic performance comprehensively. In order to select the most suitable working fluids from a list of candidates for different ORCs, the median values of net power output, specific net power output, thermal efficiency and exergy efficiency are calculated and the working fluids are selected when the net power output, specific net power output and cycle efficiencies are equal to or greater than the median values of all factors for the working fluids at the same time (Table 4–5, Table 4–6 and Table 4–7). The working fluids are listed in the order of high net power output to low net power output for each case from Figure 4–20 to Figure 4–25.

The steps then are followed to select the suitable working fluids for all types of ORCs:

- Net power output equal to or greater than the median value;
- Specific net power output equal to or greater than the median value;
- Cycle efficiencies (both cycle thermal efficiency and cycle exergy efficiency) equal to or greater than the median value;

Based on the working fluid selection criteria, the selected working fluids are marked in red in Table 4–5, Table 4–6 and Table 4–7. A final selection results are listed below:

Subcritical: R236ea, R600a (flammable), R600 (flammable), R245fa.

Superheated: R600a (flammable), R152a, R142b, R236ea, R600 (flammable).

Supercritical: R134a, R32, R600a (flammable), R22.

In sum, the proposed working fluid selection criteria for power generation utilizing the geothermal heat extracted by sCO_2 are summarized as follows:

a. Classify working fluids types (dry, wet, isentropic);
b. Follow the pre-selection procedure in Section 4.3.4 to select promising working fluids;
c. Obtain the optimal design conditions for all three ORC layouts with a proper optimization objective (maximizing net power output in this analysis due to fixed heat source conditions);
d. Compare the thermal performance for each type of ORCs with steps discussed above and make the final decision.

The wet working fluids are not suitable for the subcritical ORC due to turbine blades erosion issues. Therefore, no results for wet fluids are presented in Table 4–5.

Table 4–5 Optimized results for Subcritical ORC.

Working Fluid	Turning Point (℃)	Subcritical Case						
		$T_{evp,opt}$ (℃)	$\dot{m}_{WF,opt}$ (kg/s)	$W_{ORC,net}$ (MW_e)	$\eta_{ORC,th}$ (%)	$\eta_{ORC,ex}$ (%)	w_{net} (kW_e/(kg/s))	$T_{CO_2,IHX\ outlet}$ (℃)
R123	150.62	106.68	102.40	3.4423	15.4	63.2	33.62	67.36
R124	82.93	82.93	173.14	3.5043	11.7	58.6	20.24	30.00
R134a	wet fluid	-	-	-	-	-	-	-
R141b	166.11	103.35	76.50	3.2931	15.5	62.1	43.05	72.03
R142b	73.99	73.99	124.16	3.0681	10.7	51.6	24.71	36.10
R143a	wet fluid	-	-	-	-	-	-	-
R152a	wet fluid	-	-	-	-	-	-	-
R21	wet fluid	-	-	-	-	-	-	-
R218	55.51	55.51	343.64	1.9789	6.6	33.1	5.76	30.00
R22	wet fluid	-	-	-	-	-	-	-
R227ea	82.56	82.56	215.37	3.2317	10.8	54.1	15.01	30.00
R236fa	97.47	97.47	161.32	3.8990	13.0	65.2	24.17	30.00
R236ea	122.93	122.93	129.48	4.2861	15.6	72.6	33.10	41.30
R245fa	**127.02**	**127.02**	**93.68**	**3.9490**	**16.7**	**70.5**	**42.15**	**60.23**
RC318	100.69	100.69	207.06	3.7135	12.4	62.1	17.93	30.00
R32	wet fluid	-	-	-	-	-	-	-
R365mfc	170.44	107.85	87.95	3.5337	14.9	63.1	40.18	60.23
C_4F_{10}	103.38	103.38	226.99	3.5405	11.8	59.2	15.60	30.00
C_5F_{12}	141.17	141.17	167.11	4.0132	13.9	67.4	24.02	34.52
R600	**125.23**	**125.23**	**49.51**	**3.9578**	**16.6**	**70.4**	**79.95**	**59.26**
R600a	107.79	107.79	66.92	4.1145	14.6	69.3	61.48	37.67
R601	179.40	106.55	46.21	3.4543	15.1	62.8	74.75	64.52
R601a	171.10	110.70	47.96	3.5166	15.4	63.8	73.33	64.05

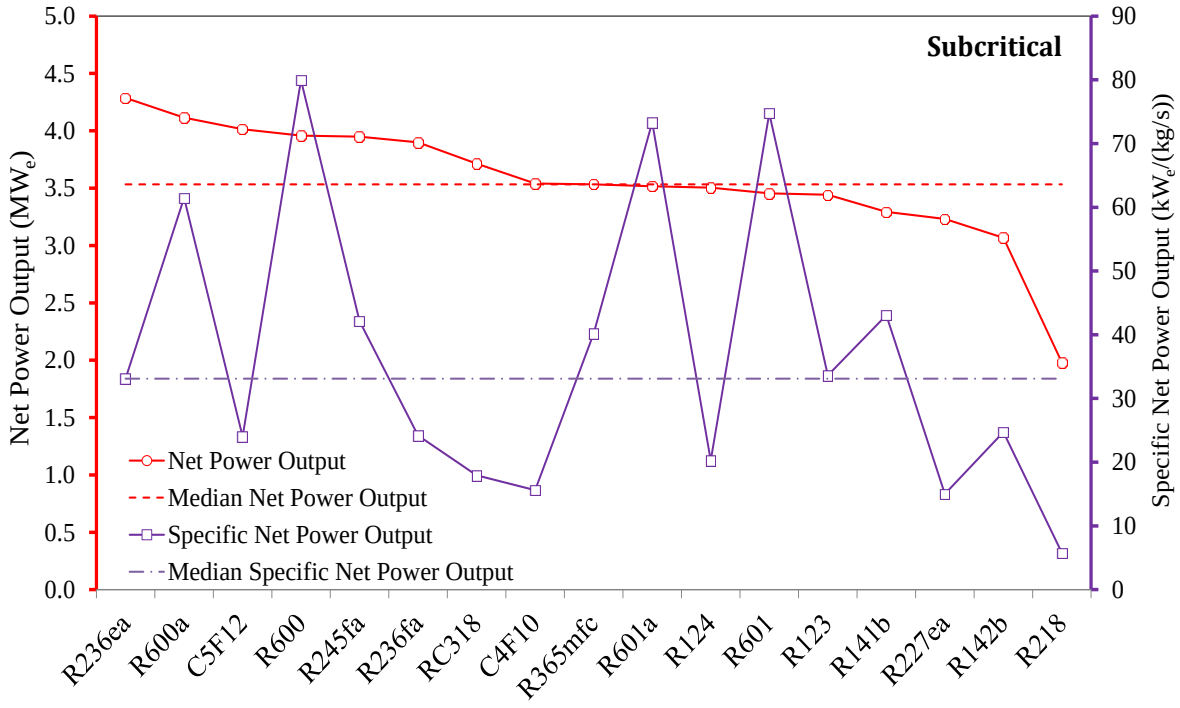

Figure 4–20 Optimal net power and specific net power of different working fluids for subcritical ORC.

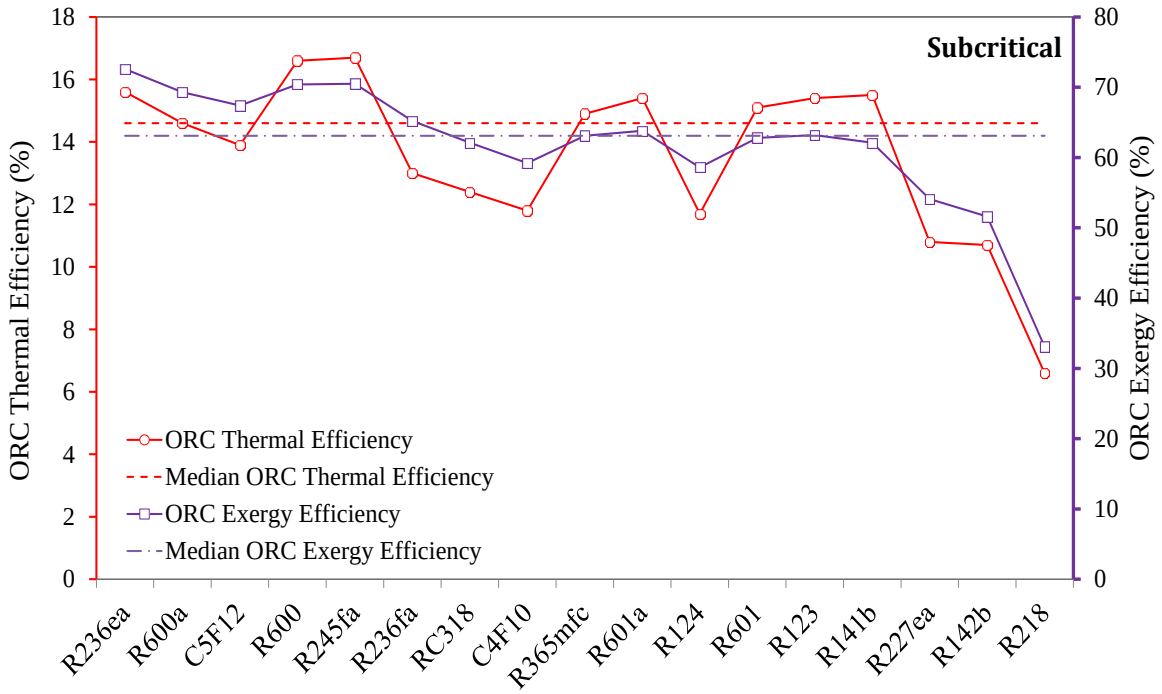

Figure 4–21 Optimal cycle efficiencies of different working fluids for subcritical ORC.

Table 4–6 Optimized results for Superheated ORC.

Working Fluid	Turning Point (℃)	Superheated Case							
		$T_{evp,opt}$ (℃)	$T_{SH,opt}$ (℃)	$\dot{m}_{WF,opt}$ (kg/s)	W_{net} (MW_e)	$\eta_{ORC,th}$ (%)	$\eta_{ORC,ex}$ (%)	w_{net} (kW_e/(kg/s))	$T_{CO_2,IHX\ outlet}$ (℃)
R123	150.62	105.00	115.00	97.66	3.3663	15.3	62.3	34.47	68.29
R124	82.93	117.28	127.28	143.90	4.2874	15.4	72.4	29.79	39.23
R134a	wet fluid	96.06	106.06	141.28	3.9223	13.2	65.6	27.76	30.00
R141b	166.11	100.52	110.52	74.86	3.2505	15.2	61.0	43.42	71.10
R142b	**73.99**	**132.11**	**142.11**	**89.52**	**4.0544**	**17.4**	**72.8**	**45.29**	**61.67**
R143a	wet fluid	67.71	77.71	164.81	2.7259	9.2	45.6	16.54	30.00
R152a	wet fluid	108.26	127.66	77.96	4.0812	15.4	69.7	52.35	45.90
R21	wet fluid	99.33	122.66	74.90	3.2186	15.4	61.2	42.97	73.42
R218	55.51	66.87	76.87	286.18	2.4244	8.1	40.5	8.47	30.00
R22	wet fluid	91.15	116.33	132.42	3.8770	13.5	65.0	29.28	33.99
R227ea	82.56	96.75	106.75	189.17	3.6467	12.2	61.0	19.28	30.00
R236fa	97.47	119.92	129.92	139.10	4.3061	15.0	72.3	30.96	34.52
R236ea	122.93	134.29	144.29	105.37	4.0303	16.4	70.8	38.25	55.86
R245fa	127.02	125.00	135.00	81.93	3.6521	16.6	67.6	44.58	68.29
RC318	100.69	110.23	120.23	184.28	3.9032	13.1	65.3	21.18	30.00
R32	wet fluid	73.11	190.00	62.85	3.5323	13.0	59.9	56.20	41.81
R365mfc	170.44	105.00	115.00	83.40	3.3836	14.4	60.7	40.57	61.67
C_4F_{10}	103.38	108.18	118.18	200.40	3.5815	12.0	59.9	17.87	30.00
C_5F_{12}	141.17	142.41	152.41	137.04	3.5646	13.7	61.4	26.01	49.43
R600	125.23	135.01	145.01	40.19	3.6654	17.5	69.5	91.21	72.96
R600a	**107.79**	**129.66**	**139.66**	**53.38**	**4.1303**	**16.5**	**72.1**	**77.37**	**53.90**
R601	179.40	104.53	114.53	43.83	3.3319	14.8	60.9	76.01	65.94
R601a	171.10	105.54	115.54	46.54	3.3726	14.7	61.2	72.47	64.05

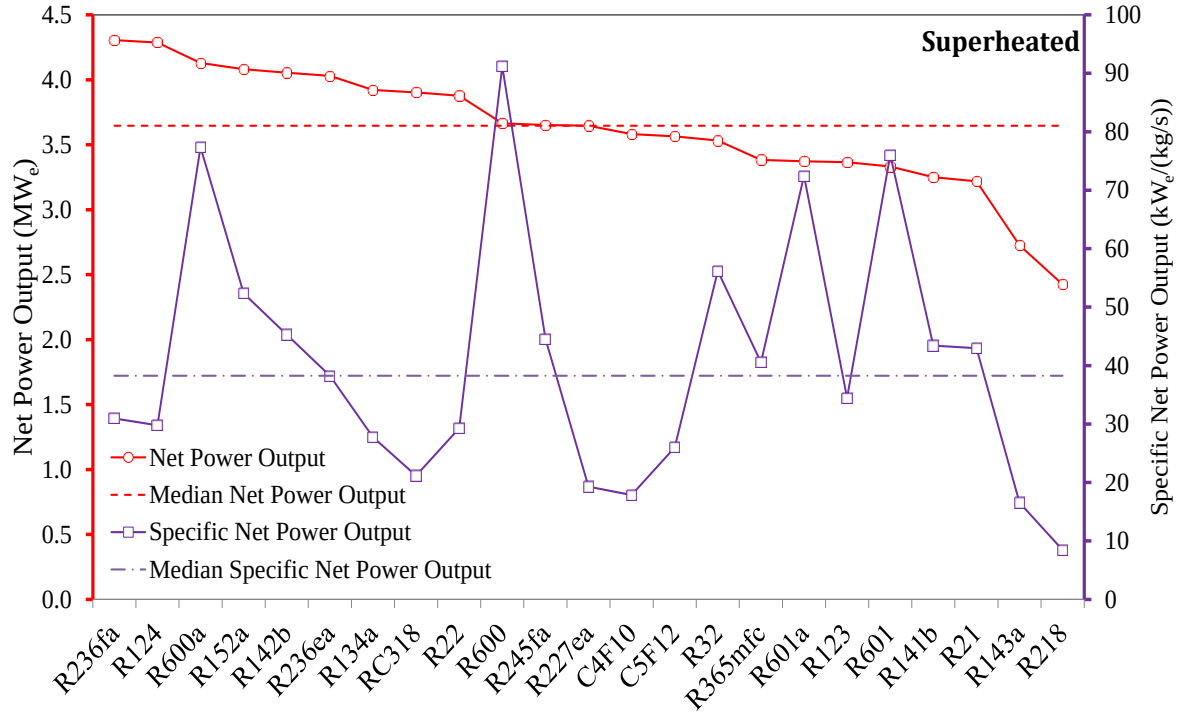

Figure 4–22 Optimal net power and specific net power of different working fluids for Superheated ORC.

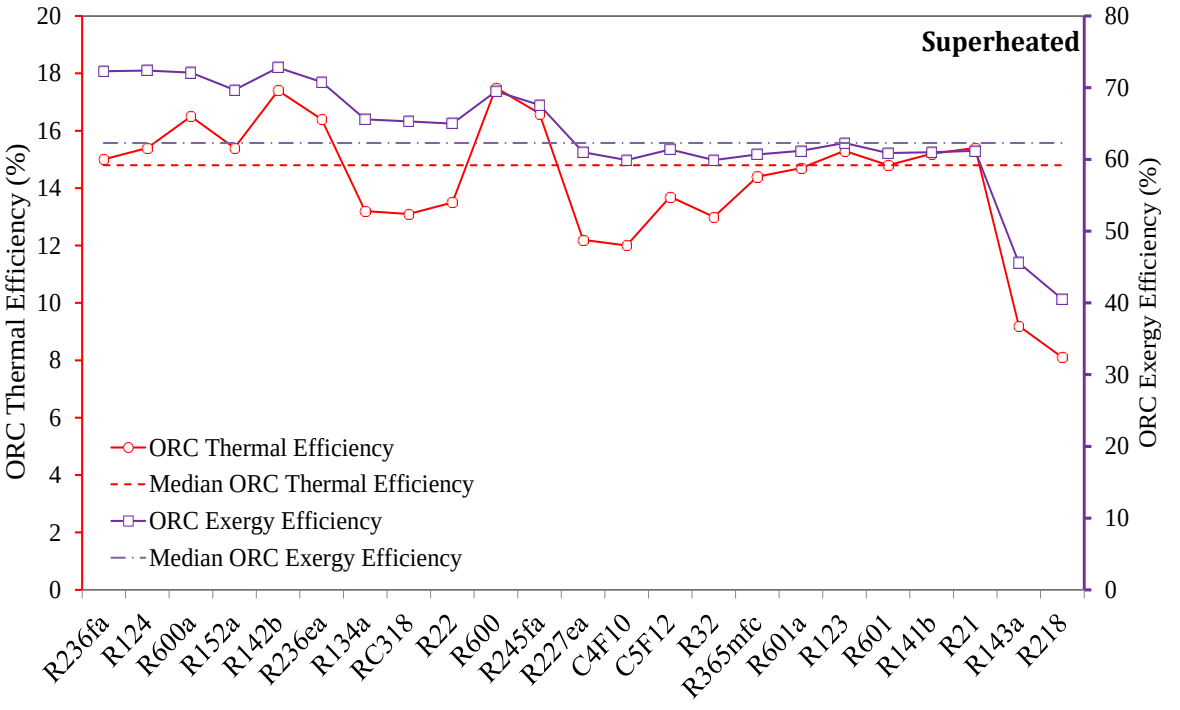

Figure 4–23 Optimal cycle efficiencies of different working fluids for superheated ORC.

It has to be mentioned that R123, R141b, R21, R365mfc, R601 and R601a are not applicable for supercritical ORC using sCO_2 with temperature of 195 ℃ due to the minimum allowable turbine inlet temperature (calculated by Equation (4.28)) is over the heat source temperature.

Table 4–7 Optimized results for Supercritical ORC.

Working Fluid	Supercritical Case							
	$T_{WF,IHX\ outlet}$ (℃)	$p_{evp,opt}$ (MPa)	W_{net} (MW_e)	$\dot{m}_{WF,opt}$ (kg/s)	$\eta_{ORC,th}$ (%)	$\eta_{ORC,ex}$ (%)	w_{net} (kW_e/(kg/s))	$T_{CO_2,IHX\ outlet}$ (℃)
R123	-	-	-	-	-	-	-	-
R124	161.01	6.6150	4.6792	145.58	17.2	79.2	32.14	41.30
R134a	162.70	10.2605	4.7535	124.45	17.2	79.9	38.20	37.67
R141b	-	-	-	-	-	-	-	-
R142b	152.14	4.5550	4.2018	92.43	17.9	75.1	45.46	60.71
R143a	163.02	20*	4.8696	138.29	17.5	81.4	35.21	30.00
R152a	157.78	6.4215	4.2977	68.88	17.8	75.8	62.40	56.84
R21	-	-	-	-	-	-	-	-
R218	123.14	20*	3.7158	280.36	13.5	62.2	13.25	30.00
R22	164.35	8.6324	4.4838	109.91	17.8	77.5	40.79	50.43
R227ea	158.82	20*	4.7240	188.11	16.5	79.0	25.11	30.00
R236fa	166.24	7.9743	4.7864	144.64	16.9	80.4	33.09	35.05
R236ea	160.09	4.6182	4.4772	119.13	17.2	77.0	37.58	48.42
R245fa	165.34	4.1510	3.9704	82.13	18.6	74.5	48.34	71.10
RC318	166.95	20*	4.8062	184.72	16.8	80.4	26.02	30.00
R32	**172.25**	**11.9532**	**4.5909**	**74.61**	**18.0**	**78.8**	**61.53**	**47.92**
R365mfc	-	-	-	-	-	-	-	-
C_4F_{10}	156.46	20*	4.4523	206.72	15.4	74.5	21.54	30.00
C_5F_{12}	170.51	4.2903	4.1216	158.75	14.8	69.6	25.96	39.23
R600	163.58	4.2960	4.0031	43.39	18.6	74.8	92.27	70.17
R600a	**158.31**	**5.0305**	**4.5232**	**59.08**	**17.5**	**77.8**	**76.55**	**48.42**
R601	-	-	-	-	-	-	-	-
R601a	-	-	-	-	-	-	-	-

Note: * - R143a, R218, R227ea, RC318 and C_4F_{10} can only be heated up to 163.02 ℃, 123.13 ℃, 158.82 ℃, 166.95 ℃ and 156.46 ℃ respectively at 20 MPa supercritical pressure.

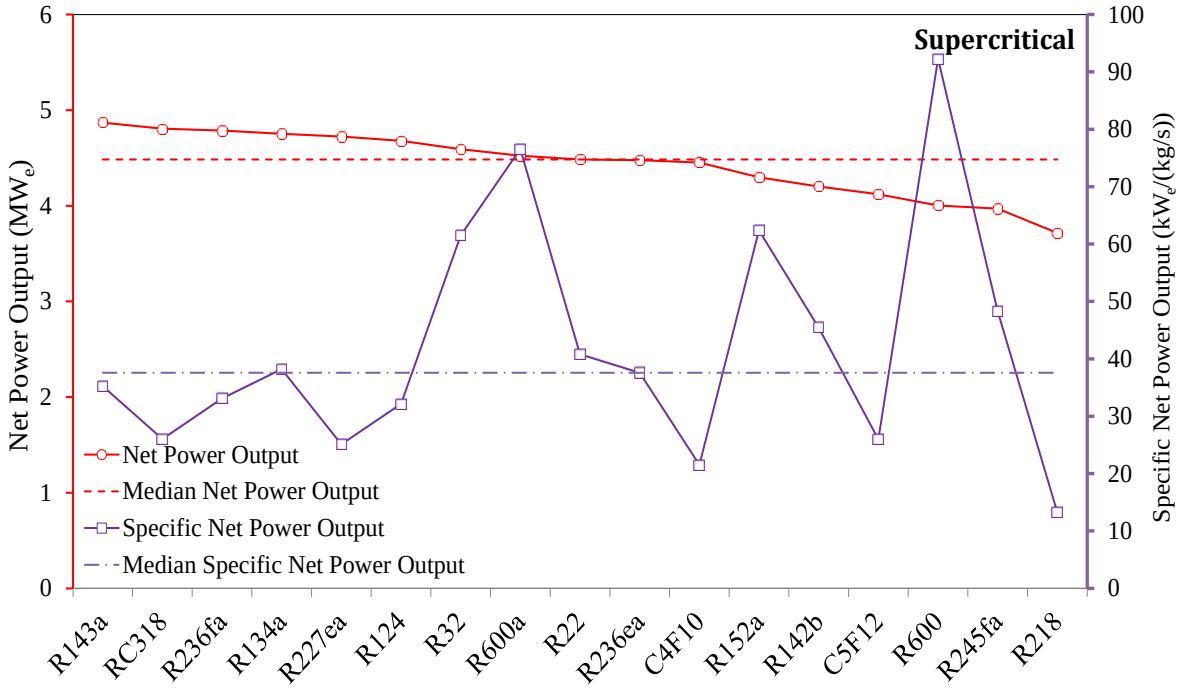

Figure 4–24 Optimal net power and specific net power of different working fluids for Supercritical ORC.

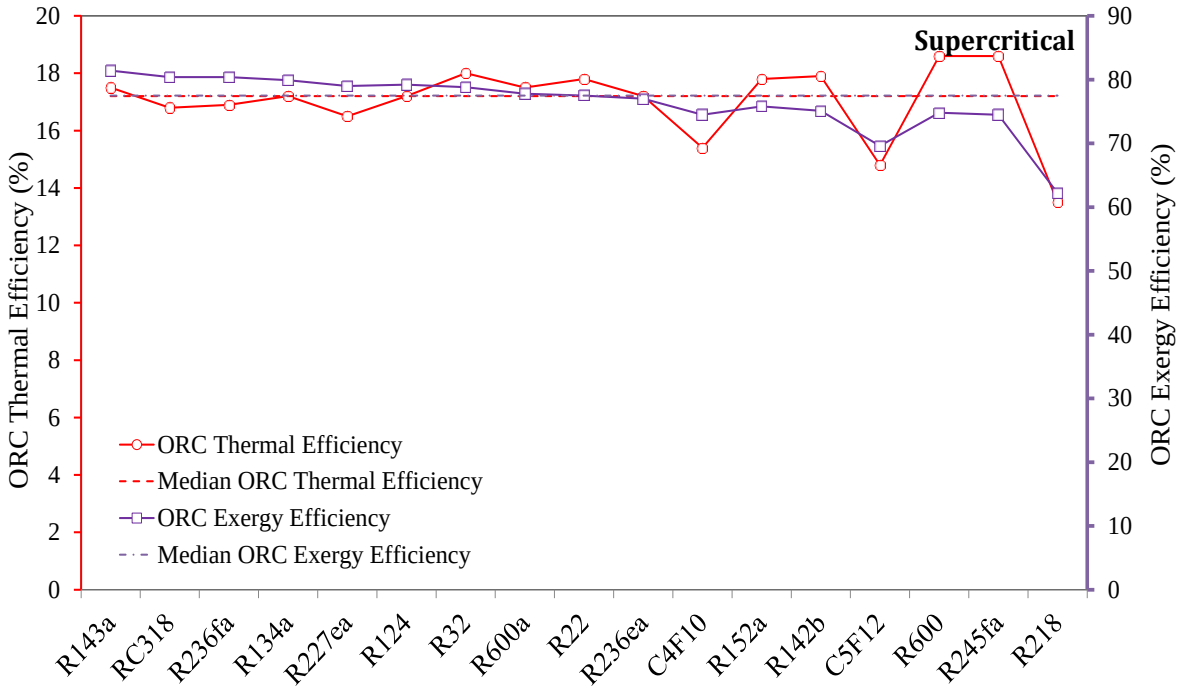

Figure 4–25 Optimal cycle efficiencies of different working fluids for supercritical ORC.

4.5 Discussion and Selected ORC Power System Using Hot Produced CO_2

As discussed above, the cycle performance is evaluated by the parameters of net power output, cycle thermal efficiency, cycle exergy efficiency, and specific net power output. It is found that alkanes as ORC working fluids have superior cycle performances. However, the flammability of a working fluid can be a concern. Therefore, another candidate other than alkanes has been included considering cycle efficiencies and specific net power output. The bolded and red marked working fluid in Table 4–5, Table 4–6 and Table 4–7 are the working fluids eligible for the further analyses.

Furthermore, the supercritical ORC runs at a high pressure level as well as the superheated ORC needs to consider the superheater design, which potentially can cause extra capital costs of ORC plants.

Table 4–8 Selected working fluid for Subcritical, Superheated and Supercritical ORCs.

Case with Optimization	Working Fluid	Net Power Output [MW_e]	$\dot{m}_{WF,opt}$ Working Fluid [kg/s]	Cyc/Sys Thermal Efficiency [%]	Cyc/Sys Exergy Efficiency [%]	Specific Net Power Output [$kW_e/(kg \cdot s)$]
Subcritical ORC	R600	3.9578	49.51	16.6/13.3	70.4/66.2	79.94
	R245fa	3.9490	93.68	16.7/13.3	70.5/66.1	42.15
Superheated ORC	R600a	4.1303	53.38	16.5/13.9	72.1/69.1	77.38
	R142b	4.0544	89.52	17.4/13.7	72.8/67.8	45.29
Supercritical ORC	R600a	4.5232	59.08	17.5/15.3	77.8/75.7	76.55
	R32	4.5909	74.61	18.0/15.5	78.8/76.8	61.53

To avoid the uncertainty of ORC plant cost caused by different working fluids and unconventional operating conditions, the subcritical ORC with R245fa, which is also the

widely used conventional ORC configuration and working fluid, is selected to perform cost estimation and optimization analyses.

Recommendations on Improvement of ORC Performance Using Hot Produced CO_2

Although only simple ORC layout is considered in this study, improvement techniques for sCO_2 Brayton cycles, such as recuperating can also be used in ORCs, which won't be covered in this dissertation. However, another important aspect has to be considered for improving the effectiveness to convert geothermal heat carried by hot produced sCO_2. As shown in Figure 4–26, there are two parts of energy cannot be converted to useful power. The first part is the exergy destruction in the IHX which is irreversibility generated during the heat transfer process, which is not reversible and reusable. This part is determined by the physical properties of CO_2 and the working fluid in their pressure and temperature ranges in the IHX. The second part is the exergy loss occurring at the CO_2 cooler, which can be utilized to convert more heat from the hot produced sCO_2. Figure 4–26 shows the temperature of sCO_2 at the IHX outlet is over 100 ℃ which still carries substantial energy. Accordingly, a concept design of the coupled ORC has been proposed and is illustrated in Figure 4–27. For instance, the top ORC are not necessary to achieve the maximum net power output which can lead to a relatively high CO_2 outlet temperature at evaporator 1 outlet (see Figure 4–27). In another word, the optimization objective is the total net power output but not the stand along ORC. Therefore, an intergraded model is needed for a working fluid group selection. This design potentially achieves more net power output as well as eliminates the substantial CO_2 cooling loads.

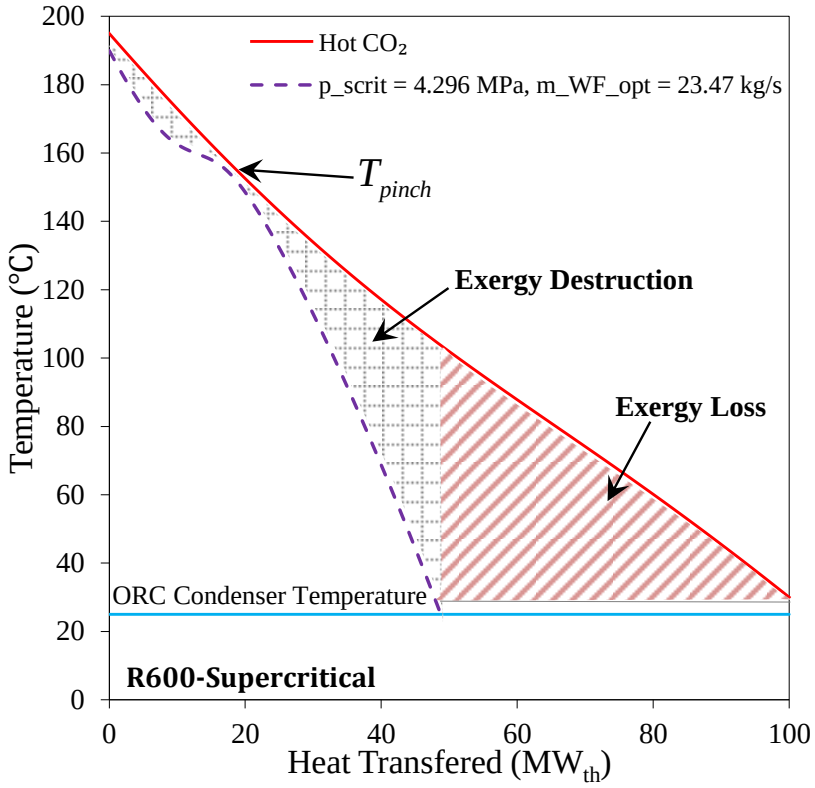

Figure 4–26 Exergy distribution for a Supercritical ORC with R600 as working fluid.

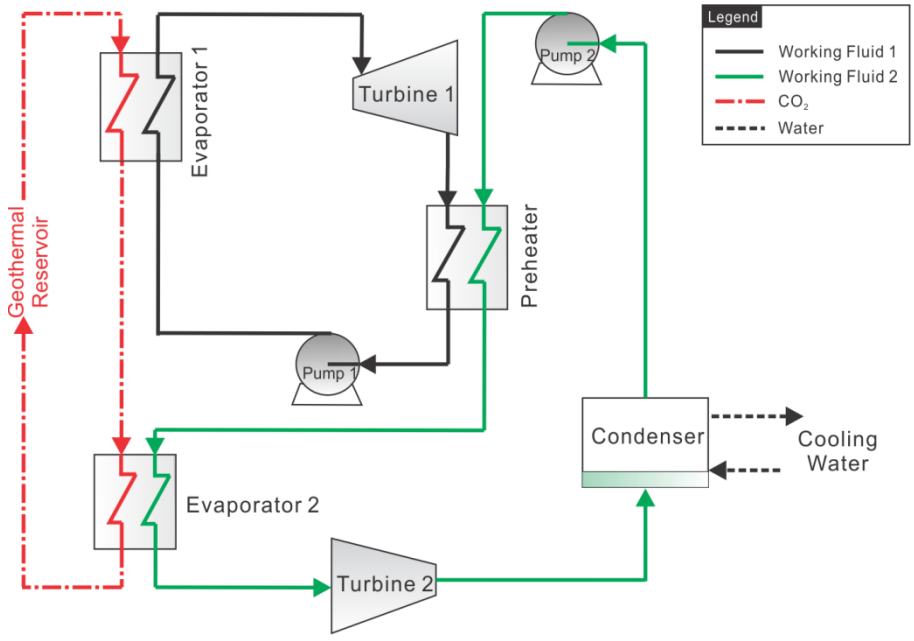

Figure 4–27 System diagram of the coupled ORC.

Chapter 5 Cost Analysis and Optimization

While the promising power cycles have been selected to utilize the geothermal energy extracted by sCO_2, it brings a great interest to explore the economics of the power generation cost using hot produced sCO_2 from geothermal reservoirs. Cost estimating is of great importance and concern since it helps the plant owners to make a decision for construction.

Preliminarily, economic analyses for sCO_2-based power cycles and ORCs have been performed which are based on the thermodynamic models comprehensively discussed in the previous chapters. A power cost calculation and optimization methodology has been developed combining of thermodynamic performance and system cost both for the geothermal heat mining system and power generation system. The power cost considered here is levelized cost of electricity (LCOE) in USD per kilowatt-hour ($/kWh) over the plant life. In addition, this cost estimation and optimization methodology has been applied to obtain the most cost-effective power generation system design with considering the geothermal energy extraction system, including optimal well size, well distances as well as CO_2 injection flow rate, which all these parameters also significantly affect the system thermodynamic performance. Therefore, the global optimization for the power generation system as well as the geothermal heat mingling system is necessary. As a consequence, the most cost-effective design has been obtained for each type of power generation system. Furthermore, the benefit from CO_2 sequestration has been emphasized.

5.1 Cost Analysis Methodology

In this section, the cost analysis methods have been proposed for geothermal heat mining systems, sCO_2-based power systems and ORC power generation systems. The empirical equations and the related constants for the cost estimation are presented. Moreover, the method for calculating LCOE of the power generation system combining the geothermal heat mining system is also demonstrated.

5.1.1 Well Cost Estimation and Optimization

As discussed in Chapter 2, there are six wells for each well set, including one injection well, four production wells, and one re-injection well. It is assumed that the geothermal heat mining system cost is just the total well cost, which includes well drilling cost, exploration cost and confirmation cost.

For each geothermal well drilling cost, it is given by Equation (5.1), which is slightly adapted and scaled up into the year of 2017 [59], the constants used in Equation (5.1) are shown in Table 5–1:

$$C_{\text{well, drilling}} = 1.33 \times \left[\zeta \left(\frac{D_{\text{well}}}{D_0} \right)^2 + (1-\zeta) \right] K e^{bz} \tag{5.1}$$

where $C_{\text{well, drilling}}$ = per-well drilling cost in 2017, \$M

D_0 = 0.23125 m used as a baseline well diameter

z = well depth, m

Table 5–1 Constants values of Equation (5.1).

K	b	ζ
0.2865	6.657×10^{-4}	0.6662

The total well drilling costs consist of injection well drilling cost, production well drilling cost and re-injection well drilling cost. The cost minimization method has been proposed. Due to the fixed well depth in this study, the well diameter is the only parameter which needs to be considered to minimize the well drilling cost.

The mass flow rate in wells can be written as:

$$\dot{m}_{inj/prod/reinj} = \frac{1}{4}\pi D_{well}^2 \rho v \tag{5.2}$$

where $\dot{m}_{inj/prod/reinj}$ = flow rate in well, kg/s

D_{well} = well diameter, m

ρ = fluid density, kg/m^3

v = flow velocity in well, m/s

In this analysis, the flow velocity in wellbore is assumed as $v_{max} \leq 3$ m/s . Therefore, Equation (5.2) can be then expressed as:

$$\frac{4\dot{m}_{inj/prod/reinj}}{\pi\rho D_{well}^2} = v \leq 3 \text{ m/s} \tag{5.3}$$

Furthermore, the required minimum well diameter can be obtained at minimum density, based on the Equation (5.3) derived from Equation (5.2):

$$D_{well,\min} = \sqrt{\frac{4\dot{m}_{inj/prod/reinj}}{3\pi\rho_{\min}}} \tag{5.4}$$

Therefore, the minimum well diameter can be obtained at the minimum flow density by Equation (5.4). Further, the minimum drilling cost can be calculated.

The exploration and confirmation cost is $390/kW in this analysis which is inflated from the previous data [94, 95]. Therefore, the total minimum well cost can be calculated by:

$$\begin{aligned} C_{\text{well set},\min} &= \min(C_{tot,\text{drilling}}) + C_{\text{exploration\&confirmation}} \\ &= \min(C_{inj,\text{drilling}} + 4\times C_{prod,\text{drilling}} + C_{reinj,\text{drilling}}) + C_{\text{exploration\&confirmation}} \end{aligned} \tag{5.5}$$

5.1.2 sCO_2-based Power Cycles Using Hot Produced sCO_2 from Geothermal Reservoirs Capital Cost Estimation

sCO_2-based power generation systems are not commercialized yet in 2017. In addition, no actually cost data are available for the cycle components as well as the operation and maintenance costs for sCO_2-based power plants. Therefore, estimating methods for the purchase cost of equipment used in sCO_2-based power cycles are discussed and summarized. However, the purchase cost of all the components needed for building a plant cannot represent the actual total cost of a plant. It is necessary to take into account factors reflecting materials, pressure levels, contingencies and other possible costs which can affect the capital cost of a plant. Therefore, factorial costs estimation techniques are discussed as follows.

Lang Factor method is a simple technique to estimate the capital cost of a power plant which tends to overestimate. It is quite simple that the total capital cost of a plant is

determined by multiplying the total purchase cost to a constant shown in Table 5–2. This multiplier is called Lang Factor [96].

Table 5–2 Lang Factors.

Plant Type	Lang Factor
Solid Processing	3.10
Solid-fluid Processing	3.63
Fluid Processing	4.74

The capital cost then can be determined by Equation (5.6):

$$C_{tot,\,\text{capital}} = F_{Lang} \sum C_{p,i} \tag{5.6}$$

where $C_{tot,\,\text{capital}}$ = total capital cost of a plant

F_{Lang} = Lang Factor

$C_{p,i}$ = purchase cost of a component

It's obviously that Lang Factor method is straightforward to calculate plant capital costs. Nevertheless, Lang Factor method is not able to consider pressure levels and materials, which is a significant downside to estimate sCO_2-based power cycle costs and perform optimization analyses. It is because the sCO_2-based power cycles are highly associated with the produced CO_2 pressure and the cycle components directly contact with produced CO_2 which requires different materials. Regarding these circumstances affecting costs, more accurate methods are necessary.

Another well-known cost estimation method, bare module factor method, has the ability to take into account operating pressures and materials effects on capital costs. In addition, the

factors considering different types of components are also available, such as shell tube heat exchangers, turbines, compressors which are adopted in this study.

Accordingly, the bare module cost method is employed for the sCO_2-based power generation system capital cost calculation. The correlations and equations are provided in this section.

5.1.2.1 Cost Factors

The cost factors, such as pressure factors, material factors and bare module factors are presented in this section.

Pressure Factor F_p

If the operation pressure of a component increases, it requires a large wall thickness to bare the increased pressure, which results in a cost raise. The increasing costs due to the operating pressure increases can be covered by using pressure factors. The pressure factor can be expressed by Equation (5.7), and the constants for different equipment are listed in Table 5–3.

The pressure factor used in this analysis can be expressed as [96]:

$$F_p = 10^{C_1 + C_2 \log P + C_3 (\log P)^2} \tag{5.7}$$

where F_p = pressure factor

P = operating pressure, bar

Table 5–3 Constant value of pressure factor in Equation (5.7).

Equipment		C_1	C_2	C_3	Pressure Range (bar)
Compressor		0	0	0	-
Turbine		0	0	0	-
Tube Shell Heat Exchanger	Both Tube and Shell	0	0	0	P<5
		0.03881	-0.11272	0.08183	5<P<140
	Tube Only	0	0	0	P<5
		-0.00164	-0.00627	0.0123	5<P<140

Since the pressure range of the applications in this study is slightly out of what is shown in Table 5–3, it can be extrapolated from Equation (5.7) using high pressure range calculation results (100 to 140 bar). Therefore, the Equation (5.7) can be modified to:

$$F_p = \begin{cases} 10^{C_1 + C_2 \log P + C_3 (\log P)^2}, & P \le 140 \\ 0.5426 P^{0.2037}, \text{ Tube and Shell}, & P > 140 \\ 0.8966 P^{0.0413}, \text{ Tube Only}, & P > 140 \end{cases} \quad (5.8)$$

where F_p = pressure factor

P = operating pressure, bar

Bare Module Factor F_{BM} and Material Factor F_M

As mentioned earlier, the direct contacts between the produced sCO_2 from geothermal reservoirs containing minerals occur in direct turbine expansion approach which requires anti-corrosive materials such as stainless steel to manufacture these components. Therefore,

material factors are introduced. In addition, bare module factors for turbines, compressors and heat exchangers are also presented for obtaining bare module costs [96].

For turbines and compressors:

$$C_{BM,t/comp} = C_{p,t/comp} \cdot F_{BM} \cdot F_P \tag{5.9}$$

It can be seen from Equation (5.7) and Table 5–3, the pressure factors for turbines and compressors equals to 1. Then Equation (5.9) can be reduced to:

$$C_{BM,t/comp} = C_{p,t/comp} \cdot F_{BM} \tag{5.10}$$

where $C_{BM,t/comp}$ = bare module cost of turbines and compressors, \$M

$C_{p,t/comp}$ = purchase cost of turbines and compressors, \$M

F_{BM} = bare module factor

Table 5–4 Values of F_{BM} for Equation (5.10).

Equipment	Material	F_{BM}
Centrifugal Compressors	Carbon Steel	2.8
	Stainless Steel	5.7
Turbines	Carbon Steel	3.5
	Stainless Steel	6.1

For tube and shell heat exchangers:

$$C_{BM,HX} = C_{p,HX} \cdot F_{BM} = C_{p,HX}(B_1 + B_2 F_M F_p) \tag{5.11}$$

where $C_{BM,t/comp}$ = bare module cost of turbines and compressors, \$M

$C_{p,t/comp}$ = purchase cost of turbines and compressors, $M

F_{BM} = bare module factor

Table 5–5 Values of F_M for Equation (5.11).

Equipment	Material	F_M
Tube Shell HX	CS-Shell/CS-Tube	1
	CS-Shell/SS-Tube	1.8
	SS-Shell/SS-Tube	2.7

Table 5–6 Constant value of Equation (5.11).

Equipment	B_1	B_2
Fixed Tube Sheet HX	1.63	1.66

Conversion Factor of Chemical Engineering Plant Index (CEPCI) F_{CE}

CEPCI is employed to updating capital cost from one period to another. The conversion factor can be defined as [97]:

$$F_{CE,A\text{ to }B} = \frac{CEPCI \text{ at year } B}{CEPCI \text{ at year } A} \tag{5.12}$$

where $F_{CE,A\text{ to }B}$ = chemical engineering plant index factor

CEPCI from 2000 to 2017 are available in Appendix A3.

Factor Considering Additional Cost F_{add}

The additional cost factor considering piping, control, labor and other overhead costs on the basis of bare module cost is:

$$F_{add} = 1.8 \tag{5.13}$$

Contingency Factor F_{contcy}

The contingency factor is a factor that accounts for unforeseeable expenses of a plant construction. These costs may result from design development changes, construction schedule adjustments, or differing site conditions for those expected, etc. The contingency factor is based on previous experience and the expected difficulty of a particular construction project. In this analysis, for a power plant, a typical contingency rate of 15% is considered:

$$F_{contcy} = 1.15 \tag{5.14}$$

5.1.2.2 Equipment Cost Estimations for sCO_2-based Power Cycles

In order to estimate bare module costs for different equipment, purchase costs for the equipment used in the sCO_2-based power cycle analyses have to be available. The equations reported by other researchers for sCO_2-based power cycles are included here.

Turbine

An economic analysis was performed by Atrens et al. for a CO_2-based EGS power plant in 2011 [59]. In terms of the compression work and the CO_2 density at turbine outlet,

Equation (5.15) can be used to calculate the CO_2 turbine purchase cost and then be converted to the cost at 2017 through the CEPCI factor expressed by Equation (5.12).

$$C_t^0 = \alpha W_t^{\beta} \rho_{CO_2,out}^{\gamma}$$
$$C_{p,t} = F_{CE,2008 \text{ to } 2017} \times C_{t,2008}^0 \quad (5.15)$$

where C_t^0 = CO_2 turbine base cost in 2008, M$

$C_{p,t}$ = CO_2 turbine purchase cost in 2017, $M

W_t = turbine power output, MW_e

$\rho_{CO_2,out}$ = CO_2 density at turbine outlet, kg/m^3

Table 5–7 Constant value of Equation (5.15).

α	β	γ
1.066	0.5439	-0.1472

Compressor

The centrifugal CO_2 compressor cost is calculated by Equation (5.16) [96]. Based on Equation (5.16), the compressor purchase cost is determined by the compression work of compressors, which will significantly lower than typical gas compressor since the actual CO_2 compression process occurs in its supercritical region. Moreover, the compressor cost in 2017 can be obtained. In addition, the predicted results by Equation (5.16) are also comparable with the technical data of CO_2 compression, transport and storage [98].

$$C_{comp}^{0} = \begin{cases} 10^{R_1 + R_2 \log W_{comp} + R_3 (\log W_{comp})^2}, & W_{comp} \le 3000 \\ \dfrac{W_{comp}}{3000} \times 10^{R_1 + R_2 \log 3000 + R_3 (\log 3000)^2}, & W_{comp} > 3000 \end{cases} \quad (5.16)$$

$$C_{p,comp} = \frac{F_{CE,2001 \text{ to } 2017} \times C_{comp,1}^{0}}{1 \times 10^{6}}$$

where C_{comp}^{0} = CO_2 compressor/pump base cost in 2001, $

$C_{p,comp}$ = CO_2 compressor/pump purchase cost in 2017, $M

W_{comp} = compressor power, kW

Table 5–8 Constant value of Equation (5.16).

R_1	R_2	R_3
2.2897	1.3604	-0.1027

Heat Exchangers (IHX, Coolers)

The heat exchangers used in sCO_2-based power cycles are IHXs and coolers. The coolers are using cold water to cool down CO_2 which are transferring heat from hot sCO_2 to cooling water. The pressure and temperature ranges of different types of heat exchangers are presented in Figure 5–1. According to design and operating conditions of sCO_2-based power cycles, shell tube HX, PCHE HX and PMHE HX are able to work properly. However, PMHE HXs and PCHE HXs are still under investigation and the cost information is very limited. As a result, a fixed tube-sheet heat exchanger is selected for the cost estimation and optimization analysis in this study. The design methods and correlations can be found in Appendix A4.

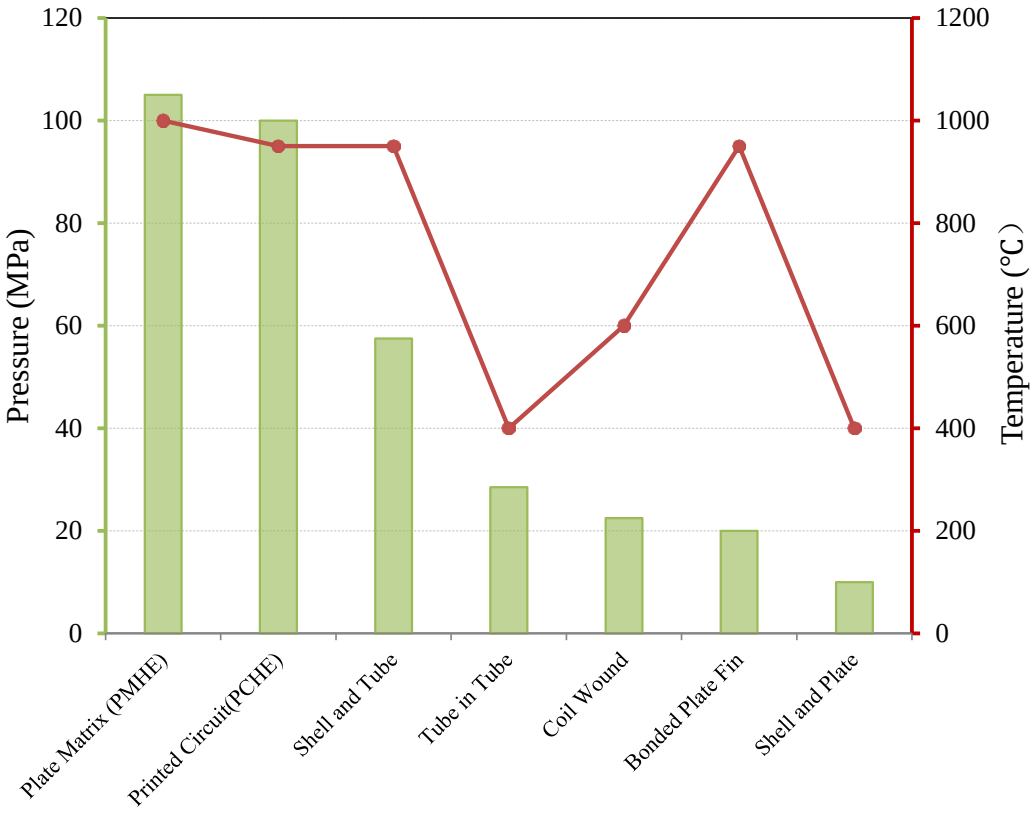

Figure 5–1 Pressure and temperature working conditions for sCO_2 HXs.

The purchased cost of fixed tube-sheet heat exchanger using carbon steel can be calculated by [96]:

$$C_{HX}^{0}=\begin{cases}10^{K_1+K_2\log A+K_3(\log A)^2}, & A\le 1000\\ \dfrac{A}{1000}\times 10^{K_1+K_2\log 1000+K_3(\log 1000)^2}, & A>1000\end{cases} \tag{5.17}$$

$$C_{p,HX}=\frac{F_{CE,2001\text{ to }2017}\times C_{HX}^{0}}{1\times 10^{6}}$$

where C_{HX}^{0} = CO_2 turbine base cost in 2001, \$

$C_{p,HX}$ = CO_2 turbine purchase cost in 2017, \$M

A = heat transfer area, m^2

Table 5–9 Constant value of Equation (5.17).

K_1	K_2	K_3
4.3247	-0.3030	0.1634

Based on the purchase cost methods described in this section, the total installed capital cost of a sCO_2-based power generation system can be obtained.

Cooling Water Chiller

The heat taken away by circulating water for cooling down CO_2 needs to be rejected by cooling equipment. The packaged centrifugal water chiller has been taken into consideration in the cost estimation. The bare module cost of centrifugal water chiller can be found with different tons of refrigeration [99]. Figure 5–2 shows the bare module cost of centrifugal water chiller changes with the total cooling load which the unit is converted from the original cost data. It can be seen that the installation cost per kW of refrigeration approaches $\$100/kW_{th}$ when the total refrigeration load increases. Therefore, the bare module cost of a water chiller can be expressed as:

$$C_{BM.chiller} = \frac{\$100}{kW_{th}} \times Q_{cooling\ water} \times 10^{-6} \tag{5.18}$$

where $C_{BM.chiller}$ = bare module cost of centrifugal chiller, \$M

$Q_{cooling\ water}$ = heat needs to be rejected from cooling water, kW_{th}

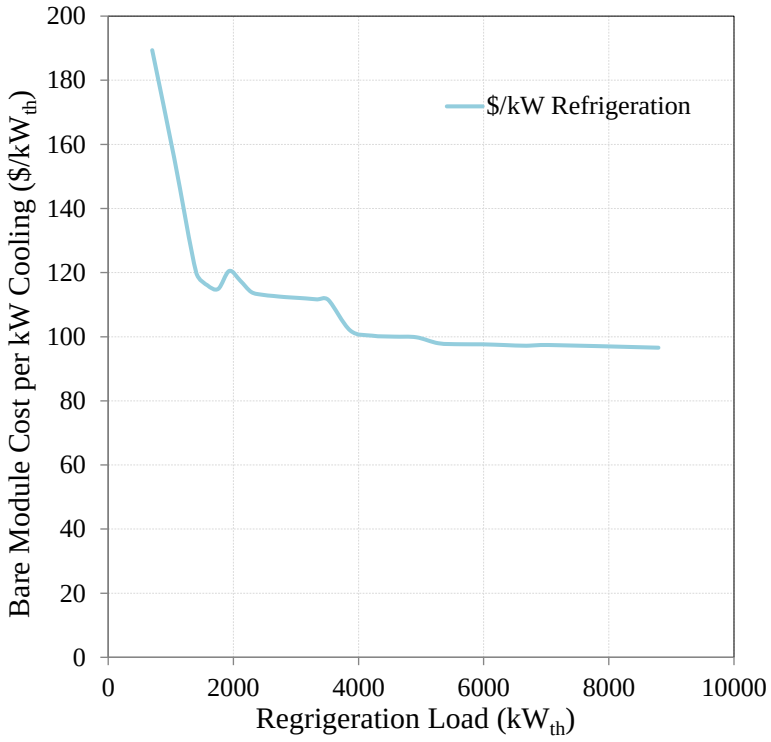

Figure 5–2 Bare module cost per kilo-watt of refrigeration vs. total refrigeration load.

CO_2-H_2O Separator

The CO_2-H_2O separator is an essential component in this study (Figure 5–3). However, there are no commercial products for the large scale application. A technique named the cost-to-capacity method is used to estimate the large scale CO_2-H_2O separator. A quote for a Mueller helical separator of $50,000 for maximum CO_2 flow of 298 L/min is obtained [100]. In addition, a rule of thumb developed and validated over the years referred to as the rule of six-tenths can be used to get the satisfactory results, which the Therefore, the bare module cost for a full scale CO_2-H_2O separator can be estimated by:

$$C_{BM,separator/wellset} = \frac{C_{BM,separator,known}\left(\frac{S_{separator/wellset}}{S_{separator,known}}\right)^{0.6}}{1\times10^{6}} \quad (5.19)$$

where $C_{BM,separator/wellset}$ = bare module cost of CO_2-H_2O separator, $M

$C_{BM,separator,known}$ = $50,000 for a separator with capacity of 298 L/min

$S_{separator/wellset}$ = CO_2 flow rate in volume per well set, L/min

$S_{separator,known}$ = 298 L/min

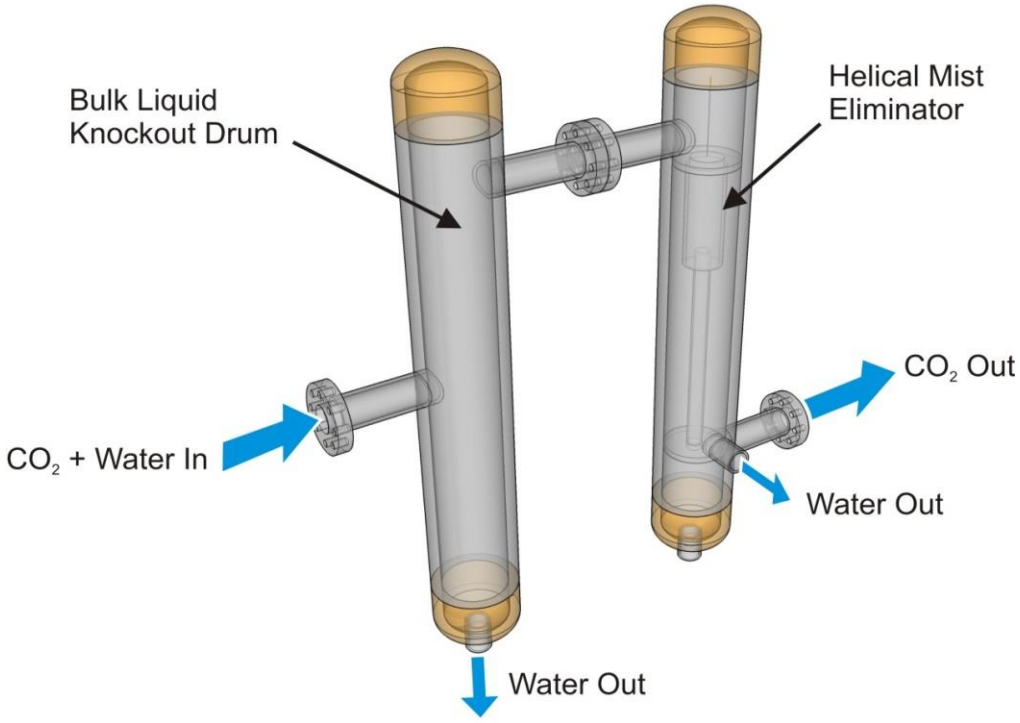

Figure 5–3 Sketch of CO_2-H_2O Separator

5.1.3 ORCs Using Hot Produced CO_2 from Geothermal Reservoirs Capital Cost Estimation

Although research on ORC systems increase rapidly, the majority are focusing on system design and thermodynamic analyses on cycle performance. Limited researches are available on actual costs of ORC systems utilizing geothermal energy. The present study includes the actual investment costs of ORC projects throughout the geothermal power plant capacity range of 1 kW_e to 35 MW_e. This cost data was gathered from economic surveys of ORC systems as well as direct quotes from ORC manufacturers.

Figure 5–4 presents the actual installed capital cost data points of ORC systems using geothermal energy from different sources. The installed capital cost of ORC plants, which is in unit of thousand dollars per kilo-watt (k$/$kW_e$), decrease with the plant capacity gets larger. Obviously, the outliers should be removed from the data base before performing curve fitting. It has to be mentioned that the effect of different working fluids on installed capital cost of an ORC plant is neglected in this analysis.

The data fitting equation can be expressed as:

$$C_{tot\ \text{capital},ORC} = \frac{12.177 W_{\text{nominal net}}^{-0.156} \times W_{\text{nominal net}}}{1000} \tag{5.20}$$

where $C_{tot\ \text{captital},ORC}$ = total installed capital cost of ORC, $M

$W_{\text{nominal net}}$ = nominal net power output of ORC, kW_e

The installed capital cost of an ORC power generation system with capacity ranging from 1 kW_e to 35 MW_e can be estimated by Equation (5.20).

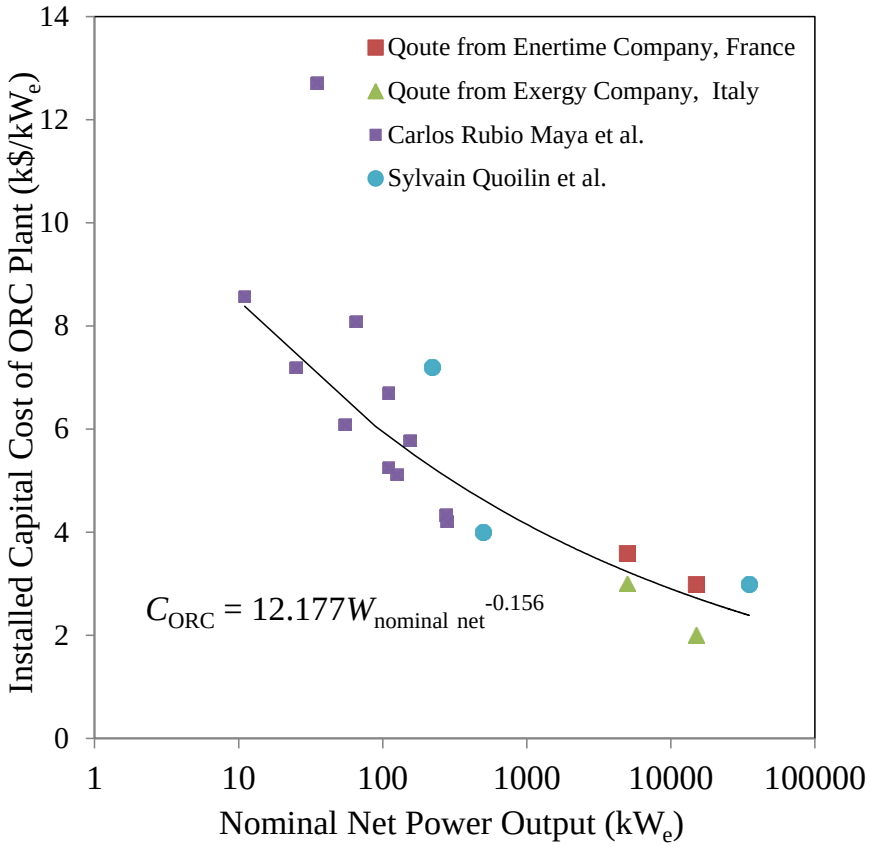

Figure 5–4 Installed capital cost of ORC plants [101-104].

5.1.4 Cost Estimation Method for Power Generation System Combining Geothermal Heat Extraction System

The objective function for the global optimization considering both power generation systems and geothermal heat mining systems are introduced in this section. Table 5–10 shows the baseline conditions taken into account for cost estimation and optimization analysis. According to geothermal heat mining with 20 years steady CO_2 production, a plant life of 20 years is considered. For the HX design of sCO_2-based power cycles, a HX effectiveness of 0.85 is used to obtain the required heat transfer area. Due to a portion of CO_2 sequestration credit should be applied to the carbon capture process which would not

be considered in the present study, the counted CO_2 sequestration credit for storage may vary. Thus, sensitivity analyses have been performed with the CO_2 credit ranging from 0 to 50 $/t for final LCOEs.

Table 5–10 Parameter values for cost estimation and optimization analysis.

Parameters	Units	Values
Plant Life	year	20
Capacity Factor	%	85
Geothermal Well Drilling Successful Rate	%	80
Annual Interest Rate i	%	4
Taxes and Insurance Factor	%	1.5
Counted CO_2 Sequestration Credit b_{co_2}	$/t	0-50
Heat Exchanger Effectiveness	-	0.85

The plant total installed capital costs can be calculated by following equations for both sCO_2-based power plants and ORC power plants.

Total installed capital cost for a sCO_2 power plant is expressed as:

$$C_{tot\ \text{captital, sCO}_2} = F_{contcy} \cdot F_{add} \cdot \sum C_{BM,i} \tag{5.21}$$

where $C_{tot\ \text{captital}}$ = total installed capital cost, $M

F_{contcy} = contingency factor

F_{add} = additional cost factor

$C_{BM,i}$ = bare module cost for different components in million USD

The installed capital cost for an ORC power plant is presented in Equation (5.22):

$$C_{tot\ \text{capital},ORC} = \frac{12.177 W_{\text{nominal net}}^{-0.156} \times W_{\text{nominal net}}}{1000} \tag{5.22}$$

where $C_{tot\ \text{captital},ORC}$ = total installed capital cost of ORC, $M

$W_{\text{nominal net}}$ = nominal net power output of ORC, kW_e

Combining with the geothermal heat extraction system cost, the total capital cost can be written as:

$$C_{tot\ \text{capital}} = C_{tot\ \text{capital, plant}} + N_{\text{well set}} \times C_{\text{well set,min}} \tag{5.23}$$

where $C_{tot\ \text{captital}}$ = total installed capital cost, $M

$C_{tot\ \text{capital, plant}}$ = total installed capital cost of power plant, $M

$N_{\text{well set}}$ = well set number needed

$C_{tot,\ \text{well}}$ = total well cost, $M

An example is illustrated in Figure 5–5, which five well sets are needed and a power plant to utilize the hot produced CO_2 from geothermal reservoirs to generate electricity.

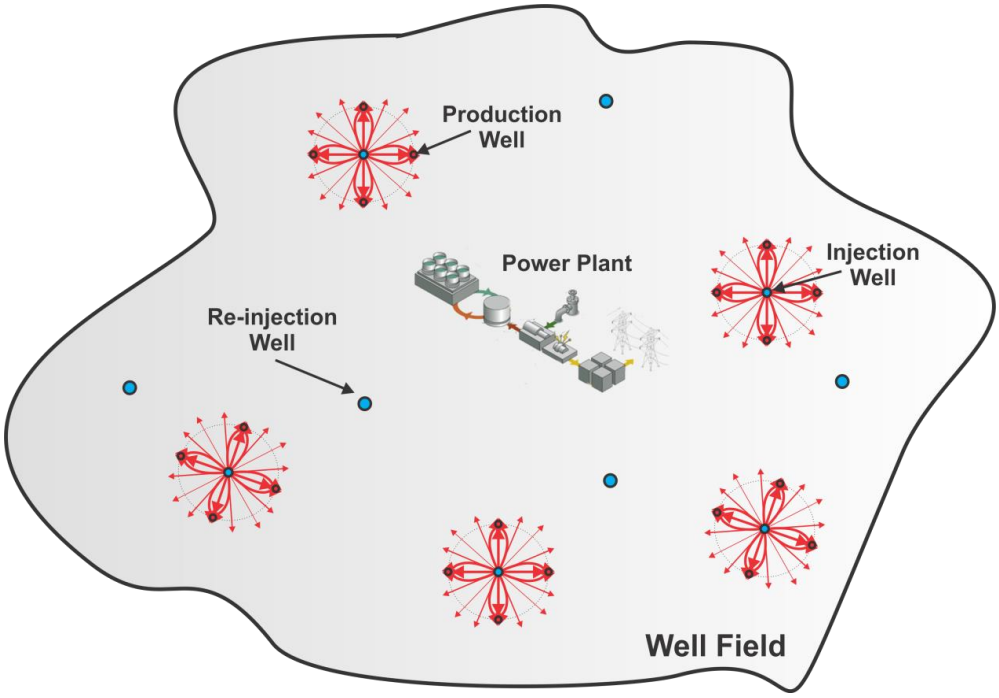

Figure 5–5 Sketch of well field with five well sets.

A capital recovery factor method is adopted to convert a present value into a stream of equal annual payments over 20 year's plant life at a specified discount rate. The total installed cost based on this factor above can be converted into an annual fixed cost that takes into consideration capital amortization and tax and insurance costs alternatively. An annual payment is derived using the following equation:

$$PF = \frac{r(1+r)^n}{(1+r)^n - 1} \tag{5.24}$$

where PF = annual payment factor

r = annual interest rate

n = period of the loan in years

The period of loan for this research is 20 years and the annual interest rate is taken to be 4%. This gives an annual payment factor of 0.07358. This annual payment factor is used to calculate the annual fixed cost ($C_{\text{annual fixed cost}}$) by following equation:

$$C_{\text{annual fixed capital}} = \left(PF + 1.5\%\right) \times C_{tot\ \text{captital}} \tag{5.25}$$

where $C_{\text{annual fixed captital}}$ = annual fixed installed capital cost, \$M

$C_{tot\ \text{captital}}$ = total installed capital cost, \$M

In Equation (5.25), 1.5% is a factor to take into account taxes and insurance and the total installed capital cost has been explained before.

Besides the plant capital cost, the operations and maintenance (O&M) is another part of cost to contribute LCOE. The typical O&M estimating method for geothermal power generation has been employed. The O&M cost of conventional hydrothermal geothermal power generation can be expressed as [105]:

$$C_{\text{fixed O\&M,Conventional Geo}} = 0.026e^{-0.0025(W_{net}-5)} \tag{5.26}$$

where $C_{\text{fixed O\&M,Conventional Geo}}$ = fixed O&M cost contributes to LCOE of conventional geothermal power plant, \$/kWh

W_{net} = plant net power output, MW_e

Equation (5.26) is suitable for a plant with capacity ranging from 5 to 150 MW_e. In addition, the variable O&M cost is neglected since there is no fuel consumption for geothermal power generation. Moreover, the makeup drilling cost is also neglected.

Additionally, due to centrifugal water chillers are used to cool down the cooling water for both cycle coolers and geothermal loop coolers, it has to be separately considering the O&M costs for the water chillers additionally to the basis of the O&M costs given by Equation (5.26). For the additional cooling load, an O&M cost factor of \$199.04/kW_{th} annually is selected [106]. Therefore, Equation (5.26) can be written as:

$$C_{\text{fixed O\&M}} = 0.026e^{-0.0025(W_{net}-5)} + \frac{\$199.04/\text{kW}_{\text{th}}}{E_{tot,annual}} \times Q_{add,cooling} \tag{5.27}$$

where $C_{\text{fixed O\&M}}$ = fixed O&M cost contributes to LCOE of conventional, \$/kWh

W_{net} = plant net power output, MW_e

$Q_{add,cooling}$ = additional cooling load, kW_{th}

$E_{tot,annual}$ = annual power generation, kWh

Finally, the levelized cost of electricity can be obtained by:

$$LCOE = \frac{C_{\text{annual fixed capital}} \times 10^6}{E_{tot,annual}} + C_{\text{fixed O\&M}} - b_{co_2} \tag{5.28}$$

where $LCOE$ = levelized cost of electricity, \$/kWh

$C_{\text{annual fixed captital}}$ = annual fixed installed capital cost, \$M

$C_{\text{fixed O\&M}}$ = fixed O&M cost contributes to LCOE, \$/kWh

b_{co_2} = counted CO_2 sequestration credit, \$/kWh

$E_{tot,annual}$ = annual power generation, kWh

Particularly for the application using hot produced CO_2 from geothermal reservoirs with CO_2 sequestrated permanently, the CO_2 credit should be counted in the cost analysis.

5.2 Cost Analysis Results and Optimization for Different Approaches

As mentioned previously, the geothermal heat extraction simulations are very time intensive. In addition, it would not be possible to create an objective function for the global optimization considering the geothermal heat extraction system. Therefore, to simplify the optimization analysis as well as avoid the unnecessary massive simulation time, a geothermal heat mining result data set is obtained. This data set contains parameters of produced CO_2 flow rate, produced CO_2 temperature, produced CO_2 pressure and required CO_2 injection pressure, considering different well distances and CO_2 injection flow rates. Based on the parameter values in geothermal simulation data set, which are the inputs for the optimization of power generation system, the optimal design of the power generation system can be determined and the maximum net power output for each well set can be calculated. The similar optimization analyses then have been carried out for all promising power generation approaches to achieve the best designs.

It has to be mentioned that as a novel technology, the capacity factor for the power plant using hot produced sCO_2 from geothermal reservoirs is hard to be predicted. Therefore, the LCOE calculated in this study is generally for a certain year over the entire plant life. For a power plant with W MW_e capacity, the LCOE for a certain year, also the objective function of optimization can be expressed as for given geothermal heat mining conditions:

$$LCOE = \frac{(PF + F_{Insurance\&Tax}) \times (\frac{W}{W_{net/\text{well set}}} \times C_{\text{capital, plant/well set}} + \frac{W}{W_{net/\text{well set}}} \times C_{\text{well set}})}{W \times F_{capacity} \times 24 \times 365} + C_{\text{fixed O\&M}} - b_{co_2} \quad (5.29)$$

where $LCOE$ = levelized cost of electricity for a certain year, \$/kWh

W = plant total capacity, MW_e

PF = annual payment factor of a certain year

$F_{Insurance\&Tax}$ = insurance and tax factor

$C_{\text{capital, plant/well set}}$ = capital cost corresponding to max output per well set, \$M

W = plant total capacity, MW_e

$C_{\text{fixed O\&M}}$ = fixed O&M cost contributes to LCOE, \$/kWh

b_{co_2} = counted CO_2 sequestration credit, \$/kWh

$F_{capacity}$ = capacity factor for a certain year

Since the plant capital cost won't change significantly with the minor variation of net power output during the thermodynamic optimization process, it is assumed the optimal plant capital cost obtained at the minimum plant capital cost is the corresponding plant capital cost at the maximum net power output. In the global optimization, the optimization objective of minimizing the LCOE can be converted to maximize the net power output and minimize well cost. However, increasing net power output of each well set will decrease the total well cost, since the power generation of each well set increases leading to less well sets needed. Therefore, the net power output of each well set and the total well cost are interacted in the optimization process.

The global optimization objective is minimizing LCOE in Equation (5.29). Based on the assumptions, discussions and equations above, this problem can be converted to minimize well set cost and maximum net power output of each well set alternatively. It can be seen that despite the effects of capacity change on O&M cost, the LCOE is uncorrelated to total plant capacity.

5.2.1 Well Set Cost Optimization Results

Table 5–11 shows the geothermal heat extraction simulation results data set. In addition, by employing Equations (5.1) and (5.4), the minimum well set drilling cost for varying well distances and CO_2 injection flow rate can be calculated. Based on the parameter values shown in Table 5–11 which are the inputs for the power cycle thermodynamic analyses, a similar optimal power cycle performance data set is able to be generated. The calculated results are comparable with reported geothermal well drilling cost [107-109].

Table 5–11 Geothermal heat mining simulation results and optimal well set drilling cost.

Geothermal Heat Mining Simulation Results (Average from 10 Years to 30 Years)						
Injection Flow Rate (kg/s)	Well Distance (m)	Produced $\dot{m}_{CO_2}$ (kg/s)	Production T (℃)	Production P (MPa)	Injection P (MPa)	Minimum Well Set Drilling Cost (Million $)
120	500	98.17	190.32	20.83	14.08	11.2341
	600	92.48	194.02	19.75	14.34	11.4088
	700	87.67	194.21	19.00	14.50	11.5117
	800	75.63	194.51	18.69	14.45	11.5695
	900	68.26	194.74	18.09	14.67	11.6699
240	600	204.53	188.95	20.71	17.75	18.3968
	700	192.83	190.92	19.77	18.02	17.6971
	800	183.90	192.00	19.19	18.32	17.1404
	900	173.12	192.91	18.36	18.61	16.8710
360	700	305.77	185.91	20.46	21.81	24.1880
	800	292.17	188.33	19.68	22.19	24.0045
	900	277.98	189.09	19.21	22.54	26.1575

5.2.2 SCO_2-based Power Cycle Simulation and Optimization Results

Based on the thermodynamic analyses results in Chapter 3, the direct expansion, sCO_2 Brayton cycle with pre-compression and inter-cooling, and transcritical sCO_2 cycle have been selected for the further cost estimations and optimizations. Since the geothermal heat mining results are discrete, which makes not possible to create a global objective function, the optimal thermodynamic results have been obtained for each power cycle approach with all the discretized data points. In this study, the proper optimization algorithm, which is the sequential quadratic programming (SQP) method, has been employed in ASPEN Plus to achieve the maximum net power output for each case.

Direct Turbine Expansion

The direct turbine expansion power cycle is an open cycle which is affected by the production well head temperature and the CO_2 thermosiphon effect significantly. The optimal results with the maximum net power output as the optimization objective are presented in Table 5–12. Obviously, the higher well distance cases have less CO_2 thermosiphon effect which leads to the larger compression work for re-injection. Consequently, the reduction rate of net power output is larger than the reduction rate of produced CO_2 flow rate when the well distance increases. In addition, although the CO_2 production flow rate raises with the CO_2 injection flow rate increases, for the same well distance, the net power output increase gets slowly due to the CO_2 thermosiphon effect recedes when the CO_2 injection flow rate gets large (see RHS of Figure 2–17).

Table 5–12 Optimal direct turbine expansion thermodynamic results.

Direct Turbine Expansion						
Injection Flow Rate (kg/s)	Well Distance (m)	Net Power (MW_e)	Produced $\dot{m}_{CO_2}$ (kg/s)	System Thermal Efficiency (%)	System Exergy Efficiency (%)	Sys Specific Net Power (kW_e/(kg/s))
120	500	4.2793	98.17	13.62	64.90	43.59
	600	3.8634	92.48	12.69	62.73	41.78
	700	3.4890	87.67	11.98	61.26	39.80
	800	2.9663	75.63	11.76	61.61	39.22
	900	2.5491	68.26	11.10	60.65	37.34
240	600	7.3358	204.53	11.10	55.69	35.87
	700	6.5629	192.83	10.34	53.47	34.03
	800	5.9673	183.90	9.75	51.62	32.45
	900	5.2160	173.12	8.93	48.98	30.13
360	700	8.4676	305.77	8.59	46.99	27.69
	800	7.5692	292.17	7.88	44.26	25.91
	900	6.7936	277.98	7.37	42.29	24.44

With the optimal thermodynamic results in Table 5–13, for a 30 MW_e power plant with direct turbine expansion, the minimum LCOE of 0.276 $/kWh is obtained at the well distance of 600 m with 120 kg/s CO_2 injection flow rate for each well set. The total CO_2 injection flow rate of 960 kg/s is required which is implemented by 8 well sets. It needs to be mentioned that the turbine, compressor and cooler tubes are considered to be made of stainless steel in the direct turbine expansion approach, since the produced CO_2 directly contacted with the components mentioned above. Accordingly, the plant capital cost increases due to using the anti-corrosive materials, which possibly offsets some benefits from the simple configuration.

Table 5–13 Optimal direct turbine expansion cost estimation results.

Parameters	Units	Values
Injection CO_2 Flow Rate	kg/s	960 (120 each)
Optimal Well Distance	m	600
Needed Well Set #	-	8
Minimal Drilling Cost	$M	114.088
Exploration and Confirmation Cost	$M	11.700
Total Well Cost	**$M**	**125.788**
Separator Installed Cost (8)	$M	5.172
Turbine Installed Cost	$M	31.330
Compressor Installed Cost	$M	14.831
Cooling Water Chiller Installed Cost	$M	17.930
Pre-cooler Installed Cost (8)	$M	1.163
Post-cooler Installed Cost (8)	$M	1.296
Total Installed Plant Capital Cost	**$M**	**129.097**
Total Capital Cost with 15% Contingency	$M	274.250
Annual Fixed Capital Cost	$M	20.591
Capital Cost Contributing to LCOE	$/kWh	0.092
O&M Cost Contributing to LCOE	$/kWh	0.024
Add. O&M Cost for Cooling Contributing to LCOE	$/kWh	0.160
LCOE	**$/kWh**	**0.276**

It can be seen from the results above that the cooling O&M cost of $0.160/kWh is needed which contributes about 58.0% of the total LCOE. Due to re-injecting CO_2 back into the geothermal reservoirs, CO_2 has to be cooled down first then be compressed to the required injection well head pressure, which will significantly reduce the compression work. However, since the heat from massive amount of CO_2 needs to be rejected, the operation costs for cooling are high.

SCO_2 Brayton Cycle with Pre-compression and Inter-cooling

As selected from potential sCO_2 Brayton cycles with considering cycle improvement methods, the sCO_2 Brayton cycle with pre-compression and inter-cooling have the capability to generate a decent amount of power by taking advantage of the low compression work for CO_2 near its critical point. In addition, different from the direct turbine expansion system, the sCO_2 Brayton cycle is a closed cycle which is less affected by the CO_2 thermosiphon effect. In other words, it has flexibility for working with different well arrangements of geothermal heat mining systems as well as a more independent cycle optimization process. For instance, the turbine inlet pressure can be optimized in this closed cycle which doesn't work in the direct turbine expansion. Table 5–14 shows the optimal thermodynamic results for the sCO_2 Brayton Cycle with Pre-compression and Inter-cooling.

Table 5–14 Optimal sCO_2 Brayton cycle with pre-compression and inter-cooling thermodynamic results.

sCO_2 Brayton Cycle with Pre-compression and Inter-cooling						
Injection Flow Rate (kg/s)	Well Distance (m)	Net Power (MW_e)	Cycle $\dot{m}_{CO_2}$ (kg/s)	System Thermal Efficiency (%)	System Exergy Efficiency (%)	Cyc Specific Net Power (kW_e/(kg/s))
120	500	3.3403	98.78	10.63	49.00	33.82
	600	3.2404	93.73	10.64	50.43	34.57
	700	3.0784	88.77	10.57	51.51	34.68
	800	2.6604	76.69	10.54	52.12	34.69
	900	2.4258	68.36	10.57	53.95	35.49
240	600	6.7886	208.48	10.28	50.64	32.56
	700	6.6293	193.95	10.44	52.93	34.18
	800	6.3876	185.23	10.43	53.99	34.48
	900	5.9655	172.23	10.21	54.30	34.64
360	700	9.4163	306.12	9.55	51.59	30.76
	800	8.7829	292.68	9.14	50.49	30.01
	900	8.1180	278.37	8.80	49.57	29.16

The optimal LCOE of $0.330/kWh is presented in Table 5–15. It can be seen that a system which consists of more components eventually will have a significantly high capital cost.

Table 5–15 Optimal sCO_2 Brayton cycle with pre-compression and inter-cooling cost estimation results.

Parameters	Units	Values
Injection CO_2 Flow Rate	kg/s	1080 (120 each)
Optimal Well Distance	m	500
Needed Well Set #	-	9
Minimal Drilling Cost	$M	126.384
Exploration and Confirmation Cost	$M	11.700
Total Well Cost	**$M**	**138.084**
Separator Installed Cost (9)	$M	5.775
Turbine Installed Cost	$M	21.664
Cycle Pre-compressor Installed Cost	$M	7.040
Cycle Main Compressor Installed Cost	$M	15.132
Cooling Water Chiller Installed Cost	$M	22.515
IHX Installed Cost (9)	$M	8.445
Cycle Pre-cooler Installed Cost (9)	$M	1.184
Cycle Cooler Installed Cost (9)	$M	1.168
System Pre-cooler Installed Cost (9)	$M	1.799
Total Installed Plant Capital Cost	**$M**	**152.502**
Total Capital Cost with 15% Contingency	$M	313.460
Annual Fixed Capital Cost	$M	23.535
Capital Cost Contributing to LCOE	$/kWh	0.105
O&M Cost Contributing to LCOE	$/kWh	0.024
Add. O&M Cost for Cooling Contributing to LCOE	$/kWh	0.201
LCOE	**$/kWh**	**0.330**

Transcritical sCO_2 Cycle

The transcritical sCO_2 cycle with low turbine discharger pressure potentially can generate more electricity compared to a regular sCO_2 Brayton cycles. Even comparing to a sCO_2 Brayton cycle with an improvement method, such as with pre-compression and intercooling, the simple transcritical sCO_2 cycle can still generate more power as the results in Table 5–14 and Table 5–16 indicate. However, since the discharge cycle CO_2 has to be cooled down to a liquid region, remarkably a large amount of heat needs to be rejected, which increases the O&M cost.

Table 5–16 Optimal Transcritical sCO_2 Cycle thermodynamic results.

Transcritical sCO_2 Cycle Approach						
Injection Flow Rate (kg/s)	Well Distance (m)	Net Power (MW_e)	Cycle $\dot{m}_{CO_2}$ (kg/s)	System Thermal Efficiency (%)	System Exergy Efficiency (%)	Specific Net Power (kW_e/(kg/s))
120	500	3.7045	97.27	11.79	55.83	38.08
	600	3.5916	91.15	11.80	57.51	39.40
	700	3.3963	86.67	11.66	58.57	39.19
	800	2.9250	75.31	11.59	59.42	38.84
	900	2.6323	68.35	11.47	60.91	38.51
240	600	7.6716	200.36	11.61	58.11	38.29
	700	7.3516	188.81	11.58	59.61	38.94
	800	7.0652	179.98	11.54	60.71	39.26
	900	6.5878	170.89	11.28	61.24	38.55
360	700	10.6119	298.45	10.76	58.85	35.56
	800	9.8867	288.09	10.29	57.54	34.32
	900	9.1816	272.06	9.96	56.84	33.75

Table 5–17 presents the optimal design results for the transcritical sCO_2 power plant. Similarly, as a closed cycle, the cycle performance won't be significantly affected by the

CO_2 thermosiphon effect. Therefore, for the transcritical sCO_2 cycle approach, the injection well and re-injection well both have large injection flow rates which decreases well head pressure difference. Based on the results shown in Table 5–11, for same amount of produced CO_2, the minimum well costs are less for the cases with larger injection flow rates.

Table 5–17 Optimal Transcritical sCO_2 cost estimation results.

Parameters	Units	Values
Injection CO_2 Flow Rate	kg/s	960 (240 each)
Optimal Well Distance	m	600
Needed Well Set #	-	4
Minimal Drilling Cost	$M	91.984
Exploration and Confirmation Cost	$M	11.700
Total Well Cost	**$M**	**103.684**
Separator Installed Cost (4)	$M	3.988
Turbine Installed Cost	$M	14.967
Cycle Main Compressor Installed Cost	$M	16.342
Cooling Water Chiller Installed Cost	$M	21.246
IHX Installed Cost (4)	$M	7.895
Cycle Cooler Installed Cost (4)	$M	0.596
System Pre-cooler Installed Cost (4)	$M	1.170
Total Installed Plant Capital Cost	**$M**	**119.167**
Total Capital Cost with 15% Contingency	$M	240.725
Annual Fixed Capital Cost	$M	18.074
Capital Cost Contributing to LCOE	$/kWh	0.081
O&M Cost Contributing to LCOE	$/kWh	0.024
Add. O&M Cost for Cooling Contributing to LCOE	$/kWh	0.189
LCOE	**$/kWh**	**0.295**

5.2.3 ORC Simulation Results and Optimization

The subcritical ORC with R245fa as the working fluid has been used to represent the ORC option to utilize hot produced CO_2 from geothermal reservoirs with reasons and considerations emphasized in Section 4.5. Table 5–18 shows the optimal thermodynamic results for an ORC power generation system using hot produced CO_2 from geothermal reservoirs. The maximum net power output decreases when the well distance increases. Additionally, for a fixed well distance, when the CO_2 injection flow rate multiply gets large, the increasing rate of produced CO_2 flow rate is larger than this multiplier. However, the net power output increasing rate slightly decreases since the produced CO_2 temperature is lower for the higher CO_2 injection rate. Furthermore, for the results in the last four rows of Table 5–18, the production well head pressure is smaller than the injection well pressure and the additional compressor is installed. Consequently, system efficiencies decrease significantly.

Table 5–18 Optimal ORC thermodynamic results.

Subcritical ORC with R245fa						
Injection Flow Rate (kg/s)	Well Distance (m)	Net Power (MW_e)	$\dot{m}_{WF,\mathrm{R245fa}}$ (kg/s)	System Thermal Efficiency (%)	System Exergy Efficiency (%)	Specific Net Power (kW_e/(kg/s))
120	500	3.9410	93.49	12.5	56.1	42.15
	600	3.8422	91.14	12.6	57.7	42.16
	700	3.6013	85.43	12.4	58.0	42.15
	800	3.1004	73.55	12.3	58.0	42.15
	900	2.7726	65.77	12.1	58.3	42.16
240	600	8.0280	190.44	12.2	58.9	42.16
	700	7.6698	181.94	12.1	60.1	42.16
	800	7.3491	174.34	12.0	60.8	42.15
	900	6.8359	163.55	11.7	61.0	41.80
360	700	10.9088	291.07	11.1	58.9	37.48
	800	10.1843	264.73	10.6	57.9	38.47
	900	9.4154	252.63	10.2	56.7	37.27

Table 5–19 shows the optimal cost estimation results of the ORC power generation system. The ORC plant cost is extrapolated from the existing investment data. However, additional components should be installed for the geothermal loop to cool CO_2 down. The bare module costs for these components including coolers and cooling water chillers are calculated using the same techniques used in the sCO_2-based power cycle cost estimation. For the cases that the injection well pressure is greater than the production well pressure, an extra compressor is also indispensable. Then, the optimal LCOE of $0.316/kWh is obtained.

Table 5–19 Optimal ORC cost estimation results.

Parameters	Units	Values
Injection CO_2 Flow Rate	kg/s	960 (240 each)
Optimal Well Distance	m	700
Needed Well Set #	-	4
Minimal Drilling Cost	M$	88.486
Exploration and Confirmation Cost	M$	11.700
Total Well Cost	**M$**	**100.186**
Separator Installed Cost (4)	$M	3.986
Cooling Equipment for Geothermal Loop CO_2 Installed Cost	$M	7.041
ORC Plant Installed Cost	$M	73.153
Total Installed Plant Capital Cost	**$M**	**151.523**
Total Capital Cost with 15% Contingency	$M	274.437
Annual Fixed Capital Cost	$M	20.605
Capital Cost Contributing to LCOE	$/kWh	0.092
O&M Cost Contributing to LCOE	$/kWh	0.024
Add. Cooling Cost Contributing to LCOE	$/kWh	0.199
LCOE	**$/kWh**	**0.316**

5.3 Discussions and Comparisons of Different Power Generation Approaches

The direct turbine expansion benefits from the CO_2 thermosiphon effect which leads to low compression work and high net power output. Based on the geothermal heat mining parametric study in Chapter 2, with considering only the parameters of well distance and CO_2 injection rate, the smaller well distance and CO_2 injection rate tend to obtain the larger well head pressure difference. This phenomenon is known as CO_2 thermosiphon effect. Therefore, the direct turbine expansion has better cycle performance in the conditions of small well distance and injection CO_2 flow rate. Furthermore, the optimal LCOE of direct turbine expansion system is also achieved at these conditions, even more well sets are needed which leads to a high well cost. The reason the optimal LCOE is obtained at the well distance of 600 m but not 500 m is that larger amount of heat needs to be rejected with the well distance of 500 m which produces more CO_2. However, the direct contact with geothermal fluids eventually leads to a quit high plant capital cost since the costly corrosion-resistant material has to be used.

Obviously, ORC power system needs less produced sCO_2 since only four well sets are required and the well distance of 700 m is eligible that is also the largest well distance among all four cases, which leads to the lowest total well cost. However, its total plant capital cost is almost twice of the total well cost (see Table 5–20). The transcritical sCO_2 cycle has similar cost formation but with the cheapest plant construction cost.

Table 5–20 Cost estimation results of different power generation approaches.

Parameters	Units	Direct Expansion	sCO_2 Brayton	Transcritical sCO_2	ORC
Injection CO_2 Flow Rate	kg/s	960	1080	960	960
Optimal Well Distance	m	600	500	600	700
Well Set # Needed	-	8	9	4	4
Minimal Drilling Cost	$M	114.088	126.384	91.984	88.486
Exploration and Confirmation Cost	$M	11.700	11.700	11.700	11.700
Total Well Cost	**$M**	**125.788**	**138.084**	**103.684**	**100.186**
Total Installed Plant Capital Cost	**$M**	**129.097**	**152.502**	**119.167**	**151.523**
Total Capital Cost with 15% Contingency	$M	274.250	313.460	240.725	274.437
Annual Fixed Capital Cost	$M	20.591	23.535	18.074	20.605
Capital Cost Contributing to LCOE	$M	0.092	0.105	0.081	0.092
O&M Cost Contributing to LCOE	$/kWh	0.024	0.024	0.024	0.024
Cooling O&M Cost Contributing to LCOE	$/kWh	0.160	0.201	0.189	0.199
LCOE	**$/kWh**	**0.276**	**0.330**	**0.295**	**0.316**

Cost studies for conventional geothermal power generation were performed and well-validated cost data were presented by the National Renewable Energy Laboratory (NREL) in the U.S. The Cost of Renewable Energy Spreadsheet Toll (CREST) is an economic cash flow model developed at NREL [110]. The results carried out from the CREST indicate a LCOE of $0.078/kWh in the low-cost case and to $0.10/kWh in the high-cost case for a conventional geothermal power plant. However, this range is not necessary to present a lower or an upper bound for any particular geothermal project. In addition, the U.S. DOE developed another tool named Geothermal Electricity Technologies Evaluation Model

(GETEM). The GETEM gives a LCOE of \$0.109/kWh for a 30 MW_e hydro-flash conventional geothermal power plant [111]. Nevertheless, the LCOEs obtained in this study are still higher compared to the conventional geothermal power plant without considering the CO_2 credits. If the lower bound LCOE of \$0.078/kWh for conventional geothermal power plant is used to compare with the LCOEs of state-of-the-art power generation technologies, the LCOE differences are plotted in Figure 5–6 for each type of the proposed power generation technology.

Figure 5–6 shows that the breakeven points of counted CO_2 credit for direct turbine expansion, sCO_2 Brayton cycle, transcritical sCO_2 cycle and ORC are \$1.46/t, \$1.86/t, \$1.60/t and \$1.76/t respectively. When the counted CO_2 credits for geothermal CO_2-based power generation systems are larger than the breakeven points, the CO_2-based plants are more cost-effective than the steam based plants. In addition, geothermal CO_2-based power generation systems have ability to sequestrate CO_2 permanently.

Excluding CO_2 transportation and storage, the electricity production price ranges from \$0.04/kWh to \$0.09/kWh for fossil-fired power plants with carbon capture. If no capture, the range is from \$0.03/kWh to \$0.06/kWh. The estimated cost of CO_2 due to capture is \$41/t for a PC plant and \$53/t for a NGCC plant [112]. The new 45Q tax code in the U.S. offers \$50/t credit for saline CO_2 sequestration which was introduced in 2017 [113]. Any new fossil-fuel power plant or carbon-dioxide producing industry that commences construction before 2024 is eligible for tax credits for up to 12 years (a time cap on the credits). It can be seen that the difference between \$50/t credit offered by 45Q and \$41/t of a PC plant capture cost is enough to exceed the breakeven points mentioned previously,

which means with CO_2 tax credits, power generation technologies proposed in this study are competitive with conventional geothermal power plants.

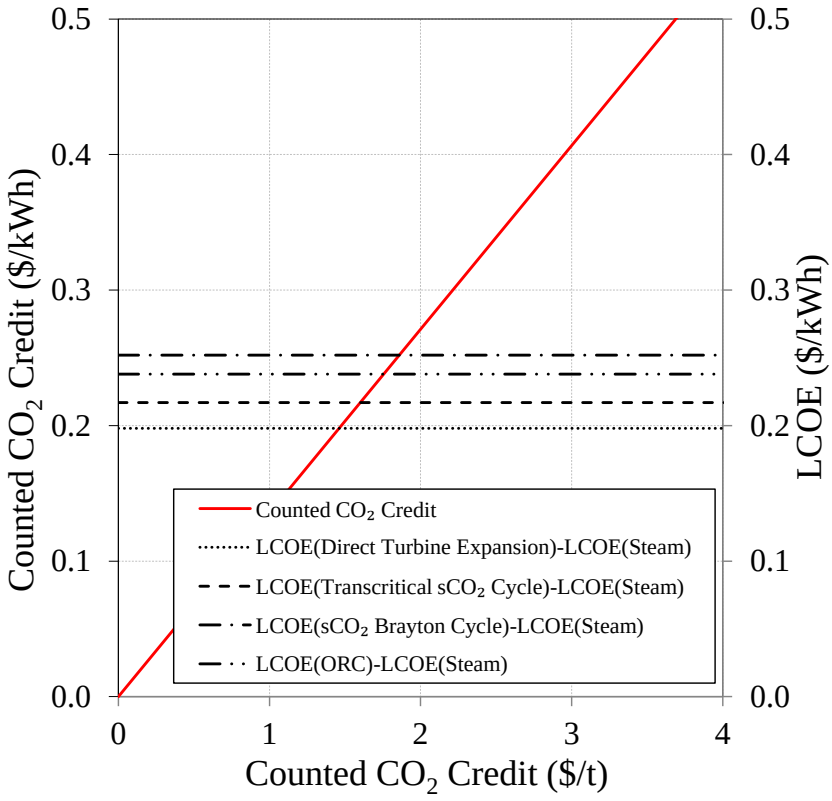

Figure 5–6 CO_2 credits and difference in LCOE for geothermal CO_2-based and geothermal steam-based power plants.

Figure 5–7 shows the LCOEs of four promising power generation approaches change with the plant capacity. When the plant size is below 30 MW_e, the LCOE is significantly affected by the well cost. However, due to the discrete well cost data points used in this analysis, the drastic fluctuation happens with the net power output below 30 MW_e. When the plant size is over 30 MW_e, the LCOEs keep constant and are unaffected by, or even unrelated to, the total plant capacity. It indicates the direct turbine expansion is the best choice to convert the geothermal heat carried by sCO_2 from geothermal reservoirs. It is because not only the direct turbine expansion directly converts the energy, but also it takes

the advantage of the CO_2 thermosiphon effect to end up with a large net power output. However, due to the direct contact with geothermal fluid which potentially contains corrosive substance even with separation devices, high anti-corrosive and expensive materials are indispensable to build turbines, compressors and HXs.

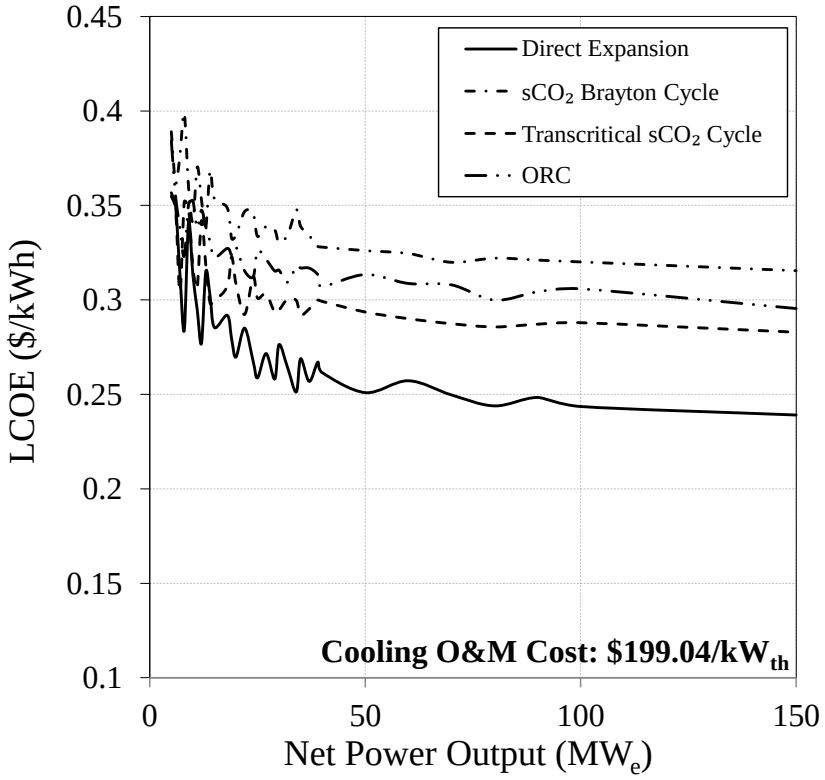

Figure 5–7 LCOE of different power generation approaches with cooling O&M cost of $199.04/$kW_{th}$.

Regarding the O&M cost for cooling process, other possible cooling techniques may be capable to reject heat at a lower cost. If the O&M cost of cooling load reduces to one quarter of the original cost, Figure 5–8 shows the LCOEs of these four power generation options are in the range of \$0.15/kWh to \$0.18/kWh for a plant of 30 MW_e. Therefore, it is necessary to examine the alternative way for heat rejection techniques for the proposed

power generation system since the cooling need is very critical to the system performance as well as the economy.

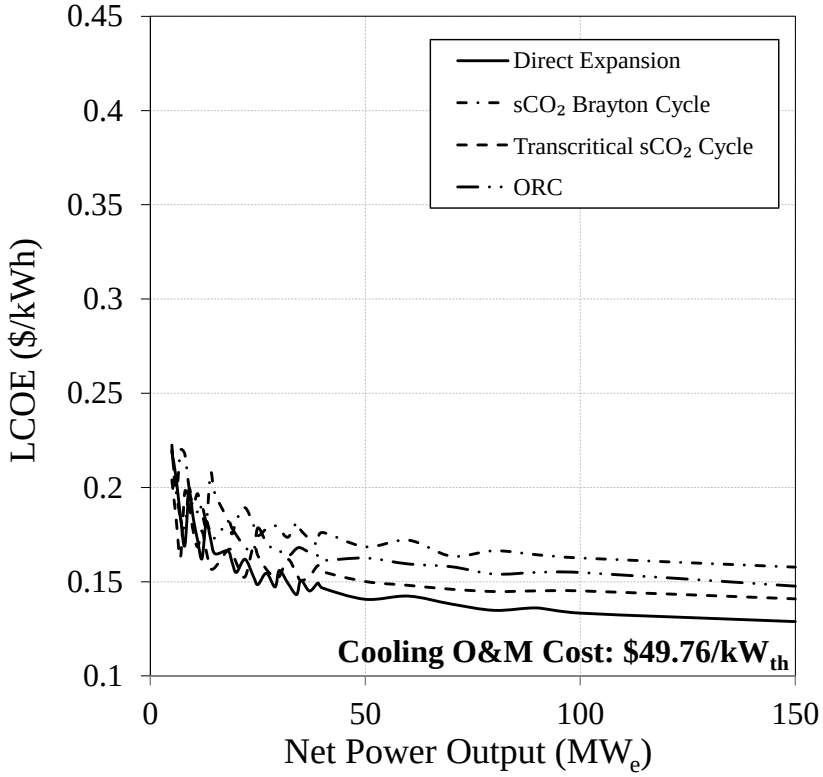

Figure 5–8 LCOE of different power generation approaches with cooling O&M cost of $\$49.76/kW_{th}$.

The results indicate the direct expansion approach is the most cost-effective among the proposed technologies in this study. If cooling techniques with lower O&M costs are available, they will be more competitive to conventional geothermal power plants.

Chapter 6 Conclusions and Recommendations

Detailed parametric study for the geothermal heat mining simulation using sCO_2 with TOUGH2 simulator has been conducted and the results are discussed in this research. Two parameters, the well distance and CO_2 injection flow rate, which are very critical to the production rate, temperature, pressure of the produced hot sCO_2 have been selected to generate a data set for the further global cost estimation and system optimization. It has been found that the CO_2 injection flow rate and well distance can have significant impacts on the well cost since a larger injection flow rate can lead to a higher drilling cost with a larger well diameter. On the contrary, a smaller well distance leads to a larger production flow rate but which may need a larger diameter production well. In a word, changes of these two parameters can result in different CO_2 production rates, CO_2 production temperatures and pressures, which eventually affect the thermal performance of the power generation systems.

As hot sCO_2 produced from geothermal reservoirs is the heat source carrying geothermal energy from the subsurface, sCO_2 power cycles have been comprehensively investigated due to the advantages of direct expansion cycle for direct utilizing produced sCO_2 with simple design as well as closed cycles for using the same working fluid without a pinch point. CO_2 physical properties near its critical point have been examined regarding the impacts on power cycle performance. The direct expansion, sCO_2 Brayton cycle with pre-compression and inter-cooling, and transcritical sCO_2 cycle have been selected for the cost estimation and optimization analyses. On the other hand, ORC is also a promising way to convert low grade heat into electricity which has been widely recognized. Working fluid

selection criteria have been proposed and thirty potential working fluids have been screened. Furthermore, subcritical ORC, superheated ORC, and supercritical ORC have been considered and the most suitable working fluids have been selected for each layout:

- Subcritical: R236ea, R600a (flammable), R600 (flammable), R245fa.
- Superheated: R600a (flammable), R152a, R142b, R236ea, R600 (flammable).
- Supercritical: R143a, R32, R600a (flammable), R22.

The geothermal heat mining simulation data set and four different power generation approaches, including sCO_2 direct expansion, sCO_2 Brayton cycle, transcritical sCO_2 cycle and ORC, are subjects of cost estimation and optimization. The cost estimation and optimization analyses have been accomplished by finding the minimum LCOE for a nominal power plant capacity of 30 MW_e for the power generation approaches mentioned above. However, as sCO_2-based power cycle is a non-commercialized-yet technology, the detailed cost study has been performed with calculating the bare module costs of all components. For ORC, actual investment data have been collected to extrapolate its installed capital cost. Table 6–1 summarizes the optimal LCOEs of four promising power generation options.

Table 6–1 LCOEs for power plants of 30 MW_e capacity.

Parameters	Units	Direct Expansion	sCO_2 Brayton	Transcritical	ORC
Injection CO_2 Flow Rate	kg/s	960	1200	960	960
Optimal Well Distance	m	500	800	600	700
Well Set # Needed	-	8	5	4	4
Total Well Cost	**$M**	**125.788**	**138.084**	**103.684**	**100.186**
Total Installed Plant Capital Cost	**$M**	**129.097**	**152.502**	**119.167**	**151.523**
LCOE without CO_2 Credit	**$/kWh**	**0.276**	**0.330**	**0.295**	**0.316**
LCOE with CO_2 Credit of $2/t	**$/kWh**	**0.005**	**0.059**	**0.024**	**0.045**

It has to be mentioned, about more than haft portion of these LCOEs is contributed by the O&M of additional cooling for heat rejections of these up-to-date cycles and CO_2 re-injection. From cost estimation results, it has been found that the compressor-based cooling technology is cost-effective to purchase but not economic for the long term running. Therefore, if the O&M cost is reduced to one quarter of the original value, the LCOEs of these four technologies range from $0.15/kWh to $0.18/kWh without counting CO_2 credit.

If the lower bound LCOE of $0.078/kWh for conventional geothermal power plant is used to compare with the LCOEs of novel power generation technologies, there are still up to $0.25/kWh differences. However, with counted $2/t CO_2 credit, the power generation technologies proposed in this study are more cost-effective and competitive than conventional geothermal power plants as well as have benefits of permanently sequestrated CO_2 from fossil-fired power plants.

As mentioned previously, the geothermal heat mining simulation is very time intensive and only discrete results can be obtained for the optimization with considering two dominate parameters in this study. Cost estimating results indicate the cooling O&M costs significantly affect the plant LCOE, which makes using higher temperature CO_2 at the re-injection well head possible to eliminate the considerable cooling loads to reduce the LCOE. Therefore, more detailed geothermal heat mining simulation and optimization analyses are necessary to be performed for obtaining the most optimized results. In addition, other options of cooling techniques are imperative to be investigated to reduce power cost. Moreover, system optimizations can be performed on considering adding bottom cycle and combining different types of power cycles which would be the prospective work proposed in this study.

List of References

[1] B. Matek, "The manageable risks of conventional hydrothermal geothermal power systems," *Geothermal Energy Association*, 2014.

[2] K. Pruess, "Enhanced geothermal systems (EGS) using CO_2 as working fluid—A novel approach for generating renewable energy with simultaneous sequestration of carbon," *Geothermics*, vol. 35, no. 4, pp. 351-367, 2006.

[3] M. Smith, R. L. Aamodt, R. M. Potter, and D. Brown, "Man-made geothermal reservoirs," Los Alamos Scientific Lab., N. Mex.(USA)1975.

[4] P. Olasolo, M. Juárez, M. Morales, and I. Liarte, "Enhanced geothermal systems (EGS): A review," *Renewable and Sustainable Energy Reviews*, vol. 56, pp. 133-144, 2016.

[5] C. Baujard, A. Genter, J.-J. Graff, V. Maurer, and E. Dalmais, "ECOGI, a new deep EGS project in Alsace, Rhine Graben, France," in *Proceedings World Geothermal Congress*, 2015, pp. 19-25.

[6] B. Bendall, R. Hogarth, H. Holl, A. McMahon, A. Larking, and P. Reid, "Australian experiences in EGS permeability enhancement–a review of 3 case studies," in *Thirty-Ninth Workshop on Geothermal Reservoir Engineering, Stanford University, California*, 2014.

[7] D. Chen and D. Wyborn, "Habanero field tests in the Cooper Basin, Australia: a proof-of-concept for EGS," *Geothermal Resources Council Transactions*, vol. 33, no. 1, pp. 159-164, 2009.

[8] N. Cuenot, C. Dorbath, and L. Dorbath, "Analysis of the microseismicity induced by fluid injections at the EGS site of Soultz-sous-Forêts (Alsace, France): implications for the characterization of the geothermal reservoir properties," *Pure and Applied Geophysics*, vol. 165, no. 5, pp. 797-828, 2008.

[9] J. W. Tester *et al.*, "The future of geothermal energy: Impact of enhanced geothermal systems (EGS) on the United States in the 21st century," *Massachusetts Institute of Technology*, vol. 209, 2006.

[10] C. Dezayes, A. Genter, and S. Gentier, "Fracture network of the EGS geothermal reservoir at Soultz-sous-Forêts (Rhine Graben, France)," *Geotherm. Resour. Council Trans,* vol. 28, pp. 213-218, 2004.

[11] S.-M. Lu, "A global review of enhanced geothermal system (EGS)," *Renewable and Sustainable Energy Reviews,* vol. 81, no. P2, pp. 2902-2921, 2018.

[12] J. B. Randolph and M. O. Saar, "Coupling carbon dioxide sequestration with geothermal energy capture in naturally permeable, porous geologic formations: Implications for CO_2 sequestration," *Energy Procedia,* vol. 4, pp. 2206-2213, 2011.

[13] A. R. Mohan, U. Turaga, V. Shembekar, D. Elsworth, and S. V. Pisupati, "Utilization of carbon dioxide from coal-based power plants as a heat transfer fluid for electricity generation in enhanced geothermal systems (EGS)," *Energy,* vol. 57, pp. 505-512, 2013.

[14] D. W. Brown, "Geothermal power production utilizing supercritical CO_2 combined with deep earth carbon sequestration.," *Abstracts of Papers of the American Chemical Society,* vol. 220, pp. U399-U399, Aug 20 2000.

[15] K. Pruess, "Enhanced Geothermal Systems (EGS) comparing water with CO_2 as heattransmission fluids," Ernest Orlando Lawrence Berkeley NationalLaboratory, Berkeley, CA (US)2007.

[16] H. Gurgenci, "Challenges for electrical power generation from EGS," in *Proceedings World Geothermal Congress, Bali, Indonesia*, 2010.

[17] A. D. Atrens, H. Gurgenci, and V. Rudolph, "CO_2 Thermosiphon for Competitive Geothermal Power Generation," *Energy & Fuels,* vol. 23, no. 1, pp. 553-557, Jan-Feb 2009.

[18] K. Pruess, "On production behavior of enhanced geothermal systems with CO_2 as working fluid," *Energy Conversion and Management,* vol. 49, no. 6, pp. 1446-1454, 2008.

[19] N. Garapati, J. B. Randolph, and M. O. Saar, "Brine displacement by CO_2 , energy extraction rates, and lifespan of a CO_2 -limited CO_2 -Plume Geothermal (CPG) system with a horizontal production well," *Geothermics,* vol. 55, pp. 182-194, 2015.

[20] B. M. Adams, T. H. Kuehn, J. M. Bielicki, J. B. Randolph, and M. O. Saar, "A comparison of electric power output of CO_2 Plume Geothermal (CPG) and brine geothermal systems for varying reservoir conditions," *Applied Energy,* vol. 140, pp. 365-377, 2015.

[21] B. M. Adams, T. H. Kuehn, J. M. Bielicki, J. B. Randolph, and M. O. Saar, "On the importance of the thermosiphon effect in CPG (CO_2 plume geothermal) power systems," *Energy,* vol. 69, pp. 409-418, 2014.

[22] L. Zhang, G. D. Cui, Y. Zhang, B. Ren, S. R. Ren, and X. H. Wang, "Influence of pore water on the heat mining performance of supercritical CO_2 injected for geothermal development," *Journal of Co2 Utilization,* vol. 16, pp. 287-300, Dec 2016.

[23] K. Pruess, "The TOUGH codes—a family of simulation tools for multiphase flow and transport processes in permeable media," *Vadose Zone Journal,* vol. 3, no. 3, pp. 738-746, 2004.

[24] K. Pruess and N. Spycher, "ECO2N - A fluid property module for the TOUGH2 code for studies of CO_2 storage in saline aquifers," *Energy Conversion and Management,* vol. 48, no. 6, pp. 1761-1767, Jun 2007.

[25] L. Pan, N. Spycher, C. Doughty, and K. Pruess, "ECO2N V2.0: A TOUGH2 fluid property module for modeling CO_2-H_2O-NACl systems to elevated temperatures of up to 300 degrees C," *Greenhouse Gases-Science and Technology,* vol. 7, no. 2, pp. 313-327, Apr 2017.

[26] L. Pan, "T2Well/ECO2N version 1.0: multiphase and non-isothermal model for coupled wellbore-reservoir flow of carbon dioxide and variable salinity water," 2011.

[27] L. H. Pan and C. M. Oldenburg, "T2Well-An integrated wellbore-reservoir simulator," *Computers & Geosciences,* vol. 65, pp. 46-55, Apr 2014.

[28] C. J. Pan, O. Chavez, C. E. Romero, E. K. Levy, A. A. Corona, and C. Rubio-Maya, "Heat mining assessment for geothermal reservoirs in Mexico using supercritical CO_2 injection," *Energy,* vol. 102, pp. 148-160, May 1 2016.

[29] E. G. Feher, "The supercritical thermodynamic power cycle," *Energy conversion,* vol. 8, no. 2, pp. 85-90, 1968.

[30] G. Angelino, "Carbon dioxide condensation cycles for power production," *Journal of Engineering for Power,* vol. 90, no. 3, pp. 287-295, 1968.

[31] V. Dostal, M. J. Driscoll, and P. Hejzlar, "A supercritical carbon dioxide cycle for next generation nuclear reactors," Massachusetts Institute of Technology, Department of Nuclear Engineering, 2004.

[32] V. Dostal, P. Hejzlar, and M. J. Driscoll, "The supercritical carbon dioxide power cycle: comparison to other advanced power cycles," *Nuclear technology,* vol. 154, no. 3, pp. 283-301, 2006.

[33] S. J. Bae, J. Lee, Y. Ahn, and J. I. Lee, "Preliminary studies of compact Brayton cycle performance for Small Modular High Temperature Gas-cooled Reactor system," *Annals of Nuclear Energy,* vol. 75, pp. 11-19, 2015.

[34] W. S. Jeong and Y. H. Jeong, "Performance of supercritical Brayton cycle using CO_2-based binary mixture at varying critical points for SFR applications," *Nuclear Engineering and Design,* vol. 262, pp. 12-20, 2013.

[35] H. J. Yoon, Y. Ahn, J. I. Lee, and Y. Addad, "Potential advantages of coupling supercritical CO_2 Brayton cycle to water cooled small and medium size reactor," *Nuclear Engineering and Design,* vol. 245, pp. 223-232, 2012.

[36] W. S. Jeong, J. I. Lee, and Y. H. Jeong, "Potential improvements of supercritical recompression CO_2 Brayton cycle by mixing other gases for power conversion system of a SFR," *Nuclear Engineering and Design,* vol. 241, no. 6, pp. 2128-2137, 2011.

[37] A. Moisseytsev and J. J. Sienicki, "Investigation of alternative layouts for the supercritical carbon dioxide Brayton cycle for a sodium-cooled fast reactor," *Nuclear Engineering and Design,* vol. 239, no. 7, pp. 1362-1371, 2009.

[38] T. Neises and C. Turchi, "A Comparison of Supercritical Carbon Dioxide Power Cycle Configurations with an Emphasis on CSP Applications," *Energy Procedia,* vol. 49, pp. 1187-1196, 2014.

[39] Z. Bai, G. Zhang, Y. Li, G. Xu, and Y. Yang, "A supercritical CO_2 Brayton cycle with a bleeding anabranch used in coal-fired power plants," *Energy,* vol. 142, pp. 731-738, 2018.

[40] S. Park, J. Kim, M. Yoon, D. Rhim, and C. Yeom, "Thermodynamic and economic investigation of coal-fired power plant combined with various supercritical CO_2 Brayton power cycle," *Applied Thermal Engineering,* vol. 130, pp. 611-623, 2018.

[41] M. Mecheri and Y. Le Moullec, "Supercritical CO_2 Brayton cycles for coal-fired power plants," *Energy,* vol. 103, pp. 758-771, 2016.

[42] Y. Le Moullec, "Conception of a Pulverized Coal Fired Power Plant with Carbon Capture around a Supercritical Carbon Dioxide Brayton Cycle," *Energy Procedia,* vol. 37, pp. 1180-1186, 2013.

[43] Y. Le Moullec, "Conceptual study of a high efficiency coal-fired power plant with CO_2 capture using a supercritical CO_2 Brayton cycle," *Energy,* vol. 49, pp. 32-46, 2013.

[44] O. Sharma, S. Kaushik, and K. Manjunath, "Thermodynamic analysis and optimization of a supercritical CO_2 regenerative recompression Brayton cycle coupled with a marine gas turbine for shipboard waste heat recovery," *Thermal Science and Engineering Progress,* vol. 3, pp. 62-74, 2017.

[45] B. D. Iverson, T. M. Conboy, J. J. Pasch, and A. M. Kruizenga, "Supercritical CO2 Brayton cycles for solar-thermal energy," *Applied Energy,* vol. 111, pp. 957-970, 2013.

[46] Y. Ahn *et al.*, "Review of supercritical CO_2 power cycle technology and current status of research and development," *Nuclear Engineering and Technology,* vol. 47, no. 6, pp. 647-661, 2015.

[47] C. S. Turchi, Z. Ma, T. W. Neises, and M. J. Wagner, "Thermodynamic study of advanced supercritical carbon dioxide power cycles for concentrating solar power systems," *Journal of Solar Energy Engineering,* vol. 135, no. 4, p. 041007, 2013.

[48] J. Wang, J. Wang, Y. Dai, and P. Zhao, "Thermodynamic analysis and optimization of a transcritical CO2 geothermal power generation system based on the cold

energy utilization of LNG," *Applied Thermal Engineering*, vol. 70, no. 1, pp. 531-540, 2014.

[49] X. Wang and Y. Dai, "Exergoeconomic analysis of utilizing the transcritical CO_2 cycle and the ORC for a recompression supercritical CO_2 cycle waste heat recovery: A comparative study," *Applied Energy*, vol. 170, pp. 193-207, 2016.

[50] Y. M. Kim, C. G. Kim, and D. Favrat, "Transcritical or supercritical CO_2 cycles using both low- and high-temperature heat sources," *Energy*, vol. 43, no. 1, pp. 402-415, 2012.

[51] Y. Song, J. Wang, Y. Dai, and E. Zhou, "Thermodynamic analysis of a transcritical CO_2 power cycle driven by solar energy with liquified natural gas as its heat sink," *Applied energy*, vol. 92, pp. 194-203, 2012.

[52] S. J. Zhang, H. X. Wang, and T. Guo, "Performance comparison and parametric optimization of subcritical Organic Rankine Cycle (ORC) and transcritical power cycle system for low-temperature geothermal power generation," *Applied Energy*, vol. 88, no. 8, pp. 2740-2754, Aug 2011.

[53] T. Guo, H. Wang, and S. Zhang, "Comparative analysis of CO2-based transcritical Rankine cycle and HFC245fa-based subcritical organic Rankine cycle using low-temperature geothermal source," *Science China Technological Sciences*, vol. 53, no. 6, pp. 1638-1646, 2010.

[54] S. G. Kim, Y. J. Kim, G. Lee, and M. S. Kim, "The performance of a transcritical CO_2 cycle with an internal heat exchanger for hot water heating," *International Journal of Refrigeration*, vol. 28, no. 7, pp. 1064-1072, 2005.

[55] Y. Chen, P. Lundqvist, A. Johansson, and P. Platell, "A comparative study of the carbon dioxide transcritical power cycle compared with an organic Rankine cycle with R123 as working fluid in waste heat recovery," *Applied thermal engineering*, vol. 26, no. 17-18, pp. 2142-2147, 2006.

[56] X. Li, H. Huang, and W. Zhao, "A supercritical or transcritical Rankine cycle with ejector using low-grade heat," *Energy Conversion and Management*, vol. 78, pp. 551-558, 2014.

[57] E. Ruiz-Casanova, A. L. Soto-Sánchez, C. Rubio-Maya, C. E. Romero, and E. K. Levy, "Use of Supercritical CO_2 Heated With Geothermal Energy for Power Production Through Direct Expansion and Heat Supply to an ORC Cycle," in *ASME 2017 International Mechanical Engineering Congress and Exposition*, 2017, pp. V006T08A018-V006T08A018: American Society of Mechanical Engineers.

[58] S. A. Wright, R. F. Radel, M. E. Vernon, G. E. Rochau, and P. S. Pickard, "Operation and analysis of a supercritical CO_2 Brayton cycle," *Sandia Report, No. SAND2010-0171*, 2010.

[59] A. D. Atrens, H. Gurgenci, and V. Rudolph, "Economic Optimization of a CO_2-Based EGS Power Plant," *Energy & Fuels*, vol. 25, no. 8, pp. 3765-3775, Aug 2011.

[60] A. Kouta, F. Al-Sulaiman, M. Atif, and S. B. Marshad, "Entropy, exergy, and cost analyses of solar driven cogeneration systems using supercritical CO2 Brayton cycles and MEE-TVC desalination system," *Energy Conversion and Management*, vol. 115, pp. 253-264, 2016.

[61] M. Driscoll, "Supercritical CO_2 Plant Cost Assessment," *Center for Advanced Nuclear Energy Systems, MIT Nuclear Engineering Department, Massachusetts Institute of Technology, Cambridge, MA, Report No. MIT-GFR-019*, 2004.

[62] U. Drescher and D. Brüggemann, "Fluid selection for the Organic Rankine Cycle (ORC) in biomass power and heat plants," *Applied Thermal Engineering*, vol. 27, no. 1, pp. 223-228, 2007.

[63] E. H. Wang, H. G. Zhang, B. Y. Fan, M. G. Ouyang, Y. Zhao, and Q. H. Mu, "Study of working fluid selection of organic Rankine cycle (ORC) for engine waste heat recovery," *Energy*, vol. 36, no. 5, pp. 3406-3418, May 2011.

[64] R. Rayegan and Y. X. Tao, "A procedure to select working fluids for Solar Organic Rankine Cycles (ORCs)," *Renewable Energy*, vol. 36, no. 2, pp. 659-670, 2011.

[65] J. Martinez-Gomez, J. Pena-Lamas, M. Martin, and J. M. Ponce-Ortega, "A multi-objective optimization approach for the selection of working fluids of geothermal facilities: Economic, environmental and social aspects," *J Environ Manage*, Jul 17 2017.

[66] N. B. Desai and S. Bandyopadhyay, "Thermo-economic analysis and selection of working fluid for solar organic Rankine cycle," *Applied Thermal Engineering,* vol. 95, pp. 471-481, Feb 25 2016.

[67] H. S. Yu, X. Feng, and Y. F. Wang, "A new pinch based method for simultaneous selection of working fluid and operating conditions in an ORC (Organic Rankine Cycle) recovering waste heat," (in English), *Energy,* vol. 90, pp. 36-46, Oct 2015.

[68] A. Sakhrieh, W. Shreim, H. Fakhruldeen, H. Hasan, and A. Al-Salaymeh, "Combined Solar-Geothermal Power Generation using Organic Rankine Cycle," (in English), *Jordan Journal of Mechanical and Industrial Engineering,* vol. 10, no. 1, pp. 1-9, Mar 2016.

[69] H. S. Yu, X. Feng, and Y. F. Wang, "Working Fluid Selection for Organic Rankine Cycle (ORC) Considering the Characteristics of Waste Heat Sources," (in English), *Industrial & Engineering Chemistry Research,* vol. 55, no. 5, pp. 1309-1321, Feb 10 2016.

[70] B. Saleh, G. Koglbauer, M. Wendland, and J. Fischer, "Working fluids for low-temperature organic Rankine cycles," *Energy,* vol. 32, no. 7, pp. 1210-1221, Jul 2007.

[71] J. Sarkar, "Property-based selection criteria of low GWP working fluids for organic Rankine cycle," *Journal of the Brazilian Society of Mechanical Sciences and Engineering,* vol. 39, no. 4, pp. 1419-1428, Apr 2017.

[72] C. Guo, X. Z. Du, D. Y. Goswami, and L. J. Yang, "Investigation on working fluids selection for organic rankine cycles with low-temperature heat sources," *International Journal of Green Energy,* vol. 13, no. 6, pp. 556-565, 2016.

[73] J. Frutiger *et al.,* "Working fluid selection for organic Rankine cycles - Impact of uncertainty of fluid properties," *Energy,* vol. 109, pp. 987-997, Aug 15 2016.

[74] J. Li, J. Z. Alvi, G. Pei, J. Ji, P. Li, and H. Fu, "Effect of working fluids on the performance of a novel direct vapor generation solar organic Rankine cycle system," *Applied Thermal Engineering,* vol. 98, pp. 786-797, 2016.

[75] A. Algieri and P. Morrone, "Comparative energetic analysis of high-temperature subcritical and transcritical Organic Rankine Cycle (ORC). A biomass application in the Sibari district," *Applied Thermal Engineering,* vol. 36, pp. 236-244, 2012.

[76] H. Chen, D. Y. Goswami, and E. K. Stefanakos, "A review of thermodynamic cycles and working fluids for the conversion of low-grade heat," *Renewable and Sustainable Energy Reviews,* vol. 14, no. 9, pp. 3059-3067, 2010.

[77] Z. Shengjun, W. Huaixin, and G. Tao, "Performance comparison and parametric optimization of subcritical Organic Rankine Cycle (ORC) and transcritical power cycle system for low-temperature geothermal power generation," *Applied Energy,* vol. 88, no. 8, pp. 2740-2754, 2011.

[78] D. Maraver, J. Royo, V. Lemort, and S. Quoilin, "Systematic optimization of subcritical and transcritical organic Rankine cycles (ORCs) constrained by technical parameters in multiple applications," *Applied energy,* vol. 117, pp. 11-29, 2014.

[79] X. H. Liu, Y. F. Zhang, and J. Shen, "System performance optimization of ORC-based geo-plant with R245fa under different geothermal water inlet temperatures," (in English), *Geothermics,* vol. 66, pp. 134-142, Mar 2017.

[80] C. Guo, X. Du, L. Yang, and Y. Yang, "Performance analysis of organic Rankine cycle based on location of heat transfer pinch point in evaporator," *Applied Thermal Engineering,* vol. 62, no. 1, pp. 176-186, 2014.

[81] M. Astolfi, M. C. Romano, P. Bombarda, and E. Macchi, "Binary ORC (Organic Rankine Cycles) power plants for the exploitation of medium low temperature geothermal sources - Part B: Techno-economic optimization," (in English), *Energy,* vol. 66, pp. 435-446, Mar 1 2014.

[82] M. Astolfi, M. C. Romano, P. Bombarda, and E. Macchi, "Binary ORC (organic Rankine cycles) power plants for the exploitation of medium–low temperature geothermal sources–Part A: Thermodynamic optimization," *Energy,* vol. 66, pp. 423-434, 2014.

[83] D. Walraven, B. Laenen, and W. D'haeseleer, "Minimizing the levelized cost of electricity production from low-temperature geothermal heat sources with ORCs: water or air cooled?," *Applied Energy*, vol. 142, pp. 144-153, 2015.

[84] K. A. Barse and M. D. Mann, "Maximizing ORC performance with optimal match of working fluid with system design," (in English), *Applied Thermal Engineering*, vol. 100, pp. 11-19, May 5 2016.

[85] M. H. Yang and R. H. Yeh, "Economic performances optimization of an organic Rankine cycle system with lower global warming potential working fluids in geothermal application," (in English), *Renewable Energy*, vol. 85, pp. 1201-1213, Jan 2016.

[86] K. Pruess, C. Oldenburg, and G. Moridis, "TOUGH2 user's guide version 2," Ernest Orlando Lawrence Berkeley National Laboratory, Berkeley, CA (US)1999.

[87] L. H. Pan, S. W. Webb, and C. M. Oldenburg, "Analytical solution for two-phase flow in a wellbore using the drift-flux model," *Advances in Water Resources*, vol. 34, no. 12, pp. 1656-1665, Dec 2011.

[88] H. Shi *et al.*, "Drift-flux modeling of two-phase flow in wellbores," *Spe Journal*, vol. 10, no. 01, pp. 24-33, 2005.

[89] E. K. Levy, X. Wang, C. Pan, C. E. Romero, and C. R. Maya, "Use of hot supercritical CO_2 produced from a geothermal reservoir to generate electric power in a gas turbine power generation system," *Journal of CO_2 Utilization*, vol. 23, pp. 20-28, 2018.

[90] E. W. Lemmon, M. L. Huber, and M. O. McLinden, "NIST reference fluid thermodynamic and transport properties–REFPROP," ed.

[91] B. T. Liu, K. H. Chien, and C. C. Wang, "Effect of working fluids on organic Rankine cycle for waste heat recovery," *Energy*, vol. 29, no. 8, pp. 1207-1217, Jun 2004.

[92] C. Invernizzi, P. Iora, and P. Silva, "Bottoming micro-Rankine cycles for micro-gas turbines," *Applied Thermal Engineering*, vol. 27, no. 1, pp. 100-110, 2007.

[93] A. Plus, "Aspen technology," *Inc., version*, vol. 11, 2009.

[94] C. N. Hance, "Factors affecting costs of geothermal power development," *Geothermal Energy Association for the US Department of Energy*, vol. 209, 2005.

[95] A. Kagel, "A handbook on the externalities, employment, and economics of geothermal energy," *Geothermal Energy Association, Washington, DC*, 2006.

[96] R. Turton, *Analysis, synthesis, and design of chemical processes*, 2nd ed. (Prentice-Hall international series in the physical and chemical engineering sciences). Upper Saddle River, N.J.: Prentice Hall/PTR, 2003, pp. xxxi, 987 p.

[97] H. Silla, *Chemical process engineering: design and economics*. CRC Press, 2003.

[98] D. L. McCollum and J. M. Ogden, "Techno-economic models for carbon dioxide compression, transport, and storage & correlations for estimating carbon dioxide density and viscosity," 2006.

[99] D. Morris, "RSMeans mechanical cost data," *40th annual edition, Cordian RSMeans Data, Rockland, MA*, 2017.

[100] J. Charles, "Communications with Sales Rep from Mueller Environmental Designs, Inc.," *http://www.muellerenvironmental.com/*, 2017.

[101] C. Rubio-Maya, E. P. Martinez, C. E. Romero, V. M. A. Diaz, and J. J. Pacheco-Ibarra, "Techno-economic assessment for the integration into a multi-product plant based on cascade utilization of geothermal energy," *Applied Thermal Engineering*, vol. 108, pp. 84-92, Sep 5 2016.

[102] S. Quoilin, M. V. D. Broek, S. Declaye, P. Dewallef, and V. Lemort, "Techno-economic survey of Organic Rankine Cycle (ORC) systems," *Renewable and Sustainable Energy Reviews*, vol. 22, pp. 168-186, 2013.

[103] X. Wang, "Communications with Exergy Company, Italy," *http://exergy-orc.com/*, 2017.

[104] X. Wang, "Communications with Enertime Company, France," *http://www.enertime.com/*, 2017.

[105] S. K. Sanyal, "Cost of geothermal power and factors that affect it," in *Proceedings World Geothermal Congress*, 2005, pp. 24-29.

[106] Enersion, "Cost of the current cooling technology," *Retrieve from: http://enersion.com/cost-of-the-current-cooling-technology/*, April 14 2017.

[107] M. R. Azim, M. S. Amin, and M. A. Shoeb, "Prospect of enhanced geothermal system in baseload power generation," in *Advanced Management Science (ICAMS), 2010 IEEE International Conference on*, 2010, vol. 3, pp. 176-180: IEEE.

[108] C. Augustine, J. W. Tester, B. Anderson, S. Petty, and B. Livesay, "A comparison of geothermal with oil and gas well drilling costs," in *Proceedings of the 31st Workshop on Geothermal Reservoir Engineering*, 2006, pp. 5-19: Curran Associates Inc. ^ eNew York New York.

[109] K. Bloomfield and P. Laney, "Estimating well costs for enhanced geothermal system applications," Idaho National Laboratory (INL)2005.

[110] J. Gifford and R. Grace, "CREST Cost of Renewable Energy Spreadsheet Tool: A Model for Developing Cost-Based Incentives in the United States. User Manual Version 4," ed, 2013.

[111] J. Nathwani and G. Mines, "Cost contributors to geothermal power generation," in *Proceedings World Geothermal Congress*, 2015.

[112] E. S. Rubin, C. Chen, and A. B. Rao, "Cost and performance of fossil fuel power plants with CO2 capture and storage," *Energy policy*, vol. 35, no. 9, pp. 4444-4454, 2007.

[113] "26 USC 45Q: Credit for carbon oxide sequestration," *Retrieve from: http://uscode.house.gov/view.xhtml?req=(title:26%20section:45Q%20edition:prelim)*, 2018.

[114] L. Pan, C. M. Oldenburg, K. Pruess, and Y. S. Wu, "Transient CO_2 leakage and injection in wellbore - reservoir systems for geologic carbon sequestration," *Greenhouse Gases: Science and Technology*, vol. 1, no. 4, pp. 335-350, 2011.

[115] L. Pan, S. W. Webb, and C. M. Oldenburg, "Analytical solution for two-phase flow in a wellbore using the drift-flux model," *Advances in Water Resources*, vol. 34, no. 12, pp. 1656-1665, 2011.

[116] A. Boiler and P. V. Code, "Section I," *Rules For Construction of Power Boilers, Table PW-39, The American Society of Mechanical Engineers, New York*, 2008.

[117] A. Boiler and P. V. Code, "Section II–Materials," *Part D–Properties*, 2008.

[118] R. Mukherjee, "Effectively design shell-and-tube heat exchangers," *Chemical Engineering Progress,* vol. 94, no. 2, pp. 21-37, 1998.

[119] T. L. Bergman and F. P. Incropera, *Fundamentals of heat and mass transfer*. John Wiley & Sons, 2011.

[120] W. S. Janna, *Design of fluid thermal systems*. Cengage Learning, 2014.

Appendixes

A1. Momentum Equations Solved in TOUGH2-T2Well/ECO2N

Conservation of mass and energy:

$$\frac{d}{dt}\int_{V_n} M^{\kappa} dV_n = \int_{\Gamma_n} \mathrm{F}^{\kappa} dV_n \cdot n d\Gamma_n + \int_{V_n} q^{\kappa} dV_n \tag{0.1}$$

Mass accumulation:

$$M^{\kappa} = \phi \sum_{\beta} s_{\beta} \rho_{\beta} X_{\beta}^{\kappa}, \text{for each mass component } \kappa \tag{0.2}$$

Mass flux:

$$\mathrm{F}^{\kappa} = \sum_{\beta} X_{\beta}^{\kappa} \rho_{\beta} \mathrm{u}_{\beta}, \text{for each mass component } \kappa \tag{0.3}$$

Porous medium

Energy flux

$$\mathrm{F}^{NK1} = -\lambda \nabla T + \sum_{\beta} h_{\beta} \rho_{\beta} \mathrm{u}_{\beta} \tag{0.4}$$

Energy accumulation

$$\mathrm{M}^{NK1} = (1-\phi)\rho_R C_R T + \phi \sum_{\beta} \rho_{\beta} S_{\beta} U_{\beta} \tag{0.5}$$

Darcy velocity

$$\mathrm{u}_\beta = -k\frac{k_{r\beta}}{\mu_\beta}(\nabla P_\beta - \rho_\beta \mathrm{g}) \text{ Darcy's Law for each phase } \beta, \text{ with } P_L - P_G = P_c \quad (0.6)$$

Wellbore

Energy flux

$$\mathrm{F}^{NK1} = -\lambda\nabla T + \sum_\beta \rho_\beta S_\beta u_\beta (h_\beta + \frac{u_\beta^2}{2} + gz\cos\theta) \quad (0.7)$$

Energy accumulation

$$\mathrm{M}^{NK1} = \sum_\beta \rho_\beta S_\beta (U_\beta + \frac{u_\beta^2}{2} + gz\cos\theta) \quad (0.8)$$

Phase velocity

$$\begin{aligned} u_G &= C_0 \frac{\rho_m}{\rho_m^*} u_m + \frac{\rho_L}{\rho_m^*} u_d \\ u_L &= \frac{(1-S_G C_0)\rho_m}{(1-S_G)\rho_m^*} u_m + \frac{S_G \rho_G}{(1-S_G)\rho_m^*} u_d \end{aligned} \quad \text{Drift-flux-model} \quad (0.9)$$

The more detailed solution methods and general conservation equations can be found in the documents listed in the reference [23, 26, 27, 86, 114, 115].

A2. Potential ORC Working Fluid Using in This Study

The *T-s* saturation curves for all working fluid candidates considered in this study are illustrated in Figure A–1 and Figure A–2. The physical properties, environmental impacts and safety data for all working fluid candidates are listed in Table A–1. For reference, the *T-s* saturation curve is plotted on both part I and Part II figures.

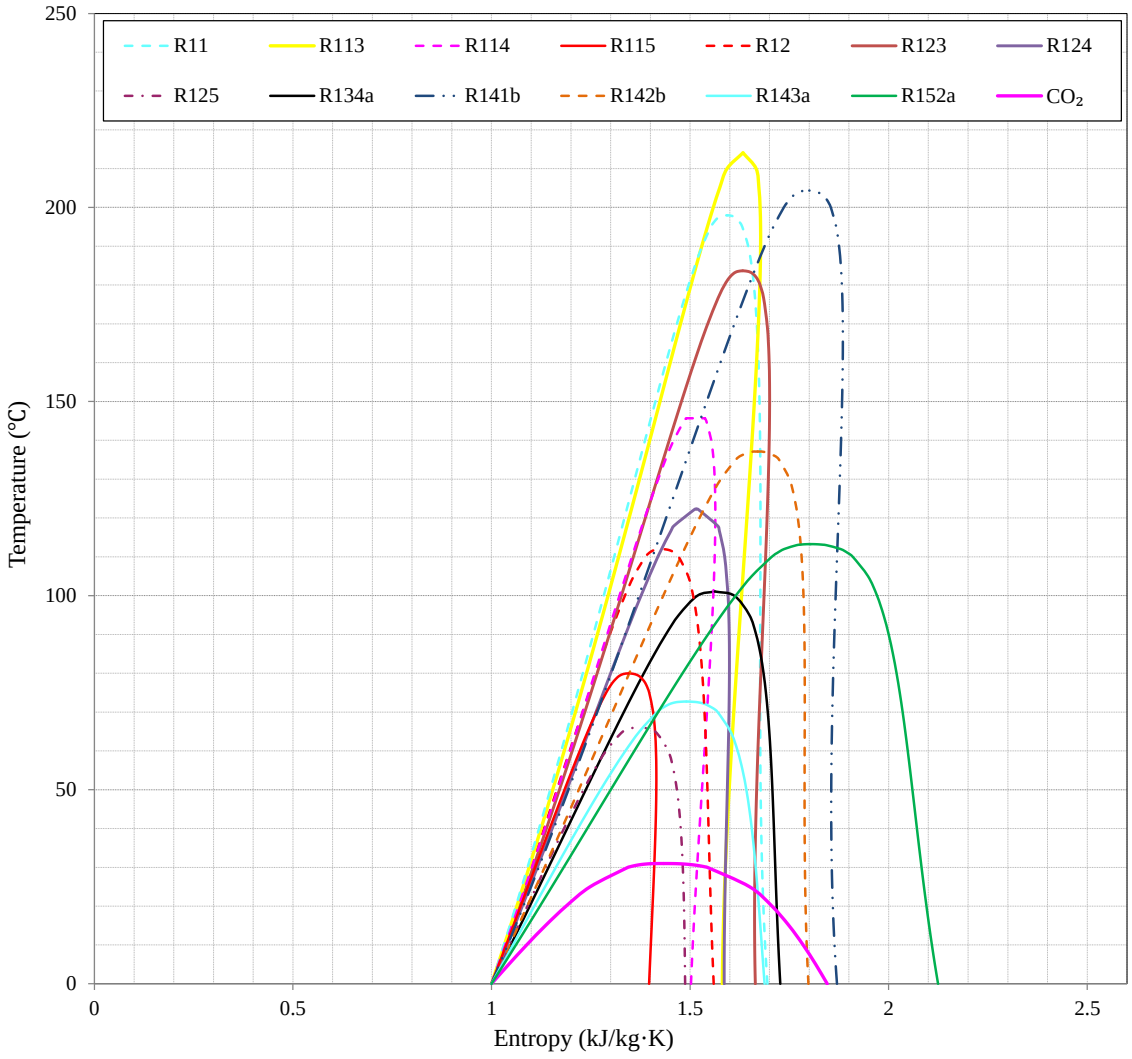

Figure A–1 *T-s* diagrams of potential organic working fluids Part I.

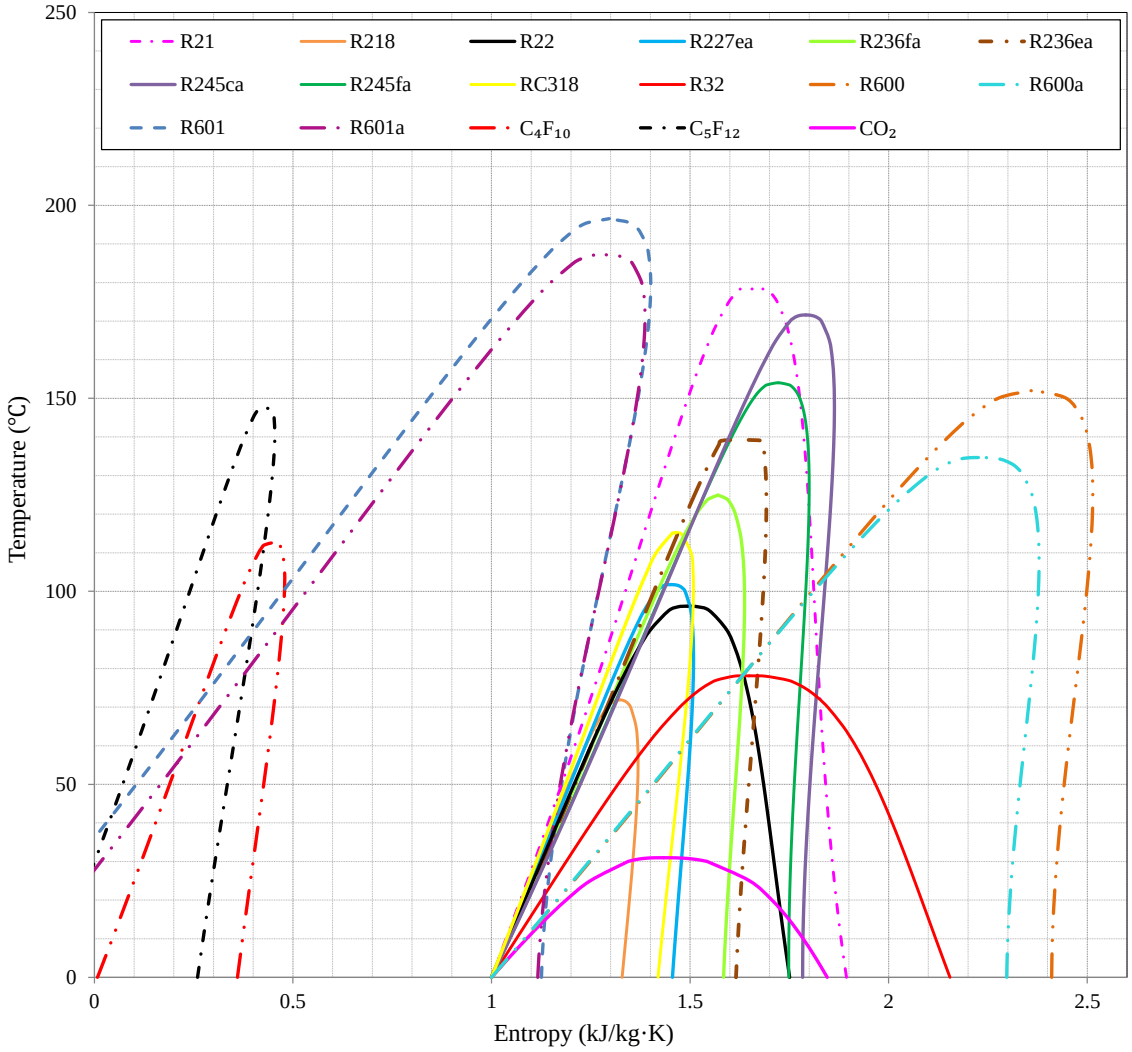

Figure A–2 *T-s* diagrams of potential organic working fluids Part II.

Table A–1 Physical properties, environmental impacts and safety data of potential working fluids.

Potential Working Fluid	Physical Properties				Environmental, Safety and Health Impact				
					Environmental		NFPA 704 Fire Diamond		
	T_{cr} (℃)	P_{cr} (MPa)	Fluid Type	Turning Point (℃)	ODP	GWP 100-yr Horizon	Flammability (Red)	Toxicity (Blue)	Instability (Yellow)
R11	197.96	4.408	Isentropic	118.78	1.0	4750	0	1	0
R113	214.06	3.392	dry	192.18	0.8	6130	0	1	0
R114	145.68	3.257	dry	121.13	1.0	10000	0	2	0
R115	79.95	3.129	dry	52.98	0.6	7370	0	1	0
R12	111.97	4.136	wet	-	1.0	10900	0	2	0
R123	183.68	3.662	dry	150.62	0.02	77	0	2	1
R124	122.28	3.624	dry	82.93	0.022	609	0	1	0
R125	66.02	3.618	wet	-	0	3500	0	1	3
R134a	101.06	4.059	wet	-	0	1430	1	2	0
R141b	204.35	4.212	Isentropic	166.11	0.12	725	1	2	0
R142b	137.11	4.055	Isentropic	73.99	0.07	2310	0	1	0
R143a	72.71	3.761	wet	-	0	4470	4	1	0
R152a	113.26	4.517	wet	-	0	124	4	2	0
R21	178.33	5.181	wet	-	0.04	151	0	1	0
R218	71.87	2.640	dry	55.51	0	8830	0	1	0
R22	96.15	4.990	wet	-	0.05	1810	0	2	1
R227ea	101.75	2.925	dry	82.56	0	3220	0	1	1
R236fa	124.92	3.200	dry	97.47	0	9810	0	1	0
R236ea	139.29	3.502	dry	122.93	0	1370	0	1	0
R245ca	174.42	3.925	dry	147.70	0	693	1	3	0
R245fa	154.01	3.651	dry	127.02	0	1030	1	2	0
RC318	115.23	2.778	dry	100.69	0	10300	0	2	0
R32	78.11	5.782	wet	-	0	675	4	2	1
R365mfc	186.85	3.266	dry	170.44	0	794	0	1	0
C_4F_{10}	113.18	2.323	dry	103.38	0	8860	0	1	0
C_5F_{12}	147.41	2.045	dry	141.17	0	9160	3	1	0
R600	151.98	3.796	dry	125.23	0	4	4	1	0
R600a	134.66	3.629	dry	107.79	0	4	4	1	0
R601	196.55	3.370	dry	179.40	0	0.1	4	1	0
R601a	187.20	3.378	dry	171.10	0	0.1	4	1	0

A3. Annual Chemical Engineering Plant Index (CEPCI)

The Chemical Engineering Plant Cost Index (CEPCI) has been widely considered as an important tool to adjust process plant construction costs from one period to another. The CEPCI data from 2000 to 2017 which have been used in this study are presented in Table A–2.

Table A–2 Annual CEPCI data from 2000 to 2017.

Year	Annual CEPCI
2000	394.1
2001	394.3
2002	395.6
2003	402.0
2004	444.2
2005	468.2
2006	499.6
2007	525.4
2008	575.4
2009	521.9
2010	550.8
2011	585.7
2012	584.6
2013	567.3
2014	576.1
2015	556.8
2016	541.7
2017	535.3

A4. Fixed Tube Sheet Heat Exchanger Design Methods Used in This Study

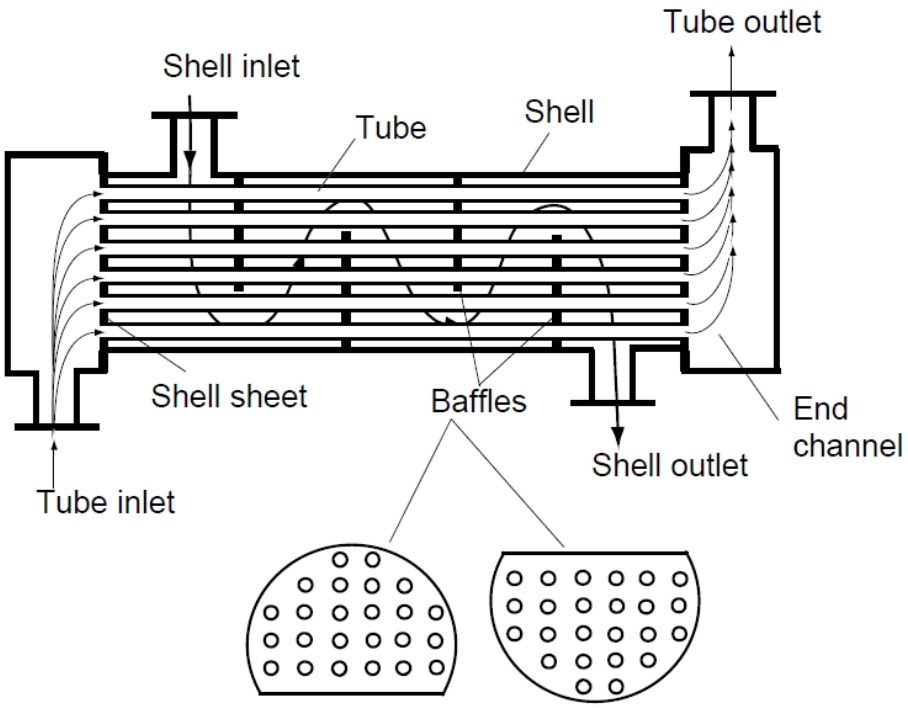

Figure A–3 One-pass fixed tube sheet heat exchanger.

Assumptions:

- Fully developed flow and steady state
- Negligible heat loss to the surroundings
- Constant properties
- Negligible fouling factor

Tube Size Selection and Tube Number Calculation

In this analysis, the bare tube is considered. The equation below is good for tubing up to and including 5 inches (125 mm) outer diameter, which can be found in ASME section I, PG-27.2.1 [116]:

$$t = \frac{Pd_o}{2S + P} + 0.005d_o + e \tag{0.10}$$

Where t = Minimum design wall thickness (in);

P = Design pressure (psi);

d_o = Tube outside diameter (in);

e = Thickness factor (0.04 for expanded tubes; 0 for strength welded tubes);

S = Maximum allowable stress for SA-179 which is 26000 psi in ASME Section II [117].

A reasonable effectiveness was picked to calculate the heat transfer area. Then, the length of the heat exchanger can be calculated. The size of the heat exchanger can be determined.

Shell-tube Heat Exchanger Sizing

Dimensions of the shell-tube heat exchanger:

L = Tube length

N_t = Number of tube

N_p = Number of pass

D_s = Shell side diameter

N_b = Number of Baffle

B = Baffle spacing which can be obtained by $L/(N_b + 1)$

d_o, d_i = Tube outer and inner diameters

D_e = Tube equivalent diameter

P_t = Tube pitch

C_t = Clearance between adjacent tubes

A_c = Cross flow area of shell

v_i = Tube flow velocity

v_o = Shell flow velocity

$ShadeArea = CL \bullet P_t^{\,2}$, where CL is the tube layout constant

CL = 1 Square-pitch layout

CL = sin (60°) Triangular-pitch layout

CTP = Tube count constant

CTP = 0.93 One pass

CTP = 0.9 Two pass

CTP = 0.85 Three pass

The squared-pitch layout is selected shown in Figure 2-4.

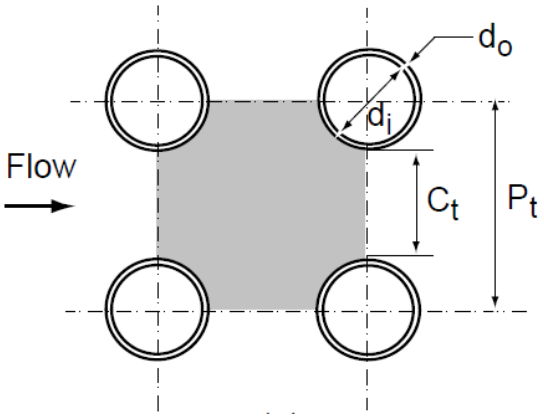

$$D_e = \frac{4\left(P_t^2 - \frac{\pi d_o^2}{4}\right)}{\pi d_o} \qquad (0.11)$$

Figure A–4 Square-pitch layout and the equivalent diameter equation.

Shell Cross Area

The number of tube can be predicted by:

$$N_t = CTP\frac{\pi D_s^2/4}{\text{ShadeArea}} = \frac{\pi}{4}\left(\frac{CTP}{CL}\right)\frac{D_s^2}{P_t^2} \tag{0.12}$$

The cross flow area of the shell:

$$A_c = \frac{D_s C_t B}{P_t} \tag{0.13}$$

The maximum baffle spacing is the shell inside diameter. The recommended minimum tube pitch is 1.25 times the tube O.D. [118].

Tube Side Heat Transfer and Pressure Drop Correlations and Calculations [119]

Tube Side Heat Transfer Correlations

The tube side Reynolds number

$$R_e = \frac{\rho v_i d_i}{\mu} \tag{0.14}$$

For laminar flow ($R_e < 2300$), the Nusselt number can be obtained from:

$$\text{Nu}_D = \frac{h_i d_i}{k_f} = 1.86\left(\frac{d_i R_e P_r}{L}\right)^{\frac{1}{3}}\left(\frac{\mu}{\mu_s}\right)^{0.14} \tag{0.15}$$

The equation has been confirmed experimentally for the range of conditions:

$$\begin{bmatrix} 0.48 < P_r < 16,700 \\ 0.0044 < \dfrac{\mu}{\mu_s} < 9.75 \\ \text{Nu}_D = 3.66 \text{ if } \text{Nu}_D < 3.66 \end{bmatrix} \tag{0.16}$$

$$f = \frac{16}{\text{Re}}$$

For turbulent flow ($\text{Re} > 2300$), the Nusselt number can be obtained from:

$$\mathrm{Nu}_D = \frac{hd_i}{k_f} = \frac{\left(\frac{f}{8}\right)(\mathrm{Re}-1000)P_r}{1+12.7\left(\frac{f}{8}\right)^{0.5}\left(P_r^{\frac{2}{3}}-1\right)} \tag{0.17}$$

The equation has been confirmed experimentally for the range of conditions:

$$\begin{bmatrix} 3000 < \mathrm{Re} < 5\times10^6 \\ 0.5 \le P_r \le 2{,}000 \end{bmatrix} \tag{0.18}$$
$$f = (0.790\ln \mathrm{Re} - 1.64)^{-2}$$

Tube Side Pressure Drop Correlations

$$\Delta P = N_p \frac{f \cdot L}{d_i}\frac{\rho v^2}{2} \tag{0.19}$$

$$f = (0.790\ln \mathrm{Re} - 1.64)^{-2} \tag{0.20}$$

Shell Side Heat Transfer and Pressure Drop Correlations

Shell Side Single Phase Heat Transfer Correlations

The shell side Reynolds number:

$$\mathrm{Re} = \frac{\rho v_o D_e}{\mu} \tag{0.21}$$

The single phase shell side Nusselt number can be obtained from:

$$\mathrm{Nu}_D = \frac{h_o D_e}{k_f} = C\,\mathrm{Re}^n P_r^{\frac{1}{3}} \tag{0.22}$$
$$2000 < \mathrm{Re} < 1\times10^6$$

Table A–3 Modified correlation of Grimson for heat transfer in tube banks of 10 rows or more for square-pitch layout.

P_t / d_o							
1.25		1.5		2.0		3.0	
C	n	C	n	C	n	C	n
0.386	0.592	0.278	0.620	0.254	0.632	0.317	0.608

Shell Side Single Phase Pressure Drop Correlations (Kern Method)[120]

$$\Delta P = f \frac{D_s}{D_e}\left(N_b + 1\right)\frac{\rho v_o^2}{2} \tag{0.23}$$

$$f = \exp(0.576 - 0.19 \ln \mathrm{Re}) \qquad 400 \le \mathrm{Re} \le 1\times10^6 \tag{0.24}$$

Heat Transfer Area Calculation (ε – NTU Method)

The overall heat transfer coefficient

$$U = \frac{1/A_o}{\dfrac{1}{h_o A_o} + \dfrac{\ln\left(\dfrac{d_o}{d_i}\right)}{2\pi k L} + \dfrac{1}{h_i A_i}} \tag{0.25}$$

Where k = Thermal Conductivity of Tube Material

For the heat exchanger type in this analysis which is counterflow heat exchangers:

$$\mathrm{NTU} = \frac{UA}{C_{min}} = \frac{1}{C_r - 1}\ln\left(\frac{\varepsilon - 1}{\varepsilon C_r - 1}\right) \qquad C_r < 1 \tag{0.26}$$

$$\mathrm{NTU} = \frac{UA}{C_{min}} = \frac{\varepsilon}{1-\varepsilon} \qquad C_r = 1 \tag{0.27}$$

where NTU = Number of transfer units

U = Overall heat transfer coefficient

A = Overall heat transfer area

$\varepsilon =$ Heat exchanger effectiveness

$C_r =$ Capacity ratio, C_{min}/C_{max}

C_{min} and C_{max} = Minimum and maximum capacity rate

A reasonable effectiveness can be selected to calculate the heat transfer area. Then, the length of the heat exchanger can be calculated. The size of the heat exchanger is determined.

VITA

Xingchao Wang was born on November 2, 1987 in Jiuquan City, P. R. China. He is the only child of Mr. Duoying Wang and Mrs. Xueqin Li. Mr. Wang received his bachelor degree in 2010 at the Department of Thermal Engineering in Tsinghua University, China with the thesis entitled "The Investigation and Design of Closed Cooling Towers on Environmental Protection and Water-saving Technologies". After graduation, he worked at Tsinghua University as an assistant engineer. Subsequently, he went to Lehigh University in the U.S. and received his Master of Science degree in Mechanical Engineering in 2014 under the supervision of Dr. Edward K. Levy with the thesis entitled "Chemkin Simulation of Mercury Oxidation in a Condensing Heat Exchanger". Xingchao Wang is expected to obtain his Doctor of Philosophy in Mechanical Engineering in May, 2018.

Xingchao Wang was involved in a number of energy-related projects funded by the U.S. Department of Energy, utility companies, and other governmental agencies. Mr. Wang has plentiful experience on resolving problems in energy areas. He is also skillful to use tools and resources for scientific research and technology development. Mr. Wang's research is focusing on utilizing a variety of energy sources for electric power generation, including using conventional fossil fuels and renewable energy.